Ollscoil na hÉireann, Corcaigh

National University of Ireland, Cork

University College Cork, Ireland
Coláiste na hOllscoile Corcaigh

Deciphering Archives of Magmatic, Tectonic and Hydrothermal Events throughout Emplacement and Crystallisation of Igneous Intrusions

Thesis presented by

Benjamin Latimer
0000-0003-0235-9693

for the degree of

Doctor of Philosophy
University College Cork
School of Biological Earth and Environmental Sciences
Head of School: Dr Antony Knights

Supervisory Team:
Dr. John Reavy
Dr. William McCarthy
Dr. Tobias Mattsson

2025

Table of Contents

Declaration

This is to certify that the work I am submitting is my own and has not been submitted for another degree, either at University College Cork or elsewhere. All external references and sources are clearly acknowledged and identified within the contents. I have read and understood the regulations of University College Cork concerning plagiarism and intellectual property.

Signed: Ben Latimer

General Acknowledgements

I’m not much of a talker, so I’ll keep this as brief as possible.

Getting to the end of the last four years would have been impossible without the support of many people, too many to thank individually. While I have a few people I’d like to mention in particular here, I do want to give a general thank you to everyone who has put up with my countless ramblings on rocks and magnets.

I would be remiss to not begin by thanking my three supervisors, who’s guidance has been vital over the last four years. Dr. J. Reavy has been an amazing support, willing to go above and beyond to help me however he can. It has been a real privilege to work with him, and I look forward to many more musings on all things magmatic in the future (ideally while on top of a Munro or Corbett!). My adventures into the dark art of magnets, magmas and fluids would not have been possible without the patience, advice and enthusiasm of Dr. W. McCarthy. Even when I seemed to be on the warpath, destroying every bit of his lab and field kit (sorry again about the drills!), he has always been willing to help, and his guidance is greatly appreciated. I met Dr. T. Mattsson on my first visit to the lab in St Andrews, where he offered me his spare room for the week and fed me meatballs, potatoes and beer. I knew immediately that he would make a great supervisor. His knowledge, advice and Swedish sensibilities have been great over the last four years, especially when one or all three of the Irish lads were starting to get carried away.

I’d like to thank everyone at the Geology Department at UCC, it’s a place with many fond memories, made possible by the fantastic work from all the teaching and admin staff there. In particular, I’d like to thank Dr. J. Reavy, Dr. P. Meere and Dr. D.E Jarvis, whose dedication to teaching made it such an amazing place to study as an undergrad. I’d also like to thank the many wonderful people that I’ve met at the at School of Earth and Environmental Sciences at the University of St Andrews while carrying out lab work. Despite turning up sporadically and unannounced every few months, it has always been such a welcoming place, with many good friends made along the way. Thanks to Maddie S, Curtis and

Celeste who all provided a bed/couch for one of my many visits, which is greatly appreciated.

A special thank you is due Oli, Emily and Vince who have all had to share a lab/office with me and the especially long rock-chats which go along with that. I'd also like to thank Charlie for her support and patience with my many questions on all things crystallographic and for introducing me to wonder of orbicular granite and curvy crystals. Thanks to Sebastian for being a great roommate, friend and for his sound wisdom that all problems are fixed with a coffee, beer or cigarette. I'd also like to thank Tesni, who has dragged me out of the house every few weeks in the lead up to submitting to stop me from going insane and for the culinary breakthrough that was 'Roast East'.

Thanks to Kevin Murphy for his advice and late-evening chats when back home in West Cork. My aunt Jenny and godfather Mike are also thanked for providing places to stay and help with critical drill logistics during my aforementioned destroying spree in the Summer of 2022.

Finally, and most importantly, I'd like to thank my parents for their unwavering support and my brother Jamie who is currently off in the Antarctic showing the rest of us how it's done. You guys are the best.

Funding Acknowledgements

This thesis and the publications generated have emanated from research conducted with the financial support of Taighde Éireann – Research Ireland under Grant number GOIPG 2021 244.

Research Data Access

All data generated from this thesis are available within the provided appendices.

Abstract

Igneous intrusions play a crucial role within magma plumbing systems, acting as sites of magma storage and evolution. Alongside their role in feeding volcanic eruptions, they provide an important source of heat within the crust, driving the circulation of hydrothermal fluids required to form economic ore deposits and geothermal resources. Therefore, there is a socio-economic importance to better constrain how igneous intrusions form and their interactions with the surrounding crust.

Throughout formation, intrusions are exposed to internal and external stress regimes, with internal stress is sourced from processes intrinsic to the formation of magma chambers. In contrast, external stress is derived from other crustal processes such as tectonic deformation. The interplay between these stress regimes controls the architecture and features that form within an intrusion, providing an archive of the palaeostresses with which it has interacted throughout crystallisation. This strain archive from intrusions has been shown to offer a unique record of external and internal events, giving insight into magmatic processes and the tectonic framework active during and after magma emplacement.

While representing a powerful tool which can be applied to gain insight into crustal events, the record of strain within igneous intrusions is flawed by several issues. In this thesis, the Fanad Pluton, NW Ireland is used as test site to address three of these issues. The results of this thesis demonstrate:

1. Magmatic enclaves can archive multiple internal fabrics, providing a unique insight into magmatic fabric development within their surrounding host intrusion and its origin from magmatic or tectonic processes.
2. Igneous intrusions preserve a highly sensitive and temporal record of strain when archives from magmatic, submagmatic and subsolidus features are compared.
3. utilising a multi-disciplinary magnetic-hyperspectral approach, a robust characterisation of the distribution and intensity of hydrothermal alteration

can be performed. This characterisation can then be used to evaluate the significance of magnetic fabrics in relation to magmatic, tectonic and hydrothermal fluid transport processes.

With these issues no longer outstanding, future studies should be able to identify a more comprehensive record of strain from igneous intrusions as it relates to magmatic, tectonic and hydrothermal alteration processes.

Chapter 1: Introduction

1.1 Project Motivation

The movement of magma from the lower crust to the Earth's surface is facilitated through complex magma plumbing systems (Cruden and Weinberg, 2018; Sparks et al., 2019). As part of these systems, magma undergoes multiple stages of lateral and upward transport, interspersed with periods of stalling and storage within the crust (Cashman et al., 2017; Magee et al., 2019). During storage, magma accumulates to form large bodies referred to (amongst other terms) as magma chambers, igneous intrusions or plutons (Marsh, 1989; Annen et al., 2015). These magma chambers act as reservoirs for subsequent magma transport to form intrusions in upper levels of the crust, or in sub-volcanic settings, to feed volcanic eruptions (Bachmann and Huber, 2016; Rhodes et al., 2024). Outside of their role within magma plumbing systems, the interaction between igneous intrusions, their surrounding country rock and tectonically controlled crustal deformation plays a critical role in a number of geological processes which are of socio-economic importance. For example, as magma chambers form and crystallise, they provide long-lasting sources of heat in the crust, driving circulation of hydrothermal fluids required in the formation of a range of economic ore deposits and geothermal resources (Sillitoe, 2010; Stimac et al., 2015; Audétat, 2019; Heap et al., 2020). When intrusions form in sub-volcanic settings, this cycling of hydrothermal fluids can also cause significant alteration to the surrounding country rock, affecting their mechanical properties and subsequent deformation during volcanic hazards (Heap et al., 2022; Pereira et al., 2024). In order to better understand these processes as they occurred in the past and in the present, there is a fundamental need to advance our knowledge of how igneous intrusions form and interact with the surrounding crust. To understand processes occurring at mid to lower crust levels, the study of plutons which formed at these depths and were later exhumed to the surface provides the most straightforward record to examine.

1.2 Intrusions as Crustal Archives

Throughout their formation, magma chambers are exposed to stress originating from internal and external sources. Internal stress is sourced from processes intrinsic to the formation of magma chambers, such as magma transport, magma remobilisation and magma overpressure (e.g., Alasino et al., 2019; Rhodes et al., 2021; Neves et al., 2023). External stress is derived from other crustal processes, normally tectonic stress, being imparted both syn- and post-crystallisation (e.g., Pawley and Collins 2002; Benn 2009; Tomek et al., 2024). As intrusions form, the stress regimes they interact with control their architecture and the features that form within them (Paterson et al., 2019; Alasino et al., 2025). These include macroscale features such as the size and shape of plutons (O'Driscoll et al., 2006; De Saint Blanquat et al., 2011); mesoscale features such as magmatic sheets, enclaves and subsolidus faults/fractures (e.g., Molyneux and Hutton 2000; Paterson et al., 2008; Ardill et al., 2020); and microscale alignment of minerals, forming so called petrofabrics (e.g., Žák et al., 2007; Tomek et al., 2017; Mattsson et al., 2024). Therefore, the structure of intrusions can be examined at multiple spatial scales, using this as an archive of the palaeostresses with which they have interacted throughout crystallisation.

This record of strain from intrusions has been used in numerous studies in the testing of hypotheses around magmatic and tectonic processes. For example, the validity of magma emplacement mechanisms has been tested repeatedly through the features formed within intrusions, with the incorporation of new records of strain often leading to reinterpretation of active mechanisms (Stevenson et al., 2008b; McCarthy et al., 2015b; Stevenson and Grove, 2018). Similarly, the role of magmatic and/or tectonic strain on the formation of plutons has been tested using a range of strain archives, often decrypting a complex interplay between external stress regimes and intrinsic stress (e.g., Petronis et al., 2012; McCarthy et al., 2015b; Lawrence et al., 2022).

Intrusions often provide a unique archive of external and internal events, due in part to the rheological transitions they undergo throughout crystallisation (Vigneresse et al., 1996; Marsh, 1996; Cashman et al., 2017). This allows them to record stress regimes while in a magmatic (intrusion is predominantly a magma with minimal crystal content), submagmatic (intrusion is mainly crystals with interstitial magma) and subsolidus (i.e., fully crystallised) state, with the non-Newtonian properties of magma allowing both deformation mechanisms to occur simultaneously at certain rheologies (Hibbard and Watters, 1985; Smith, 1997). Submagmatic rheologies can be refined further, with magma initially behaving as crystal-rich suspension, before transitioning into a rigid crystal framework with interstitial magma referred to as a mush-state (Hibbard and Watters, 1985).

However, while igneous plutons have been applied as powerful tools to gain insight into crustal events, their record of strain is flawed by several issues. The work of this thesis attempts to address three of these issues, forming the basis of the data chapters. In doing so, the work of this thesis represents an advancement in our understanding of the strain archive of intrusions, obviating three outstanding issues, and allowing future studies to decipher a more comprehensive record of strain as it relates to magmatic, tectonic and hydrothermal alteration processes.

1.3 Key Research Questions

1.3.1 Determining the Origin of Magmatic Fabrics

Petrofabrics are one of the most commonly interpreted records of strain within igneous intrusions, especially as a tool to understand magmatic and tectonic processes (Horsman et al., 2005; Mattsson et al., 2018; Fiannacca et al., 2021). Petrofabrics are often classified based on the timing of their formation relative to crystallisation, as indicated by microstructural evidence, generally categorised as having a magmatic, submagmatic or subsolidus origin (Hutton, 1988; Paterson et al., 1989; Passchier and Trouw, 2005). Establishing the relative timing of petrofabric formation can exclude certain processes as their source; for example, a pervasive fabric formed in the subsolidus likely reflects an external, tectonic stress regime, rather than a magmatic process (Hutton, 1982; Žák et al., 2012; Bella Nke et al., 2022). However, for magmatic and submagmatic fabrics which formed during magma chamber crystallisation, petrofabrics can originate from an external or internal stress regime. This has led to magmatic fabrics being reported as a 'primary emplacement fabric' formed in response to magma chamber accumulation within some intrusions (e.g., Stevenson et al., 2007; Magee et al., 2012), while simultaneously being interpreted to reflect an overprint by tectonic deformation within others (McCarthy et al., 2015c; Burton-Johnson et al., 2019, 2022a).

The distinction between potential stress regimes from petrofabrics alone is often ambiguous, with other magmatic features required to give further insight into the origin of wider petrofabric formation (e.g., Žák and Klomínský 2007; Paterson et al., 2008; Stevenson 2009). A feature previously used extensively to complement petrofabrics within granitic intrusions was magmatic enclaves, the disaggregation of a more mafic to intermediate magma within the pluton, commonly found in magma mingling zones (Vernon, 1990; D'lemos, 1996). Since the characterisation of the magmatic origin of enclaves (Vernon, 1984), their morphological properties (size, shape, alignment) in relation to petrofabrics and the wider architecture of plutons have been used as an archive of magma chamber processes (e.g., Miller and Paterson 1994; Carreras et al., 2004; Muir and Vaughan 2017). However, the use of enclave morphology as an archive of strain is impaired by the rheology contrast to the surrounding granitic magma that develops throughout cooling, arising from compositional differences between magmas (Scaillet et al., 2000; Paterson et al., 2004; Caricchi et al., 2012). While negating the use of morphology in isolation to record strain, it is more ambiguous how this rheology contrast impacts the internal petrofabric of enclaves and its insight into the fabric of its surrounding intrusion (Hrouda et al., 1999; Smith, 2000; Žák et al., 2010).

The first data chapter of this thesis (Chapter 4) investigates the significance of internal enclave petrofabrics when compared to their morphological properties, determining if they can elucidate the palaeostress responsible for magmatic fabrics within the wider igneous intrusion.

1.3.2 The Sensitivity of Intrusions to Successive Strain Events

As part of magma plumbing systems, multiple magma chambers are often formed in succession or simultaneously, creating so called batholiths or igneous complexes (Neilson et al., 2009a; Anderson et al., 2018; Searle et al., 2024). This allows for the records of strain from the plutons within igneous complexes to be compared, giving insight on regional-scale magmatic and tectonic processes (Jacques and Reavy, 1994; Stevenson et al., 2008a; Gonçalves et al., 2025). This can allow intrusions to help refine kinematic models for orogenic events, preserving a record of strain which can complement data from other sources within the crust (Hutton and Alsop, 1996; McCarthy et al., 2015c; Strachan et al., 2020). However, a consistent archive of strain across an orogenic front can become disjointed when records across multiple igneous complexes are examined, with some intrusions reportedly dominated by internal magmatic strain, while adjacent, coeval intrusions record pervasive tectonic deformation (e.g., Stevenson et al., 2007; Petronis et al., 2012; Anderson et al., 2018).

While pluton-scale studies often define a single magmatic or tectonic process as the source of strain, the ability to preserve multiple strain archives within a single intrusion is well established, in the form of different magmatic structures and/or through multiple iterations of the same structure (Žák et al., 2008b; Di Chiara et al., 2020; Mattsson et al., 2024). While multiple fabrics may form in response to the same palaeostress regime (e.g., Pawley and Collins 2002; Ardill et al. 2020; Köpping et al. 2023), they can reflect subsequent overprinting from a transition in an active stress regime (Zibra et al., 2012; Tomek et al., 2017; Neves et al., 2023).

The second data chapter of this thesis (Chapter 5) aims to understand the sensitivity of a single pluton to successive palaeostresses, determining if a record from multiple magmatic and tectonic processes can be identified. Records of strain preserved throughout crystallisation are utilised, comparing the measured record to proposed kinematic models and available geochronological data, assessing how a comprehensive archive of strain from a single intrusion compares to archives obtained across multiple igneous complexes within an orogenic setting.

1.3.3 Does Hydrothermal Alteration Destroy Strain Archives

Hydrothermal alteration is a process frequently observed within igneous intrusions, often associated with features of tectonic deformation, yet its impact on archives of strain is poorly constrained. In particular, there is a lack of consensus on the impact of hydrothermal alteration on magnetic fabrics, a tool commonly used to measure petrofabric development (e.g., Ferré et al., 1999; Raposo et al., 2004; Petronis et al., 2009). Fluid-rock interactions have been reported to induce a range of mineralogical changes in the phases which control magnetic fabrics, with partial to complete obliteration of magnetic fabrics observed (e.g., Just et al., 2004; Petronis et al., 2011; Quintela et al., 2025). This range of responses indicates that there is a potential threshold to alteration intensity, below which magnetic fabrics can still be used as a significant tool to understand petrofabric development, and above which any pre-existing petrofabrics are obliterated. However, determining a systematic trend in alteration intensity using characterisation methods that directly correlate with magnetic properties has not been carried out successfully, questioning the validity of interpretations from magnetic fabric data collected from hydrothermally altered rocks (Just and Kontny, 2012; Nédélec et al., 2015).

The final data chapter of this thesis (Chapter 6) aims to provide a framework of analysis to determine the threshold of alteration intensity where magnetic fabrics from hydrothermally altered rocks can no longer provide a meaningful record of strain from magmatic and tectonic processes. A multi-disciplinary approach is taken to quantifying hydrothermal alteration, before measuring multiple magnetic fabrics to investigate what sources of stress they preserve with varying alteration intensities.

Chapter 2: Analytical Methods

2.1 Introduction

As part of this thesis, several methods are used to extract archives of strain formed during and after crystallisation of an igneous intrusion. This includes techniques analysing intrapluton feature alignment at the outcrop-scale and those measuring grain-scale fabric development. To complement fabric measurements, two types of characterisation methods were also carried out. Firstly, several techniques were used to characterise the mineralogy controlling a given fabric. This was then followed by a characterisation of the nature of the fabric, distinguishing pre-existing fabrics from those formed during subsequent overprinting events. As part of each data chapter, a detailed breakdown of the analytical methods is provided, specific to the approach used in each study. This chapter provides an overview of all methods utilised, their general theory and any caveats to the interpretation of the data they generate.

2.2 Magnetic Fabric Analysis

A key method applied within all three data chapters is the measurement of magnetic fabrics, whereby the anisotropy of magnetic susceptibility (AMS) or the anisotropy of magnetic remanence (AMR) within orientated samples is used to define bulk mineral alignment, or the alignment of a sub-group of minerals (Jackson, 1991; Tarling and Hrouda, 1993). AMS and AMR fabrics are a common component of studies of igneous (Koopmans et al., 2022; Jones et al., 2025a; Williams et al., 2025), sedimentary (Parés, 2004; Pueyo Anchuela et al., 2011; Chatterjee et al., 2023) and tectonic processes (e.g., Borradaile and Jackson 2004; Almqvist et al., 2011; Hrouda and Chadima 2020), providing time-efficient measurement of petrofabric development across metre-scale to kilometre-scale research areas.

AMS and AMR are applied within the context of this thesis to understand the development of petrofabrics in response to magmatic, tectonic and hydrothermal alteration processes. AMS is used as a proxy for bulk mineral alignment, with multiple methods of AMR measured to investigate anomalous fabric measurement from AMS and test for the development of subfabrics masked from bulk magnetic methods (Tarling and Hrouda, 1993; Mattsson et al., 2021).

2.2.1 Sample Collection and Preparation

AMS and AMR fabrics were measured from orientated rock core samples, allowing the measured mineral alignment to be analysed based on its in-situ position in the field.

Rock core samples were predominantly drilled in the field, with 25 mm diameter cores collected using a handheld drill attached with non-magnetic drill bits, orientated with a Pomeroy orientation fixture and Brunton Compass. These core samples were then taken to the drilling and cutting facility of the M^3Ore lab at the University of St Andrews, with each core cut into 25 mm x 22 mm cylindrical subsamples using a non-magnetic saw. Alongside field drilling, block samples were orientated and collected in the field, with the 25 mm diameter cores drilled at the University of St Andrews using a drill press and cut into cylindrical subsamples as described previously.

Alongside their use for AMS and AMR, the prepared subsamples were also used as part of rock magnetic characterisation, petrography and hyperspectral reflectance analysis.

2.2.2 Magnetic Susceptibility and Remanence Theory

2.2.2.1 Crystal-Scale Magnetic Susceptibility and Remanence

When an electromagnetic field is applied in a given direction on a mineral, a magnetic moment is formed in response from the aligned orbiting and axial spin of electrons within its atomic structure, inducing magnetisation (Tarling and Hrouda, 1993; Dunlop and Özdemir, 1997). As shown in equation (1), this magnetisation (M) is a function of the strength of the applied field (H) and the magnetic susceptibility (μ) of the mineral, a dimensionless parameter given in SI units (Tarling and Hrouda, 1993):

$$(1)\ M = \mu H$$

Minerals which induce a very weak magnetisation in the opposite direction of the applied field are termed diamagnetic, while those which induce a weak magnetisation parallel to the direction of the applied field are termed paramagnetic (Dunlop and Özdemir, 1997). Most minerals are diamagnetic or paramagnetic in nature, with major silicate minerals such as quartz, feldspar and calcite being diamagnetic, while Fe-Mg minerals amphibole, biotite and pyroxene are paramagnetic (Tarling and Hrouda, 1993). A subset of minerals are ferromagnetic (*senso lato*), which includes iron oxides such as magnetite and hematite, iron hydroxides such as goethite and iron sulphides such as pyrrhotite (Tarling and Hrouda, 1993; Worm et al., 1993). Ferromagnetic minerals induce a much larger magnetisation in an applied field relative to paramagnetic and diamagnetic minerals, due to the coupling of electron spins in outer orbitals of cations, causing a spontaneous magnetisation of minerals (Tarling and Hrouda, 1993). Once imparted, this magnetisation is retained when the applied field is removed, referred to as a remanent magnetisation or magnetic remanence and is a diagnostic property of ferromagnetic minerals (Dunlop and Özdemir, 1997).

2.2.2.2 Magnetic Domains within Ferromagnetic Minerals

The spontaneous magnetisation of ferromagnetic minerals is caused by two quantum-mechanical forces, depending on whether coupled electrons are from immediately adjacent cations, forming an exchange force, or if an intermediate anion separates them, forming a superexchange force (Tarling and Hrouda, 1993). These forces form an internal magnetising and external demagnetising field, which are equal in strength and opposite in direction (Tarling and Hrouda, 1993; Dunlop and Özdemir, 1997). Within areas of minerals ≈0.1 μm, parallel electron couplings form a so-called magnetic domain, producing a single internal and external field (Tarling and Hrouda, 1993). Once >0.1 μm, it is more energy efficient to divide coupled electrons into multiple ≈0.1 μm domains within a mineral, which are separated by Bloch walls (Tarling and Hrouda, 1993; Dunlop and Özdemir, 1997). Therefore, ferromagnetic minerals can be separated based on their ‘domain state’, with those ≤0.1 μm referred to as single domain (SD) grains and those ≥0.1 μm referred to as multidomain (MD) grains (Tarling and Hrouda, 1993; Dunlop and Özdemir, 1997). Minerals smaller <0.03 μm are too small for coupling of electrons to occur and display super-paramagnetic (SP) behaviour, whereby they rapidly magnetise but do not retain a remanent magnetisation (Dunlop and Özdemir, 1997).

2.2.2.3 Rock-Scale Magnetic Susceptibility and Remanence

When a rock sample is placed within an electromagnetic field of known strength and direction, the induced magnetisation is a combined response from all minerals in the sample, from which the bulk susceptibility (*k*) of the lithology can be calculated from equation (2) (Tarling and Hrouda, 1993):

$$(2)\ k = \frac{M}{H}$$

Due to the relative difference in magnetisation induced under the same strength of field, ferromagnetic minerals may dominate the bulk susceptibility of a lithology even when present in very low modal abundance (>0.1%), with paramagnetic minerals becoming dominant when ferromagnetic minerals are absent or <0.1% (Tarling and Hrouda, 1993). While diamagnetic minerals will contribute to bulk susceptibility, they are unlikely to be the dominant phase unless there is a near-absence of ferromagnetic and paramagnetic minerals (Biedermann, 2018).

2.2.3 Measurement of Anisotropy of Magnetic Susceptibility (AMS)

AMS is a measurement of the directional dependency of magnetic susceptibility in three dimensions (Tarling and Hrouda, 1993). Subsamples are placed within a kappabridge and rotated while a constant electromagnetic field is applied, with *k* measured in 15 – 320 different orientations, depending on the setup used. The measured *k* values are used to calculate a second-rank magnetic susceptibility tensor (Jelinek, 1977). The eigenvalues of this tensor define three axes, which are the direction of maximum (k_1), intermediate (k_2) and minimum (k_3) magnetic susceptivity (Khan, 1962). These axes are used to define a triaxial ellipsoid, which represents the magnetic fabric from AMS, with k_1 defining the magnetic lineation and the plane intersecting k_1 and k_2 where k_3 is the pole defining the magnetic foliation (Tarling and Hrouda, 1993). AMS is measured in all subsamples at a given sampling site and averaged to get a representative magnetic fabric (Jelinek, 1978; Tarling and Hrouda, 1993).

2.2.3.1 Statistical Parameters of AMS

Alongside the orientation of the magnetic lineation and foliation, a number of statistical parameters can be calculated for the AMS ellipsoid which describe the magnetic fabric and can be used to compare its variation across individual subsamples and sample sites (Jelinek, 1981; Tarling and Hrouda, 1993).

Whereas multiple parameters can be calculated (see Tarling and Hrouda 1993) three parameters are used across the data chapters to describe the variation in AMS fabrics. Mean susceptibility (*Kmean*) reflects the arithmetic mean of the k_1 – k_3 axes and gives a broad indicator of the dominant contribution of ferromagnetic or paramagnetic minerals to an AMS ellipsoid

$$(3)\ Kmean = \frac{k_1+k_2+k_3}{3}$$

The corrected degree of anisotropy (P_j) calculates the separation of the k_1 – k_3 axes, describing the strength of the measured AMS fabric

$$(4)\ P_j = \exp\sqrt{2((\eta_1-\eta_{mean})^2+(\eta_2-\eta_{mean})^2+(\eta_3-\eta_{mean})^2)}$$

$$\text{where } \eta_x = \ln(k_x)\,, x = 1,2,3$$

while the corrected shape factor (T) describes shape of the AMS ellipsoid (Jelinek, 1981; Tarling and Hrouda, 1993)

$$(5)\ T = \frac{2\eta_2-\eta_1-\eta_3}{\eta_1-\eta_3}$$

Additionally, an F-test (Hext, 1963; Jelinek, 1977) was carried out for each subsample, testing the statistical significance of the measured AMS ellipsoid. For subsamples with an F-test ≥4, it can be said with 95% confidence that the difference in k_1 – k_3 axes is large enough that the AMS ellipsoid measures an anisotropy to magnetic susceptibility, while subsamples below this value likely measure an isotropic magnetic susceptibility.

2.2.4 Measurement of Anisotropy of Magnetic Remanence (AMR)

AMR measures the directional dependency of magnetic remanence in three dimensions within a measured subsample (Jackson, 1991). Remanent magnetisation is strongest when ferromagnetic minerals are magnetised along their crystallographic long axis direction (Dunlop and Özdemir, 1997). Therefore, by magnetising a subsample at a given strength of field in one direction, measuring the remanent magnetisation once the field is removed, then demagnetising the subsample and reapplying the same field for multiple different directions, a second rank tensor or magnetic remanence can be generated, which defines the alignment of ferromagnetic minerals (Potter, 2004). An AMR ellipsoid can be calculated from this tensor, defining an axis of maximum, intermediate and minimum magnetic remanence direction, used to define a magnetic lineation and foliation in the same manner as the AMS ellipsoid (Hext, 1963; McCabe and Jackson, 1985).

2.2.4.1 AMR Method

Multiple methods of AMR measurement are possible, based on the type of field used to impart a remanent magnetisation (Jackson, 1991). By changing the applied field, different populations of ferromagnetic minerals can be targeted, allowing subfabrics from the different mineral populations to be measured (Fig. 2.1) (Potter, 2004). Two methods of AMR are used as part of this thesis: low-field Anisotropy of Isothermal Remanent Magnetisation (AIRM) and Anisotropy of Anhysteretic Remanent Magnetisation (AARM). AIRM measures the directional dependency of isothermal remanent magnetisation (IRM) which is imparted under by direct current (DC) field, while AARM measures the variation in anhysteretic remanent magnetisation (ARM) imparted using an alternating current (AC) field biased by a weak DC field (Fig. 2.1) (Jackson, 1991).

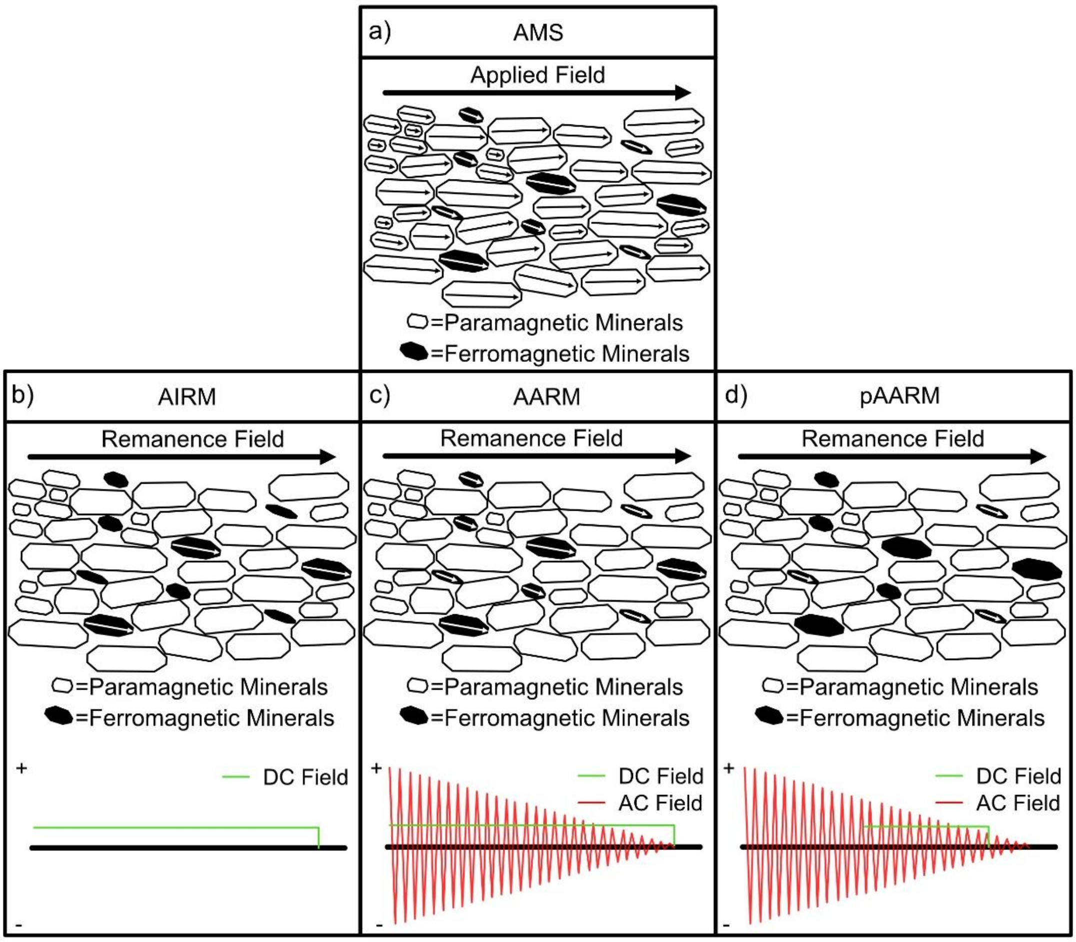

Figure 2.1 – Schematic representation of different methods of magnetisation. (a) Anisotropy of Magnetic Susceptibility (AMS). (b) Anisotropy of Isothermal Remanent Magnetisation (AIRM). (c) Anisotropy of Anhysteretic Remanent Magnetisation (AARM). Partial Anisotropy of Anhysteretic Remanent Magnetisation (pAARM).

Relative to low-field IRM, an ARM will magnetise higher coercivity ferromagnetic minerals within a sample, meaning the alignment of these minerals can be targeted with AARM (McCabe and Jackson, 1985). This allows for AIRM, which will only measure the alignment of low coercivity ferromagnetic minerals, to be compared with AARM and determine if subfabrics are preserved within the different ferromagnetic mineral populations (Stephenson et al., 1986). An alternative method to characterise different ferromagnetic mineral populations is through the measurement of partial Anisotropy of Anhysteretic Remanent Magnetisation (pAARM) (Jackson, 1991; Mattsson et al., 2021). pAARM is measured in the same way as AARM, but the DC bias field is only applied over a specific range of the AC field, magnetising a subset of the ferromagnetic minerals (Fig. 2.1) (Jackson, 1991). This means that by changing the field range where the DC bias field is applied, different coercivity ranges can be magnetised using pAARM.

2.2.4.2 Statistical Parameters of AMR

The same statistical parameters calculated for AMS tensors can be generated for AMR measurements, with the arithmetic mean of the magnetic remanence axes referred to as *Rmean* instead of *Kmean*, while the corrected degree of anisotropy and shape factor are still denoted by *Pj* and *T*, respectively (Jelinek, 1981).

2.2.5 Caveats of Magnetic Fabric Analysis

Various caveats are associated with the use of magnetic fabrics, in particular AMS, as a proxy for the petrofabric within a lithology. These caveats and their mitigation are discussed below.

2.2.5.1 Normal and Anomalous (Inverse and Oblique) AMS Fabrics

A key assumption to AMS fabrics correlating to petrofabrics within a lithology is that k_1 parallels the bulk alignment of crystallographic long axes, k_2 parallels the intermediate crystallographic axes and k_3 parallels crystallographic short axes. While this relationship is true for the majority of paramagnetic minerals, being termed a ‘normal’ AMS fabric, important exceptions occur.

While MD ferromagnetic grains measure a ‘normal’ AMS fabric, SD grains in a weak inducing field are more easily magnetised along their short axis (Tarling and Hrouda, 1993). This results in an ‘inverse’ AMS fabric, where k_1 parallels the crystallographic short axis and k_3 parallels the long axis (Potter and Stephenson, 1988; Rochette et al., 1992). Similarly, ‘oblique’ fabrics can be measured within certain paramagnetic mineral groups such as amphiboles, where the $k_1 – k_3$ axes deviate from the crystallographic axes due to their mineral chemistry, distortion of their crystal lattice and overall rock texture (Biedermann et al., 2018).

The impact of anomalous AMS measurements can be mitigated via several analytical approaches. Firstly, averaging of a large number of subsamples per sample site allows for anomalous measurements to be highlighted during data analysis and investigated (Jelinek, 1981). The dominance of inverse AMS fabrics from SD particles can be mitigated through comparison of AMR and AMS fabrics, as magnetic remanence is always strongest parallel to the crystallographic long axis, regardless of the number of magnetic domains (Jackson, 1991). Therefore, in samples which show parallel maximum and minimum axes from both AMS and AMR, SD grains cannot be present, making the AMS fabric 'normal'. Oblique fabric formation can be mitigated through comparison of alternative methods of petrofabric measurement, such as Crystallographic Preferred Orientation (CPO) (Biedermann et al. 2018).

2.2.5.2 Subfabric Interference

In natural rock samples, multiple mineral populations contribute to AMS and AMR fabrics, meaning that sub-populations of minerals may have a different alignment, forming a magnetic subfabric (Williams et al., 2025). When this occurs, subfabrics can destructively or constructively interfere with the primary fabric developed within a sample site, resulting in a so-called 'intermediate' fabric to be measured (Ferré, 2002).

Intermediate fabrics, similar to the presence of oblique and inverse fabrics, can be mitigated through the incorporation of multiple magnetic fabrics and non-magnetic petrofabric analysis, such as CPO. By comparing AMS and AMR fabrics, the fabric from a bulk response of all minerals can be compared to the isolated alignment of ferromagnetic minerals, allowing oblique or competing fabrics within paramagnetic and diamagnetic minerals to be identified (Borradaile and Jackson, 2010). This can be advanced further through the use of multiple AMR methods, or the same AMR method but at different field strengths, to identify the alignment of different ferromagnetic mineral populations within samples. (McCabe and Jackson, 1985; Stephenson et al., 1986).

2.2.5.3 Distribution Anisotropy

Distribution anisotropy occurs when ferromagnetic minerals are in close proximity and can magnetically interact, potentially forming an intermediate fabric during AMS measurement (Grégoire et al., 1998; Borradaile, 2001). The influence of distribution anisotropy can be mitigated through comparison of AMS and AMR fabrics to investigate how the bulk mineral response varies to the isolated alignment of ferromagnetic grains, as well as incorporating petrofabric data from non-magnetic methods such as CPO and X-Ray Computed Tomography (Mattsson et al., 2021).

2.2.5.4 Contribution from Isotropic Ferromagnetic Minerals

While ferromagnetic minerals will dominate bulk magnetic susceptibility measurements, they may be isotropic and feature no directional dependence, masking paramagnetic minerals which control the anisotropy measured from AMS (Biedermann and Bilardello, 2021b). The presence of isotropic ferromagnetic minerals can be determined through the calculation of deviatoric susceptibility (*K'*), which compares the AMS ellipsoid to an isotropic sphere of diameter equal to *Kmean* (Jelinek, 1984; Biedermann et al., 2014b; Koopmans et al., 2022). *K'* values can be compared to single-crystal values of known paramagnetic minerals within a lithology, with any *K'* values greater than any single-crystal value requiring ferromagnetic minerals to contribute to AMS.

2.3 Rock Magnetic Characterisation

While the caveats of rock magnetic fabrics can be mitigated through the use of multiple petrofabric techniques, their meaningful interpretation is only possible if complemented with a robust rock magnetic characterisation to establish the magnetic mineralogy of samples (e.g., Ferré 2002; Borradaile and Jackson 2010; Biedermann and Bilardello 2021). Here, an overview of the characterisation methods utilised as part of this thesis is provided.

2.3.1 Temperature-Dependent Magnetic Susceptibility

The magnetic susceptibility of paramagnetic and ferromagnetic minerals varies with temperature, while diamagnetic minerals show no variation in their magnetic susceptibility with temperature (Dunlop and Özdemir, 1997). Therefore, by measuring bulk susceptibility through a range of temperatures, referred to as a temperature-dependent magnetic susceptibility (T-χ) experiment, the magnetic mineralogy within a lithology can be identified (Fig. 2.2) (Dunlop and Özdemir, 1997).

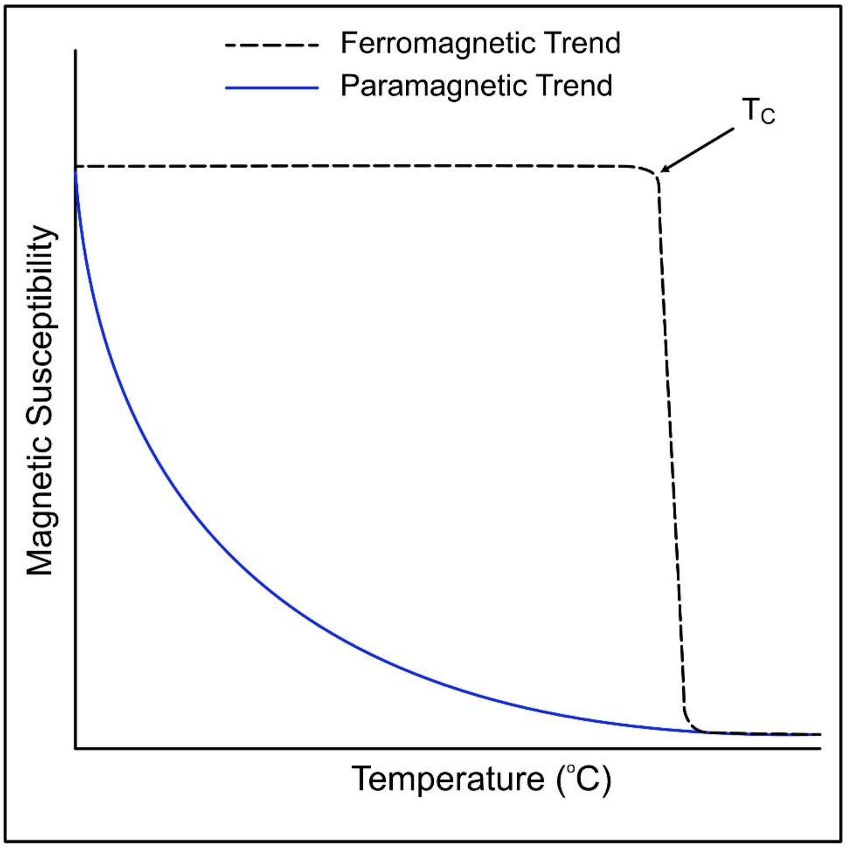

Figure 2.2 – Schematic of paramagnetic and ferromagnetic behaviour during temperature-dependent magnetic susceptibility (T-χ) experiments.

T-χ experiments are usually carried out over a temperature range of -194°C to 700°C to capture the diagnostic behaviour of common rock-forming minerals (Tarling and Hrouda, 1993; Dunlop and Özdemir, 1997). Across this temperature range, paramagnetic minerals will show a hyperbolic decline in magnetic susceptibility, while ferromagnetic minerals demonstrate a complex relationship with temperature, dependent on the mineral present, its size and its composition

(Dunlop and Özdemir, 1997). While certain ferromagnetic minerals display diagnostic features at specific temperatures, such as the Verwey transition of magnetite (Verwey and Haayman, 1941), a key characteristic of all ferromagnetic minerals is the presence of a Curie temperature (T_C), where magnetic susceptibility sharply declines and begins to behave paramagnetically (Dunlop and Özdemir, 1997). The temperature range at which the T_C is observed can be diagnostic of a given ferromagnetic mineral phase, with variations in mineral chemistry causing subtle changes to the T_C range, as seen for magnetite and its titanium content (Akimoto, 1962; Tarling and Hrouda, 1993; Dunlop and Özdemir, 1997; Lattard et al., 2006).

As T-χ experiments are based on the bulk magnetic susceptibility of the sample, the trend measured reflects the combined response of all minerals within the lithology. However, if there is a large population of ferromagnetic minerals, the signature of paramagnetic minerals and any subpopulations of other ferromagnetic minerals can often be masked during the experiment (Dunlop and Özdemir, 1997; Hrouda, 2010). Therefore, it is important to combine T-χ experiments with other characterisation methods which can assist in identifying multiple populations of magnetic minerals.

2.3.2 Remanent Magnetisation Characterisation methods

2.3.2.1 Saturation Isothermal Remanent Magnetisation

Saturation isothermal remanent magnetisation (sIRM) experiments measure the variation in IRM as increasing DC fields are imparted along a given direction (Dunlop and Özdemir, 1997). Magnetisation will increase up to a given field strength, at which point no further remanent magnetisation is imparted, as all ferromagnetic minerals have been saturated (Fig. 2.3) (Dunlop and Özdemir, 1997). The field at which saturation is reached is dependent on the ferromagnetic minerals present and their domain state, with magnetically ‘soft’ minerals such as MD magnetite saturated at relatively low fields, allowing them to be separated by while magnetically ‘hard’ minerals such as SD magnetite and hematite require a larger IRM to be imparted (Dunlop and Özdemir, 1997).

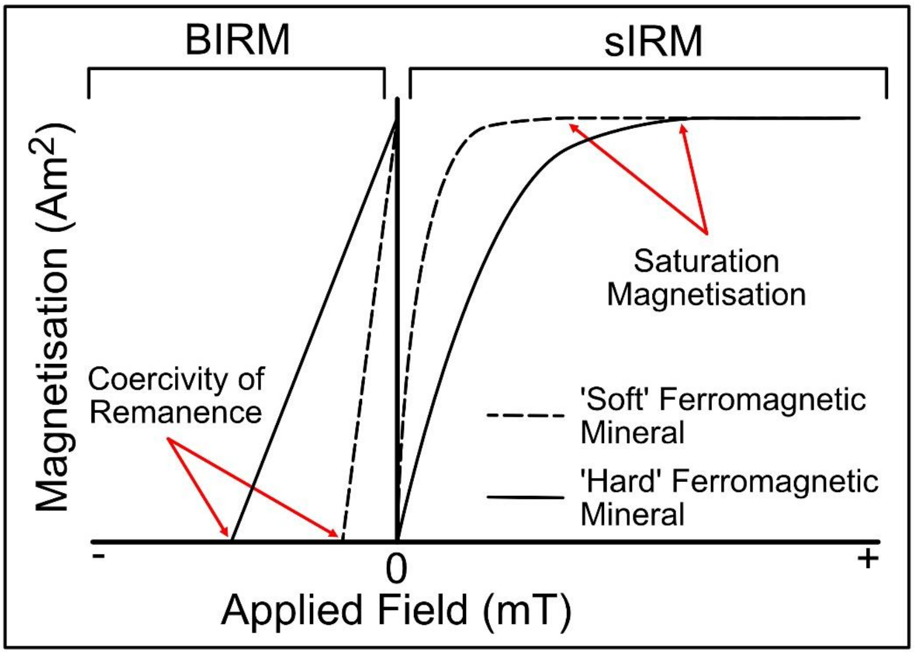

Figure 2.3 – Schematic of saturation Isothermal Remanent Magnetisation (sIRM) and Backfield Isothermal Remanent Magnetisation (BIRM) experiments.

2.2.2.2 Backfield Isothermal Remanent Magnetisation

Backfield isothermal remanent magnetisation (BIRM) experiments are measured immediately after sIRM experiments, when a sample is magnetically saturated or at the maximum field used as part of the sIRM experiment is applied (Fig. 2.3). An IRM in imparted in the opposite direction to the one used for sIRM experiments, to assess the field required to demagnetise the sample. This field defines the coercivity of remanence (H_{cr}), with magnetically softer ferromagnetic minerals having a lower H_{cr} than harder ferromagnetic minerals (Dunlop and Özdemir, 1997).

2.3.3 Induced Magnetisation Characterisation Methods

2.3.3.1 Magnetic Hysteresis Loops

Magnetic hysteresis loop measurements are performed by applying a bidirectional field on a sample, with magnetisation measured throughout field application (Fig. 2.4) (Tarling and Hrouda, 1993; Dunlop and Özdemir, 1997). When an X/Y plot of applied field vs magnetisation is generated, a loop is created which reflects the properties of magnetic particles/minerals within the sample

(Dunlop and Özdemir, 1997). For ferromagnetic minerals, magnetisation will initially rise rapidly before gradually levelling off once all minerals are saturated, this is the saturation magnetisation (M_{Sat}) (Dunlop and Özdemir, 1997). As the field is applied in the opposite direction, the magnetisation of the sample when the field strength is zero is termed the saturation remanent magnetisation (M_{RSat}), and the field required to fully demagnetise the sample is called the coercivity (H_c). These parameters can be used to identify specific ferromagnetic minerals and separate the same mineral present at different domain states (Dunlop and Özdemir, 1997). Paramagnetic minerals can also be characterised from magnetic hysteresis loops, measuring a positive linear trend with no coercivity present (i.e., the loop passes through the origin of axes) (Tarling and Hrouda, 1993; Dunlop and Özdemir, 1997).

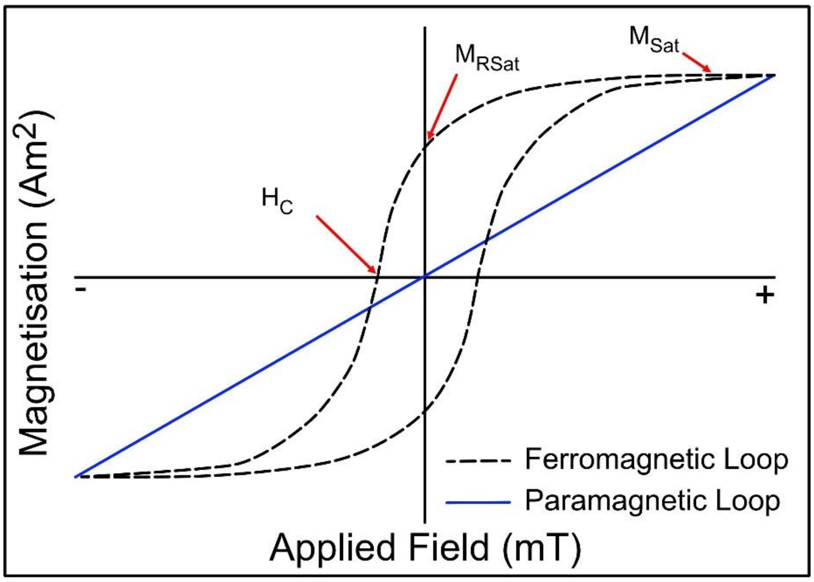

Figure 2.4 – Schematic of magnetic hysteresis loops showing ferromagnetic and paramagnetic behaviour.

When multiple ferromagnetic minerals are present within a sample and contribute significantly to the induced magnetisation, the shape of the hysteresis loops can become asymmetric (Tauxe et al., 1996), while a large contribution from paramagnetic minerals can result in loops failing to reach saturation within the applied field in both directions (Dunlop and Özdemir, 1997). The paramagnetic component of magnetic hysteresis loops can be removed using data processing software such as HystLab (Paterson et al., 2018). However, when multiple ferromagnetic minerals are present, other analytical methods are required to identify the full magnetic mineralogy.

2.3.3.2 First Order Reversal Curves

First-order reversal curves (FORCs) are a sensitive tool for identifying multiple ferromagnetic minerals and particle populations within a sample (Roberts et al., 2000, 2014). A FORC is a partial hysteresis loop, where a sample is saturated, demagnetised to a set starting field and then remagnetised to saturation (Roberts et al., 2000). Multiple FORCs are measured, each one being measured from a different, evenly spaced starting field and amalgamated to make a FORC diagram (Fig. 2.5) (Roberts et al., 2014). FORC diagrams are a Cartesian plot which shows the coercivity (B_c) and interaction fields (B_u) between ferromagnetic minerals within a sample (Roberts et al., 2014). By comparing FORC diagrams from samples to diagrams from mineral standards of known composition and domain state, the presence of one or more ferromagnetic minerals can be identified (Roberts et al., 2014, 2019).

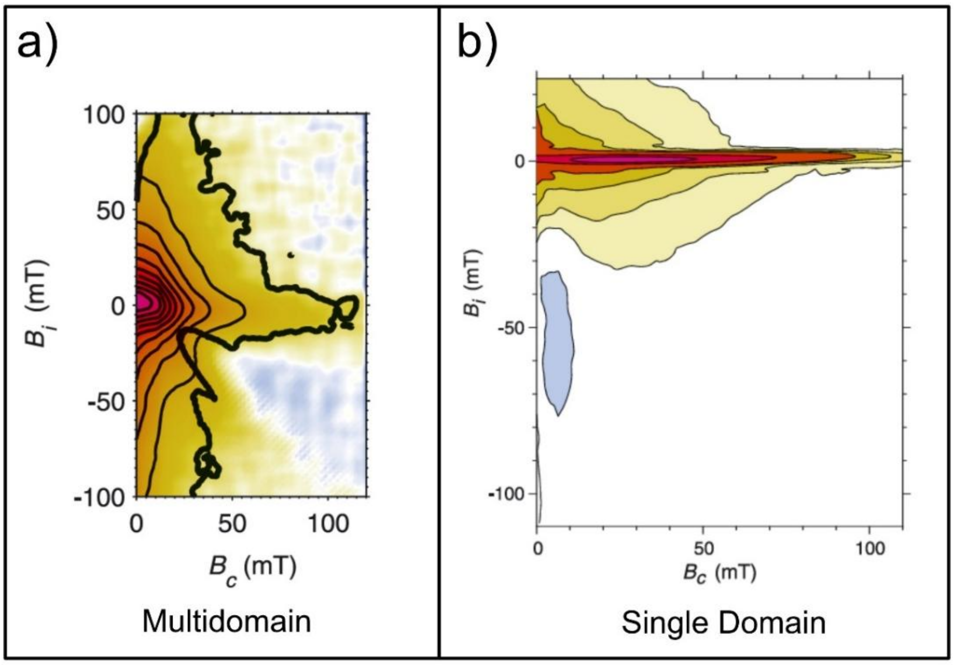

Figure 2.5 – Schematic of First Order Reversal Curve (FORC) Diagrams. (a) shows multidomain particle behaviour while (b) shows single domain particle behaviour. Modified from Roberts et al. (2014).

2.4 Petrography and Crystallographic Preferred Orientation

To complement magnetic fabric analysis, polished thin sections were prepared from a subset of samples, allowing for transmitted light microscopy and scanning electron microscope (SEM) analysis of petrographic properties. Within Chapter 4, these sections were orientated so that they were subparallel to the plane featuring the k_1 and k_3 axes. For Chapter 6, sections were cut parallel to the top of the core rather than in relation to magnetic fabric measurements

2.4.1 Transmitted Light Microscopy

Transmitted light microscopy was used for textural analysis and the identification of deformation features formed at different rheologies throughout crystallisation (Passchier and Trouw, 2005; Vernon, 2018). This provides a crucial context for the relative timing of petrofabrics measured using AMS and AMR (e.g., McCarthy et al., 2015a; Koopmans et al., 2022; Williams et al., 2025).

2.4.2 Crystallographic Preferred Orientation

An SEM was used to gather Electron Backscatter Diffraction (EBSD) data from samples and measure the CPO of major silicate mineral phases (Prior et al., 1999). In comparison to magnetic fabric analysis, where measurement of a subsample takes a few minutes and allows rapid measurement and averaging of multiple cylindrical subsamples over a sample site, collection of quality CPO data for a single thin section can take several hours to collect and process (Prior et al., 2009). This makes the use of only CPO data to analyse petrofabric development at large spatial resolutions time intensive in comparison to magnetic fabric techniques. Similarly, the CPO of minerals may not directly correlate with outcrop-observed petrofabrics, instead being defined by the shape-preferred orientation (SPO) of minerals (Renjith et al., 2016). However, as AMS and AMR fabrics of a sample are controlled by the crystallographic orientation of minerals, the verifiable measurement of these orientations using CPO makes it a valuable tool to contextualise magnetic fabrics when analysed for a representative subset of samples (e.g., Renjith et al., 2016; Bella Nké et al., 2018; Jones et al., 2025).

2.5 Fracture Analysis

Aside from microstructural evidence, one of the most prominent macroscale features of submagmatic and subsolidus strain within intrusions is the development of faults and fractures (McCaffrey, 1994; Žák et al., 2009; Alasino et al., 2025). In submagmatic settings, these structures form as a response to strain embrittlement of mush-state magma, preserved through the emplacement of synmagmatic dykes along these structures (Hibbard and Watters, 1985; McCaffrey, 1994; Smith, 1997). In subsolidus conditions, faults and fractures are observed as distinct deformation planes crosscutting the intrusion, being subsequently infilled by late-stage magma or hydrothermal alteration products. Fracture analysis can be a powerful tool to assess records of external tectonic strain within an intrusion, particularly when strain is transcurrent in nature (El Desouky et al., 1996). In these tectonic settings, a systematic pattern of Riedel shear structures will evolve in response to shortening in a given direction and shear sense, determined from field mapping or unmanned aerial vehicle imaging of fault/fracture networks (Riedel, 1929; Kirkland et al., 2008; Kocks et al., 2014).

A caveat to the analysis of subsolidus faults and fractures within intrusions is that their formation could be in response to unroofing during exhumation, or from tectonic stress which post-dates intrusion formation rather than palaeostress active as the intrusion crystallised (Žák et al., 2009; Ellis and Blenkinsop, 2019). This can be mitigated by comparing subsolidus features to those formed in a submagmatic state, with the correlation between strain archives suggesting subsolidus faults and fractures reflect tectonic deformation active during and immediately preceding intrusion crystallisation (e.g., McCaffrey 1994).

2.6 Hyperspectral Reflectance

Hyperspectral analysis is a non-destructive method of mineralogical characterisation, based on the spectral response of a sample to electromagnetic radiation (Hunt, 1977). Measured via remote sensing or a portable spectrometer, hyperspectral analysis focuses on the spectral reflectance of a sample, linking this reflectance to the presence of certain mineral groups (Hunt and Ashley, 1979; Clark et al., 1990). Analysis is commonly conducted in the range of Visible Near Infrared (VNIR) to Shortwave Infrared (SWIR) radiation (325 – 2500nm) as this is where most diagnostic responses from minerals occur (Hunt, 1977). From these spectra, mineral groups are identified from sudden drops in reflectance, referred to as so-called absorption troughs. These absorption troughs are controlled by the atomic structure of minerals, either via electronic processes from the valence state of transition metal ions or vibrational processes within water (H_2O), hydroxyl (OH^-) and carbonate (CO_3^{2-}) group bonds (Clark et al., 1990). While this limits the minerals which can contribute to the spectral response of a lithology, hyperspectral analysis is an incredibly sensitive tool to the presence of different hydrous silicate (e.g., amphibole, mica, chlorite, epidote), oxide (e.g., goethite, limonite, hematite) and carbonate (e.g., siderite, calcite, dolomite) phases (Cloutier and Piercey, 2020).

For in situ measurements and the measurements of drilled core samples, a handheld spectrometer is placed up to the surface of an outcrop/drill core, emitting electromagnetic radiation and measuring the reflected spectra (Cloutier and Piercey, 2020). Mineral groups are identified based on the occurrence of one or more absorption troughs at key wavelengths, with subtle variations in these troughs linked with compositional variation in minerals such as chlorite (Cloutier et al., 2021). The relative abundance of a mineral phase is defined by the depth of absorption troughs, with deeper troughs indicating a greater contribution from a mineral group (Clark et al., 1990).

Caveats with hyperspectral analysis occur due to the properties controlling spectral responses. The absorption of radiation due to water, and the measurement of the spectral reflectance from surface readings, make accurate measurements difficult if an outcrop/drill core is wet or weathered. These can be mitigated by ensuring samples or an outcrop surface are dry and clean, with the spectrometer used on the most even surface possible.

Chapter 3: Geological Setting

3.1 Introduction

All data chapters are based on an analysis of the Fanad Pluton in Donegal, Ireland (Fig. 3.1). The intrusion is one of a series of granitic plutons which form the Donegal Igneous Complex (DIC), one of several igneous complexes emplaced during the late Caledonian Orogeny (Pitcher and Berger, 1972). As with the analytical methods, the background geology of the intrusion, its place within the DIC and the tectonic framework into which it was emplaced are covered in detail within each data chapter. This chapter instead provides a broad overview of the regional geology, the current understanding of the Fanad Pluton and its applicability to answer the aims of this thesis.

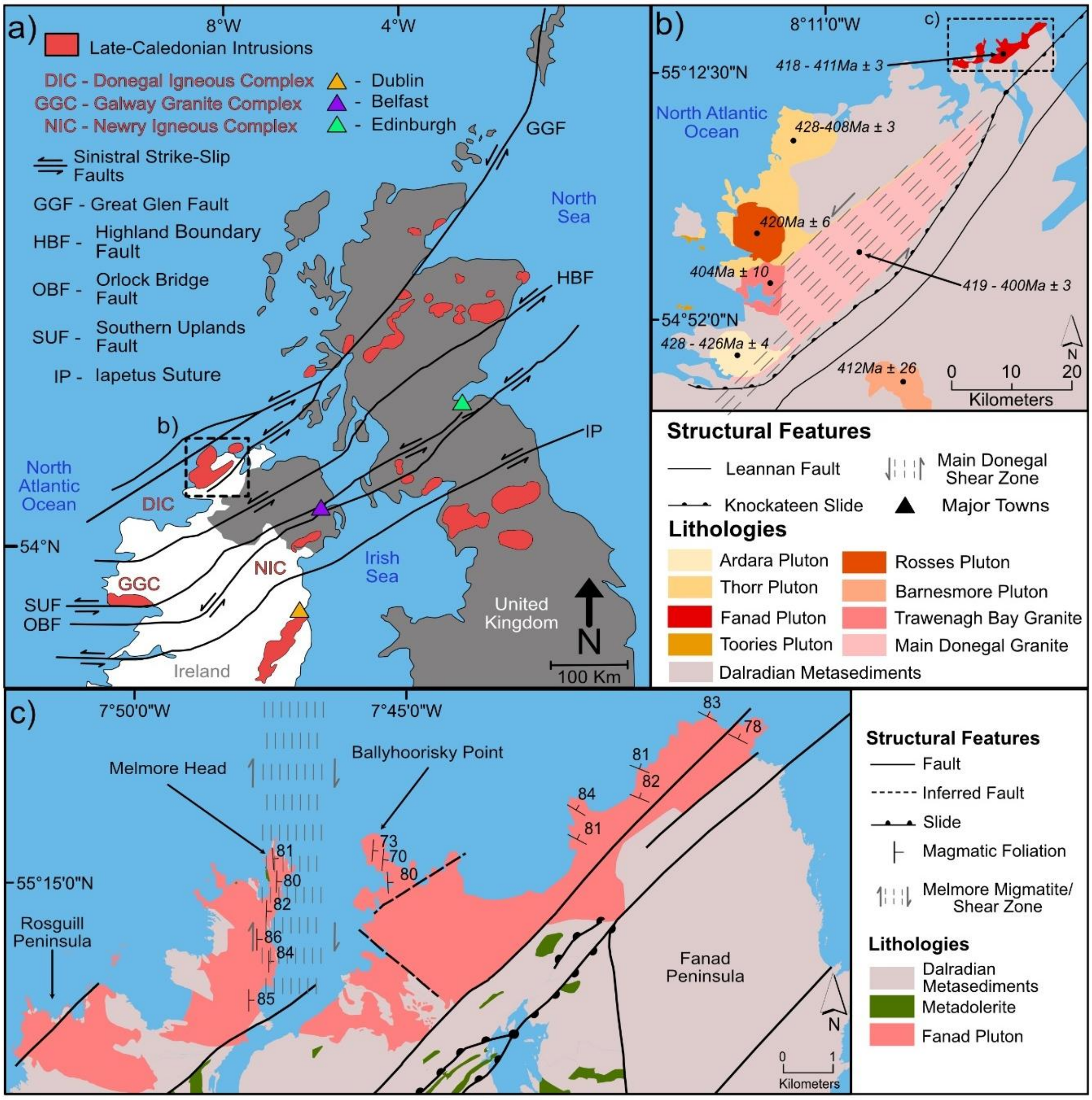

Figure 3.1 – (a) Structural framework of late Caledonian magmatism in Ireland and the UK. (b) Layout and components of the Donegal Igneous Complex (geochronology data from Archibald et al., 2021 based on U-Pb on zircon). (c) Bedrock of the Fanad pluton.

3.2 The Caledonian Orogeny

The Caledonian Orogeny occurred from the Ordovician to the Silurian, representing the amalgamation of the Laurentia, Baltica and Avalonia continents, which closed the Iapetus Ocean (Pickering et al., 1988; Woodcock, 1990; McKerrow et al., 2000). While many aspects of the orogeny are well constrained, the kinematic evolution of the Caledonian Orogeny and its role in the punctuated magmatism which occurred throughout is somewhat ambiguous, with multiple models proposed (e.g., Dewey and Strachan 2003; Searle 2021; Prave et al., 2024).

Across the Ireland the UK, two major orogenic events are defined throughout the orogeny based on their regional metamorphism and deformation, although recent work reports an intermediate phase of metamorphism which links these into a single protracted orogenic phase (Friend et al., 2000; Law et al., 2024; Lamont et al., 2025). Early Ordovician accretion of a magmatic arc onto the Laurentian margin during the onset of the Iapetus Ocean closure resulted in the Grampian orogenic event, causing regional-scale folding, metamorphism and the intrusion of gabbroic and granitic intrusions from *ca.* 475 – 460 Ma (Friedrich et al., 1999; Johnson et al., 2017). Following the Grampian orogenic event, potentially bridged by the intermediary phase of regional metamorphism and deformation proposed of Lamont et al. (2025), Baltica and Laurentia orthogonally collided to form Laurasia which then docked sinistrally oblique with Northern Avalonia from *ca.* 435 – 400 Ma (Woodcock, 1990; McKerrow et al., 2000). Associated with this oblique docking at the end of the Orogeny is the onset of transcurrent deformation (Soper et al., 1992; Dewey and Strachan, 2003; Soper and Woodcock, 2003), with further emplacement of granitic intrusions along deep seated structures within the Southern Uplands, Midland Valley Grampian and Northern Highland Terranes, termed the 'Newer' granites (*sensu* *lato*) to separate them from the 'Older' granites emplaced during the Grampian orogenic event (Jacques and Reavy, 1994; Brown et al., 2008).

Numerous models have been proposed for the transcurrent deformation at the end of the orogeny, particularly its kinematic evolution and the timing in transitions in shortening direction (Soper et al., 1992; Dewey and Strachan, 2003; Searle, 2021; Prave et al., 2024). There is a general consensus on these models that the Iapetus ocean closure during oblique Avalonia docking initially caused a phase of sinistral transpression under a N – S aligned shortening direction from *ca*. 435 – 420 Ma (Soper et al., 1992; Dewey and Strachan, 2003; Soper and Woodcock, 2003). In Ireland and Scotland, this deformation was facilitated by regional scale NE – SW trending faults along which terranes involved in the Caledonian Orogeny are juxtaposed (Fig. 3.1a) (Soper et al., 1992). After this phase of sinistral transpression, the shortening direction is proposed to rotate anti-clockwise to cause orthogonal collision (Soper et al., 1992; Kirkland et al., 2008), or rotate clockwise to induce sinistral transtension (Dewey and Strachan, 2003). While multiple models support a transpressive-transtensive kinematic evolution to the late Caledonian Orogeny, the timing of this transition is contested, proposed to occur at *ca*.420 Ma (Dewey and Strachan, 2003), or as late as 410 – 405 Ma (Soper and Woodcock, 2003). More recently, alternative models propose a single phase of orthogonal NW – SE shortening and a post-Caledonian activation of regional NE – SW faults (Searle, 2021), or an intermediate model favouring transcurrent deformation during the late Caledonian Orogeny, but to a lesser extent than older models (Prave et al., 2024).

The ambiguity around the kinematic evolution of the late Caledonian Orogeny reflects a gap in strain markers which can constrain the feasibility of proposed models. The records of strain from the 'Newer' granites emplaced during the late Caledonian may provide the additional context needed to investigate the proposed models and determine their feasibility (Brown et al., 2008).

3.3 The Donegal Igneous Complex

While several petrogenic models are proposed for late Caledonian magmatism, it is broadly accepted that slab-breakoff of the Iapetan crust facilitated asthenospheric rise and the partial melting of overlying Laurentian crust (Atherton and Ghani, 2002; Oliver et al., 2008; Neilson et al., 2009a; Miles et al., 2016). Across Ireland and the UK, granitic plutons show a genetic relationship in terms of their siting and ascent with subvertical strike-slip faults and other deep crustal structures formed during the Caledonian Orogeny, preserved in the petrofabrics within intrusions (Jacques and Reavy, 1994; Cooper et al., 2013).

The DIC is one of four igneous complexes emplaced in Ireland as part of the late Caledonian Orogeny (Fig.3.1b) (Pitcher and Berger, 1972). The DIC consists of eight plutons, of which six (the Adara, Thorr, Toories, Rosses, Trawenagh Bay and the Main Donegal Granite) form the Donegal Batholith, with the Barnesmore and Fanad Plutons being satellite plutons of the batholith (Stevenson et al., 2008a). The complex was intruded from 430 – 400 Ma with the Fanad Pluton emplaced coevally with the initial plutons of the Donegal Batholith and the Barnesmore Pluton coeval with the final stages of magmatism (Archibald et al., 2021).

The range of reported strain archives from plutons of the DIC provides an ideal test site to investigate the interplay of magmatic and tectonic processes within igneous intrusions (e.g., Hutton 1982; Stevenson et al., 2007). The Donegal Batholith is sited at the intersection of two major structures, the sinistral NE-SW main Donegal Shear Zone and the NNE – SSW Donegal Lineament, providing a tectonic control to the ascent of magma (Sanderson et al., 1980; Hutton, 1982; Hutton and Alsop, 1996). However, the reported records of strain within the composite plutons of the Donegal Batholith, except for the Main Donegal Granite, are dominated by internal stress from mechanisms of magma emplacement (Hutton, 1982; Molyneux and Hutton, 2000; Stevenson et al., 2007a, 2008a; Stevenson, 2009). Within the Main Donegal Granite, which is emplaced within the Main Donegal Shear Zone, a pervasive NE – SW trending sub-vertical petrofabric is developed, with the solid-state nature of fabric development reflecting a pervasive tectonic overprint (Hutton, 1982; Stevenson et al., 2008a). In contrast, within the Ardara, Thorr, Rosses and Trawenagh Bay Plutons, magmatic to submagmatic petrofabrics are observed, referred to as 'primary emplacement fabric' within some intrusions (Molyneux and Hutton, 2000; Stevenson et al., 2008a; Stevenson, 2009). In the Ardara Pluton, petrofabrics and enclave alignments are concentric in nature, previously argued to reflect a diapiric emplacement as a large spherical body (Akaad, 1956; Vernon and Paterson, 1993; Paterson and Vernon, 1995), but with the incorporation of rock magnetic fabrics is interpreted to reflect ballooning of the intrusion once emplaced (Molyneux and Hutton, 2000; Siegesmund and Becker, 2000). The Thorr Pluton is interpreted as a large tabular, laccolith reflecting magma emplaced westwards from the Main Donegal Shear Zone, similar to the Trawenagh Bay pluton, whose petrofabric suggests incremental laccolith growth through emplacement of magma flow lobes (Stevenson et al., 2007a, 2008a). The Rosses Pluton records a complex emplacement, with multiple sheets, emplaced westwards from the main Donegal Shear Zone and forcefully intruding within the Thorr Pluton. Limited studies of the Toories Pluton have been made due to the lack of available outcrop and the lack of connection between the Barnesmore Pluton and the rest of the DIC has made it difficult to place within the tectonic framework of the Donegal Batholith (Pitcher and Berger, 1972; Stevenson et al., 2008a).

3.4 The Fanad Pluton

In comparison to the composite plutons of the Donegal Batholith, the Fanad Pluton is relatively understudied. As such, the role of the pluton within the tectonomagmatic system proposed for the formation of the Donegal Batholith is poorly constrained, despite its emplacement from 418 – 411±3 Ma (U-Pb on zircon) being coeval with batholith formation (Stevenson et al., 2008a; Archibald et al., 2021). Therefore, the integration of the strain archive within the Fanad Pluton may provide new context on the role of external and internal palaeostresses during formation of the DIC, and the regional kinematic evolution of the Caledonian Orogeny (Fig. 3.1c).

Being NE of the Donegal Batholith, the Fanad Pluton is sited just north of the intersection of the NNE – SSW Fanad Lineament and the NE – SW Leannan Fault (Alsop, 1992; Cooper et al., 2013). The Leannan Fault represents a major sinistral strike-slip fault, reported as a splay of, or the continuation of the Great Glen Fault, one of the key Caledonian Terrane boundaries in NW Scotland (Kirkland et al., 2008; Prave et al., 2024), while the Fanad Lineament represent a deep-crustal structure parallel to the Donegal Lineament (Cooper et al., 2013). The intrusion is only partially exposed along the NW coast of Donegal on the Rosguill and Fanad Peninsulas, limiting studies investigating its emplacement (Pitcher and Berger, 1972; Evans and Whittington, 1976). However, previous work has favoured a passive stoping model for magma emplacement similar to the Thorr Pluton (Pitcher and Berger, 1972; White and Hutton, 1985; Chew and Stillman, 2009).

The Fanad Pluton is a dioritic to granodioritic intrusion which shows abundant regions of magma mixing and mingling, and zones of entrained country rock present as centimetre-scale xenoliths or metre-scale rafts (Pitcher and Berger, 1972; Ghani and Atherton, 2006; Archibald et al., 2021). The xenoliths align to define a broadly concentric fabric parallel to the southern contact of the intrusion. A deviation in fabric orientation is seen at the NE end of the Rosguill Peninsula, where a N-S trending zone referred to as the 'Melmore Migmatite' is exposed (Pitcher and Berger, 1972). Within the Melmore Migmatite, xenoliths are aligned N–S and partially migmatised with a petrofabric observed in the granite that is sub-vertical in nature, anastomosing around the xenoliths (Fig. 1C; Pitcher and Berger, 1972). A dextral shear sense is preserved through formation of xenolith boudins and the steep folding of rafts (Pitcher and Berger, 1972). The migmatisation of xenoliths suggests deformation was active throughout or immediately after magma emplacement, however, the role of this stress on magma emplacement is unclear from previous studies (Pitcher and Berger, 1972; White and Hutton, 1985).

Chapter 4: Enclaves as mushy magma strain archives: New perspectives on composite magmatic fabrics in plutons

The data from this chapter are published as part of an article in Geosphere and can be found under the following citation:

Latimer, B., McCarthy, W., Mattsson, T. and Reavy, J. 2024. Enclaves as mushy magma strain archives: New perspectives on composite magmatic fabrics in plutons. *Geosphere*, 20, 1390–1410, https://doi.org/10.1130/GES02786.1.

B. Latimer completed the fieldwork, performed the analyses, generated the figures, and wrote the chapter, with guidance and input from all co-authors.

4.1 Introduction

Igneous intrusions record palaeostress regimes via strain-induced fabric development expressed as grain-scale crystal alignment and preferred orientation of magmatic structures (Žák et al., 2008b). Rock fabrics can arise from magmatic processes such as magma flow, crystal settling, from chemical differentiation (e.g., Paterson et al., 2019; Koopmans et al., 2022; Köpping et al., 2023; Mattsson et al., 2018 Mattsson et al., 2024) or tectonic forces interacting with unsolidified magma giving rise to tectonic petrofabrics recorded in the magmatic state i.e. tectonomagmatic interactions (e.g., Žák et al., 2008b; McCarthy et al., 2015a; Tomek et al., 2017; Burton-Johnson et al., 2022; Tomek et al., 2024). The mode in which magma deforms and forms fabrics is controlled by magma-effective viscosity, a function of melt composition, crystal percentage and crystal shape (Marsh, 1996; Petford, 2009). Throughout crystallization, magmas transition through several rheological states based on crystal concentration and connectivity, which alter the mechanics and distribution of strain within the magma (Bergantz et al., 2017). This impacts fabric development within homogeneous magmatic bodies as well as magma mingling zones where contrasts in effective viscosity between mingling magmas are expected (Vigneresse et al., 1996).

Magma mingling zones are commonly associated with swarms of enclaves, globules of mafic to intermediate magma within the main intrusion (Carreras et al., 2004; Paterson et al., 2004; Žák et al., 2007; Weinberg et al., 2021). Enclave shape, alignment and internal fabric have been interpreted as a record of strain (e.g., Molyneux and Hutton, 2000; Žák et al., 2008, Žák et al., 2010). Enclave shape and alignment are understood to be controlled by their state of rheological contrasts from the surrounding host magma (Scaillet et al., 2000; Caricchi et al., 2012). Rheological contrast tends to be lower in the early stages of crystallization, allowing enclaves to act as active strain markers initially. However, as mafic magmas crystallize at higher temperatures, they will transition to passive strain markers in the relatively ductile felsic magma as cooling progresses (Scaillet et al., 2000). As such, enclaves will initially deform and align under background stress within an intrusion, but as they continue to crystalize and develop a greater rheology contrast with the surrounding host magma, enclaves are restricted to passively rotating relative to stress with no change to morphology, and/or can cause fabric refraction in the host magma (Smith, 2000; Caricchi et al., 2012).

However, the control of rheology contrast on enclave internal fabrics is less clear, in particularly where enclaves have begun passively rotating and are oblique to the petrofabric of the surrounding host rock (Paterson et al., 2004). Fabric deflection around or into the enclave can show if an enclave was more strained than the surrounding host intrusion (Smith, 2000). Internal fabrics aligned parallel to the enclave long-axis or oblique to both the enclave long-axis and the host rock petrofabric indicate grain-scale fabric development stalled at the rheological threshold where enclaves became a passive marker. In contrast, if enclaves feature an internal fabric aligned to the wider palaeostress field with a residual fabric aligned to the enclave long-axis, a clear overprinting of earlier fabrics has occurred independent of enclave morphology (Paterson et al., 2004). Were the latter relationship observed, it would have a major impact in connecting fabrics to primary magmatic processes or secondary stresses within an intrusion, associated with the regional tectonic strain.

Therefore, enclaves may play a critical role in understanding pluton emplacement in relation to the regional tectonic stress regime, especially within orogenic settings such as in the Caledonian orogenic belt (Hutton, 1982; Petronis et al., 2012; McCarthy et al., 2015b). Whereas studies of Caledonian plutons acknowledge the influence of the tectonic setting on magma emplacement, it is often unclear why fabrics have been interpreted to reflect primary magma flow processes (Stevenson et al., 2007a; Stevenson, 2009) or related to tectonic strain (McCarthy et al., 2015b; Di Chiara et al., 2020). Here we investigate if enclaves can be used to discriminate if pluton fabrics are related to internal magma body forces or reflect a secondary realignment within the ambient tectonic stress field. By quantitatively analysing fabrics in enclaves and their surrounding host rock within a magma mingling zone of the late-Caledonian Fanad Pluton, NW Ireland, we investigate if magmatic enclaves can provide an insight into the magmatic vs. tectonomagmatic fabric development of the wider pluton.

4.2 Background Geology

The Fanad Pluton, NW Ireland is part of the Donegal Granite Complex, a series of granitoid intrusions emplaced from 418 to 411±3 Ma (U-Pb on zircon) associated with late-Caledonian tectonism (Fig. 4.1) (Archibald et al., 2021).

The Caledonian Orogeny, which occurred from the Ordovician to the Devonian is associated with continental collision between Baltica and Avalonia with Laurentia expressed across Ireland, Scandinavia, and the north of the UK (McKerrow et al., 2000; Dewey and Strachan, 2003; Soper and Woodcock, 2003). The late stage of the orogeny can be broken down into an initial sinistral transpression phase until 420 Ma followed by sinistral transtension from 420–400 Ma after closure of the Iapetus Ocean, with displacement across Ireland and the UK accommodated by several regional-scale NE-SW trending faults (Soper and Woodcock, 2003). While magmatism is associated with all phases of the Caledonian orogeny (Milne et al., 2022), a clear surge in intermediate to felsic magmatism occurred from 425-395Ma, associated with the latter phase of sinistral strike-slip and continued into the subsequent Acadian orogeny which is associated with closure of the Rheic Ocean in Ireland and the UK from 400-380Ma (Fig. 4.1a) (Brown et al., 2008; Neilson et al., 2009b; Miles et al., 2016). These so-called ‘late-Caledonian Intrusions’, emplaced into the Neo-Proterozoic country rock, show a strong association with the active tectonic framework of the Caledonian in terms of their petrogenesis and location of magma ascent (Miles et al., 2016). Several petrogenetic models have been proposed for the intrusions (e.g., Atherton and Ghani, 2002; Oliver et al., 2008; Neilson et al., 2009; Miles et al., 2016) that centre around post-collisional subduction slab breakoff and upwelling of mantle material as the source of magma. These models highlight mantle underplating as the source of crustal melting, with subsequent hybridization between generated magmas causing the observed range of magma compositions (Neilson et al., 2009; Miles et al., 2016). This slab breakoff is approximately contemporaneous with the transition in stress regime from sinistral transpression to transtension along regional-scale faults such as the Great Glen Fault, with the change in structural kinematics providing a series of tectonically controlled ascent sites for the newly generated magma (Jacques and Reavy, 1994; Miles et al., 2016).

Despite an active tectonic framework during late-Caledonian magmatism, the role of the regional tectonic stress regime on magma emplacement varies across studies of intrusions/complexes (McCarthy et al., 2015b; Anderson et al., 2018; Lawrence et al., 2022). This is seen in the contrast between the inferred role of tectonic stress within the Galway Granite Complex (GGC) and the Donegal Igneous Complex (DIC) in Ireland (Fig. 4.1a) (Chew and Stillman, 2009).

Based primarily on mineral fabric and geochronological data, the siting of the earlier plutons of the GGC are reported to be controlled by NW-SE faults during regional transpression around ~420 Ma while the later plutons are interpreted to be controlled by orogen parallel strike slip faults during regional transtension around 410-400 Ma (McCarthy et al., 2015a; McCarthy et al., 2015b). The transition from transpression to transtension in this part of the orogen is therefore interpreted to have occurred around 410Ma during the construction of the GGC. (McCarthy et al., 2015a; McCarthy et al., 2015b).

In contrast, the DIC shows a lack of influence from regional tectonic stress on the siting of most of its constituent plutons (Fig. 4.1b). The complex consists of eight intrusions emplaced from 422-400 Ma, six of which form a main batholith alongside two outlying intrusions (Pitcher and Berger, 1972; Archibald et al., 2021). Magma ascent of the main batholith is controlled by the intersection of the NE-SW trending sinistral Main Donegal Shear Zone, a splay of the Great Glen Fault, and the NNE-SSW aligned Donegal Lineament (Hutton and Alsop, 1996). However, unlike the GGC where intrusions are centred on their ascent structures, intrusions of the main batholith are emplaced away from the ascent site reflecting batches of magma transported westwards from the shear zone (Molyneux and Hutton, 2000; Stevenson et al., 2007; Stevenson et al., 2008; Stevenson, 2009). Stress from magmatic flow and inflation are interpreted as the dominant control on pluton construction and fabric development rather than the regional tectonic stress, with studies of the main DIC batholith interpreting the development of mineral fabrics in a magmatic to submagmatic state as a 'primary emplacement fabric' (Stevenson et al., 2007; Stevenson et al., 2008; Stevenson, 2009). This contrasts with the tectonomagmatic interpretation of similar fabrics within the GGC, showing the ambiguity associated with measuring mineral fabrics within intrusions formed in a tectonic framework (Stevenson et al., 2007; Stevenson, 2009; McCarthy et al., 2015a).

The controls of ascent and emplacement of the Fanad Pluton are poorly constrained, as it is one of the satellite intrusions of the DIC with magmatism not related to the Main Donegal Shear Zone/Donegal Lineament intersection site, (Fig. 4.1b–c) (Pitcher and Berger, 1972; Chew and Stillman, 2009). The pluton is only partially exposed along the NW coast of Donegal on the Rosguill and Fanad Peninsulas, with the majority of the intrusion offshore (Evans and Whittington, 1976). The pluton is dioritic to granodioritic in composition, reflecting hybridization between the melted continental crust and underplating mafic magma (Ghani and Atherton, 2006; Archibald and Murphy, 2021). This hybridized origin is also inferred from numerous regions of mingling and mixing enclave swarms and dykes exposed along the Fanad Peninsula (Chew and Stillman, 2009; Archibald et al., 2021). Pitcher and Berger (1972) suggested the Fanad Pluton was emplaced via passive stoping, with the SE margin of the pluton defined by the NE-SW aligned Leannan Fault, a secondary splay of the Great Glen

Fault active during pluton emplacement (Fig. 4.1c) (White and Hutton, 1985). The "Melmore Migmatite" outcrops on the eastern margin of the Rosguill Peninsula, characterized by partially migmatised metasedimentary and metadolerite xenoliths and rafts that align parallel to a subvertical N-S trending, pervasive fabric in the granite that anastomoses around the xenoliths (Fig. 4.1c) (Pitcher and Berger, 1972). Dextral deformation structures are preserved within the Melmore Migmatite via formation of xenolith boudins within the interstitial host intrusion and steep vertical folding of rafts, with this deformation alongside magma emplacement linked to the migmatisation (Pitcher and Berger, 1972).

The primary research site of the study is a zone of magma mingling is situated on the NW edge of Ballyhoorisky Point, chosen for its density of enclaves (approximately 150 enclaves over 600m^2), as well as a magmatic foliation, referred to as its petrofabric, carried by mafic minerals in the quartz monzodiorite (referred to below *sensu lato* as the 'host monzodiorite'), which facilitated the study of strain archiving processes in enclaves (Fig. 4.1c). Secondary sites were analysed across the Fanad Pluton to contextualize the results of the primary site.

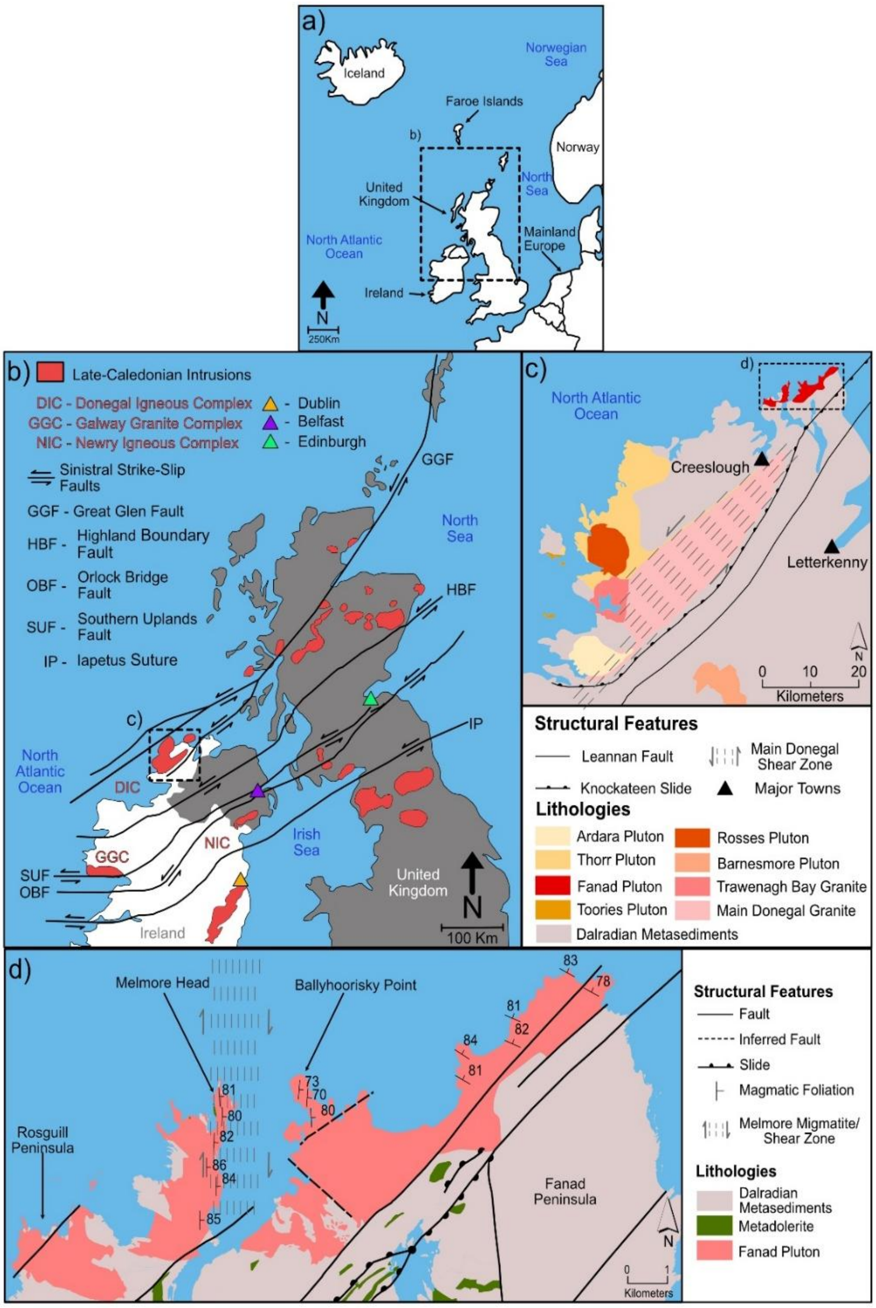

Figure 4.1 – (a) Wider geographical context of research site. (b) Structural framework of late Caledonian magmatism in Ireland and the UK. (c) Layout and components of the Donegal Igneous Complex. (d) Bedrock of the Fanad pluton.

4.3 Methodology

4.3.1 Fieldwork and Sample Selection

The mingling zone was mapped at meter-scale to describe the fabric, textural and geometric relationship between enclaves and the surrounding host monzodiorite (Fig. 4. 2). The host monzodiorite petrofabric was calculated from an average of

40 separate measurements across the locality, with any local changes in mineral abundance noted. The number, shape, and long-to-short-axis (X/Z) ratios of all enclaves as represented on the outcrop surface were recorded, as well as their long-axis orientation in the current surface exposure.

Eight representative enclave sites were chosen for sampling (FE001-FE008), with each site incorporating the enclave and surrounding host monzodiorite (Fig. 4.2). Two sites (FE004 and FE007) where enclave long-axis orientations are aligned parallel to the field observed host petrofabric were chosen as control sites. Six sites (FE001, FE002, FE003, FE005, FE006 and FE008) were selected as representatives of enclaves whose long axes are oblique to the field observed host petrofabric.

Core sampling was carried out by drilling cores of the enclave and surrounding host monzodiorite with a modified Stihl BT45 drill using a non-magnetic abrasive core drill bit. Core samples were drilled to an average depth of 100mm, with downhole orientation measured using a Brunton magnetic compass. At each sample site, core samples were collected at 5 – 10 cm intervals along the long axis and across at least one short axis of the enclave. Each core sample traverse extended at least half the enclave axis length into the host monzodiorite (Fig. 4.2c–j). For petrofabric-oblique enclaves, two additional sample traverses were collected parallel to the short axis of the enclave. The core samples were cut into 25x22mm cylindrical sub-samples using a non-magnetic saw, with an average of 4 sub-samples per drilled sample collected. A total of 355 core samples were drilled producing 896 sub-samples.

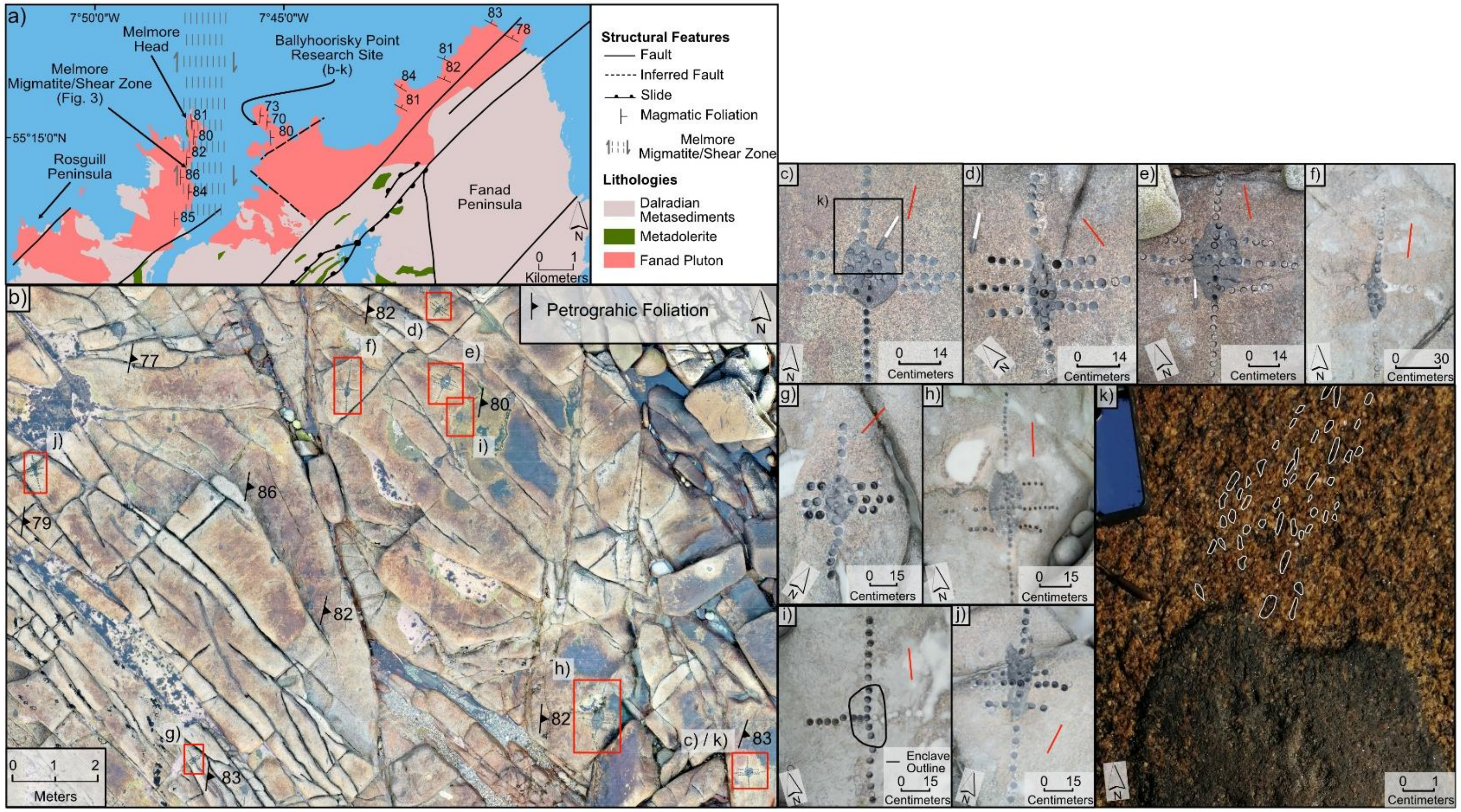

Figure 4.2 – (a) Bedrock of the Fanad pluton with research locality highlighted. (b) Drone imagery of locality. (c– j) Close-up images of sample sites (red line shows trend of fabric in host monzodiorite): (c) FE001, (d) FE002, (e) FE003, (f) FE004, (g) FE005, (h) FE006, (i) FE007, (j) FE008. (k) Close- up image of FE001 showing fabric within the host monzodiorite, where a subset of mafic crystals has been outlined in white to show alignment

4.3.2 Petrography

Petrographic analysis was carried out to determine textural features within the host monzodiorite and enclaves with a view to comparing these to magnetic fabric data. Oriented thin sections of eight sub-samples were prepared from site FE004 (a petrofabric-aligned enclave) and FE008 (a petrofabric-oblique enclave). Thin section selection represents enclave, host monzodiorite and contact sub-samples, and included sub-samples with representative strong, weak and anomalous magnetic fabrics as determined from AMS results. Each thin section was analysed using a transmitted light petrographic microscope to examine the mineralogical and microstructural characteristics of each sub-sample.

4.3.3 Magnetic Mineralogy Characterisation Methods

Eight representative sub-samples were chosen for magnetic mineralogy characterization to constrain principal carriers of magnetic susceptibility and, ultimately, validate the AMS fabric results. Four sub-samples were selected from site FE004, two from the host monzodiorite and two from the enclave. Two sub-samples were also selected from the enclave and the host monzodiorite at site FE008.

4.3.3.1 Temperature-Dependent Magnetic Susceptibility

The temperature dependence of magnetic susceptibility (T-$\mathcal{X}$) is a diagnostic feature of magnetic minerals (Dunlop and Özdemir, 1997). The response of sub-samples to cooling and heating can be compared to the response from standardized values of common minerals to identify the key contributors to a sub-sample's bulk susceptibility (Hrouda, 2010). All sub-samples were crushed and pulped using a ceramic pestle and mortar, and the bulk susceptibility of approximately 0.35g of material was analysed in low- and high-temperature cycles using the AGICO KLY-5A Kappabridge with CS-L and CS4 units attached. The crushed sub-sample was first cooled to -194°C using liquid nitrogen, then allowed to warm to 0°C. Next, the sub-specimen was heated from 20°C to 700°C at a rate of 14 °C/minute, before being cooled back to room temperature and then cooled again to -194°C before warming to 0°C. Throughout these three cycles, the bulk susceptibility was measured at 25-second intervals (Field: 400 Am^{-1}; Frequency: 1220Hz). The data was processed and corrected in the Cureval8 program (Chadima, 2012).

4.3.3.2 Isothermal Remanence Magnetisation

Saturation Isothermal Remanence Magnetization (sIRM) and Backfield Isothermal Remanence Magnetization (BIRM) were measured to determine the saturation IRM and approximate coercivity of remanence (H_{cr}) from ferromagnetic grains within the enclaves and host monzodiorite (Dunlop and Özdemir, 1997; McCarthy et al., 2015b). For sIRM, Sub-samples were initially demagnetized via 2-axis tumbling within a 200mT alternating current (AC) field using the LDA-5 demagnetizer from AGICO. Once demagnetized, the sub-samples were then remagnetized with an Isothermal Remanent Magnetization (IRM) along their Z-axis in a stepwise manner using an MMPM10 pulse magnetizer from Magnetic Measurements. The magnetization steps were used: 0, 30, 50, 70, 100, 130, 160, 200, 250, 300, 400, 500, 700, 900, 1200 mT. Magnetic remanence was measured using the AGICO JR-6A spinning magnetometer at normal acquisition time with 87 revs/s between each magnetization step. Once the 1200mT field was reached, BIRM was measured by imparting an IRM in the opposite direction along the Z-axis to sIRM. The steps in BIRM were: 0, 10, 12, 14, 16, 18, 20, 22, 24, 26, 28, 30 mT.

4.3.3.2 Magnetic Hysteresis Loops and First Order Reversal Curve Measurements

Magnetic hysteresis loops and First Order Reversal Curves (FORCs) were produced using a LakeShore 8604 series Vibrating Sample Magnetometer (VSM). Each sub-sample was crushed into mm-sized chips using a ceramic pestle and mortar, approximately 0.25g of material was placed into a 5mm in diameter gel capsule and secured with glue before being placed in the VSM for analysis. Sub-samples were degaussed in a 2370mT field and then magnetized bidirectionally to up to 1500mT to generate magnetic hysteresis loops. The shape of a loop is controlled by the saturation magnetization (M_s), remanence magnetization (M_r) and coercivity (H_c) of particles within the samples (Dunlop and Özdemir, 1997). Once collected, the hysteresis loop data was processed using HystLab v.1.1.3 (Paterson et al., 2018). Loops were corrected for drift during measurement, a correction was applied to sub-sample data to remove the paramagnetic slope present in most hysteresis loops using the 'Linear High-Field' function.

FORC diagrams are produced by the stacking of multiple partial hysteresis loops, with the diagrams showing the coercivity (B_c) and distribution of interacting fields between magnetic particles and the applied magnetic field (B_u) (Roberts et al., 2014). This provides an extremely sensitive tool to determine the magnetic properties of particles within a specimen (Roberts et al., 2014; Harrison et al., 2018). FORC diagrams were made for all of the selected sub-samples, with 200 FORCs at 2.5mT spacing with a maximum field 900mT used to cover a B_c of 0 to 200mT and B_u of 100 to -200mT. Once the raw FORC diagrams were collected, the data was processed using the VARIFORC smoothing (Sc_0=5 Sb_0=6 Sc_1=8 Sb_1=8) in the FORCinel software to remove noise and highlight the dominant signal of each diagram (Harrison and Feinberg, 2008; Egli, 2013).

4.3.4 Rock Fabric Analysis

4.3.4.1 Anisotropy of Magnetic Susceptibility

Anisotropy of Magnetic Susceptibility (AMS) is a highly sensitive and efficient method for measuring petrofabrics (Tarling and Hrouda, 1993). AMS is a magnetic fabric based on variations in directional magnetic susceptibility in an induced field, providing a detailed constraint on the petrofabrics within a lithology in a time-efficient manner not possible from petrographic data alone (Tarling and Hrouda, 1993). AMS measures the bulk magnetic response of all minerals in a sample in 3D from which a second-rank tensor represented by an ellipse analogous to a strain ellipsoid is calculated (Borradaile and Jackson, 2010).

The magnetic susceptibility of each sub-sample from all eight sample sites was measured in 320 unique orientations with the KLY-5A Kappabridge and the 3D-rotator attachment (Field: 400 Am-1; Frequency: 1220Hz). The value of magnetic susceptibility in each of these 320 orientations is used to calculate a tensor of magnetic susceptibility per sub-sample. The eigenvectors and eigenvalues of this tensor outline three axes, reflecting the principal directions of maximum (k_1), intermediate (k_2) and minimum (k_3) susceptibility (Khan, 1962). These axes form a triaxial ellipsoid, with k_1 representing the magnetic lineation and k_3 representing the pole of the magnetic foliation plane (Tarling and Hrouda, 1993). Parameters including mean susceptibility (K_{mean}), corrected degree of anisotropy (P_j) and shape factor (T) describe the geometry of the AMS ellipsoid (Jelinek, 1981; Tarling and Hrouda, 1993). K_{mean} represents the arithmetic mean of the principal susceptibilities:

$$K_{mean} = \frac{k_1+k_2+k_3}{3}. \text{ (1).}$$

P_j describes the separation between the natural logarithm values of the principal direction of susceptibility, i.e. the corrected degree of susceptibility (Jelinek, 1981):

$$P_j = \exp\sqrt{2((\eta_1 - \eta_{mean})^2 + (\eta_2 - \eta_{mean})^2 + (\eta_3 - \eta_{mean})^2)}. \text{ (2),}$$

where:

$$\eta_x = \ln(k_x)\,, x = 1,2,3. \text{ (3),}$$

T describes the shape of the triaxial ellipsoid based on the relative lengths of the natural logarithm of k_1, k_2 and k_3:

$$T = \frac{2\eta_2-\eta_1-\eta_3}{\eta_1-\eta_3}. \text{ (4),}$$

With T = 1 defining an oblate ellipsoid, T = -1 defining a prolate ellipsoid and T ≈ 0 defining a triaxial ellipsoid (Jelinek, 1981). AMS data was collected using the software SAFYR 7 before being reorientated and analysed in the software Anisoft 5 (Chadima et al., 2018a).

The mineral that makes the largest contribution to bulk magnetic susceptibility may not necessarily be the same mineral that controls overall anisotropy, for example a relatively low susceptibility mineral may control AMS if magnetite is present but perfectly distributed and isotropic in a rock (Biedermann and Bilardello, 2021a). To assess the dominant mineralogical control of AMS, deviatoric Susceptibility (*K'*) was calculated for each sub-specimen, which compares the deviation of the AMS ellipsoid of the sub-specimen to that of an imaginary sphere of diameter equal to that sub-sample K_{mean} (Jelinek, 1984; Biedermann et al., 2014a; Koopmans et al., 2022):

$$K' = \sqrt{\frac{((k_1-1)*k_{mean})^2+((k_2-1)*k_{mean})^2+((k_3-1)*k_{mean})^2}{3}}. \quad (5).$$

The deviatoric susceptibility of sub-samples can then be compared to *K'* values of single crystals to test the mineralogical controls of the specimen AMS.

4.3.4.2 Anisotropy of Magnetic Remanence

The shape and orientation of an AMS ellipsoid may be complicated by variations in magnetic mineralogy, or if a sample contains competing mineral fabrics, producing an intermediate or inverse fabric (e.g., Potter and Stephenson, 1988; Ferré, 2002; Mattsson et al., 2021). Anisotropy of Magnetic Remanence (AMR) can be used to determine the magnetic fabric defined from only ferromagnetic grains, deconvoluting the AMS fabric into potential resultant components to test for the presence of multiple rock fabrics (Jackson, 1991; Borradaile and Jackson, 2010; Mattsson et al., 2021). As with AMS, AMR can be used to generate a fabric from the eigenvector of its tensor (McCabe and Jackson, 1985). In this study, two forms of AMR were measured on 48 representative sub-samples, 24 sub-specimens from site FE004 and 24 sub-samples from site FE008. Anisotropy of Anhysteretic Remanence Magnetization (AARM) tested for fabrics defined by relatively high coercivity minerals, such as single domain magnetite. Low field Anisotropy of Isothermal Remanence Magnetization (AIRM) was used to test for fabrics defined by relatively low coercivity minerals, such as multidomain magnetite, determining if different coercivity ferromagnetic grains preserve a different fabric.

AARM measures the variation in Anhysteretic Remanent magnetization (ARM) with orientation which will preferentially magnetize relatively higher coercivity grains in a sub-sample (McCabe and Jackson, 1985). An ARM was imparted in 15 directions rotational measurement scheme (P Mode) (Hext, 1963; Jelinek, 1978) per sub-sample using the PAM-1 pulse magnetizer, applying an AC field of 140mT and a DC field of 100μT. Remanence was induced in a given direction, measured using the JR-6A spinner magnetometer, then the sub-sample was fully demagnetized by tumbling in a 120mT AC field in the LDA-5 demagnetizer and repeated for all orientations.

Low field AIRM measures the variation of Isothermal Remanent Magnetization (IRM) with orientation using a weak DC field, preferentially targeting low coercivity phases (Stephenson et al., 1986). The same position protocol used for AARM of inducing a remanence magnetization was used in measuring AIRM. Magnetization was imparted in a given direction with a 20mT DC field using the PAM-1, before measuring remanence using the JR-6A. After measurement, the LDA-5 was used to demagnetize the sub-samples, with a 2-axis tumbler in a peak AF of 120 mT. To avoid confusion with AMS, the AMR maximum, intermediate and minimum principal directions are referred to as a_1, a_2 and a_3 for AARM and i_1, i_2 and i_3 for AIRM respectively.

4.3.4.3 Crystallographic Preferred Orientation

Crystallographic data can contextualize magnetic fabrics by defining the crystallographic alignment of silicate crystals, the so-called Crystallographic Preferred Orientation (CPO) (Žák et al., 2008a; Vernon, 2014; Bella Nké et al., 2018). In this test, Electron Backscatter Diffraction (EBSD) uses the diffraction patterns from polished surfaces of oriented thin sections or block samples to define the crystallographic preferred orientation (Prior et al., 2009). The generation of CPO data is especially valuable in studies using AMS and AMR as they ensure that the bulk magnetic fabric and fabric carried by ferromagnetic particles is representative of the wider silicate-defined alignment.

Crystallographic Preferred Orientation (CPO) was measured in the enclave from sites FE004 (a petrofabric-aligned enclave), and FE008 (a petrofabric-oblique enclave) using Electron Backscatter Diffraction (EBSD) on one thin section per site (sub-samples FE004_K1 and FE008_K1, respectively). Thin sections were orientated to be subparallel to the plane containing the k_1 and k_3 axes. Before analysis, the sections were polished using colloidal silica then given a 5nm carbon coat to reduce charging. EBSD was measured using an FEI Scios focused ion beam-scanning electron microscope (FIB-SEM) equipped with an Edax Hikari EBSD camera. EBSD patterns were collected using the Edax TEAM Analysis system and indexed with OIM Analysis 8.0 from Ametek-Edax. To ensure a representative number of crystals were analysed from each sub-sample, seven 1.7x1.3mm areas were mapped per thin section. The SEM was operated with a 20kV acceleration voltage and 26nA beam current. A constant sample tilt of 70° was applied with an average working distance of 14mm and EBSD mapped at a step size of 10μm. CPO was measured from equal area pole figures (PF) of all silica phases within the enclaves for comparison with magnetic fabrics.

4.4 Results

4.4.1 Field and Thin Section Petrography

4.4.1.1 Field Observations

A traverse of the pluton was carried out to gain a consensus on petrofabric variation within the monzodiorite. A continuous petrofabric, observed in the field as a foliation without a clear macroscopic lineation, is defined across the pluton by euhedral mafic minerals (hornblende and biotite) and feldspars with the strike varying from N-S to NW-SE trending (Fig. 4.2). The petrofabric is most intense at the pluton's centre at Melmore Head, becoming less intense toward the periphery (Fig. 4.2). At Melmore Head the petrofabric is a prominent N-S striking, sub-vertical foliation. The petrofabric is associated with the 'Melmore Migmatite', described by Pitcher and Berger (1972). Partially molten pelite and metadolerite country rock rafts and xenoliths are incorporated into the well-defined granite foliation, with the palaeosomes showing a dextral shear-sense indicating that this is a dextral, N-S shear zone (Fig. 4.3). Moving East into Ballyhoorisky point, the petrofabric is much weaker with the strike rotating to an NNE-SSW foliation (Fig. 4.2). The variation in petrofabric strike is indicative of fabric vergence away from the shear zone. Moving further East to Fanad Head, the petrofabric rotates to become NW-SE aligned at Fanad Head at the eastern extent of the Pluton. The weakening of the petrofabric intensity from the shear zone at Melmore Head, alongside the rotation of its strike suggests it was active during magma intrusion, as suggested by Pitcher and Berger (1972).

Across the research site a consistently aligned petrofabric is recorded in the host monzodiorite, consisting of a locality-averaged sub-vertical foliation of 015/83E, forming an apparent NNE-SSW aligned fabric (Fig. 4.4 and Table S1). The 320 m^2 research site consists of two wave-washed outcrops separated by a dilational fracture (Fig. 4.4). Outcrops within the zone show a number of minor fractures (≈5m long) related to dilation during pluton uplift to the surface, as well as regions which are covered in black and green algae and rock pools which have a pink lichen. Enclaves range in size from long-axes lengths of 60 to 655mm and morphologies range from irregular spheres to strongly elongate. All enclaves show a consistent internal phenocrystic texture with contacts between enclaves and the host monzodiorite varying from sharp and well-defined in nature where enclaves protrude slightly from the outcrop surface, to lobate and gradational where enclaves are flush with the surface. The enclave long-axis orientations define three trends: 1) aligned with the host monzodiorite petrofabric, trending 015 to 025, 2) oblique to the petrofabric trending 030 to 040 and 3) oblique to the petrofabric trending 340 to 360 (Fig. 4.4 and Table S1). Long/short axis ratios from 150 enclaves vary from 1.05 to 8.50 with a mean ratio of 2.59. Aside from enclave long-axis alignment and the petrofabric of the host monzodiorite, no other kinematics of strain are observed in the research site.

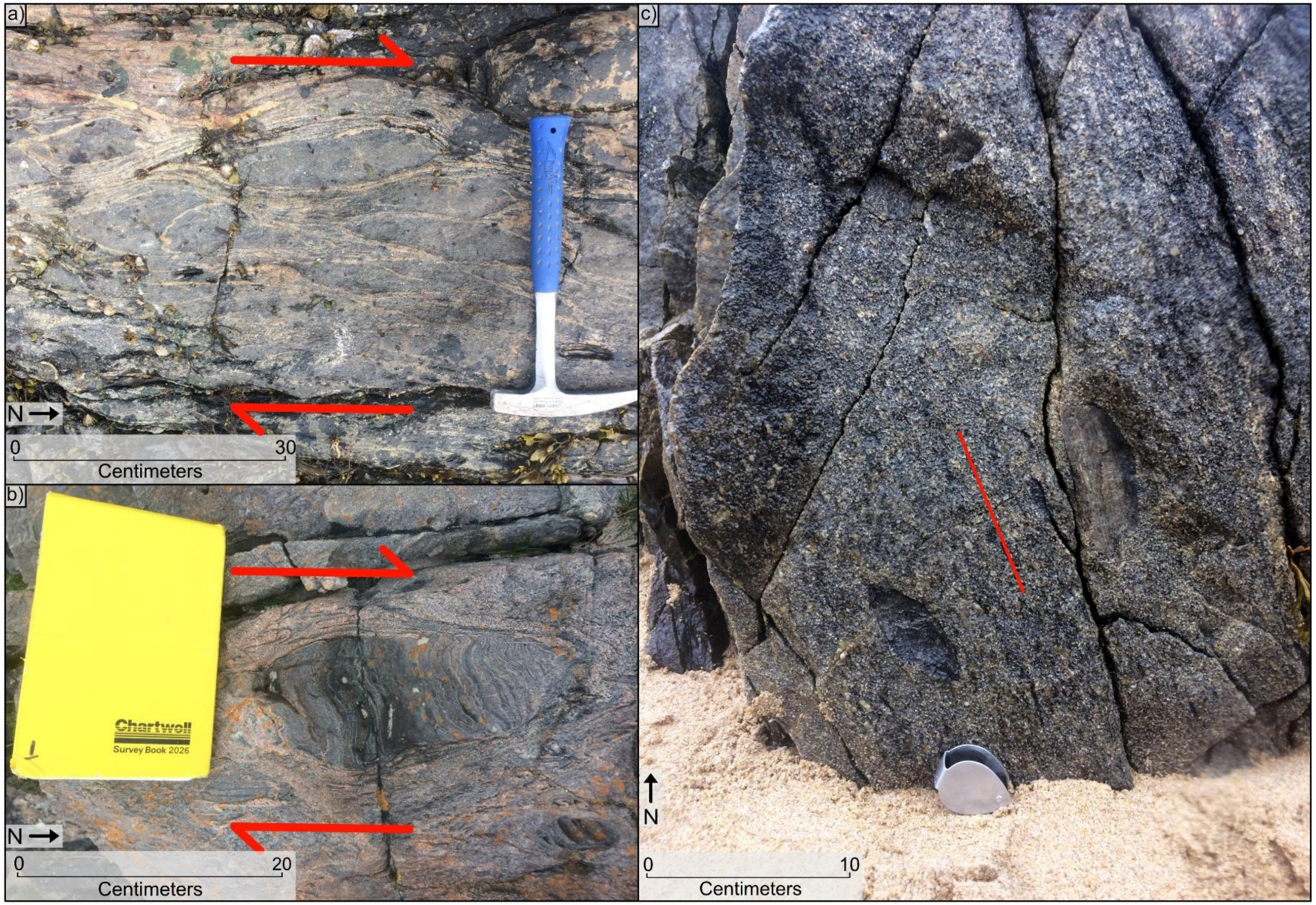

Figure 4.3 – (a) Metadolerite boudins and (b) pelitic xenoliths within the Melmore Migmatite showing dextral shearing. (c) Vertical section exposure highlighting the fabric of the host monzodiorite (red line) within the Melmore Head shear zone and pelite and quartzite xenoliths.

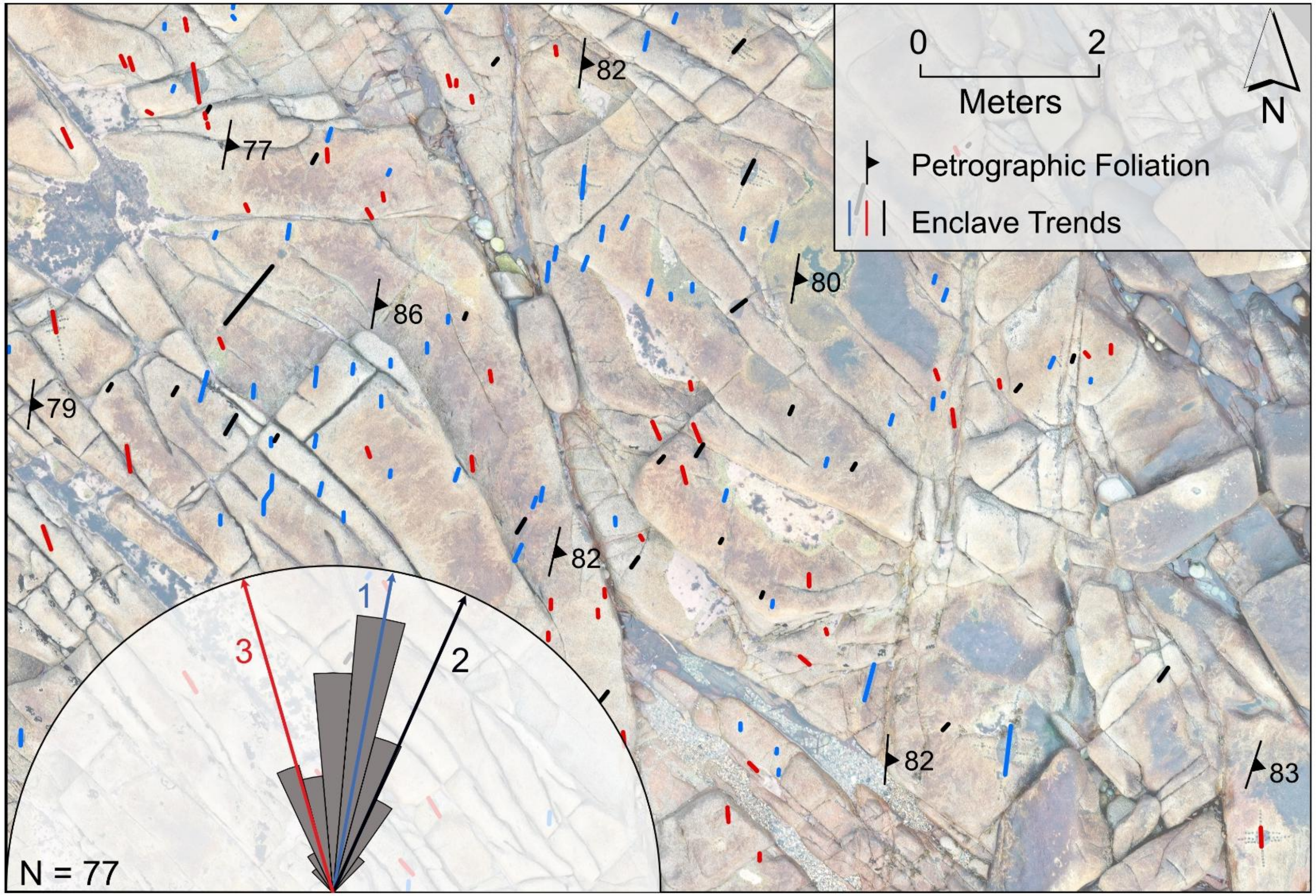

Figure 4.4 – Enclave long- axis orientation measurements across research locality with rose diagram (inset) showing three trends in enclave orientations: (1) 015– 025 (blue), (2) 030– 040 (black), and (3) 340– 360 (red). All enclaves are denoted by a coloured line, with any unmarked areas of black, green, or pink representing algae or lichen growth on the outcrop.

4.4.1.2 Host Monzodiorite Petrography

The host monzodiorite is medium to coarse-grained (1-5mm) quartz monzodiorite containing plagioclase feldspar (55%), alkali feldspar (5%), hornblende (10%), biotite (15%) and quartz (10%) with minor amounts of oxides and rutile (Fig. 4.5a–c). Feldspars are euhedral to subhedral with weak to moderate alteration and are unzoned or weakly zoned (Fig. 4.5a). Plagioclase shows simple Carlsbad and multiple twinning, with alkali feldspar commonly perthitic, both feldspar types show biotite and hornblende inclusions. Rare deformation textures are preserved, with plagioclase predominantly exhibiting deformation twinning, while alkali feldspar shows patchy flame perthite formation (Fig. 4.5b). Plagioclase and alkali feldspar both exhibit a weak undulose extinction with the point of extinction sweeping from contacts with mafic grains. Rare occurrences of myrmekite are also observed at feldspar-quartz contacts (Fig. 4.5b). Quartz is interstitial to feldspars and mafic grains, showing amoeboid shapes. A range of deformation textures are recorded within quartz, the most dominant of these being undulose extinction originating at the contacts between quartz and surrounding mafic grains. Rare evidence of grain boundary migration recrystallization, as well as sub-grain rotation recrystallization are also recorded (Fig. 4.5c). Mafic minerals are smaller (≈1mm) than feldspars and quartz (≈3-5mm) in most sections and form distinct clusters or trends which align with the weak fabric. Hornblende forms clear euhedral grains with deformation twinning and kinking observed parallel to the long axis alignment (Fig. 4.5c). Biotite shows a similar texture with euhedral grains, with deformation observed as rare broken or fibrous ends to grains (Fig. 4.5c). Oxides are present primarily as inclusions within hornblende as seen in the enclave, as well as large, isolated grains away from mafic grains (Fig. 4.5c). The rare deformation textures within feldspars, quartz, hornblende and biotite suggest a very minor level of dynamic recrystallization with magmatic state textures dominating the host monzodiorite.

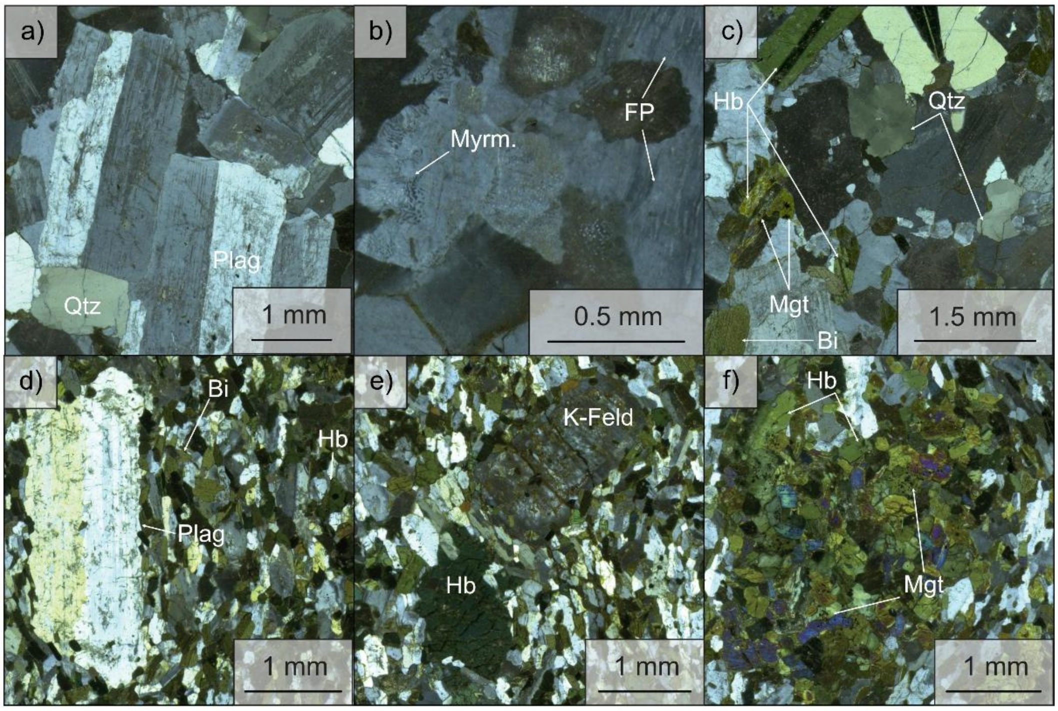

Figure 4.5 – (a) Cross- polarized transmitted light (XPL) image of host monzo diorite subhedral plagioclase and alkali feldspar. (b) Cross- polarized light (XPL) image of host monzodiorite showing flame perthite and myrmekite development. (c) Host monzodiorite showing deformation textures in hornblende and biotite, as well as the development of grain boundary recrystallization in quartz and presence of oxides. (d) XPL image of enclave showing plagioclase feldspar phenocryst and groundmass alignment, forming a magmatic foliation alongside minor deformation kinking in groundmass hornblende. (e) XPL image of enclave alkali feldspar and hornblende phenocrysts enveloping the magmatic foliation within fine-grained groundmass. (f) XPL image of enclave showing hornblende glomerocryst with interstitial oxides. Bi – biotite; FP – flame perthite; Hb – hornblende; K-Feld – alkali feldspar; Mgt – magnetite; Myrm. – myrmekite; Plag – plagioclase feldspar; Qtz – quartz.

4.4.1.3 Enclave Petrography

The enclaves from both FE004 and FE008 are porphyritic diorite consisting of plagioclase feldspar (40%), alkali feldspar (5%), hornblende (30%), biotite (25%) and minor amounts of magnetite and rutile (Fig. 4.5d–f). Phenocrysts are 1-3mm in length and are primarily plagioclase although rare alkali feldspar and hornblende phenocrysts also occur within the fine-grained (≈80μm) groundmass (Fig. 4.5e). A strong to weak long-axis alignment of phenocrysts and groundmass crystals is observed, with deflections of the alignment of groundmass crystals around the phenocrysts (Fig. 4.5d–e). Phenocrysts are euhedral to subhedral with inclusions of biotite, hornblende, and rare inclusions of oxides. Crystals range from unzoned to weakly zoned, with both growth and rare deformation twinning preserved (Fig. 4.5d–e). Weak undulose extinction is preserved within phenocrysts, with extinction dispersing through crystals perpendicular to the observed alignment and starting where phenocrysts are in contact with mafic grains. External contacts of phenocrysts commonly show distinct haloes of mafic grains (Fig. 4.5d–e). Partial to moderate alteration is also observed within the phenocrysts. Within the groundmass, euhedral to subhedral plagioclase displays simple Carlsbad twinning and rare multiple twinning. Rare undulose extinction is also seen in the plagioclase dispersing perpendicular to their long axis alignment at mafic crystal contacts. Within the groundmass, hornblende grains are euhedral to subhedral and occur as individual crystals and as glomerocrysts which vary from 1-3mm in size (Fig. 4.5f). Rare evidence of deformation twinning and kinking is also observed (Fig. 4.5d). Euhedral biotite within the groundmass is often in contact with hornblende grains. Deformation textures are rarely observed but present as distinct grain fractures/forking (Fig. 4.5d). Oxides are preferentially associated with hornblende, incorporated within glomerocrysts and as inclusions within single hornblende grains (Fig. 4.5f).

4.4.2 Characterisation of Magnetic Carriers

4.4.2.1 Temperature-Dependent Magnetic Susceptibility

T-$\mathcal{X}$ data reveals a high degree of consistency regarding the magnetic properties of both the enclave and host monzodiorite sub-samples in sites FE004 and FE008 (Fig. 4.6). This suggests that the representative sample set has a common dominant magnetic mineralogy.

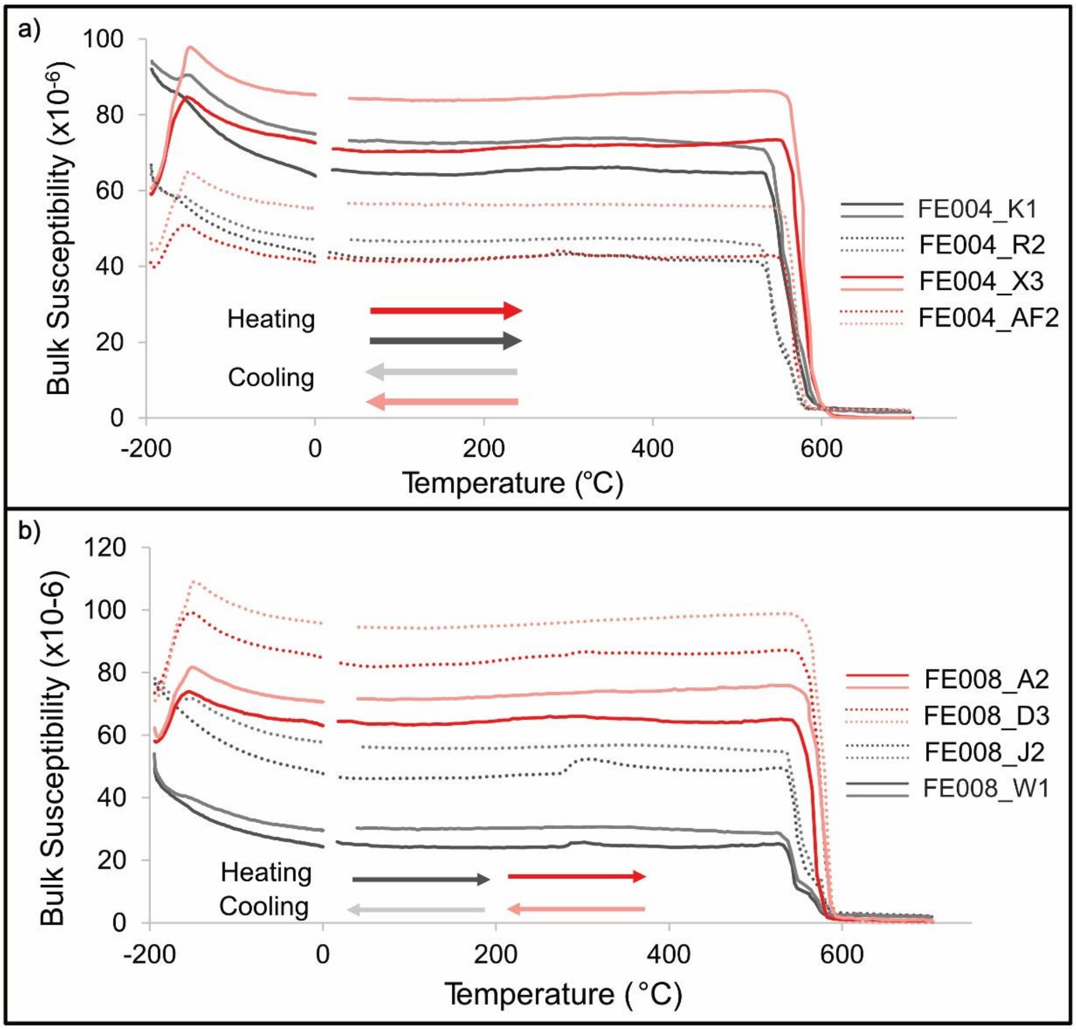

Figure 4.6 – Temperature dependence of magnetic susceptibility (T-χ) results for (a) enclave site FE004 and (b) enclave site FE008. Subsamples from the host monzodiorite are shown in red, while subsamples from enclaves are shown in grey.

In host monzodiorite sub-samples, initial heating curves show a clear Verwey transition (V_T) inflecting at -160°C, Bulk susceptibility then remains constant until a sudden drop in bulk susceptibility from 550°C, the Curie Temperature (T_C) of the sub-samples (Fig. 4.6). A reversible trend is seen during cooling from 700°C to room temperature and then reheating from -194°, with a 10% overall increase in bulk susceptibility observed (Fig. 4.6).

Enclave sub-samples samples from FE004 exhibit similar bulk susceptibility values at room temperature and T_C around 530°C. However, in contrast to the monzodiorite, enclave sub-sample data from FE008 show irreversible heating-cooling curves with a hyperbolic decline in susceptibility during initial heating from -200°C, the V_T is absent, and an inflection is observed around 277°C during heating only (Fig. 4.6). On cooling from 700°C, the 277°C inflection is removed, bulk susceptibility at room temperature increases by 10% and a Vt is detected at -160°C (Fig. 4.6).

4.4.2.2 Isothermal Remanence Magnetisation, Hysteresis Loop Measurements and FORCs

sIRM/BIRM, hysteresis loops and FORC diagrams are similar in all sub-samples from the enclaves and host monzodiorite at sites FE004 and FE008, suggesting that both rocks have the same dominant ferromagnetic minerals (Fig. 4.7). Results from sIRM/BIRM for a representative enclave sub-sample (FE008_J1) and host sub-sample (FE008_D1) are summarized in (Fig. 4.7a). A representative hysteresis loop and FORC diagram from one enclave sub-sample (FE008_J2) and one host monzodiorite sub-sample (FE008_D3) are shown in (Fig. 4.7b–c). Results for the other sub-samples are available in the Supplementary Material (Figs. S1–S3 and Table S2).

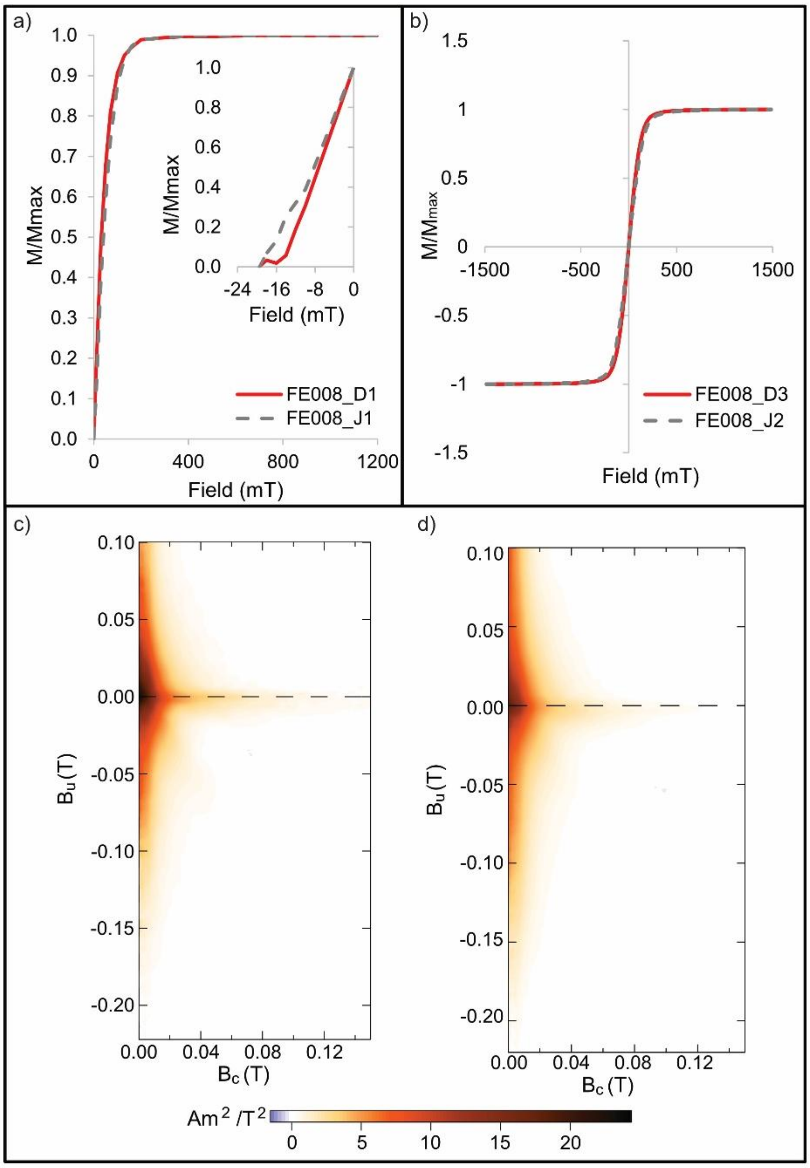

Figure 4.7 – Magnetic characterization results for representative subsamples of host monzodiorite and enclave (full data sets are given in Figures S1– S3 and Table S2 in the Supplemental Material [see text footnote 1]): (a) Saturation isothermal remanence magnetization measurements with backfield isothermal remanence magnetization inset. (b) Hysteresis measurements. (c) First- order reversal curve (FORC) diagram of FE008_D3, with smoothing Sc_0 = 5, Sb_0 = 6, Sc_1 = 8, Sb_1 = 8. (d) FORC diagram of FE008_J2, with smoothing Sc_0 = 5, Sb_0 = 6, Sc_1 = 8, Sb_1 = 8. B_c —coercivity; B_u —distribution of interacting fields between magnetic particles and the applied magnetic field.

IRM/sIRM = 0.95 was reached from 130 to 200mT in all sub-samples (Fig. 4.7a). BIRM measurements show H_{cr} varies from 23 to 16mT when a trend is drawn from each sub-sample from its lowest magnetization to where it becomes zero (Fig.

4.7a). Hysteresis loops show identical trends within the enclaves and host monzodiorite at sites FE004 and FE008 (Fig. 4.7b). Despite applying a field to 1500mT, all sub-samples failed to saturate to give a M_s value as seen during sIRM measurement indicative of paramagnetic hysteresis properties (Tauxe, 1998). After slope correction in HystLab (Paterson et al., 2018), all sub-specimens reach a M_s/M_r ratio of 1 between 200 to 300mT, overlapping with the 95% sIRM values, with a H_c of 1-2mT (Fig. 4.7b).

FORC diagrams show a universal trend within both lithologies at sites FE004 and FE008. (Figs. 4.7c). A greater amount of smoothing was required in sub-specimens from cores of enclaves at sites FE004 and FE008, indicating the influence of paramagnetic grains on the signal (Sc_0=4 Sb_0=10 Sc_1=10 Sb_1=10). All sub-specimens show a ridge extending parallel to B_u axes with a peak at the origin (Fig. 4.7c–d). Alongside this ridge is a minor lobe extending parallel to the B_c axes from 0 to 20mT (Fig. 4.7c–d).

4.4.2.3 Magnetic Mineralogy

Magnetic characterization results delineate a single common, dominant ferromagnetic phase in the enclaves and host monzodiorite (Figs. 4.6, 4.7, S1–S3 and Table S2). T- $\mathcal{X}$ results show the Curie temperature is reached at ~580°C, this is consistent with very low Ti titanomagnetite being the dominant magnetic mineral in both the enclaves and host monzodiorite. A subtle inflection is noted only on some heating curves around 270°C (e.g. FE008), this is consistent with the presence of titanomaghemite as a very minor (<10%) contributor to bulk magnetic susceptibility (Akimoto, 1962; Moskowitz, 1981; Dunlop and Özdemir, 1997; Lattard et al., 2006). The lack Hopkinson peaks in T- $\mathcal{X}$ experiments indicate titanomagnetite is multidomain (MD) in all samples (Tarling & Hrouda, 1993; Dunlop and Özdemir, 1997), this is consistent with the results from sIRM/BIRM, hysteresis loops and FORC diagrams that are available in the Supplementary Material (Figs. S1–S3 and Table S2).

MD titanomagnetite is shown to be the dominant magnetic mineral within the enclaves and host monzodiorite. This precludes the presence of inverse AMS fabrics associated with single-domain grains. These results allow the direct comparison of AMS, AMR and CPO fabrics in the context of our field and petrographic data (Potter and Stephenson, 1988; Tarling and Hrouda, 1993; Ferré, 2002).

4.4.3 Anisotropy of Magnetic Susceptibility

Anisotropy of Magnetic Susceptibility (AMS) results vary systematically into two types, 1) those where the enclave long-axis is orientated parallel to the petrofabric observed in the field and 2) where the enclave long-axis is oblique to the petrofabric observed in the field (Fig. 4.8). Therefore, detailed results are described for two representative sites, FE004 (petrofabric parallel to the enclave) and FE008 (a petrofabric-oblique to the enclave) (Fig. 4.9). The full datasets for all sites provided in the Supplementary Material (Table S3).

4.4.3.1 FE004 – Representative Enclave Aligned to the Petrofabric

Mean susceptibility (K_{mean}) varies from 2.15x10^{-3} to 5.06x10^{-3} within FE004, with higher K_{mean} values clustered within the host monzodiorite at the southern enclave-host contact (Fig. 4.9a–f). A low K_{mean} anomaly is seen within the enclave itself, with elevated K_{mean} in samples M and N (Fig. 4.9a–f). The corrected degree of susceptibility (P_j) varies from 2.9 to 9.4% across site FE004 (Fig. 4.9a–f). Most samples range from 3 to 7%, with the highest degrees of anisotropy seen in the NW of the enclave site in samples V, X and Y (Fig. 4.9a–f). Fabric shape (T) shows a dominance of prolate fabrics within the enclave and host monzodiorite (Fig. 4.9a–f). Most T values range from -0.200 to -0.815, with fifteen samples showing triaxial values (0.200 to -0.200) (Fig. 4.9d). k_1 axes from the host monzodiorite and enclave show a strong alignment, marking a shallow plunging (0 to 20°) NNE trending lineation (Fig. 4.9a–f). k_3 axes outline a moderately to steeply (30 to 65°) dipping foliation striking NNE-SSW (Fig. 4.9a–f). This alignment of AMS fabrics across the site correlates to both the petrofabric in the host monzodiorite and enclave long-axis orientation (Fig. 4.9a–f). The alignment of the magnetic fabric is independent of the variations in K_{mean}, P_j and T (Fig. 4.9a–f). This non-dependent relationship precludes a mineralogical control of fabric strength and shape (Tarling & Hrouda, 1993).

4.4.3.2 FE008 – Representative Enclave Oblique to the Petrofabric

K_{mean} varies from 1.99x10^{-3} to 4.90x10^{-3} across the enclave site (Fig. 4.9g–l). Values of K_{mean} are elevated within the host monzodiorite relative to the enclave, with a high K_{mean} anomaly seen in the SE of the site. A low K_{mean} anomaly is seen in the enclave in samples J and W (1.99x10^{-3} to 2.35x10^{-3}) (Fig. 4.9g–l). P_j values vary from 3.7 to 9.1% (1.037 to 1.091) across the site, with an increase in the host monzodiorite to the NW (Fig. 4.9g–l). P_j is lower within the enclave, with a low Pj recorded in samples I, J, K and W (Fig. 4.9g–l). T shows a transition towards more oblate shape fabrics relative to FE004 (0.200-0.714), with fourteen samples showing triaxial values (Fig. 4.9g–l). k_1 axes predominantly trend to the NNE, forming a shallow plunging (0 to 30°) lineation (Fig. 4.9g–l). k_3 axes again highlight a moderately to steeply dipping (35 to 70°) foliation striking NNE-SSW. Unlike site FE004, this consistent NNE-SSW trending magnetic fabric within the enclave at site FE008 is misaligned to its long-axis orientation (Fig. 4.9g-l). As with site FE004, the alignment of the magnetic fabric is independent of the variations in K_{mean}, P_j and T showing a non-mineralogical control to the fabric (Fig. 4.9g–l).

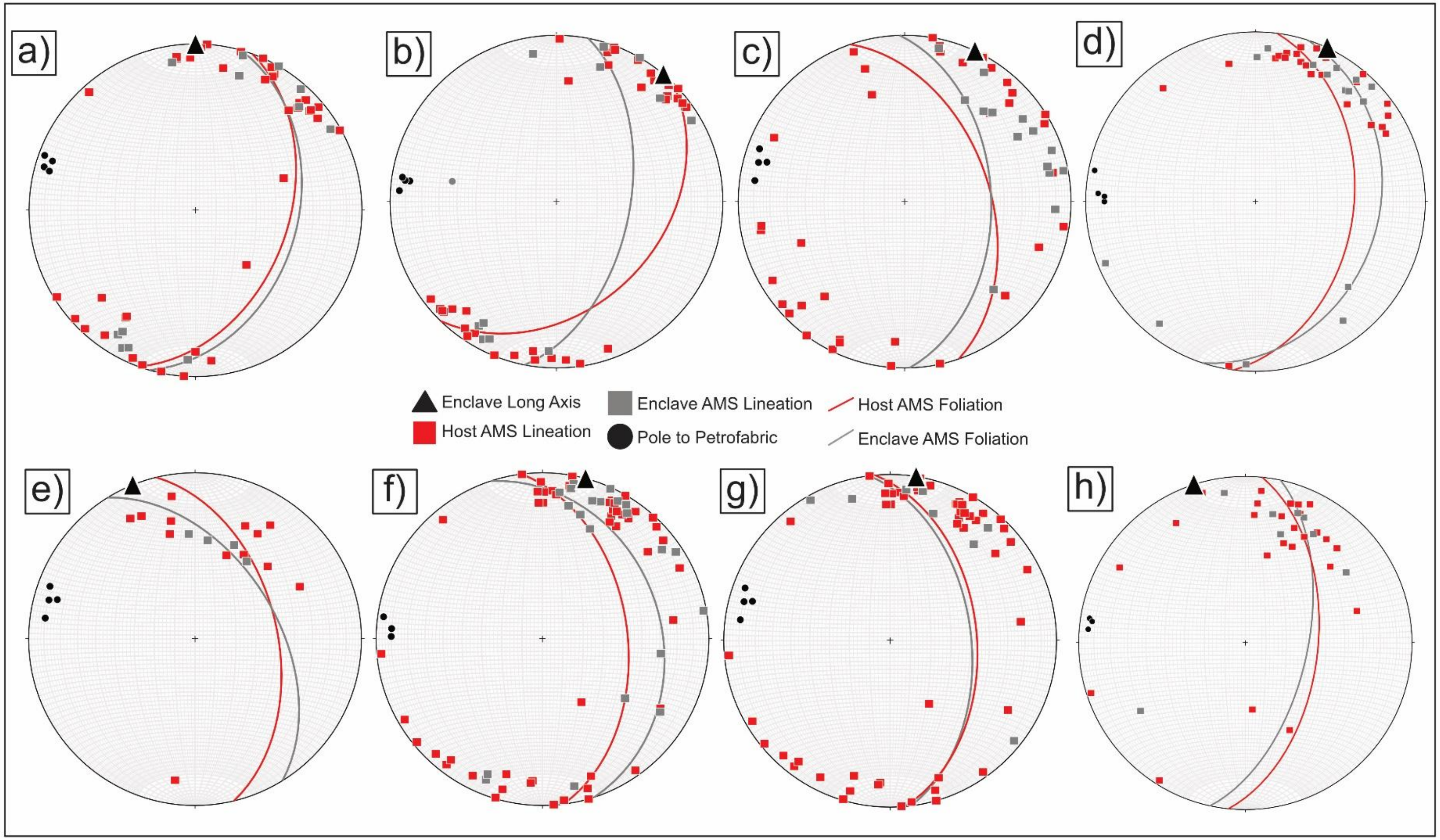

Figure 4.8 – Stereonets of anisotropy of magnetic susceptibility (AMS) data for eight enclave sites: (a) FE001, (b) FE002, (c) FE003, (d) FE004, (e) FE005, (f) FE006, (g) FE007, and (h) FE008.

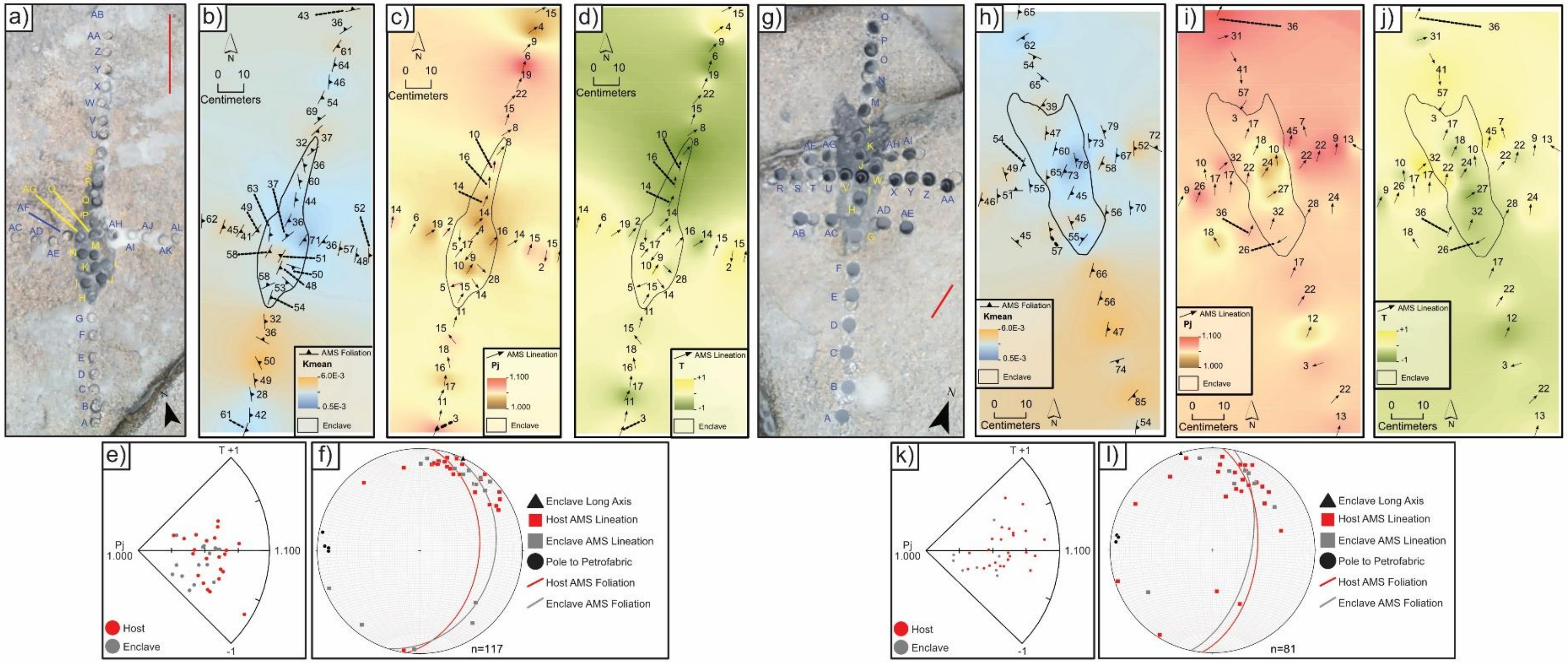

Figure 4.9 – (a – f) Anisotropy of magnetic susceptibility (AMS) data for enclave site FE004: (a) core sites, (b) AMS foliation data and interpolated mean susceptibility (Kmean) surface, (c) AMS lineation data and interpolated corrected degree of anisotropy (Pj) surface, (d) AMS lineation data and interpolated shape factor (T) surface, (e) Cartesian plot of Pj vs. T, and (f) stereonet of AMS and petrofabric data poles to foliation. (g– l) AMS data for enclave site FE008: (g) core sites, (h) AMS foliation data and interpolated Kmean surface, (i) AMS lineation data and interpolated Pj surface, (j) AMS lineation data and interpolated T surface, (k) Cartesian plot of Pj vs. T, and (l) stereonet of AMS and petrofabric data poles to foliation.

4.4.3.3 Deviatoric Susceptibility

Deviatoric Susceptibility (*K'*) varies from 2.28×10^{-5} to 2.16×10^{-4}, several orders of magnitude greater than single crystal values of hornblende (1.19×10^{-8}) and biotite (4.96×10^{-8}) (Biedermann et al., 2014, Biedermann et al., 2015) (Fig. S4 and Table S4). Together with the magnetic characterization, this result shows that AMS in all sites must be dominated by a low coercivity, high susceptibility ferromagnetic mineral such as multi-domain, low Ti titanomagnetite.

4.4.4 Anisotropy of Magnetic Remanence

Anisotropy of magnetic remanence (AMR) data will be presented from site FE004 (a petrofabric-aligned enclave) and FE008 (a petrofabric-oblique enclave) simultaneously, with AARM described before moving onto AIRM. A summary of the data is provided in (Fig. 4.10), with full datasets provided in the Supplementary Material (Table S3).

At FE004, the AARM lineation defined by a_1 (the maximum principal remanence direction), appears to show no trend across the site, with no distinct alignment recorded amongst the enclave or host monzodiorite sub-samples (Fig. 4.10a). The plunge of a_1 is also steeper relative to k_1, with most sub-samples having a shallow to steep plunge (7 to 61°, average 35°). When all sub-samples are viewed together, an approximate NNE-SSW aligned girdle is recorded AARM foliations show a consistently steep dip (51 to 88°, average 70°) which varies from West to East dipping (Fig. 4.10c). At site FE008, the a_1 axes again show a sporadic nature, with the divergence from the NNE alignment seen in the AMS fabric and an overall steepening of the lineation plunge (7 to 61°, average 35°). A similar girdling of a_1 is seen when all sub-samples are viewed together, which appears to correlate with the dominant strike of the foliations across the site. Two AARM foliation orientations are seen at site FE008, one NNE-SSW aligned and seen in the host monzodiorite, the other NNW-SSE aligned within the enclave, concordant to its long-axis orientation (Fig. 4.10b–d).

The AIRM fabric shows a number of similar features relative to AARM. AIRM Lineations defined by i_1 (the maximum principal remanence direction) are observed across the enclave and host monzodiorite plunge less than that of the equivalent AARM lineation (2 to 47°, average 17°). A roughly NNE-SSW alignment of the host monzodiorite AIRM lineations is seen, with the lineations in enclave sub-samples sporadic in orientation. When all sub-samples are viewed together, an approximate NNE-SSW girdle of i_1 is seen in both sites, which correlates with the orientation of the foliation of the AIRM fabric (Fig. 4.10).

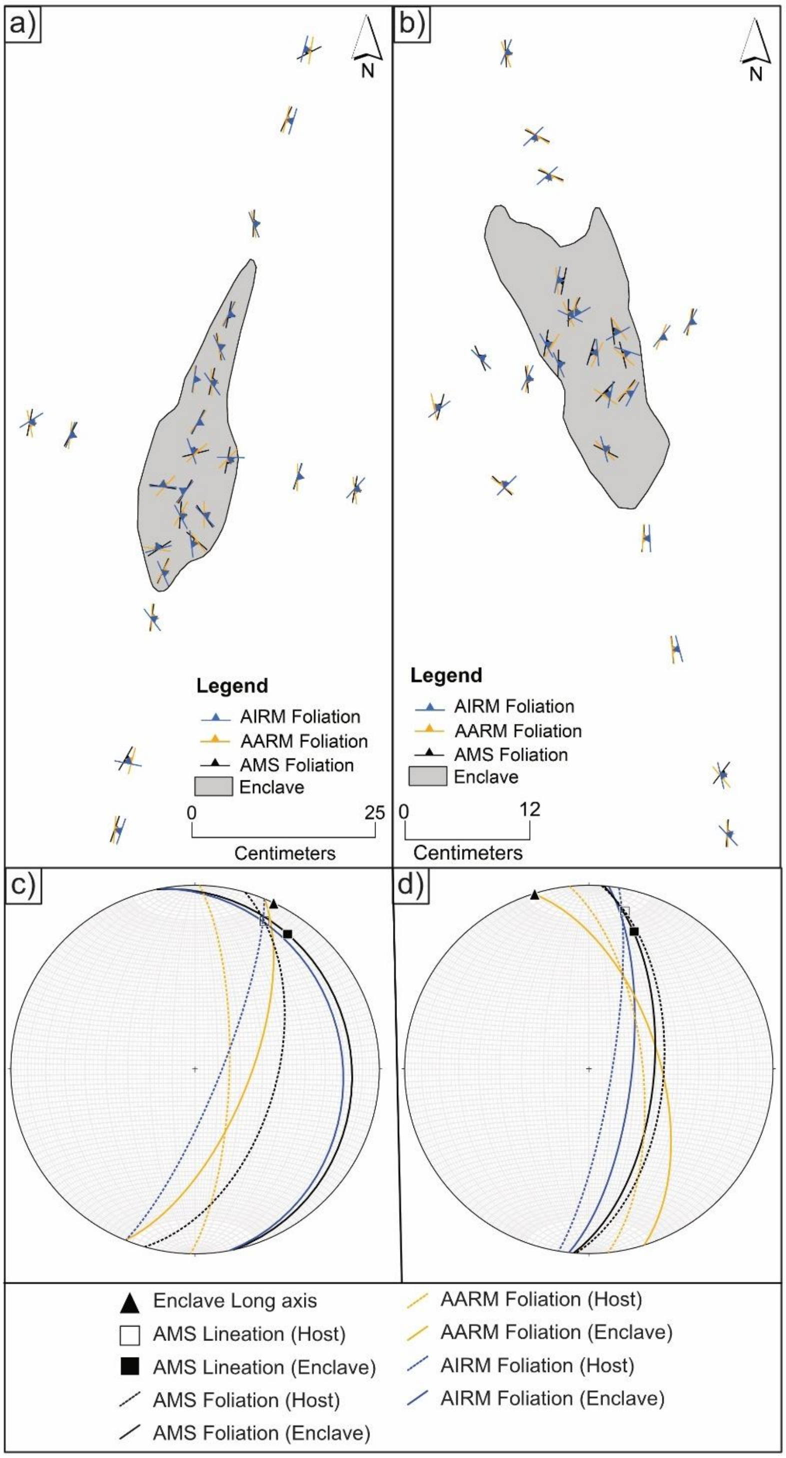

Figure 4.10 – (a) AMR and AMS data for enclave site FE004, (b) AMR and AMS data for enclave site FE008, (c) stereonet of data for FE004, and (d) stereonet of data for FE008.

4.4.5 Crystallographic Preferred Orientation

Within site FE004, plagioclase feldspar [001] axes (crystal c-axis) form a distinct girdle parallel to the magnetic foliation, with [010] axes (crystal b-axis) overlapping with the k_1 axes (Fig. 4.11a and Table S5). Biotite [001] axes (crystal c-axis) align with k_3 axes, with [010] (crystal b-axis) and [100] (crystal a-axis) aligning with k_2 and k_1 respectively. Hornblende shows [001], [010] and [100] axes aligning with the k_1, k_2 and k_3 respectively.

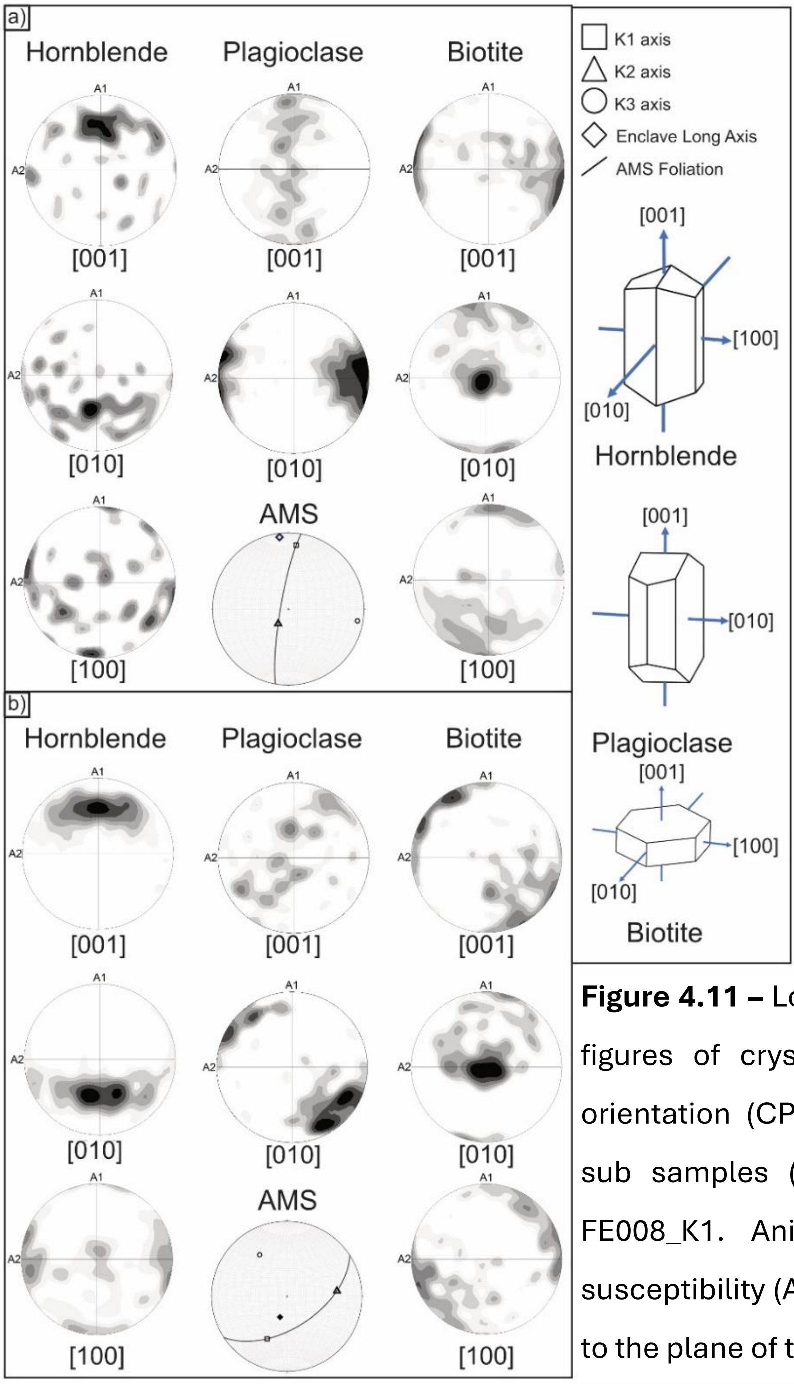

Figure 4.11 – Lower- hemisphere pole figures of crystallographic preferred orientation (CPO) data from enclave sub samples (a) FE004_K1 and (b) FE008_K1. Anisotropy of magnetic susceptibility (AMS) data were rotated to the plane of thin section.

A similar trend is seen in the CPO of silicate mineral is seen in site FE008 (Fig. 4.11b). However, there is a clear variation in hornblende crystallographic orientation. [010] shows alignment with the k_1 axis within the sub-sample, while [100] appears to correlate with k_3 and [001] is oblique to the AMS axes (Fig. 4.11b and Table S5).

4.5 Discussion

In line with our field observations, our analysis quantifies two types of fabric development within enclaves based on long-axis orientation: Type 1 enclaves with their long axes aligned parallel to the visible petrofabric in the host monzodiorite (a foliation with no visible lineation), and Type 2 enclaves with their long axes aligned oblique to the petrofabric (Fig. 4.9 and Tables S3 and S5). Interpretation of each enclave type will focus on a representative enclave from each group, with FE004 representing Type 1 and FE008 representing Type 2. Results from the remaining six enclaves are available in the Supplementary Material (Tables S3 and S5).

4.5.1 Outcrop-Scale Fabrics

Outcrop-scale fabrics can be observed from visible petrofabrics observed in the host monzodiorite and the long-axis orientation of the enclaves within the mingling zone. The host monzodiorite shows a consistent NNE-SSW striking sub-vertical foliation across the mingling zone, with textural observations of thin sections highlighting its development in a magmatic state (Fig. 4.5). This suggests the stress regime developing this petrofabric was active syn-emplacement of the Fanad Pluton. The observed spatial dependence to fabric orientation and strength is strongly indicative that the petrofabric developed as a result of active tectonic strain within the N-S aligned shear zone at Melmore Head (Fig. 4.2). This suggests that the field observed petrofabric of the Fanad pluton is an archive of a tectonomagmatic interaction rather than a magma transport or emplacement-related fabric.

A more nuanced understanding of fabric development is preserved in the enclave long-axis alignment. They occur in isolation from dykes or other magma injection sites and are therefore interpreted to have been transported through the pluton, changing their morphology and orientation to varying degrees in response to forces associated with ascent, emplacement and tectonism (Žák et al., 2007). Mapping of enclave orientations defines three trends of long-axis orientations, one parallel to the petrofabric orientation (Type 1 enclaves), and two trends oblique to the petrofabric (Type 2 enclaves) (Fig. 4.4). Type 1 enclaves reflect globules of mafic magma with similar rheologies to the host monzodiorite during transport, causing them to align to the host monzodiorite petrofabric (see Scaillet et al., 2000; Caricchi et al., 2012) In contrast, Type 2 enclaves represent mafic magma that had a large rheological contrast to the surrounding host monzodiorite, passively rotating under the applied palaeostress.

Combining outcrop-scale fabrics of the mingling zone shows a consistent tectonomagmatic interaction recorded in the enclaves and their surrounding host monzodiorite related to the shear zone at Melmore Head. The N-S orientation and dextral shear-sense of the shear zone are similar to hypothesized ascent structures in the Galway Granite Complex, which are oblique and genetically related to the regional-scale NE-SW sinistral faults active during the Caledonian Orogeny (McCarthy et al., 2015a; McCarthy et al., 2015b). This indicates that while dextral in shear-sense, the shear zone at Melmore Head is related to orogen-scale sinistral transtension along structures such as the nearby Leannan Fault which was active during magma emplacement (White and Hutton, 1985). However, studies of other late-Caledonian intrusions with similar mineral fabric development have inferred fabrics to be related to magmatic flow (e.g., Stevenson et al., 2007; Stevenson, 2009; Petronis et al., 2012). By comparing these outcrop-scale fabrics to the underutilized grain-scale fabrics within enclaves, we can test the emplacement-derived nature of such fabrics.

4.5.2 Grain-Scale Fabrics

AMS, CPO and AIRM record a consistently aligned NNE-SSW fabric concordant to the visible petrofabric in the host monzodiorite formed under late-Caledonian sinistral transtension (Figs. 4.9–11). This causes the grain-scale fabric to be aligned to the long-axis of Type 1 enclaves, but systematically misaligned to the long-axis orientation of Type 2 enclaves. This suggests the development of the grain-scale fabric in Type 2 enclaves was independent of enclave shape rotation recorded at the outcrop scale, but no further context for this misalignment can be made.

The AARM subfabric in site FE008 (Fig. 4.10b–d) related to a sub-population of high coercivity particles within Type 2 enclaves is strongly indicative of a relic primary fabric formed prior to the dominant NNE-SSW fabric. This primary fabric was aligned with the enclave long-axis, with the majority of silicate and ferromagnetic minerals subsequently realigned to be concordant with the fabric in the surrounding host monzodiorite. This realignment provides quantitative evidence of tectonic overprinting of fabrics by late-Caledonian transtension, an overprint unobserved in outcrop-scale fabrics or the grain-scale fabrics in the host monzodiorite.

4.5.3 Mush-State Fabric Overprinting

The nature of the tectonic overprint of the primary magmatic fabrics can be identified from subtle petrographic and magnetic property variations between the host monzodiorite, petrofabric-aligned enclaves (Type 1) and petrofabric-oblique enclaves (Type 2). Thin section petrography highlights no evidence of pervasive solid-state recrystallisation within the enclaves or host monzodiorite, meaning that the grain-scale fabric must have developed whilst the dioritic enclaves and host monzodiorite were in magmatic to submagmatic state (Fig. 4.5). However, the variation in long-axis orientation of Type 2 enclaves indicates that petrofabric-oblique enclaves must have been rigid enough to inhibit enclave shape deformation under continued bulk strain (Scaillet et al., 2000; Caricchi et al., 2012). This restricts fabric realignment of the Type 2 enclaves to have occurred in a partially crystallized, mushy magma (Marsh, 1996). Evidence for fabric mush-state realignment is often difficult to observe once a magma has fully crystallized, however, numerical modelling by Burgisser et al., (2020) and Carrara et al., (2024) suggests that deformation of a mushy magma occurs via the development of force-chain strain partitioning as the stress regime is applied. While our data cannot irrefutably confirm the presence of force chain development, the subtle variations in the fabric between Type 1 and Type 2 enclave behavior are consistent with mush-state fabric realignment associated with force chains (Figs. 4.8 & 4.10). These variations are primarily seen in the hornblende crystallographic axes and AMS fabric shape (T). Hornblende CPO in the FE004 (petrofabric aligned) shows clustering of [001], [010] and [100] axes relative to k_1, k_2 and k_3 respectively, but with a weak girdling of orientations of [010] and [100] also measured, defining a c-fibre texture (Biedermann et al., 2018). In contrast, the hornblende crystallographic axes in FE008 (petrofabric oblique) show clear point distributions, with [001] and [010] oblique relative to k_1 and k_2 (Fig. 4.11). These transitions in hornblende CPO occur with changes in AMS T values to triaxial and oblate in FE008 (Fig. 4.9).

4.5.4 Multifabric Development in Enclaves

Based on our quantitative analysis of outcrop-scale and grain-scale fabrics, we propose a new model for enclave fabric development, showing their ability to archive multiple fabrics throughout pluton construction (Fig. 4.12). This multi-fabric development shows enclaves act as long-lasting archives of strain, beyond the proposed limits to active strain expression based on enclave shape as proposed by Scaillet et al., (2000) and Caricchi et al., (2012).

At the outcrop-scale, three separate phases of magma transport into the mingling zone are defined from the observed trends in enclave long-axis orientation (Fig. 4.4). One of these trends is aligned to the petrofabric of the surrounding host monzodiorite (Type 1 enclaves), while the other two trends are oblique to the petrofabric of the surrounding host monzodiorite (Type 2 enclaves). All enclaves were likely transported into the mingling zone under late-Caledonian sinistral transtension, but Type 1 enclaves were transported while at a similar rheology to the host monzodiorite while Type 2 enclaves were at a rheological contrast to the surrounding magma due to partial crystallization. The variation in rheology between enclave types likely relates to the relative timing of transport into the mingling zone, with Type 2 enclaves formed in an earlier phase than Type 1 enclaves. The low rheology contrast of Type 1 enclaves allowed them to act as strain indicators with the host monzodiorite, developing an NNE-SSW long-axis alignment and corresponding grain-scale fabric, consistent with the petrofabric of the host monzodiorite under late-Caledonian transtension (Fig. 4.12).

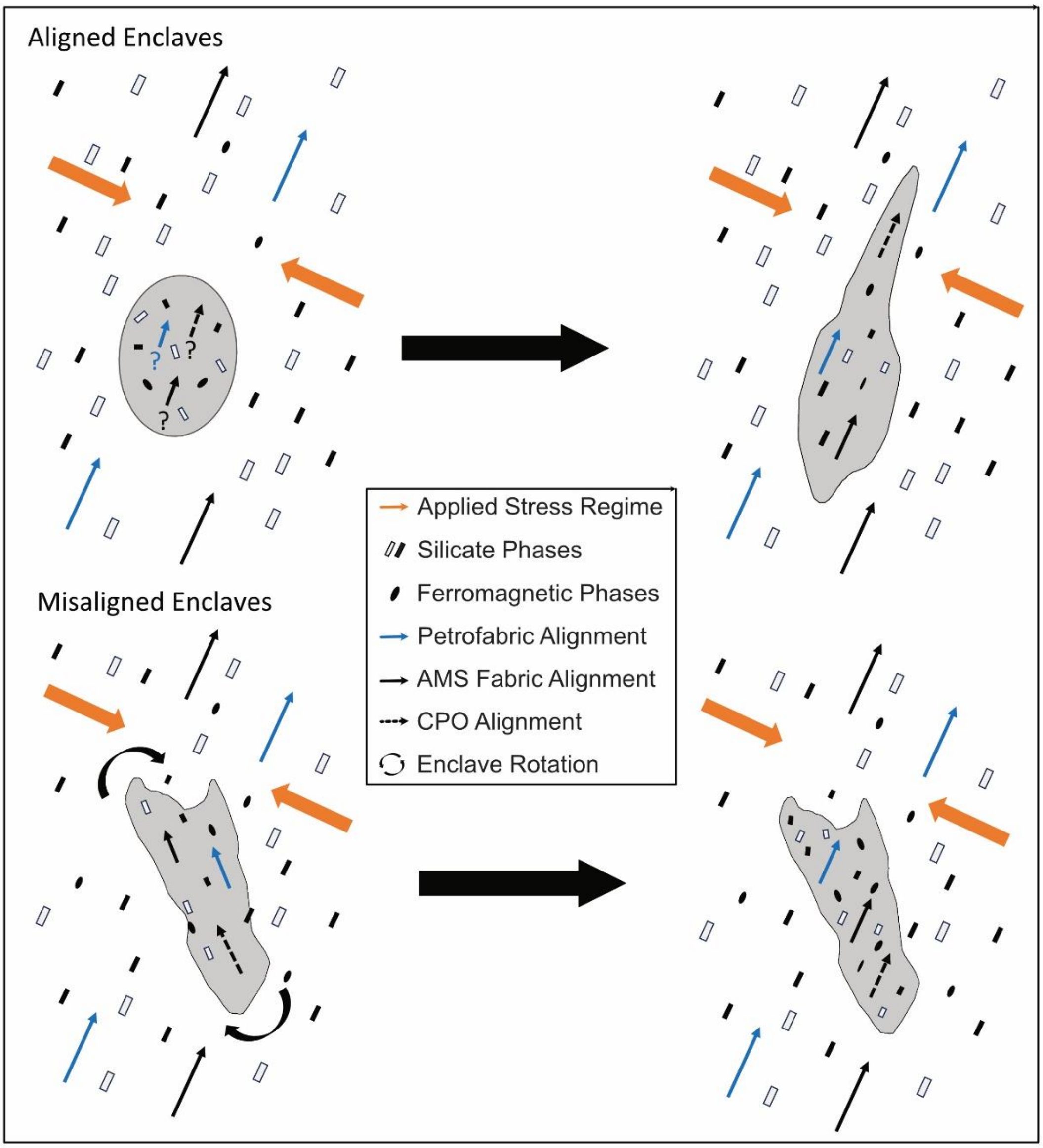

Figure 4.12 – Schematic of fabric formation within the enclaves and surrounding host magma. AMS=anisotropy of magnetic susceptibility; CPO=crystallographic preferred orientation.

Type 2 enclaves would also have initially deformed as strain markers similar to the Type 1 enclaves, forming a long-axis aligned grain-scale fabric petrofabric (Fig. 4.12). However, with continued crystallization, these enclaves would begin to increase in rheology contrast to the surrounding host monzodiorite, entering a mush- magma state. The resultant crystal framework from partial crystallization would impede changes to overall enclave morphology but facilitate internal magma realignment. Therefore, under continued bulk strain of late-Caledonian transtension, the Type 2 enclaves were passively rotated into their current long-axis orientations (Fig. 4.12). The once long-axis aligned grain-scale fabric was then overprinted by the continuing stress from late-Caledonian transtension, leaving only a partial relic of the original fabric carried by higher coercivity ferromagnetic particles in Type 2 enclaves (Fig. 4.12).

4.5.4.1 Insight into Intrusion Fabrics from Enclaves

By distinguishing multiple fabrics for Type 2 enclaves, a previously unrecorded potential for enclaves to give new insight into the development of fabrics across a wider igneous intrusion has been identified. Our results provide unequivocal evidence that the fabric within the Fanad Pluton is a mush-state tectonic overprint, only perceivable when fabrics from multiple magmas are compared. This precludes the emplacement-derived nature of fabric development, as indicated by combined outcrop-scale fabrics and grain-scale fabrics in the host monzodiorite. By demonstrating a magmatic state response to rheological change and ambient tectonic strain, a potential issue is highlighted in the interpretation of magmatic processes based on a ‘primary emplacement fabric’ where fabrics from regions of coeval magma mingling cannot be compared (e.g., Stevenson et al., 2007; Petronis et al., 2012; Magee et al., 2012).

4.6 Conclusion

This study investigates fabric development within enclaves and their surrounding host monzodiorite to determine if new insight into strain within intrusions can be uncovered by comparing fabrics. Using quantitative magnetic and petrographic methods, we show evidence of multiple fabrics preserved within the enclaves.

These fabrics formed while the enclaves and the surrounding host magma were still in a magmatic state, and record strain from magmatic flow processes and regional tectonic strain. Our detailed deconstruction of composite magma fabrics therefore caveats the interpretation of magmatic state fabrics as an archive of primary magma emplacement, with a systematic review of such fabrics required before asserting their origin.

Preservation of multiple fabrics is facilitated by the rheological contrast between mingled magmas, with magmatic flow processes recorded in enclave morphologies whilst grain-scale fabrics reflect a subsequent tectonomagmatic overprint. This overprint is the result of a mush-state realignment, with our study providing quantitative data on how force-chain facilitated fabric development is expressed within mingled magmas.

Our study highlights how the complex strain history of tectonomagmatic interactions interplaying with strain from magma transport and other petrogenetic processes can be contextualized through the comparison of multiple fabrics. Our use of magnetic fabrics alongside CPO and field petrographic data provides a clear example of how a complex strain archive can be unravelled into its separate components and then reinterpreted to identify how regional tectonic stress interacts with different stages of a magmatic system.

Chapter 5: Intrusions are Sensitive, Temporally Constrained Strain Archives

The data from this chapter are published as part of an article in the Journal of the Geological Society and can be found under the following citation:

Latimer, B., McCarthy, W., Mattsson, T. and Reavy, J. 2025. Intrusions are Sensitive, Temporally Constrained Strain Archives. *Journal of the Geological Society*, https://doi.org/10.1144/jgs2025-066.

B. Latimer completed the fieldwork, performed the analyses, generated the figures, and wrote the chapter, with guidance and input from all co-authors.

5.1 Introduction

The development of a kinematic model for an orogenic event is underpinned by the availability and distribution of temporally constrained strain archives (e.g., Görz and Hielscher, 2010; Domeier and Torsvik, 2014). Such models are valuable not only to a given event but can provide new insight into orogenic processes in general, thus facilitating revaluation of other orogenies (e.g., Rosenbaum, 2014; Searle, 2021). In palaeogeographic reconstructions, understanding the tectonic framework of a given orogeny has, for example, important connotations in terms of terrane accretion, assisting in understanding variations in depocenter processes (Lescoutre and Manatschal, 2020; Matenco et al., 2022). Similarly, strain transitions within orogenic systems have been shown as an important aspect in the evolution of life and in palaeoclimatic change, with orogenies involved in nutrient supply through exposure of fresh continental crust to weathering and in the alteration of the climate via gas dispersed during syn-orogenic magmatism (Spencer et al., 2018; Stern and Gerya, 2024). However, the archives upon which kinematic models are formed are often temporally and/or spatially limited along an orogenic front, creating ambiguity in the kinematic evolution from which multiple competing hypotheses arise (e.g., Shaw et al., 2012; Pastor-Galán et al., 2015). In this study, we address this problem by studying a combination of strain records formed during the cooling of an orogenic pluton and compare their relative timing to the broader tectonic stress field to provide new insight into the evolving palaeostress regime.

Previous studies show that modern quantitative rock fabric analysis can detect subtle strain records in igneous plutons, with these data often an archive of regional tectonic strain (e.g., McCarthy et al., 2015a; Sant'Ovaia et al., 2024; Siachoque et al., 2024). Intrusions archive strain across a range of magmatic to solid rheological states through mineral fabric development and the alignment of intrapluton features, allowing multiple records of strain to be developed (Žák et al., 2008b). Post-crystallisation, the development of faults and fractures within an intrusion must reflect an archive of external tectonic strain that was, for example, active throughout and immediately after crystallisation or during some later stress regime flux such as unroofing (Pawley and Collins, 2002; Žák et al., 2009; Ellis and Blenkinsop, 2019). In fluid magmatic to mushy-magma states, intrusions preserve external stress through the development of sub-magmatic mineral fabrics and the alignment of semi-rigid magmatic features, such as dyke emplacement via strain embrittlement of the host intrusion (McCaffrey, 1994; McCarthy et al., 2015b). At even lower crystallinities, regional tectonic strain archives have been reported through the development of magmatic state fabrics and alignment of intrapluton features such as enclaves to the regional tectonic stress field (El Desouky et al., 1996; Latimer et al., 2024).

Alongside external tectonic stress, previous studies also demonstrate that plutons can archive strain derived internally from the stress intrinsic to magma chamber processes (Alasino et al., 2019; Neves et al., 2023; Mattsson et al., 2024). This internal stress accumulates from processes throughout intrusion construction, ranging from magma transport within the intrusion, magma remobilisation at magmatic to sub-magmatic states and during phases of magma overpressure during emplacement(Stevenson and Grove, 2018; Ardill et al., 2020; Witcher et al., 2024). These processes result in the development of magmatic state fabrics that are often indicative of the direction of crustal or pluton scale magmatic transport, as well as intrapluton features such as ring structures and hybridised magmatic sheets formed from dynamic magma chamber subsidence and crystal settling (Žák and Klomínský, 2007; Magee et al., 2012; Ardill et al., 2020; Koopmans et al., 2022; Cruz et al., 2022; Köpping et al., 2023).

As both internal and external stress can be imparted throughout crystallisation, strain features derived from either stress source can be microstructurally similar, with the imparting of successive or simultaneous stress regimes preserved as complex, composite fabrics within an intrusion (Petronis et al., 2012; Mattsson et al., 2024). Successive processes, such as multiple injections of magma during piece-meal pluton construction, will produce multiple partial fabrics as latter processes crosscut earlier strain records, as seen in the Sawmill Canyon area of the Tuolumne Batholith where the emplacement of the Cathedral Peak granodiorite truncates earlier viscous deformation of the Half Dome Granodiorite (Paterson et al., 2008). Simultaneous preservation of stress regimes, for example during a tectonomagmatic interaction between the regional stress field and intruding magma, may produce a fabric which is intermediate to all active stress regimes and requires detailed analysis to decipher (Petronis et al., 2012; Latimer et al., 2024).

Where strain arising from tectonic stress can be distinguished from magma chamber processes, the utility of modern fabric analysis and geochronological methods unlock new opportunities to constrain the kinematic evolution of the orogeny (Neves et al., 2023; Knight et al., 2024). For example, within the Variscan Orogeny in the Iberian Massif, the combination of previously published geochronology with anisotropy of magnetic susceptibility (AMS) fabric data identifies temporally constrained transitions in magnetic fabric development, consistent with the evolution of orogen kinematics (Sant'Ovaia *et al.* 2024). Similarly, the integration of AMS, anisotropy of anhysteretic remanence magnetisation (AARM) and microstructural analysis with geochronology data has been shown within Permian and Jurassic plutons in the southern Colombian Andes to detect a kinematic evolution from dextral transpression towards pure-shear orthogonal collision (Siachoque et al., 2024). Across Ireland and the UK, studies have been carried out on igneous plutons which combine the temporal constraints of plutons with magnetic fabric and microstructural data to constrain the kinematic evolution of the Caledonian Orogeny (McCarthy, 2013; Anderson et al., 2018; Knight et al., 2024). However, while successful at constraining orogen kinematics at the local scale, for example in the analysis of the Omey and Roundstone plutons of the Galway Granite Complex, consensus on the kinematic development of the broader Caledonian belt is limited as comparable detailed strain records are not yet available (McCarthy et al., 2015c, 2015b).

This study examines the strain archive in the Fanad Pluton, NW Ireland, to assess how features intrinsic to magma chamber processes are differentially recorded to those associated with regional tectonic strain. Using a combination of unmanned aerial vehicle (UAV)-based fracture analysis, AMS data and petrographic observations, we analyse archives formed during and after crystallisation. We compare our results to the available regional geochronological data to evaluate how the strain archive in this pluton feeds into the regional kinematic framework of the Caledonides. We demonstrate that detailed, quantitative strain analysis yields new insight on the interplay between magmatic and regional tectonic stress during late Caledonian orogenesis and highlight that this approach can provide temporally constrained strain archives along orogenies in general.

5.2 Background Geology

The Caledonian Orogeny represents the Ordovician to Silurian amalgamation of Laurentia, Avalonia and Baltica during the closure of the Palaeozoic Iapetus Ocean (Pickering et al., 1988; Woodcock, 1990; Soper et al., 1992). The Early Ordovician accretion of a magmatic arc to the Laurentian margin resulted in the Grampian orogenic event that triggered regional scale folding and metamorphism of the Dalradian Supergroup into which a suite of gabbros and granitoids intruded from *ca.* 475 – 460 ±2Ma (U-Pb on zircon) (Friedrich et al., 1999; Friend et al., 2000; Johnson et al., 2017). This was followed by the orthogonal collision of Baltica and Laurentia to form Laurasia, followed by oblique docking of Laurasia with the northern Avalonian margin from *ca.* 435 – 400Ma (Woodcock, 1990; McKerrow et al., 2000). This late-stage oblique docking at the end of the orogeny is reported to initiate extensive transcurrent deformation (Dewey and Strachan, 2003; Soper and Woodcock, 2003; Prave et al., 2024). Several phases of punctuated magmatism occurred during the Caledonian orogeny; in NW Ireland and Scotland granitoid intrusions are broadly divided into the 'Older' granites (*sensu lato*) associated with the Grampian event and the 'Newer' granites related to the docking of Baltica and Avalonia which appear to ascend along deep-seated structures formed throughout the orogeny (Jacques and Reavy, 1994; Brown et al., 2008).

Competing kinematic models are reported for the extent and timing of regional transcurrence associated with the oblique convergence of Avalonia (Soper et al., 1992; Dewey and Strachan, 2003; Soper and Woodcock, 2003). It is broadly accepted that final closure of the Iapetus Ocean initially resulted in a phase of sinistral transpression that juxtaposed the Northwest Highlands, Grampian and Southern Uplands Terranes along NE – SW faults from around 440 – 420Ma under an N-S aligned maximum shortening direction (Soper et al., 1992; Dewey and Strachan, 2003; Soper and Woodcock, 2003). However, during the waning of orogenic compression kinematic models differentially proposed a transition to orthogonal collision with a rotation of maximum shortening to an NW-SE direction (Soper et al., 1992) or a phase of sinistral transtension and rotation of maximum shortening to NE-SW (Dewey and Strachan, 2003; Soper and Woodcock, 2003). While the transpression-transtension models are kinematically consistent, the timing of the kinematic transition is debated to be earlier than 420Ma (Soper and Woodcock, 2003) or as late as 410 – 405 Ma (Dewey and Strachan, 2003; McCarthy, 2013).

An alternative hypothesis on the tectonic evolution of the Caledonides favours a single-event model whereby Grampian arc collision is followed by continued southward Iapetan subduction and continued near orthogonal convergence of the orogen from 470 – 420Ma (Searle, 2021). This model requires a continuous NW-SE maximum shortening direction, removing the requirement for regional sinistral transpression, with the NE – SW faults that traverse Ireland and the UK representing structures initiated at the end of the orogeny. Based on detrital zircon analysis of the metasedimentary country rock and geochemical analysis of igneous complexes around the Great Glen Fault, Prave et al. (2024) propose an intermediary model between a regional oblique convergence model and the near orthogonal model of Searle (2021). This model favours a strike-slip displacement along NE – SW faults during the orogeny, but with displacement of 200 – 300km rather than the 1,200km reported by Dewey and Strachan (2003). The feasibility of contrasting models such as these can be tested by providing additional temporally constrained strain markers along the orogen. These strain markers allow determination of the direction of maximum shortening across the orogenic front throughout its evolution, thus facilitating comparison between competing models.

5.2.1 The Donegal Igneous Complex

It is broadly accepted that late Caledonian magmatism was caused by breakoff of the subducted Iapetan slab beneath Laurentia, triggering asthenosphere upwelling and partial melting of the overlying crust (e.g., Atherton and Ghani, 2002; Oliver et al., 2008; Neilson et al., 2009a; Miles et al., 2016). Across Ireland and the UK, late Caledonian granitoid plutons are sited along sub-vertical strike-slip faults (Fig. 5.1). The spatial distribution and geometry of the plutons, as well as the alignment of regional faults and magmatic to sub-magmatic state fabrics within these plutons, indicate that magma ascent was directed along these pre-existing structures (Jacques and Reavy, 1994; Hutton and Alsop, 1996; Cooper et al., 2013).

The Donegal Igneous Complex (DIC) in NW Ireland includes the Donegal Batholith, consisting of six plutons, and two smaller satellite plutons located outside the batholith (Fig. 5.1) (Pitcher and Berger, 1972). The main pluton of the batholith stitches the NE – SW Main Donegal Shear Zone and is centred on the intersection between this structure and the NNE – SSW Donegal Lineament (Sanderson et al., 1980; Hutton, 1982; Hutton and Alsop, 1996). The Barnesmore Pluton and the Fanad Pluton occur to the south and northeast of the Donegal Batholith, respectively (Fig. 5.1b). The complex intruded between 430 – 400Ma, the Fanad Pluton was contemporaneous with the initial plutons of the main batholith, while the Barnesmore Pluton was intruded as one of the latest phases of magmatism within the complex (Pitcher and Berger, 1972; Archibald et al., 2021). The ascent of the main batholith is interpreted to have occurred at the intersection of the NE – SW sinistral Main Donegal Shear Zone and the NNE – SSW Donegal Lineament (Hutton and Alsop, 1996). The main pluton of the Donegal Batholith shows a pervasive, sub-vertical NE – SW foliation interpreted to reflect the interplay between magma ascent and NE-SW shearing along the Main Donegal Shear Zone (Hutton, 1982). Fabric studies on other plutons of the Donegal Batholith reveal broadly concentric foliation patterns that have been differentially related to laccolith or inflation processes (Molyneux and Hutton, 2000; Stevenson et al., 2007a, 2008a; Stevenson, 2009). However, detailed rock fabric analysis demonstrates the preservation of both magma transport and tectonic fabrics in the Fanad Pluton, suggesting that subtle AMS fabrics recorded elsewhere in the DIC may also be tectonic in origin (Latimer et al., 2024).

The Fanad Pluton (418 – 411±3 Ma) (U-Pb on zircon) (Archibald et al., 2021) is partially exposed along the North coast of Donegal, with a dioritic to granodioritic composition and is similar to other Caledonian intrusions derived from a hybridised magma source (Ghani and Atherton, 2006). The pluton is associated with two major structures; the NE – SW aligned Leannan Fault and the N – S Melmore Shear Zone (Fig. 5.1) (White and Hutton, 1985; Latimer et al., 2024). The left-lateral Leannan Fault is interpreted as a splay of the Great Glen Fault (Alsop, 1992; Kirkland et al., 2008)or, more recently, as the continuation of the Great Glen Fault into Ireland (Prave et al., 2024). Geochronological and crosscutting relationships report sinistral displacement occurred along the Leannan Fault up to *ca*. 422Ma before an apparent 10Ma hiatus in displacement and subsequent onset of an NW-SE directed compressional regime during the transition from sinistral transpression to orthogonal convergence (Soper et al., 1992; Kirkland et al., 2008). Fabric analysis in the magma mingling zone adjacent to the dextral Melmore Shear Zone demonstrates the preservation of distinct magmatic state fabrics that differentially reflect magma transport and tectonic overprinting processes (Latimer et al., 2024). However, the full magmatic to solid-solidus strain archive is understudied and thus the position of the intrusion in the broader kinematic regime is ambiguous.

Here, we assess magmatic and sub-solidus strain records to better constrain the strain history of the Fanad Pluton and to test the utility of intrusions as regional strain archives. The 422 – 411Ma period of emplacement intersects three potential tectonic stress regimes; 1) the proposed kinematic transition of Dewey and Strachan (2003) from sinistral transpression to transtension, 2) sinistral transtension expected in the model of Soper and Woodcock (2003), or 3) a reported lack of regional tectonic strain under the model of Searle (2021), which proposes the end of tectonic stress at 420Ma. Within stress regimes 1) and 2), strain records within the Fanad Pluton should preserve an archive of magmatic and tectonic processes, while in regime 3), in the absence of tectonic stress only magmatic processes should control the record of strain. Our study assesses these competing hypotheses by presenting new structural data.

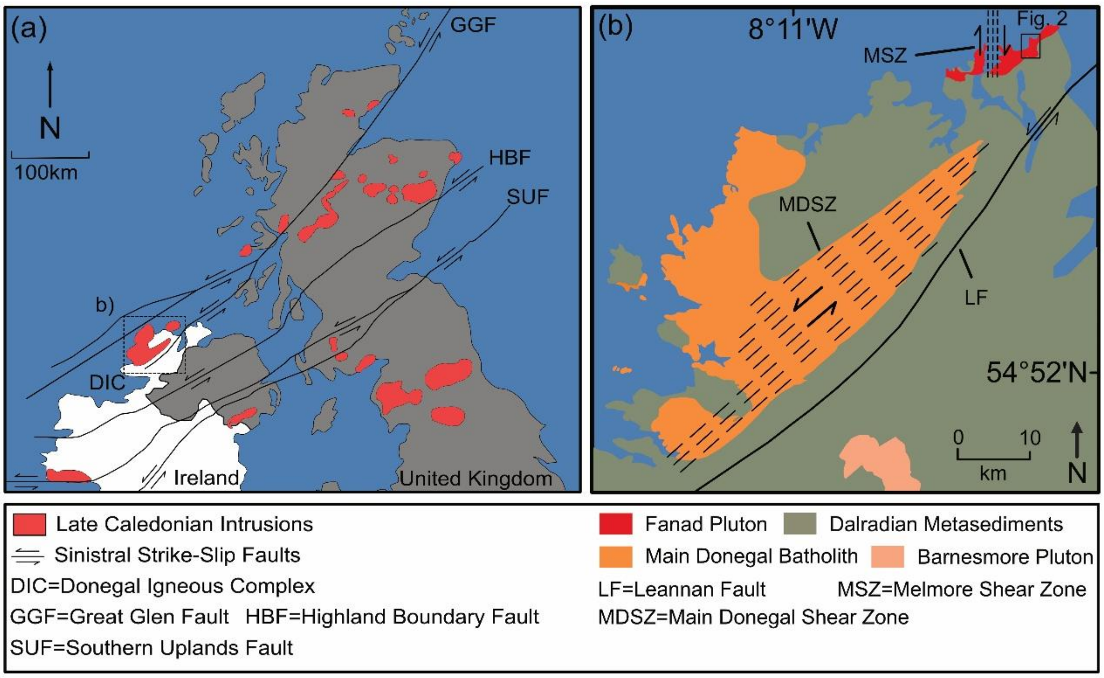

Figure 5.1 – (a) Overview of late Caledonian intrusions in the north of Ireland and the UK. (b) Regional map of the Donegal Igneous Complex.

5.3 Methodology

5.3.1 Field and UAV Observations

An 800 m strip of coastal outcrop of the Fanad pluton known as Currin Point, exhibiting a combination of monzodiorite, enclaves, sheets, faults and fractures was selected for this study to maximise the opportunity to measure multiple strain records during and after magma cooling (Fig. 5.2a). The area was mapped over two field seasons, describing the relationship between intrapluton features and collecting structural data from magmatic and sub-solidus structures. Grid mapping at 1:80 scale was conducted around magmatic sheets, enclave swarms and faults. While the majority of the outcrop is flat-lying wave-washed outcrop, fractures, rock fabrics and intrusive contacts were measured wherever possible.

Unmanned aerial vehicle (UAV) image mosaic recorded contact relationships between intrusive contacts and the orientation of enclaves, dykes and fractures. UAV images were captured using a Mavic II Pro drone with a 20-megapixel camera at a fixed height of 50m and 20m above the surface with a 70% overlap. Images were combined into an orthomosaic image using PIX4Dmapper software (PIX4D S.A., 2024). All visible linear features and the long axes of enclaves were measured from the mosaic in ArcMap (ESRI, 2020). The orientation data were analysed in Stereonet 11 (Allmendinger et al., 2012) on equal-area rose diagrams with measurements binned in 20° increments based on the statistical methods of Sanderson and Peacock (2020). Trends in orientation were first characterised based on their formation in a magmatic or sub-solidus setting, before examining orientation trends independent of feature types to determine shared orientations across the temporal evolution of the study area.

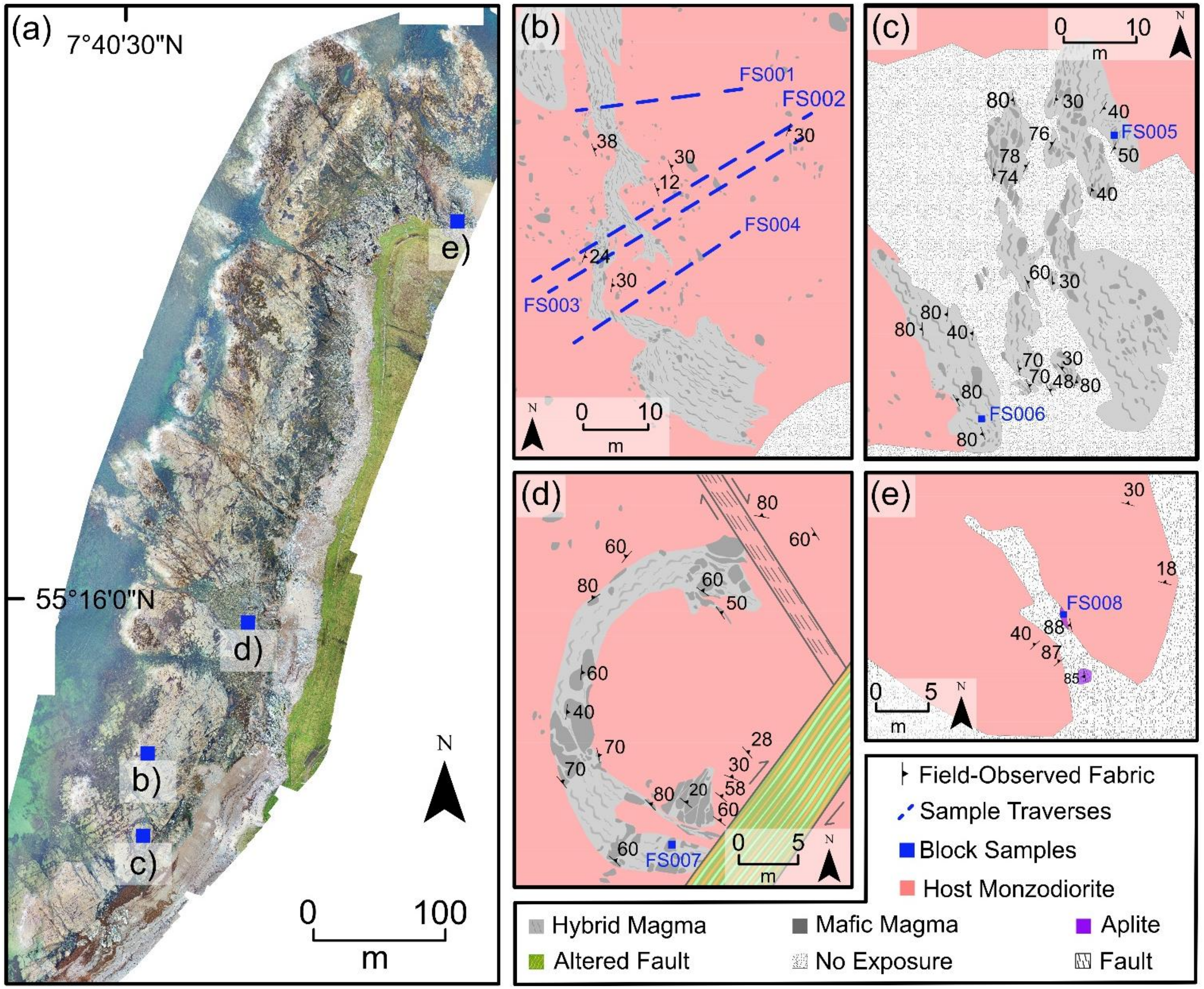

Figure 5.2 – (a) UAV imagery of the Currin Point area (shown in Fig. 5.1). (b) Map of magmatic sheet S1 showing the location of sample traverses FS001–FS004. (c) Map of magmatic sheet S2 showing the location of block samples FS005 and FS006. (d) Map of ring structure S3 showing the location of block sample FS007. (e) Map of aplite S4 showing the location of block sample FS008.

5.3.2 Rock Magnetic Fabric Analysis

To complement field observations, anisotropy of magnetic susceptibility (AMS) was used to investigate the grain-scale strain record and determine if the magnetic fabric was consistent with intrinsic magma chamber or external tectonic processes (Sawyer, 2000; Žák et al., 2008b; De Saint Blanquat et al., 2011; Latimer et al., 2024). Provided an adequate magnetic characterisation is carried out, AMS is broadly recognised as an efficient method for measuring the bulk alignment of minerals within a rock sample based on the three-dimensional variation of magnetic susceptibility about a cylindrical specimen rotated in an induced magnetic field (Tarling and Hrouda, 1993; Borradaile and Jackson, 2010; Mattsson et al., 2021).

Samples were taken from four areas across Currin Point for AMS measurement and magnetic characterisation (Fig. 5.2). Sample traverse sites S1, S2 and S3 sampled separate magmatic sheet features and site S4 sampled an aplitic dyke. Sampling traverses were drilled along S1 while S2 – S4 were block sampled to investigate any variation in magnetic fabric proximal to sheet intrusions. At S1, four traverses (FS001 – FS004) orientated perpendicular to the strike of a mafic sheet were sampled using a 2.5cm diameter nonmagnetic drill bit and Brunton compass. Each traverse was between 25 – 60m in length, and clusters of 6 cores were taken at 2 – 10m intervals. Within areas showing evidence of magma mixing or mingling, a continuous line of cores was drilled at a 2.5 – 10cm spacing to capture intricate coeval magma interactions. Any enclaves encountered along each traverse of suitable size for drilling were also sampled parallel to the long axis of the enclave. A total of 470 cores were drilled across traverses FS001 – FS004. Each core was subsequently cut into 2.5cm x 2.2cm subsamples using a non-magnetic saw, with an average of 2 subsamples per core. Block samples were taken from sites S2 (samples FS005 – FS006), S3 (sample FS007) and S4 (sample FS008) to confirm the rock magnetic behaviour was consistent across the study area (Fig. 5.2). Blocks were orientated in the field with a compass clinometer, drilled at the M^{3}Ore lab at the University of St Andrews using a drill press and cut into subsamples. 5 – 15 rock cores were drilled per block sample (a total of 32 cores), with a minimum of 13 subsamples generated from each block sample.

AMS was measured on each subsample using an AGICO KLY-5A kappabridge. Each subsample was measured in 320 orientations (field: 400Am-1, frequency: 1220Hz) using the 3-D rotator attachment, producing a second-rank tensor with principal direction of maximum (k_1), intermediate (k_2) and minimum (k_3) magnetic susceptibility (Khan, 1962; Borradaile and Jackson, 2010). These axes define the magnetic fabric within the subsample where k_1 is the magnetic lineation orientation, and the plane of k_1 and k_2, of which k_3 is the pole define the magnetic foliation (Tarling and Hrouda, 1993). Mean susceptibility (k_{mean}) gives the mean magnetic susceptibility of the subsample, corrected degree of anisotropy (P_j) gives the strength of the magnetic fabric, and corrected shape factor (T) describes the shape of the magnetic susceptibility ellipsoid (Jelinek, 1981; Tarling and Hrouda, 1993). AMS data was reduced using the Safyr7 software (Chadima, 2022) and Anisoft6 (Chadima and Hrouda, 2023). The arising data represents the bulk mineral fabric of the subsample, provided interfering magnetic mineralogies are not present.

5.3.3 Magnetic Mineralogy and Characterisation Methods

Several experiments we conducted to characterise the magnetic mineralogy that controls the AMS signal. The magnetic susceptibility of common ferromagnetic minerals (e.g. magnetite, hematite) is orders of magnitude higher than diamagnetic (e.g., quartz, feldspar) and paramagnetic (e.g. biotite, hornblende) minerals (Tarling and Hrouda, 1993; Dunlop and Özdemir, 1997). AMS measurements are therefore more likely to be dominated by ferromagnetic minerals where they make up >0.01% of rock mode. The grain-scale AMS of ferromagnetic minerals is dependent on crystallographic axis orientation and domain state (Tarling and Hrouda, 1993). Coarse, multidomain grains have a “normal” response i.e. the AMS long axis is parallel to the crystallographic long axis, whilst fine, single domain grains have an “inverse” AMS i.e. the AMS short axis is parallel to the crystallographic long axis (Potter and Stephenson, 1988). If more than one ferromagnetic mineral is present, or if more than one petrofabric is present, constructive or destructive interference may result in an "intermediate" fabric (Ferré, 2002). Establishing both domain state and mineralogy of study subsamples is therefore crucial to establish the relationship between AMS data and the physical alignment of minerals in a rock sample i.e. the petrofabric.

Temperature-dependent magnetic susceptibility (T-x) was measured to identify the magnetic mineralogy and determine the role of ferromagnetic and paramagnetic minerals on the bulk magnetic susceptibility of each lithology (Tarling and Hrouda, 1993; Dunlop and Özdemir, 1997). The ferromagnetic mineralogy of each lithology was further characterised through the measurement of magnetic hysteresis loops and first-order reversal curves (FORCs) to determine the magnetic domain state of particles in the rock and if multiple ferromagnetic particle populations are present and therefore potentially different magnetic subfabrics (Ferré, 2002).

A comprehensive description of sample preparation, subsamples measured and the applied parameters for each experiment are given in the Supplementary Material.

5.4 Results

Results from field observations and unmanned aerial vehicle (UAV) data are separated into magmatic and sub-solidus features based on the rheological state of the host monzodiorite during their formation. Full datasets for measured orientations from UAV images and field measurements are given in the Supplementary Material.

5.4.1 Magmatic Features

5.4.1.1 Fabric of the Host Monzodiorite

The Fanad Pluton is predominantly a quartz monzodiorite (referred *sensu lato* below as the 'host monzodiorite') consisting of plagioclase feldspar, alkali feldspar, amphibole, biotite and quartz in hand specimen (see Latimer et al., 2024 for a detailed petrographic description) (Fig. 5.3d). Crystals are euhedral to subhedral in nature, with no evidence of plastic deformation, grain fracturing or melt infill (Fig. 5.3d). Unlike other areas of the Fanad Pluton described in Latimer et al. (2024), no visible alignment of minerals is observed across the majority of the study area (Fig. 5.3d). Two exceptions are observed; 1) proximal to magmatic sheets and enclave swarms, a contact parallel foliation is observed in the host monzodiorite and 2) strong, solid-state S-C fabrics, defined by thin C-bands of fine-grained altered minerals and S-bands of deformed feldspar, quartz ribbons and smeared biotite, are observed within a NE-SW sinistral fault which crosscuts the host monzodiorite (Fig. 5.3e).

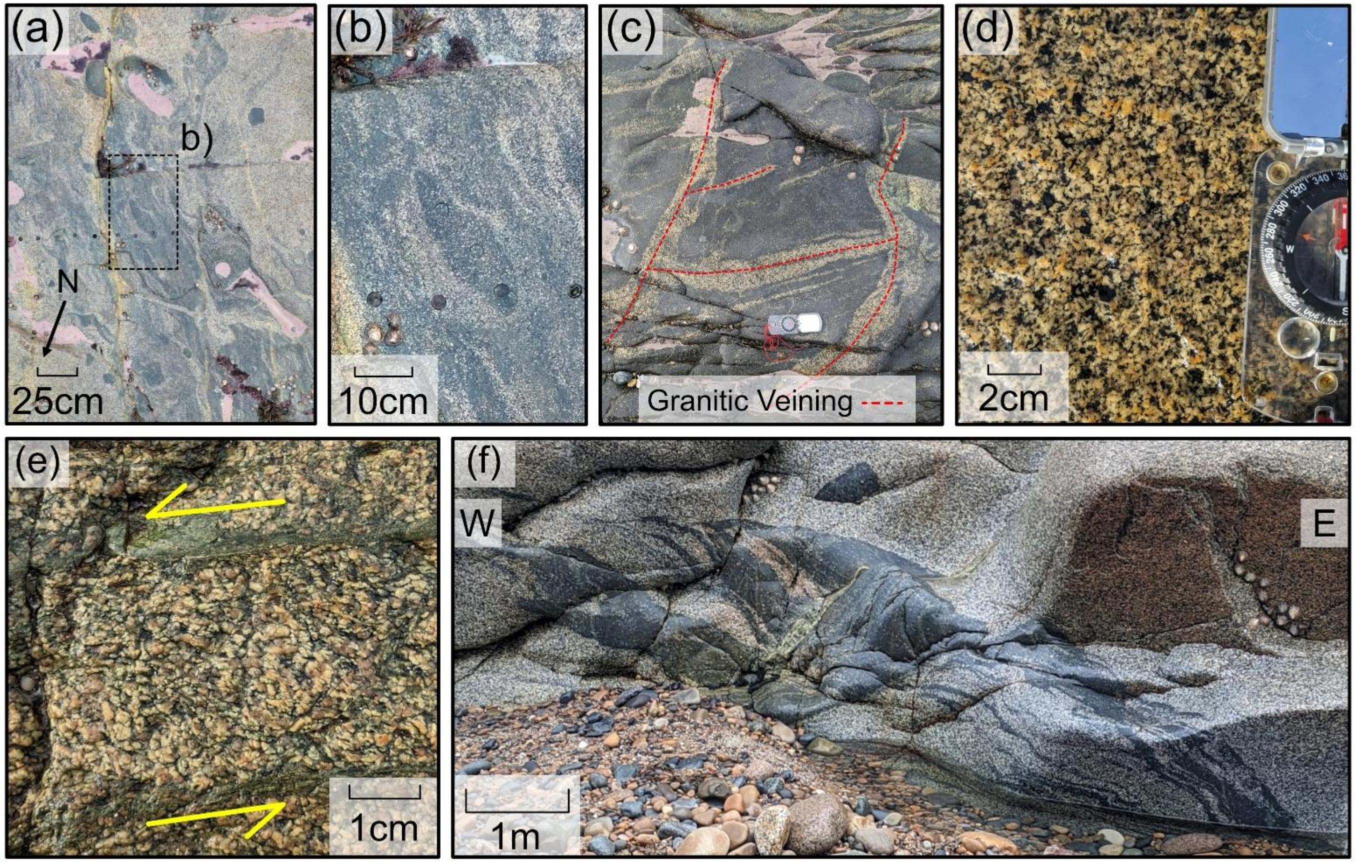

Figure 5. 3 – (a) Example of the mixing and mingling textures within the magmatic sheets. (b) Close-up of a mafic-rich globule within a magmatic sheet with hybridized melt wrapping around it. (c) Zone of granitic veining, with the host monzodiorite infilling around the fractured magmatic sheet. (d) Host monzodiorite showing euhedral to subhedral crystals and an apparent lack of mineral alignment. (e) Host monzodiorite showing alignment within a sinistral fault. (f) Vertical

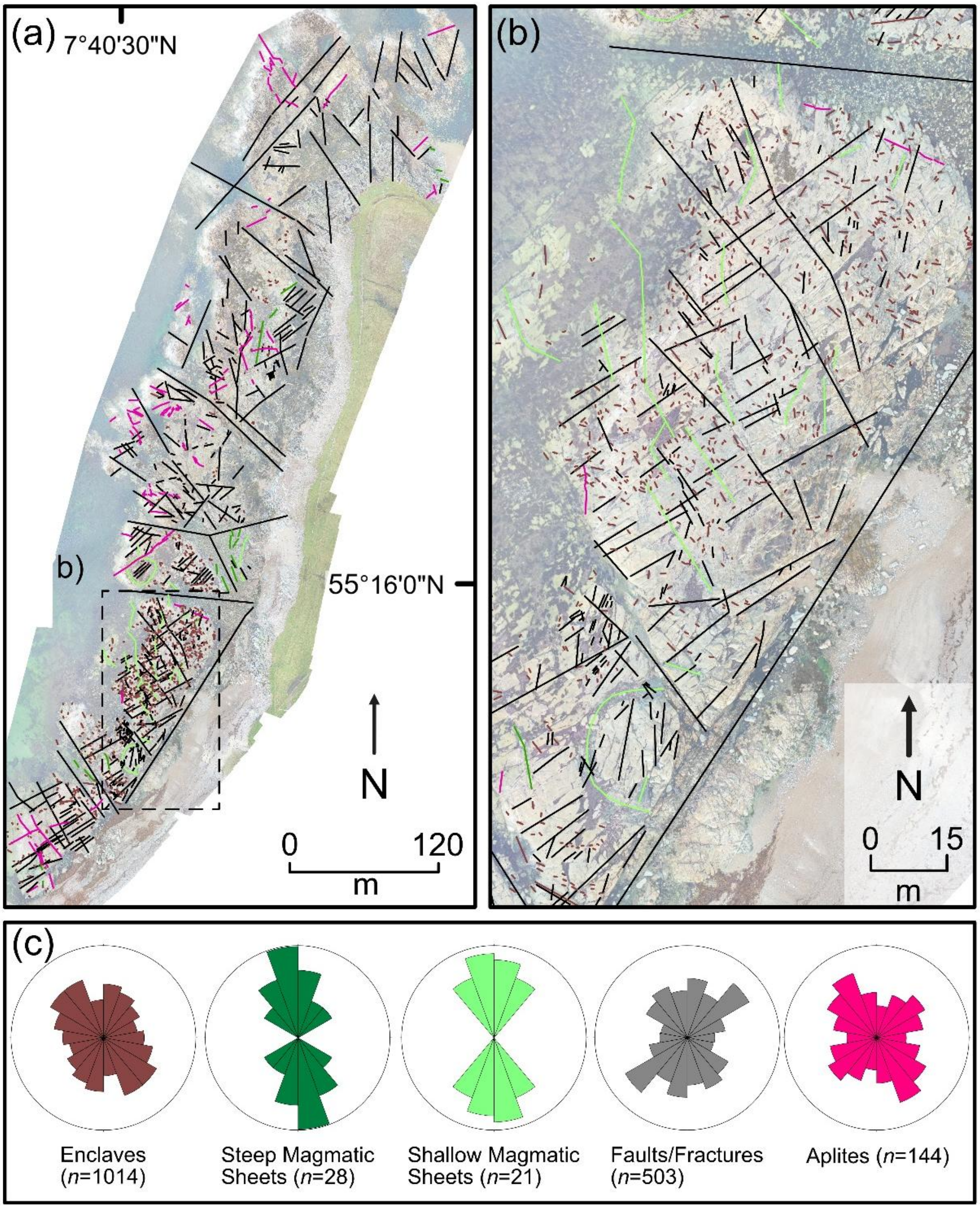

Figure 5.4 – (a) Overview of magmatic and subsolidus features mapped from UAV imagery in the Currin Point area. (b)Close-up map of the southern section of the study area. (c) Rose diagrams for the orientation trends of each feature (bin size of 20°).

5.4.1.2 Magmatic Sheets and Ring Structures

The most striking magmatic intrapluton feature is a series of banded magmatic sheets that are divided into two subsets distinguished by their inclination: 1) gently inclined sheets (20 – 40°) and 2) steeply dipping sheets (70 – 90°). Both sheet types are typically 10 – 100m long, 2 – 10m wide, with a heterogeneous grain size between bands (0.5 – 5mm) and a broadly granitic composition, with varying amounts of feldspar, quartz, amphibole and biotite. Compositional banding within these sheets is parallel to the sheet contact, darker bands are richer in amphibole and biotite, and lighter bands contain more feldspar. The thickness and number of bands vary between magmatic sheets (Fig. 5.3f). Complex mingling and mixing textures are observed within magmatic sheets and between the host monzodiorite. Mingling textures are commonly seen around mafic-rich globules within sheets, with the surrounding magma wrapping around these globules rather than interacting with them (Fig. 5.3a – b). Some gently inclined magmatic sheets show sub-magmatic fracturing, producing sub-angular to angular edges, with subsequent infilling from the host magma, referred to as granitic veining (Fig. 5.3c). Magma mixing is seen in the lighter regions within sheets, which form transient schlieren-like layers that are parallel to the strike of the sheet (Fig. 5.3a). The sheets also feature gradational boundaries with the surrounding host monzodiorite rather than a sharp contact suggesting the magmas were coeval and underwent a degree of hybridisation.

Both steep and gently inclined sheets show a consistent dip and dip direction along their length. Twenty-one gently inclined sheets were recorded and delineate a N – S trend, with most features striking 340 – 020 (Fig. 5.4). In contrast, the 28 steep sheets observed delineate a single major NNE – SSW (340-360) strike trend, with minor trends either side of this (Fig. 5.4). Locally, both gently inclined and steep magmatic sheets show deviations from their length-averaged orientation, such as branching into second-order sheets (Fig. 5.3). Where such deviations occur, the internal pattern within both types of magmatic sheets curve to follow the deviations. The gently inclined magmatic sheet sampled as site S1 features two folds in its trend which follow a NE – SW axial plane, mineral bands follow the curvature of these folds whilst mafic globules in these regions feature internal cm-scale layers oblique to folding (Fig. 5.5). These layers within the globules are rich in white feldspar and trend NNW – SSE, in line with the straight sections of the magmatic sheet. Only one sheet appears to have its termination point exposed, showing a gradual decrease in width and transitioning into a dense swarm of enclaves. The remaining sheets are offset by later faults before they terminate or are not exposed.

Alongside the linear magmatic sheets, two ring-like sheets are also exposed (referred to as ring structures). While one ring is shown in full form, the other has been crosscut by later faults (this is sampled magmatic sheet S3) (Fig. 5.2d). These ring structures show the same compositional and textural properties as the linear sheets, but form closed loops in map view that dip outwards at moderate to sub-vertical angles (40 – 80°). Magmatic sheet S2 also features a region of sub-horizontal dips, reflecting a large lobe-like body of the more mafic-rich magma seen within the sheet (Fig. 5.2d).

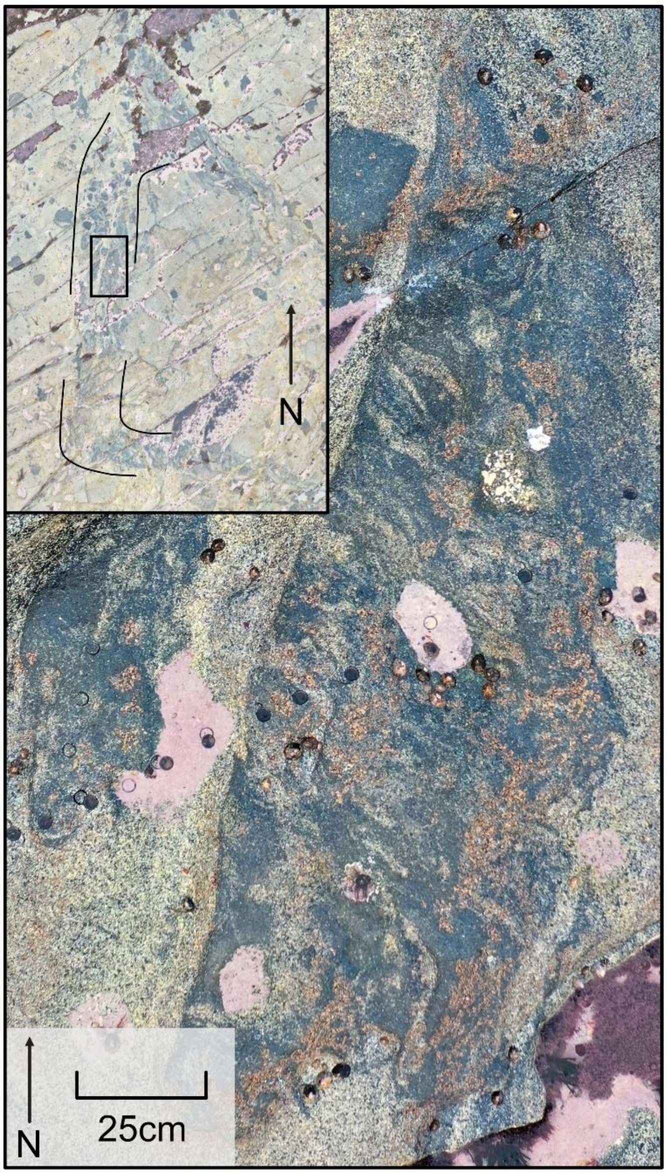

Figure 5.5 – Inset shows magmatic sheet S1 and the two folds along its strike. The main image highlights a mafic-rich globule with white, feldspar-rich layers oblique to this folding but aligned to the bulk NW–SE trend of the sheet.

5.4.1.3 Enclaves

Alongside the sheets, the Currin Point area is rich in fine-grained dioritic enclaves. Enclaves vary from a few centimetres to 3m in their long axis and range from near spherical to strongly elongate, occurring as both swarms and isolated enclaves. Contacts with the host monzodiorite are mainly sharp, varying from sub-rounded to lobate in nature, with some enclaves featuring more gradational contacts (Fig. 5.6a – b). Within the sheets, globules that appear to be entrapped enclaves are shown to be 'stringing off', with once elliptical enclaves showing wispy tails which gradually integrate into the surrounding sheet magma. UAV images return 1014 enclave long axis orientation measurements, from which two main strike trends are observed: 1) 300 – 340 and 2) 000 – 040, with several other minor trends seen (Fig. 5.4). These trends reflect the occurrence and alignment of enclaves around magmatic sheets, with enclaves being parallel or slightly oblique to the trend of proximal magmatic sheets, becoming random in orientation when isolated from other magmatic features.

5.4.1.4 Aplites

A number of aplites and rare pegmatites are intruded along fracture and fault planes (Fig. 5.6c – d). The aplites are 0.2 – 1.2m in width and are dominated by fine-grained pink feldspar and mm-sized biotite crystals, with chilled to gradational contacts (Fig. 5.6c – d). Pegmatites are coarse-grained (1 – 3cm), 2 – 5cm wide, and consist of quartz, plagioclase feldspar and alkali feldspar. From the 144 aplites measured, two dominant orientations are delineated, NW – SE (320 – 340) and NE – SW (040 – 060).

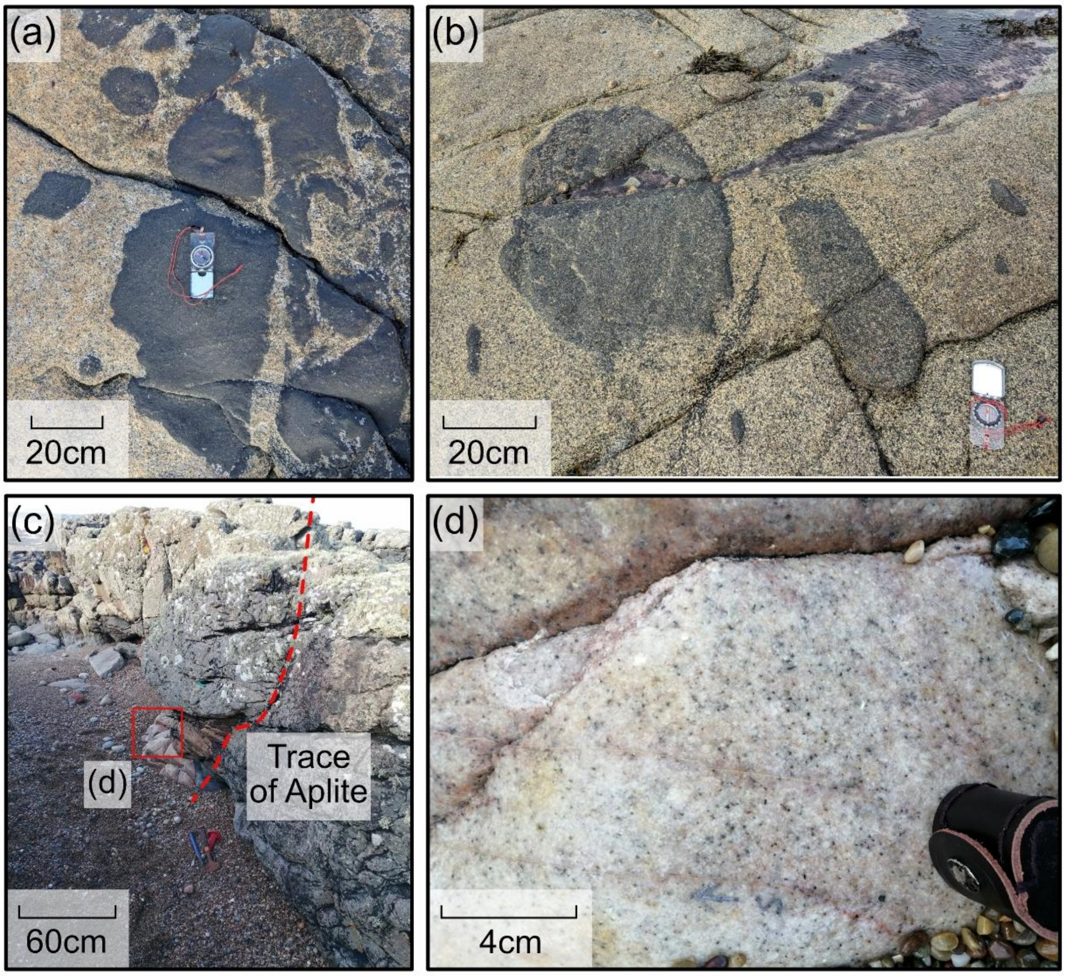

Figure 5.6 – (a) Enclaves within a swarm showing sharp, lobate contacts. (b) Isolated enclaves showing sharp to gradational, subrounded contacts. (c) Aplite S4 showing a subvertical contact with the host monzodiorite. (d) Close-up of the internal texture showing millimetre-scale biotite.

5.4.2 Subsolidus Features

Crosscutting the Currin Point area is a series of sub-vertical faults and tensile fractures. While the flat, coastal outcrop of Currin Point makes determining the presence of dip-slip faults or lineation measurements difficult, sinistral and dextral strike-slipping is recorded in the area. Faults range in width from single cm-scale fracture planes to metre-scale regions of dense fractures, which show displacement on either side. Fractures are often seen as distinct planes with no offset across them, as well as hairline fractures. Extensive epidote-chlorite-sericite alteration occurs along fault and fracture planes, crosscutting all other petrographic features in the study area (Fig. 5.3a & e). A total of 503 faults and fractures were observed within the drone imagery, recording a major NE – SW strike trend of 040 – 060, with trends also seen from NNE – SSW (000-040) and NW –SE (300 – 340) (Fig. 5.4).

5.4.3 Orientation Trends Common to Magmatic and Subsolidus Features

Combining the orientation of magmatic and sub-solidus intrapluton features, seven common trends are observed (T1 – T7) (Fig. 5.7). An oldest (T1) to youngest (T7) relative timing between is established based on the rheological state aligned and crosscutting features. Gently inclined magmatic sheets are not included in any of the seven trends as their moderate dip is disparate to the sub-vertical nature of the steep magmatic sheets and sub-solidus features. The enclaves are

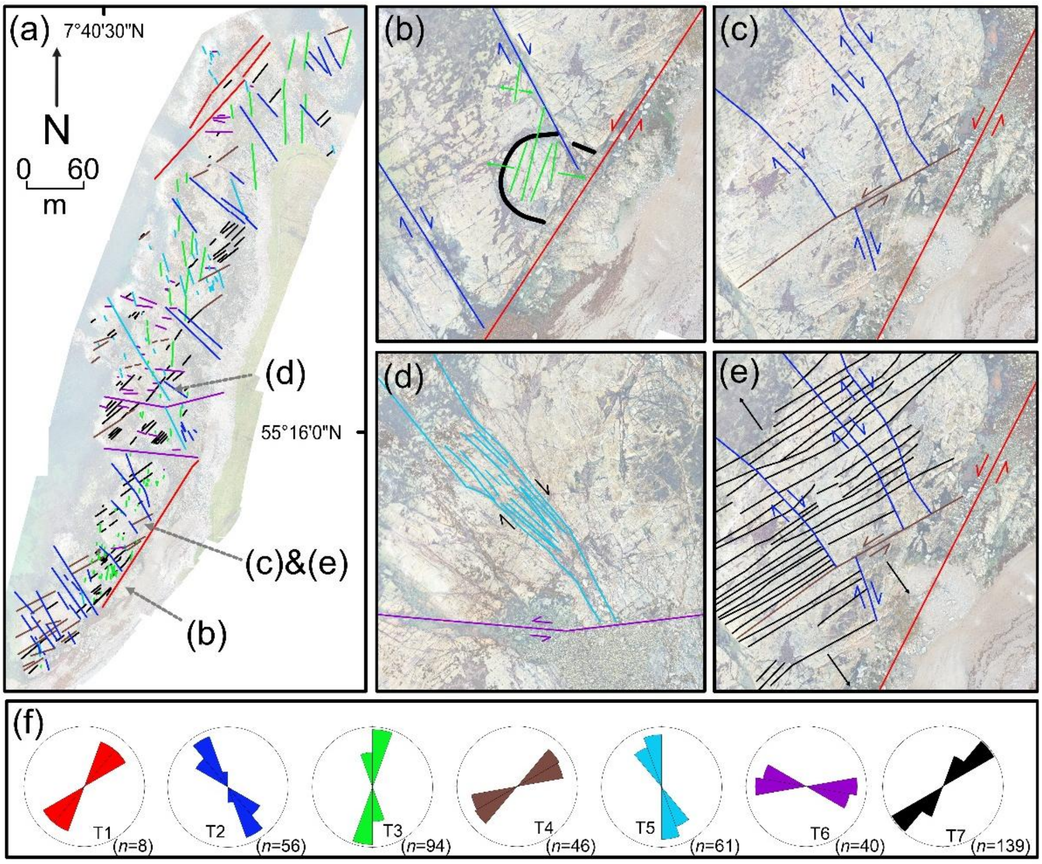

Figure 5.7 – (a) Map of seven orientation trends (T1–T7) across Currin Point.(b)–(e) Display examples of temporal relationships between orientation trends: (b) trendsT1–T3 (the black crescent is magmatic sheet S3); (c) trendT4; (d) trendsT5 and T6; and (e) trend T7. (f) Rose diagrams for the orientation trends of each trend (bin size of 20°).

also excluded as the lack of adequate exposure limits the measurement of their three-dimensional orientation.

The earliest three trends (T1 – T3) appear to form in close succession based on the features which follow each trend and their crosscutting relationships. Therefore, while they can be differentiated from the subsequent four orientation trends, field observations alone cannot temporally distinguish T1 –T3 from each other. T1 is the most prominent of the three, striking NE – SW (020 – 060), the major sinistral faults that crosscut the southern and northern extents of Currin Point best exemplify this trend. T2 runs NW – SE (300 – 340), followed by steep magmatic sheets and dextral sub-solidus faults, which terminate against T1 faults. T3 is orientated N – S (340 – 020) and is defined by steep magmatic sheets and solid-state tensile fractures. A temporal distinction is made between T4 and T7. T4 is defined by a series of sinistral faults trending NE – SW (040 – 060), which crosscut earlier magmatic and sub-solidus features (Fig. 5.7). T5 is followed by m-scale zones of NNE – SSW (320 – 360) fractures with dextral offset on either side, while T6 is characterised by a large WNW – ESE (260 – 280) trending sinistral fault (Fig. 5.7). The final trend, T7, is recorded by NE – SW (020 – 060) orientated tensile fractures which crosscut all other features and represent the most abundant sub-solidus feature in the area. Aplites and alteration from fluids occur along all seven trends, the relative ages of these features is unclear, but we note that T1 to T3 aplites are generally wider and fluid alteration is most extensive along the major T1 faults (Fig. 5.7).

5.4.4 Rock Magnetic Fabric and Characterisation

A summary of rock magnetic results is provided here; full datasets and calculated parameters are given in the Supplementary Material.

5.4.4.1 Magnetic Mineralogy

From magnetic characterisation experiments, representative samples from the magmatic sheets and host monzodiorite consistently return a Curie temperature (T_C) between 550 – 570°C, highlighting a control on bulk susceptibility by a ferromagnetic component within each lithology. Hysteresis loops which reach a magnetic saturation (M/M_{MAX}) at 200 – 300mT with a coercivity (H_C) of 1 – 4mT, together with FORCs that consistently show value concentrations at the origin of the B_U/B_C axes conclude this ferromagnetic component is multidomain magnetite and is the dominant magnetic mineral in these samples. We observe no evidence for single domain particles within any of our samples, indicating the magnetic fabric is aligned with the long-axis orientation of ferromagnetic particles and is representative of the particle shape fabric (Potter and Stephenson, 1988). This also precludes the observed magnetic fabric from AMS correlating to an intermediate fabric from composite magnetic mineralogy sources (Ferré, 2002). The identification of a common magnetic mineralogy to all samples also ensures the magnetic fabric from anisotropy of magnetic susceptibility (AMS) for each lithology is reasonably comparable.

5.4.4.2 Anisotropy of Magnetic Susceptibility

Mean susceptibility (K_{mean}) values vary from 0.530 x 10^{-3} – 5.49 x 10^{-3} across traverses FS001 – FS004 (967 subsamples) and block samples FS005 – FS008 (74 subsamples). The average K_{mean} value for FS001 – FS004 is 1.67 x 10^{-3} while the average for FS005 – FS008 is 0.989 x 10^{-3}. The corrected degree of anisotropy (P_j) from FS001 – FS008 ranges from 2.2 – 14.6%, with an average of 6.6% and one standard deviation range of 4.8 – 8.4%. The shape factor (T) varies from -0.663 to 0.961 (Mean value 0.279), and the majority of cores show positive T values. Their AMS ellipsoids are, therefore, oblate to triaxial ($-0.200 \leq T \leq 0.200$) in nature. The moderately ($-0.200 \leq T \leq -0.400$) to strongly prolate ($-0.400 \leq T \leq -0.800$) samples are associated with enclaves rather than the host monzodiorite or magmatic sheets.

Across the traverses FS001 – FS004 of magmatic sheet S1, several trends are seen in the AMS fabrics (Fig. 5.8). With samples showing oblate T values, maximum (k_1) and intermediate (k_2) susceptibility axes are seen forming a girdle plane which minimum (k_3) axes form a cluster perpendicular to. Therefore, magnetic lineations, defined by k_1, show very little consistency along each traverse, while magnetic foliations defined by the plane to k_3 form an NNW – NNE striking trend which follows the measured orientation of the sheet (Fig. 5.8). This foliation shows a consistent sub-horizonal to shallow dip (0 – 32°) sub-parallel with the field measured 24 – 38° dip of the sheet contact, with only 18 of 470 measured samples showing steeper dips to a maximum of 55° (Fig. 5.8). This NNW – NNE striking foliation is seen within the magmatic sheet and the surrounding host monzodiorite across FS001 – FS004, up to 40m away from the magmatic sheet. When viewed as individual traverses, the strike of the magnetic foliation changes in agreement with local heterogeneities (Fig. 5.8). This includes internal magnetic foliations of enclaves inside and outside of the sheet being inconsistent to their surrounding host lithology, as well as fluctuations in strike where intermediate magma is seen wrapping around mingled mafic-rich regions (Fig. 5.8). Samples from traverses FS003 and FS004 near one of the two major folds in sheet S1, preserve a magnetic fabric which follows the trend of the feldspar-rich layers rather than the limb of the fold (Fig. 5.8).

From magmatic sheet S2, block sample FS005 delineates a magnetic lineation with k_2 and k_3 axes forming a girdle and k_1 forming a point cluster (Fig. 5.9). Plunging 22° towards 216, the magnetic lineation is sub-parallel (within 10°) to nearby field measurements of the sheet contact. In sample FS006, a triaxial AMS ellipsoid is formed with a magnetic foliation (dipping 36° towards 082) and lineation (plunging 4° towards 166) preserved (Fig. 5.9). This magnetic lineation trends parallel to the plane of nearby field measurement for sheet S2, as seen in sample FS005. The sub-horizontal magnetic foliation features a strike parallel (within 6°) to field measurements with a dip consistent with along-strike field measurements (within 4° and the +/-5° error of drill core sampling) (Fig. 5.9).

Sample FS007, taken from magmatic ring structure S3, show a magnetic foliation (dipping 28° towards 128) and lineation (9° plunge towards 111) (Fig. 5.9). The sub-horizontal magnetic lineation and moderately NW-dipping magnetic foliation are consistent with the measured sheet contacts, with the foliation striking parallel to field measurements and the lineation trending within 25°. The magnetic foliation from the aplite S4, as measured from block sample FS008, is consistent with in trend with the dyke contacts (31° towards 240), being 20 ° oblique and slightly shallower in dip (Fig. 5.9). The magnetic lineation is oblique to the dyke strike, plunging 24° towards 200, raking 54° along the plane of the magnetic foliation.

Overall, the magnetic fabrics across the sampling locations is sub-parallel in orientation with field observations and measured sheet contacts. Magnetic lineations are predominantly sub-horizontal and occur along the plane of sheet contacts, except for the aplite S4 which is slightly oblique to the trend of the dyke. Magnetic foliations dip slightly shallow or equal to the dip of field measurements in most samples, with the detailed sampling of FS001 – FS004 showing the magnetic fabrics following local heterogeneities when examined in detail.

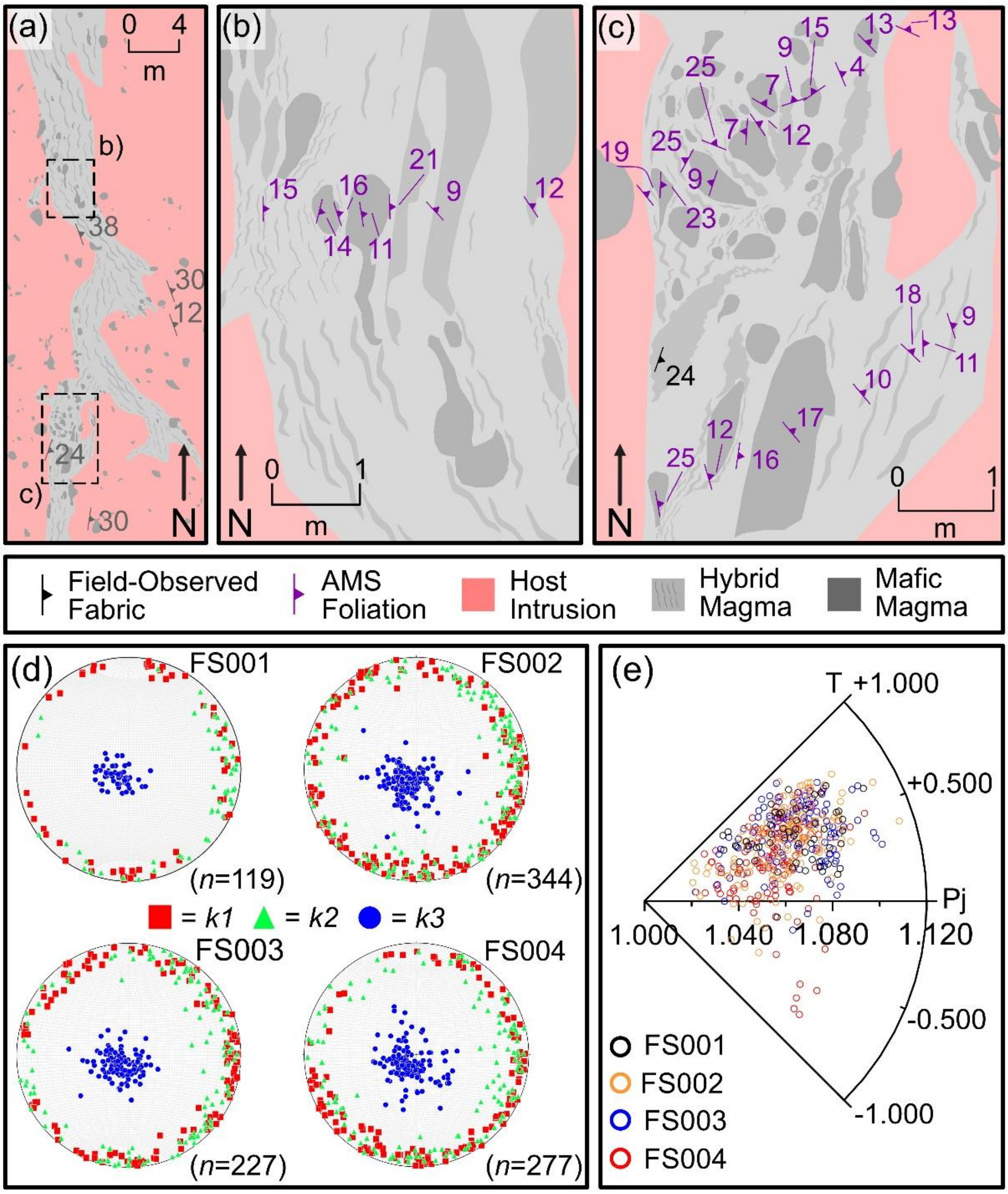

Figure 5.8 – (a) Map of magmatic sheet S1 showing location of two close up maps. (b) Subsection of sample traverse FS001 showing the magnetic fabric measured from anisotropy of magnetic susceptibility (AMS). (c) Subsection of sample traverse FS002 and FS003 showing the magnetic fabric measured from AMS and the fabric from field measurements. (d) Stereonets of AMS Data across sample traverses FS001 –FS004. (e) Polar plot of corrected degree of anisotropy (P_j) against shape factor (T) across sample traverses FS001 –FS004.

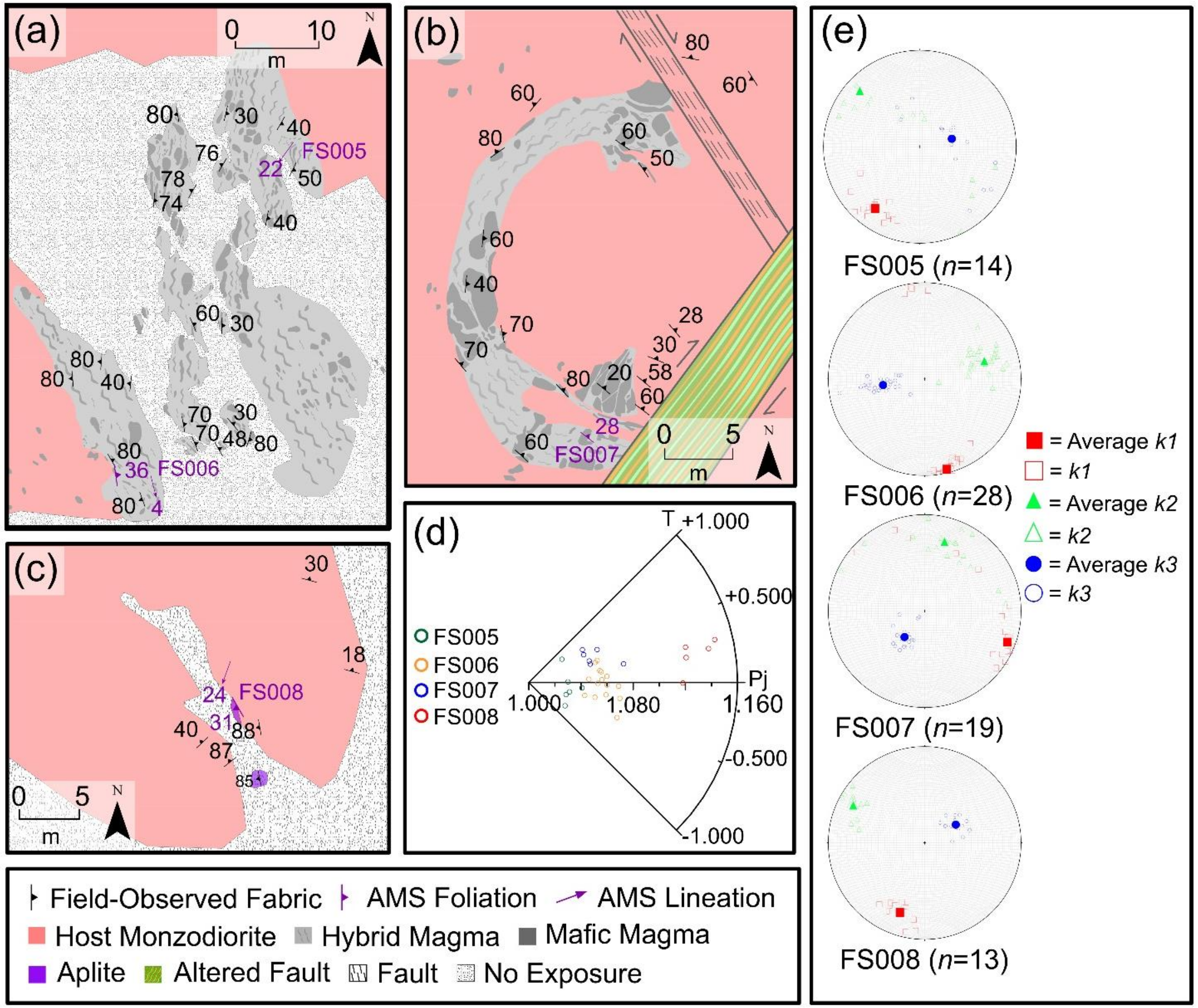

Figure 5.9 – (a) Map of magmatic sheet S2 showing field measured fabric data and the magnetic fabric of block samples FS005 and FS006 measured from anisotropy of magnetic susceptibility (AMS). (b) Map of magmatic sheet S3 showing field measured fabric data and the magnetic fabric of block sample FS007 measured from AMS. (c) Map of magmatic sheet S4 showing field measured fabric data and the magnetic fabric of block sample FS008 measured from AMS. (d) Polar plot of corrected degree of anisotropy (P_j) against shape factor (T) for block samples FS005 –FS008. (e) Stereonets of AMS Data for block samples FS005 –FS008.

5.5 Discussion

Across the Currin Point area, lithological, rock fabric and fracture observations highlight a range of rheological conditions where strain has been archived. We investigate the record of strain across magmatic to sub-solidus features, correlating them to intrinsic stress from magma chamber processes and external stress from tectonic deformation. For magmatic features, we distinguish the strain of magma chamber processes from tectonic stress based on observed fabric characteristics of each strain source from previous studies (e.g., Stevenson et al., 2007; Magee et al., 2012; McCarthy et al., 2015a; Burton-Johnson et al., 2019; Mattsson et al., 2024; Alasino et al., 2025). We exclude the aplites from this analysis, as their highly felsic nature and close association with faults and fractures suggests they are a residual melt from final crystallisation of the pluton and cannot be directly linked to other processes at Currin Point. Sub-solidus features are then compared with magmatic features derived from tectonic stress to contextualise the orientation and kinematics of strain from the interpreted contemporaneous palaeostress during and immediately after emplacement of the Fanad Pluton (McCaffrey, 1994; Kirkland et al., 2008; Kocks et al., 2014). This careful consideration of potential sources of strain ensures the strain preserved in sub-solidus features is reflective of regional tectonic stress active throughout the Caledonian Orogeny (Žák et al., 2009). Once all sources of strain are identified throughout crystallisation of the Fanad Pluton, we then contextualise our proposed kinematic evolution to the reported evolution of other Caledonian intrusions.

5.5.1 Archived Magma-Chamber Processes

5.5.1.1 Fabric of the Host Monzodiorite

In the field, the majority of the area features a host monzodiorite consisting of unaligned crystals, with magmatic state crystal alignment only observed proximal (less than 1m) to intrapluton features (Fig. 5.3). Anisotropy of magnetic susceptibility (AMS) data show a sub-horizontal NNW – NNE striking magnetic foliation within the monzodiorite, consistent with the trend of the gently inclined magmatic sheets and field measurements across Currin Point (Figs. 5.4 & 5.8). The correlation between outcrop-scale and grain-scale measurements, rather than the misalignment recorded within intrapluton features in other areas of the Fanad Pluton (Latimer et al., 2024), suggests the fabric is a record of strain intrinsic to magma chamber processes, rather than external tectonic stress (e.g., Benn, 2009; Paterson et al., 2019).

5.5.1.2 Gently Inclined Magmatic Sheets and Ring Structures

The magmatic sheets and ring structures reflect magma injected into the Fanad Pluton, which has undergone mingling and hybridising with the host monzodiorite. Internally, the sheets and ring structures are heterogeneous, with schlieren-like layering following subtle contact geometry and orientation variations in the sheet/ring contacts, suggesting they represent magma flow structures within the sheet. AMS data collected from three separate magmatic sheets (S1 – S3) show a direct correlation between magnetic fabrics and the complex banding and mingling textures of the sheets. Two groups of magmatic sheets are identified based on their variation in dip, without compositional change, suggesting a change in active stress regime during pluton construction. Granitic veining within the gently inclined sheets, indicating brittle fracturing and subsequent host monzodiorite infill, is absent within the steep magmatic sheets (Fig. 5.3c). This indicates the gently inclined sheets are an earlier injection of magma, recording an earlier stress regime within the pluton, with the steep sheets reflecting a subsequent change in the active stress field.

Previous studies in other igneous complexes have related shallow dipping, schlieren-like features to a range of magmatic processes from dynamic shear flow to static thermal/compositional gradient control and viscous deformation of the surrounding host magma (Ardill et al., 2020; Mattsson et al., 2024; Alasino et al., 2025). The visible mixing-mingling textures and corresponding AMS fabric (Figs. 5.8 & 5.9), alongside evidence of deformation along the length of the magmatic sheet S1, provide evidence that these gently inclined magmatic sheets formed in a dynamic setting as a function of magma flow rather than a static process within the magma chamber (Ardill et al., 2020). Similarly, ring-like structures have been correlated to intrapluton plume features, recording magma flow due to Rayleigh-Taylor instabilities (Paterson et al., 2019). The two distinct folds along the strike of the sheet S1 (Fig. 5.5) are similar to the deformation in shallow dipping, schlieren-like sheets reported by Paterson et al. (2008) that may record magma emplaced during viscous Mode 1 opening fracturing of a magmatic mush. The AMS fabric around the hinges of these folds aligns with feldspar-rich layers within the deforming mafic bands (Fig. 5.5), suggesting the deformation occurred penecontemporaneous to magma injection. This viscous deformation, combined with the textural and AMS data evidence of magma flow, highlights a record of strain from multiple magma chamber processes within the gently inclined magmatic sheets and ring structures across the study area.

5.5.1.3 Enclaves

Enclaves are compositionally similar to the magmatic sheets across Currin Point, representing magma globules transported through the host monzodiorite (Paterson et al., 2004; Žák et al., 2007; Latimer et al., 2024). AMS data from sampled enclaves closely reflects their morphology, indicating the record the strain preserved from the enclave long axis and internal AMS fabric was imparted while in a magmatic to sub-magmatic state and does not reflect a tectonic overprint (Latimer et al., 2024). The long axis of enclaves located in close proximity to gently inclined magmatic sheets are sub-parallel to their trend, suggesting they are influenced by the same magma chamber processes (Paterson et al., 2004; Žák et al., 2010). This alignment may have occurred after the enclaves had near-fully crystallised, but the continuous wrapping of AMS fabrics within the surrounding host monzodiorite and magmatic sheets indicates the alignment must have occurred as they were actively crystallising and reflect the shortening direction at that time (Paterson et al., 2004). Some enclaves distal form the magmatic sheets are randomly orientated and distributed or form small swarms and, therefore, have a localised long axis alignment. This lack of alignment indicates that these enclaves were crystallised to the point of rheological lock up of the magma, no longer acting as active strain markers

(Scaillet et al., 2000; Paterson et al., 2004; Latimer et al., 2024). These enclaves, therefore, formed earlier relative to those aligned parallel to the gently inclined magmatic sheets, with strain likely transmitted through force chain development through the crystallising mush rather than enclave rotation to stress (Carrara et al., 2024).

5.5.1.4 Construction of the Fanad Pluton

Combining the records of magma chamber processes, we are able to gain insight into mechanisms active during the construction of the Fanad Pluton. The consistent relationship between AMS fabrics and demonstrably intra-pluton magma transport features such as shallowly dipping magma sheets, enclaves and ring structures describes the progressive growth of a dynamic magma chamber (Figs. 5.5, 5.8 & 5.9). Importantly, the recorded geometry and orientation of these features closely reflect those expected in magma chambers and they are difficult to reconcile with the regional tectonic stress field (Fig. 5.4) (Paterson et al., 2019). The correlation between outcrop-scale and grain-scale measurements is in contrast to other parts of the pluton that record strong magmatic state tectonic fabric(Latimer et al., 2024), validating that our AMS data do not measure a tectonic overprint of a previous strain record (e.g., Petronis et al., 2012; Di Chiara et al., 2020; Latimer et al., 2024). Our results closely reflect those of similar field studies where vertical magma ascent during pluton construction is followed by lateral transport of magma due to the partitioning of internal magmatic strain within a mush-state host intrusion (Jacques and Reavy, 1994; Mattsson et al., 2024). We similarly interpret our collective dataset as a late-stage magma transport record, detecting strain intrinsic to magma chamber processes.

5.5.2 Archived Regional Tectonic Strain

5.5.2.1 Steep Magmatic Sheets

A comparison of sheet orientations with fracture data at Currin Point shows that the earliest fracture sets, T1 – T3, are parallel to the sub-vertical magma sheets

(Fig. 5.7). Several studies (e.g., McCaffrey, 1994; Pawley and Collins, 2002; Neves et al., 2023) highlight tectonic strain embrittlement of crystal-rich magmas results in similar sub-vertical magma sheets and fractures. In this so-called mushy magma, the host intrusion is comprised of a crystal framework with interstitial magma, forming a strength contrast (Hibbard and Watters, 1985). Under tectonic stress, the structurally weak, magma-rich zones concentrate stress, causing fracturing of the mush along strain partition zones, which fills with magma from the surrounding magmatic system. The direct correlation of steep sheet orientations with that of the earliest preserved sub-solidus features indicates they are a record of the same tectonic strain, initiating during the last stages of pluton crystallisation.

5.5.2.2 Enclaves

As observed for gently inclined sheets, AMS fabrics and the long axes of enclaves recorded proximal to steep magmatic sheets align sub-parallel to those sheets (Fig. 5.4). The co-alignment of steep sheets and enclaves suggests these enclaves were rotating under the tectonic stress forming the steep magmatic sheets, in the same manner as the enclaves proximal to the gently inclined sheets forming from internal magmatic stress.

5.5.2.3 Subsolidus Strain Records

Two regional-scale faults, the Leannan Fault and the Melmore Shear Zone (Fig. 5.1), were active during the emplacement of the Fanad Pluton (White and Hutton, 1985; Latimer et al., 2024). Previous studies show Riedel shear systems developed in response to movement along the major NE-SW trending shear zones (Alsop, 1992; Kirkland et al., 2008) and along similar regional faults within the Caledonian Orogeny (Kocks et al., 2014). We compare Riedel shear fractures expected for both faults (Riedel, 1929; Kirkland et al., 2008; Ren et al., 2021), with the two sets of fractures recognised at Currin Point, T1 – T3 and T4 – T7, placing our results in the context of the expected regional tectonic stress field (Fig. 5.10).

Trends T1 – T3 follow NW – SE, NW – SE and N – S aligned orientations, respectively (Fig. 5.7), matching with R-shear, R’-shear, and T-fracturing of a sinistral Riedel shear system which translates to 045 – 225 orientated maximum shortening direction (Fig. 5.10). In contrast, T4 – T7 which crosscut T1- T3 and are orientated NE – SW, NNE – SSW, WNW – ESE and NE – SW, respectively (Fig. 5.7), which is consistent with R'-shear, P-shear, X-shear and T-fracturing of a dextral Riedel system corresponding to a 005 – 185 orientated maximum shortening direction (Fig. 5.10). The lack of R-shear development relative to P-shear and X-shear within the later fracture sets suggests an increase in dilation during deformation (Moore and Byerlee, 1992) (Fig. 5.10). This demonstrates an evolution of local strain, rotating from NNE – SSW to NE – SW orientated maximum shortening, with the inversion of shearing direction between the formation of fracture sets T1 – T3 and T4 – T7.

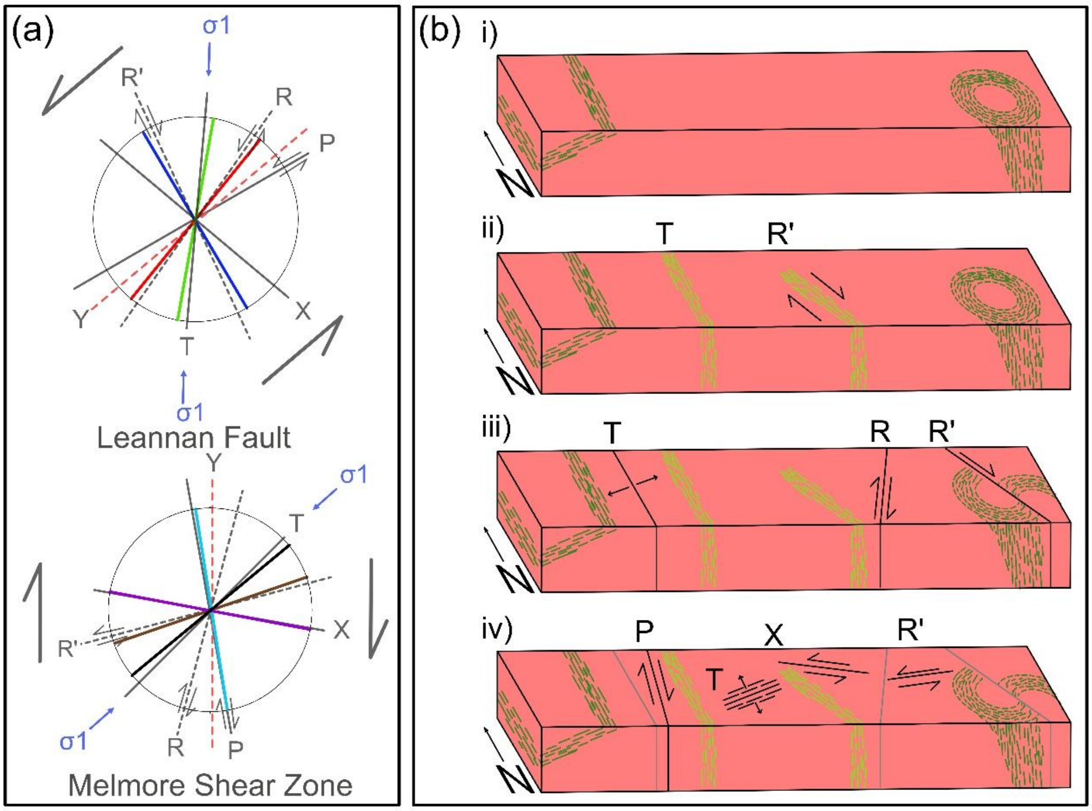

Figure 5.10 – (a) Expected Riedel shear system orientations for the Leannan Fault and the Melmore Shear Zone with the measured orientation for trends T1–T7 overlayed. (b) Schematic of the kinematic evolution across the Currin Point area from magmatic and sub-solidus features.

The faults and fractures of T1 – T3 correlate with the expected Riedel system for deformation along the Leannan Fault, while the faults and fractures of T4 – T7 correlate with the Riedel system for deformation along the Melmore Shear Zone (Fig. 5.10). We note only faults and fractures consistent with the deformation related to the Leannan Fault or Melmore Shear Zone, with no sub-horizontal fractures present to indicate processes such as late-stage pluton uplift (Žák et al., 2009; Ellis and Blenkinsop, 2019). Therefore, we establish two contrasting Riedel shear systems were active at Currin Point, associated with deformation along nearby regional faults and record rotation of the regional tectonic stress field.

5.5.3 Kinematic Evolution of the Fanad Pluton

Combining the strain records from magmatic and solid-solidus features, we detect three distinct phases of strain at Currin Point: 1) internal magmatic strain, 2) the onset of regional tectonic strain and 3) regional tectonic strain rotation. From these three phases, alongside the available geochronological data for the Fanad Pluton, we propose a kinematic evolution for the Fanad Pluton in the context of the broader tectonic stress field (Fig. 5.10). While this geochronological data provides temporal constraints to the observed changes in strain, the interpreted timings and their relation to strain evolution across the Fanad Pluton are restricted by the lack of dating specific to the features measured within this study.

5.5.3.1 Phase 1: Internal Magmatic Strain

Gently inclined magma sheets, enclaves and ring structures provide insight into a dynamic magma chamber environment, where successive internal stress events such as dynamic flow and shear and Rayleigh-Taylor instabilities interacted. Evidence of penecontemporaneous deformation of magmatic sheets (Fig. 5.5) suggests that the intrusion of successive magma sheets and ring-structures was facilitated by viscous deformation. AMS fabrics closely mapping to internal mixing and mingling textures confirm no subsequent tectonic overprinting and the absence of tectonic strain immediately after the emplacement of the Fanad Pluton. Previous work by Kirkland et al. (2008) similarly records an apparent hiatus in deformation along the Leannan Fault from 422 – 412 ±3 Ma (U-Pb on zircon) based on analysis of country rock deformation. Our data is also compatible to static biotite crystallisation at 417±3.6 Ma (Ar-Ar on biotite) within the country rock of Malin Head, correlated to static metamorphism during emplacement of the Donegal Igneous Complex in the absence of deformation (Condon et al., 2006). With the earliest dates from Archibald et al. (2021) for the Fanad Pluton at 418±3 Ma (U-Pb on zircon), our initial archive of internal magmatic strain further supports the presence of such a hiatus in external tectonic stress around that time.

5.5.3.2 Phase 2: Onset of regional Tectonic Strain

As the Fanad Pluton continued to cool, reaching a mush-state in the Currin Point area, the intrusion of sub-vertical magma sheets records the first evidence for regional tectonic strain (Fig. 5.10). These sheets represent magma transport along tectonically controlled dilational zones, as tectonic stress causes shear thickening and embrittlement of the mushy magma. The steep magma sheet orientations match that of Riedel shearing from displacement along the nearby Leannan Fault, constraining maximum shortening to an NNE-SSW orientation (Fig. 5.10). As the Fanad Pluton fully crystallised at Currin Point, the ongoing tectonic strain continued to be recorded as sub-solidus Riedel shears in the same orientation as the steep magmatic sheets (Fig. 5.10). This preservation of tectonic strain from a sub-magmatic to sub-solidus state constrains the commencement of tectonism, with dating of enclave material near Currin Point by Archibald et al. (2021) to 416±3 Ma (U-Pb on zircon) providing the latest date for tectonic strain onset.

5.5.3.3 Phase 3: Regional Tectonic Strain Rotation

The final phase of strain recorded in Currin Point preserves the clockwise rotation of the maximum shortening direction to NE – SW, activating the nearby Melmore Shear Zone and forming a series of Riedel shears associated with the structure (Fig. 5.10). While preserved in a sub-solidus state at Currin Point, this second phase of tectonic strain is recorded in the magma mixing zone adjacent to the Melmore Shear Zone as a mushy magma overprint (Latimer et al., 2024). This demonstrates that tectonic stress rotated while the host monzodiorite was actively crystallising around the Melmore Shear Zone, with no evidence of subsequent shear zone reactivation proximal to the structure (Latimer et al., 2024). Geochronology from the nearby host intrusion returns an age of *ca*. 411±3 Ma (U-Pb on zircon) by Archibald et al. (2021) constraining the latest date for tectonic stress rotation. A similar rotation of strain axes is proposed at 412±3 Ma (U-Pb on zircon) by Kirkland et al. (2008) who highlight the formation of faults incongruent with deformation along the Leannan Fault. However, they suggest a counterclockwise rotation of the maximum shortening direction to NW –SE, with post-412Ma structures 005 and 040 trending but with opposing shear-sense to similarly orientated structures at Currin Point (Kirkland et al., 2008). The inconsistency in shear-sense recorded within the Fanad Pluton and in the surrounding host rocks, suggests that the structures within the country rock may represent deformation that occurred prior to the emplacement of the intrusion. Alternatively, the variation may reflect a localised variation in shortening direction due to irregularity along the deformation front during sinistral transpression and transtension (Harland, 1971; Sanderson and Marchini, 1984).

5.6 Comparison to Other Late Caledonian Igneous Complexes

Our analysis of the Fanad Pluton deciphers a complex record of strain, sensitive to progressive internal magmatic stress, the onset of regional tectonic stress and its subsequent variation throughout cooling of the pluton. Here, we reflect on the significance of these findings in the context of similar data from other intrusions across the Irish and British Caledonides (Fig. 5.11).

Within the Donegal Igneous Complex, while magma ascent is reported to have a clear tectonic control (Hutton and Alsop, 1996), fabric studies report only the main pluton to measure tectonic strain, with the remaining plutons preserving strain intrinsic to pluton construction (Hutton, 1982; Molyneux and Hutton, 2000; Stevenson et al., 2007a, 2008a; Stevenson, 2009). The record of strain within the

Fanad Pluton is initially in agreement with these plutons, measuring strain from magma chamber processes (Figs. 5.5 & 5.10). However, the subsequent record of tectonic strain within the intrusion, associated with displacement of the nearby Leannan Fault and Melmore Shear Zone is contemporaneous and kinematically sub-parallel to strain along the NE –SW Main Donegal Shear Zone and the NNE – SSW Donegal Lineament during ascent of the Donegal Batholith (Hutton, 1982; Hutton and Alsop, 1996; Stevenson et al., 2008a). Therefore, the Fanad Pluton provides an archive of magmatic to sub-solidus strain connecting internal magmatic stress preserved during the emplacement of the Donegal Batholith, to the concurrent regional tectonic stress field, with the preserved tectonic strain of the intrusion akin to the solid-state foliation of the main pluton of the batholith (Hutton, 1982).

In contrast to the Donegal Batholith, combined field and rock fabric studies on the Galway Granite Complex, western Ireland, are interpreted to record a direct tectonic control on magma ascent and emplacement (McCarthy et al., 2015c, 2015b). The so-called earlier plutons (*ca.* 420Ma) are sited along NW-SE shear zones contemporaneous with regional transpression, with later plutons (410-400±7.6Ma, U-Pb on zircon) emplaced into orogen parallel W-E shear zones, as maximum principal stress rotated during a transition from regional sinistral transpression to transtension (El Desouky et al., 1996; McCarthy, 2013; McCarthy et al., 2015c, 2015b). Our analysis of the Fanad Pluton identifies a similar rotation of the shortening direction, where activation of the Melmore Shear Zone at *ca.* 411Ma temporally coincides with the interpreted transpression-transtension transition in the Galway Granite Complex, ≈250 km to the south.

The Newry Igneous Complex (414 –407±3.5Ma, U-Pb on zircon) in Northern Ireland is interpreted to have ascended at the intersection of NNE – SSW aligned crustal lineaments and dilational jogs that crosscut the Iapetan metasedimentary accretionary prism (Cooper et al., 2016; Anderson et al., 2018). Anisotropy of magnetic susceptibility (AMS) data demonstrates the development of contact parallel, concentric mineral fabrics and sub-vertical pluton contacts that are interpreted as inflation of the pluton within the overall tectonically controlled pluton architecture (Anderson et al., 2018). The Newry Igneous Complex is broadly in agreement with our analysis of Fanad and records magma intruding into a sinistral transtension regime between 414 – 407Ma (Cooper et al., 2016; Anderson et al., 2018).

Our results are also consistent with the reported strain record of the *ca*. 425±4.6Ma (U-Pb on zircon) (McAteer, 2009) Ross of Mull granite, Scotland (Zaniewski et al., 2006; Petronis et al., 2012). Field mapping and AMS data from this intrusion reveal a prominent NNW-SSE magmatic to sub-magmatic foliation that is interpreted to reflect a partial overprint of an earlier fabric inherent to magma emplacement processes during regional shortening (Petronis et al., 2012). This record of successive strain events agrees with the Fanad Pluton, with similar tectonomagmatic overprinting in the magma mixing zone adjacent to the Melmore Shear Zone (Latimer et al., 2024). Being emplaced prior to the Fanad Pluton, the record of regional shortening within the Ross of Mull Granite may reflect the stress regime active prior to our observed hiatus in regional tectonic strain (Fig. 5.10).

The Fanad Pluton is thus shown to preserve a strain archive that closely tracks the strain history of several other igneous complexes across Ireland and the UK, providing a new insight on the interplay between the physical process of magma transport and pluton growth in the context of the evolving tectonic regime (Fig. 5.11). Crucial to recognition of internal and external palaeostress regimes within the Fanad Pluton is the measurement of strain from sub-solidus faults and fractures and their comparison with the magmatic sheets, enclaves and fabrics (Figs. 5.4, 5.7 –5.9). Combining similar strain records from sub-solidus features in other Caledonian igneous complexes may add further resolution to tectonic strain preserved within those intrusions. For example, in the Donegal and Newry Igneous Complexes, where magmatic-state strain reportedly preserves only magma chamber processes, sub-solidus faults and fractures may reflect post-emplacement strain from the regional tectonic framework, while in the Galway Granite Complex and Ross of Mull Granite, such structures may preserve the proposed rotation of the maximum shortening direction we see at the Fanad pluton. The compatibility of our results across the Irish and UK Caledonides complements the reported macroscale influence of regional tectonic stress on Caledonian igneous complexes from Knight et al. (2024), which compared bulk magnetic fabrics in coevally dated intrusions. Their study reports a distinct transition in bulk magnetic fabric alignment from NNE – SSW to E – W aligned at ≈420Ma, consistent with the transition from regional transpression to transtension recorded in previous kinematic models (Dewey and Strachan, 2003; Soper and Woodcock, 2003). Our results demonstrate that by integrating data such as AMS, geochronology, petrogaphy, and UAV-based fracture mapping, further resolution can be added to macroscale interpretations, which explain the variation in reported strain archives between igneous complexes and provide greater temporal constraints on the kinematic transition from transpression to transtension.

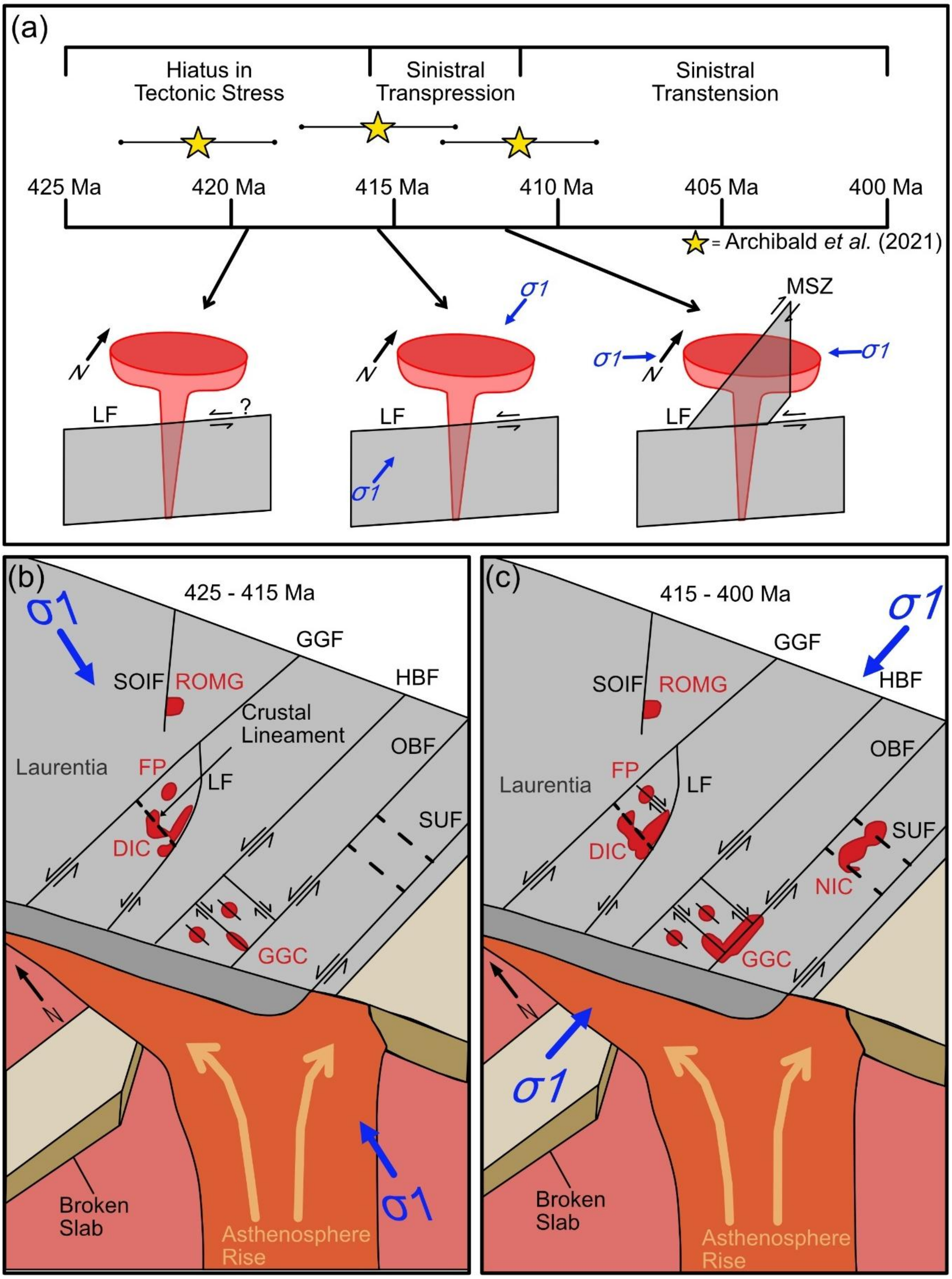
(a)
Hiatus in Tectonic Stress
Sinistral Transpression
Sinistral Transtension
425 Ma
420 Ma
415 Ma
410 Ma
405 Ma
400 Ma
= Archibald et al. (2021)
MSZ
σ1
N
LF
?
(b)
425 - 415 Ma
σ1
GGF
HBF
SOIF
ROMG
Crustal Lineament
Laurentia
OBF
FP
LF
SUF
DIC
GGC
N
Broken Slab
Asthenosphere Rise
(c)
415 - 400 Ma
NIC

Figure 5.11 – (a) Regional-scale kinematic transitions from the Fanad Pluton based on our measured strain archive from Currin Point, combined with the geochronological data of Archibald et al. (2021). (b) – (c) Overview of the proposed kinematic evolution of the late Caledonian Orogeny based on the archive of strain within the Fanad Pluton (this study and Latimer et al. 2024) and other igneous complexes across the orogenic front in Ireland and the UK (Stevenson et al. 2007, 2008; Stevenson 2009; Petronis et al. 2012; McCarthy 2013; McCarthy et al. 2015a, b; Anderson et al. 2018). (b) Sinistral transpression to sinistral strike-slip from 425 – 415 Ma. (c) Sinistral strike-slip to sinistral transtension from 415 –400 Ma. Abbreviations: DIC, Donegal Igneous Complex; FP, Fanad Pluton; GGC, Galway Granite Complex; GGF, Great Glen Fault; HBF, Highland Boundary Fault; LF, Leannan Fault; NIC, Newry Igneous Complex; OBF, Orlock Bridge Fault; ROMG, Ross of Mull granite; SOIF, Sound of Iona Fault; SUF, Southern Uplands Fault.

5.7 Conclusions and Implications for the Kinematic and Temporal Evolution of the Caledonian Orogeny

The collective archive of strain across several late Caledonian igneous complexes, including the Fanad Pluton, preserve several phases of strain which are transpressive-transtensive in nature. These data are highly compatible with models that describe the late Caledonian convergence of Baltica and Laurentia followed by a regional sinistral transcurrent regime (Dewey and Strachan, 2003; Soper and Woodcock, 2003). Models that require no substantial transcurrent regime (Searle, 2021) are difficult to reconcile with the reported data. Interestingly, our data record no substantial tectonic strain during magma emplacement, which may be interpreted as either a hiatus in transpression or, potentially, a scenario where transpression instigated later than *ca*. 422Ma with relatively modest amounts of offset along the Great Glen Fault, perhaps in the region of 200-300 km as envisaged by Prave et al. (2024).

This study aimed to determine the sensitivity of igneous plutons to kinematic variations via records of strain formed throughout their cooling history. Combining field observations, rock magnetic fabrics and orientation analysis from UAV imagery, a complex interplay between several stress regimes has been deconvoluted into three separate phases of strain within the Fanad Pluton. We distinguish structures recording internal magmatic strain, reflecting multiple magmatic processes, from structures related to regional tectonic strain, which commenced as the host monzodiorite of the study area was actively crystallising from a mushy magma to solid rock. This study further emphasises the need for careful consideration of multiple strain records within a pluton in order to understand the processes linked to their formation. In particular, where the fabric formed within a given intrusion has been deemed a tectonic overprint, analysis of the multiple magmatic and solid-state features may archive the remnants of previous magmatic system processes.

Chapter 6: The Significance of Magnetic Fabrics Preserved in Hydrothermally Altered Rocks

The data from this chapter are submitted and currently under review for publication in the Journal of Geophysical Research-Solid Earth with the author list: Ben Latimer, William McCarthy, Tobias Mattsson and John Reavy

B. Latimer completed the fieldwork, performed the analyses, generated the figures, and wrote the chapter, with guidance and input from all co-authors.

6.1 Introduction

Studies concerned with the development of petrofabrics (mineral alignments in rocks) routinely employ anisotropy of magnetic susceptibility (AMS) and anisotropy of magnetic remanence (AMR) as convenient, sensitive and semi-quantitative approaches to constraining the strain record in a vast array of geological settings (e.g., Pueyo Anchuela et al., 2011; Maffione et al., 2015; Tomek et al., 2017). Both techniques, in particular AMS, have been implemented to investigate petrofabrics formed in response to key geological processes such as the transport of magma within the Earth's crust (Magee et al., 2012; Koopmans et al., 2022), palaeoflow direction in sedimentary environments (Bilardello, 2021; Chatterjee et al., 2023) and tectonic deformation (McCarthy et al., 2015a; Goswami et al., 2018). However, the incorporation of other petrofabric analysis methods, such as shape preferred orientation (SPO) and crystallographic preferred orientation (CPO), demonstrate that AMS fabrics are susceptible to being overprinted or destroyed by successive geological processes such as magma remobilization (Köpping et al., 2023; Latimer et al., 2024), tectonic overprinting (Parés, 2004; Petronis et al., 2012) and fluid migration (Jones et al., 2025a; Williams et al., 2025).

Within igneous intrusions, AMS and AMR fabrics associated with magmatic processes have been shown as susceptible to overprinting under tectonic strain (e.g., Žák et al., 2008b; Knight et al., 2024; Tomek et al., 2024). Where magnetic fabrics arising from tectonic overprinting are distinguished from precursor magmatic processes, intrusions can act as a sensitive, temporally constrained strain archives at orogenic scale, making them an important tool in refining kinematic models of orogenic events (e.g., Žák et al., 2008b; McCarthy et al., 2015c; Siachoque et al., 2024). Tectonic overprints often originate from the development of subtle shear zones within an intrusion that develop into prominent fault zones through progressive deformation during magma cooling (McCaffrey, 1994; Mattsson et al., 2024; Latimer et al., 2025). Due to the crystalline, low permeability of igneous intrusions, fault damage zones are important fluid corridors in many orogenic systems, controlling the type, intensity and distribution of hydrothermal alteration and mineralization (Stevenson, 2009; Bense et al., 2013; Oriolo et al., 2024).

Previous studies demonstrate that ferromagnetic, paramagnetic and diamagnetic mineral phases are partially or completely replaced during hydrothermal alteration (e.g., Ferré et al., 1999; Just et al., 2004; Just and Kontny, 2012; Nédélec et al., 2015). This alteration mineral assemblage has, for example, been used to constrain the thermal and alteration history within granitic intrusions (Petronis et al., 2011; Olšanská et al., 2025) or to assess the siting of Cu porphyry deposits along deep-seated crustal shear zones (Lamont et al., 2024). Where magnetic fabrics have been measured in altered rocks, some studies suggest that minimal change in fabric orientation occurred (Krása and Herrero-Bervera, 2005), whilst others observe a near complete destruction of precursor magmatic fabrics (Just et al., 2004; Quintela et al., 2025). The array of AMS and AMR fabric responses suggests there is a threshold to the intensity of hydrothermal alteration, above which precursor petrofabrics are overprinted. However, recognizing the threshold conditions that cause magnetic fabrics to become partially or completely overprinted by hydrothermal alteration remains highly challenging because data arising from traditional mineral alteration studies (e.g., Laakso et al., 2016; Lypaczewski et al., 2020; Cloutier and Piercey, 2020) are difficult to compare to magnetic data sets (e.g., Žák et al., 2010; Petronis et al., 2012; Tomek et al., 2024). As such, the significance of magnetic fabrics arising from hydrothermally altered rocks remain highly ambiguous (e.g., Quintela et al., 2025).

This study examines hydrothermal alteration and rock fabrics across a fault zone within the Fanad Pluton, NW Ireland, to establish a threshold that describes where hydrothermal overprinting first impacts and finally obliterates magnetically defined petrofabrics. In our study area, precursor magmatic fabrics are demonstrably crosscut by a tectonic fabric, with both petrofabrics overprinted by hydrothermal alteration. An integrated magnetic-hyperspectral methodology is employed to characterize alteration type and intensity across the fault zone. We then used AMS to measure bulk mineral alignment and AMR to determine the alignment of different generations of iron oxides across the mapped alteration zones. Our study links the formation and destruction of magnetic fabrics to the changes in alteration intensity across the fault zone to determine which sets of fabrics reflect magnetic, tectonic and hydrothermal processes. Through this approach, we provide a framework to assess the significance of magnetic fabrics preserved in hydrothermally altered rocks and their ability to record multiple processes within intrusions.

6.2 Background Geology

The Fanad Pluton is one of eight plutons that constitute the late Caledonian Donegal Igneous Complex (DIC) (Pitcher and Berger, 1972) (Fig. 6.1a). Partially exposed along the North coast of Donegal, the pluton is dioritic to granodioritic in composition and is associated with two regional structures; the NE – SW aligned Leannan Fault and the N – S aligned Melmore Shear Zone (White and Hutton, 1985; Ghani and Atherton, 2006; Latimer et al., 2025) (Fig. 6.1a). Recent work on the intrusion reports a complex strain archive that records the interplay between magma chamber processes and external tectonic stress syn- to post-emplacement (Latimer et al., 2024, 2025). In particular, the Currin Point area in the eastern part of the pluton (Fig. 6.1a) features a number of magmatic and sub-solidus features which record the transition from strain derived internally from magma transport to the onset and rotation of tectonic strain during the transpressive – transtensive regime documented during the end of the Caledonian Orogeny (Latimer et al., 2025). Sub-solidus faults and fractures developed at Currin Point have been constrained to seven structural trends (Fig.

6.1a). The earliest three trends form a Riedel shear system related to displacement along the nearby Leannan Fault during regional transpression, with the subsequent four trends formed as a Riedel shear response to the clockwise rotation in shortening direction and activation of the Melmore Shear Zone during regional transtension (Latimer et al., 2025).

Hydrothermal alteration is associated with a number of faults and fractures observed at Currin Point. Centimetre-scale bleaching haloes occur around hairline fractures, and meter-scale alteration haloes occur around large-scale faults ranging 1 – 15 m wide. Within the local tectonic framework constrained by Latimer et al. (2025), this study focuses on the impact of hydrothermal alteration on magnetic fabrics across a 15 m-wide fault zone along the southeastern edge of Currin Point, named here as the Currin Point Fault Zone (CPFZ) (Fig. 6.1a – b). The fault zone is one of the earliest formed sub-solidus structures at Currin Point, kinematically aligned with the interpreted R-shear during displacement along the Leannan Fault under regional sinistral transpression between 422 – 415 Ma (Dewey and Strachan, 2003; Latimer et al., 2025). Here, we link changes in magnetic fabric development to the distribution of hydrothermal alteration within the CPFZ, separating fabrics formed in response to tectonic overprinting of previous magmatic processes from alteration-derived fabric formation and destruction.

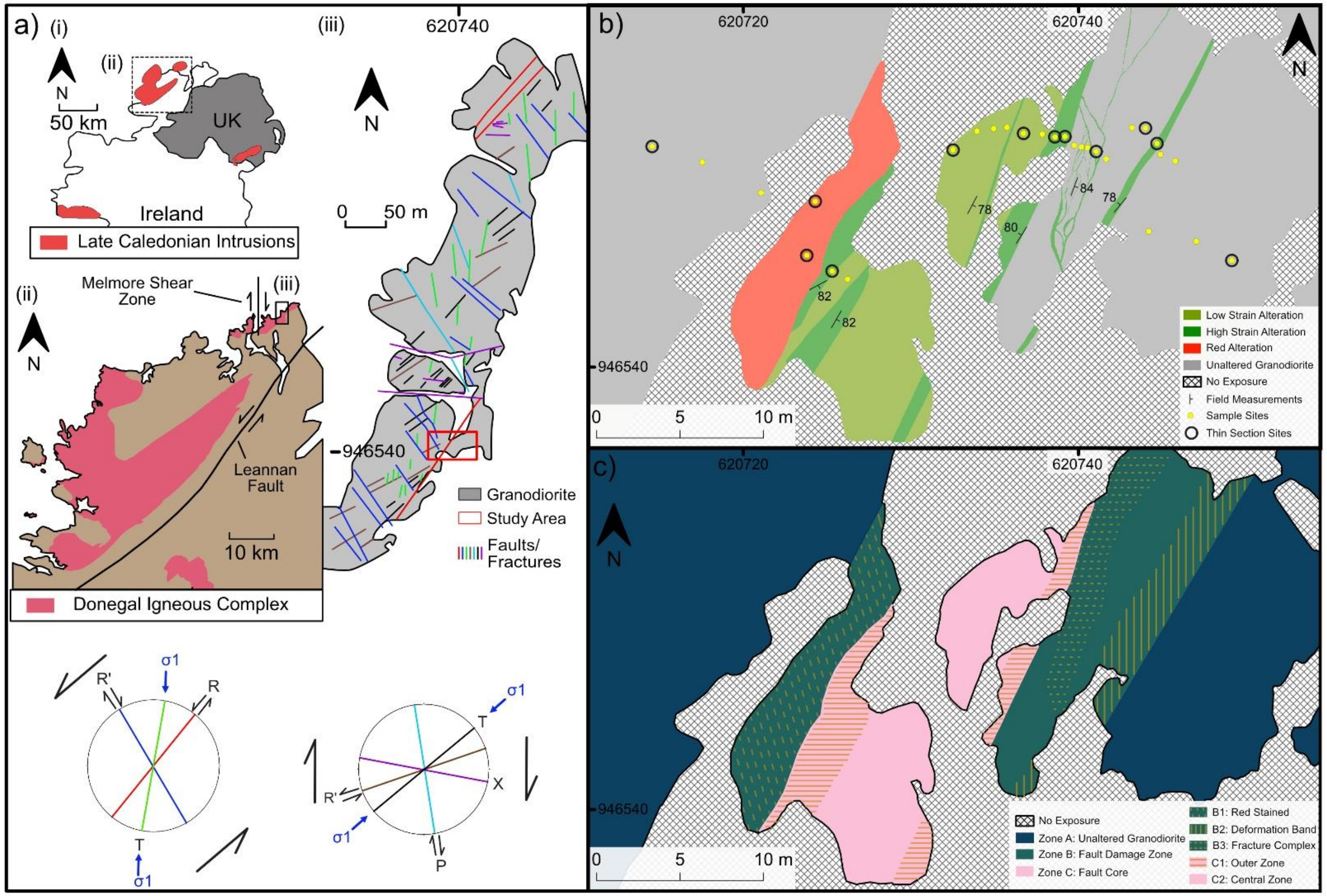

Figure 6.1 – (a) (i) Overview of late Caledonian intrusions in the north of Ireland. (ii) Regional map of the Donegal Igneous Complex. (iii) Map of the Currin Point area and fault/fracture orientation trends showing the location of the Currin Point Fault Zone. (b) Map of the Currin Point Fault Zone showing sites of field sampling and location of subsamples used for thin sections. (c) Map of alteration zones around the Currin Point Fault Zone.

6.3 Methodology

6.3.1 Field Observations and Sampling

A 50 x 35 m traverse of the fault zone was mapped, focusing on field observable transitions in hydrothermal alteration type and intensity alongside any evidence for strain partitioning. Foliation measurements were collected across the fault zone from the contact of fractures and deformation bands crosscutting the granodiorite, and their internal fabrics when observed in the field.

Field mapping reveals three petrographically defined alteration zones about which sampling was coordinated (Fig. 6.1b – c). Orientated core samples were taken at a total of 28 sites along the traverse perpendicular to the strike of the fault zone, targeting the unaltered granodiorite peripheral to the fault, outcrops that appear altered and/or mylonitised within the fault damage zone and from outcrops at the fault core which appear altered and brecciated. Samples were drilled using a modified Stihl BT45 drill and non-magnetic drill bit measuring 25 mm in diameter and varying from 50 – 110 mm in length. Each core sample was then cut into 25 mm x 22 mm cylindrical subsamples using a nonmagnetic saw at the M^{3}Ore laboratory at the University of St Andrews. The number of cores drilled for each site varies from four to seventeen; at least eight subsamples were obtained at each sample site, so a statistically significant magnetic fabric could be measured (Jelinek, 1978). In total, 144 cores, producing 435 subsamples, were collected.

6.3.2 Petrography

Thin sections were taken from 12 representative cylindrical subsamples to determine textural changes across the different zones of alteration using a transmitted light petrographic microscope (Fig. 6.1b). These included two thin sections from each alteration zone and two from the unaltered intrusion on either side of the fault zone. Sections were cut parallel to the top of each cylindrical subsample.

6.3.3 Hyperspectral Characterisation

Hyperspectral characterization was carried out to determine changes in the type and intensity of hydrothermal alteration across the fault zone. Hyperspectral measurements use the absorption of different wavelengths of electromagnetic radiation, most commonly in the visible-near infrared (VNIR) to shortwave infrared (SWIR) range, to non-destructively characterize the minerals present in a sample (Hunt, 1977; Hunt and Ashley, 1979). Within the SWIR range, the spectral signature of a sample will be controlled by hydrous mineral assemblages, which contain a hydroxyl group (OH), with different mineral assemblages identified from absorption troughs at specific wavelengths and the depth of troughs indicating their relative abundance (Hunt and Ashley, 1979; Clark et al., 1990; van Ruitenbeek et al., 2005; Cloutier and Piercey, 2020; Cloutier et al., 2021).

Hyperspectral spot measurements were taken from the subsamples at each sample site using an Analytical Spectral Devices (ASD) TerraSpec Halo handheld spectrometer. Taken from a clean, dry, and fresh surface on each subsample, the generated spectral data was analysed using The Spectral Geologist 8 (TSG 8) software (CSIRO, 2022). A baseline local continuum removal was applied to all data prior to detailed processing to normalize the position and depth of absorption troughs in the reflectance curve generated for each spot measurement. Based on the absorption troughs present, several scalar parameters were calculated for each spot measurement, shown in Table 6.1, based on the parameters of Cloutier and Piercey (2020).

Scalar name	Target mineral Group	Calculation
W2200	White Mica	Wavelength of absorption trough minimum calculated using a fourth-order polynomial function fitted and focused between 2180 and 2220 nm
D2200	White Mica	Depth of absorption trough minimum calculated using a fourth-order polynomial function fitted and focused between 2180 and 2220 nm
W2250	Chlorite & Epidote	Wavelength of absorption trough minimum calculated using a fourth-order polynomial function fitted and focused between 2230 and 2,270 nm
D2250	Chlorite & Epidote	Depth of absorption trough minimum calculated using a fourth-order polynomial function fitted and focused between 2230 and 2270 nm
W2340	White Mica & Chlorite	Wavelength of absorption trough minimum calculated using a fourth-order polynomial function fitted and focused between 2320 and 2360 nm
D2340	White Mica & Chlorite	Depth of absorption trough minimum calculated using a fourth-order polynomial function fitted and focused between 2320 and 2360 nm

Note. A baseline local continuum removal applied to all calculations. Adapted from Cloutier and Piercey (2020).

Table 6.1 – Scalar Parameters Calculated from Hyperspectral Data.

6.3.4 Magnetic Characterisation

A total of 26 subsamples representing the diversity of hydrothermal alteration across the sampled transect were selected for magnetic characterization using a combination of magnetic susceptibility and remanence techniques. Magnetic characterization experiments were carried out to distinguish the contribution of different magnetic minerals to the AMS and AMR ellipsoids across the fault zone and to determine how alteration conditions within the fault zone led to the growth and destruction of ferromagnetic and paramagnetic mineral phases. In particular, experiments were carried out to identify the relative contribution of various ferromagnetic/antiferromagnetic (oxides such as magnetite, maghemite and hematite), paramagnetic (e.g., amphibole, biotite and feldspars) and diamagnetic (e.g., calcite and quartz) mineral phases to bulk rock magnetic susceptibility and magnetic remanence (Tarling and Hrouda, 1993; Dunlop and Özdemir, 1997). Characterizing the magnetic properties of ferromagnetic and antiferromagnetic phases is critical to a robust assessment of magnetic fabrics, as when present even in low modal abundances, these phases will dominate measurements using techniques such as anisotropy of magnetic susceptibility (AMS) and always control anisotropy of magnetic remanence (AMR) (Tarling and

Hrouda, 1993; Borradaile and Jackson, 2010; Mattsson et al., 2021). Furthermore, ferromagnetic/antiferromagnetic phase characterization provides a detailed record of oxide and sulphide phase assemblages within a sample lithology, even when said phases are not observed optically (Dunlop and Özdemir, 1997; O'Driscoll et al., 2024; Jones et al., 2025a).

AMS fabrics from ferromagnetic/antiferromagnetic phases are defined by their crystallographic axis orientation and magnetic domain state, with multidomain grains having a 'normal' fabric (AMS long axis is parallel to the crystallographic long axis), while single domain grains produce an 'inverse' fabric (AMS long axis is parallel to the crystallographic short axis) (Potter and Stephenson, 1988; Tarling and Hrouda, 1993). The presence of more than one ferromagnetic/antiferromagnetic phase or a single phase which features alignment in more than one petrofabric can also constructively or destructively interfere to produce an 'intermediate' fabric (Ferré, 2002). Therefore, clear constraints on the number of ferromagnetic and antiferromagnetic phases, as well as their domain states, are required for a meaningful interpretation of magnetic fabrics to be carried out (Cruz et al., 2022; Mattsson et al., 2024; Latimer et al., 2024, 2025; O'Driscoll et al., 2024). In addition, by establishing a detailed record of changes in oxide and sulphide phase assemblages and their magnetic properties across the fault zone, we provide insight into the hydrothermal alteration oxide and sulphide mineral assemblage that complements the hyperspectral characterization. For example, low coercivity phases such as multidomain magnetite are commonly found in unaltered intrusions, while hematite, a high coercivity phase, can be produced during hydrothermal fluid alteration (Just et al., 2004; Petronis et al., 2011). As such, we can use coercivity spectra alongside magnetic susceptibility to identify regions with elevated alteration intensity (Just and Kontny, 2012; Nédélec et al., 2015).

6.3.4.1 Temperature-Dependent Magnetic Susceptibility

The bulk magnetic mineralogy across the fault zone was characterized via temperature-dependent magnetic susceptibility experiments (T-χ), identifying different mineral phases by comparing the measured trends in bulk magnetic susceptibility across a range of temperatures with standardized trends from common minerals (Dunlop and Özdemir, 1997; Hrouda, 2010). An approximately 0.35 g aliquot of pulp from each subsample, crushed using a ceramic mortar and pestle, was measured following the procedure of Latimer et al. (2024), with the arising thermomagnetic data processed on Cureval8 (Chadima, 2012) to evaluate the magnetic mineralogy.

6.3.4.2 Coercivity Spectra Analysis

Coercivity spectra data were collected using a Lakeshore 8604 vibrating sample magnetometer (VSM) to evaluate ferromagnetic mineralogy coercivity spectra in each of the samples selected for magnetic characterization. An aliquot of approximately 0.27 g of pulped material from the same subsamples used for T-χ experiments was placed in a gel capsule and secured with glue to a plastic straw for mounting onto the VSM.

Saturation isothermal remanent magnetization (sIRM) and back-field isothermal remanent magnetization (BIRM) curves were measured to determine the field of isothermal remanence saturation and coercivity of remanence (B_{cr}) of ferromagnetic/antiferromagnetic phases (Dunlop and Özdemir, 1997; McCarthy et al., 2015b). Each subsample capsule was initially degaussed in a 1960 mT field before being magnetized in a stepwise, unidirectional field to a maximum field of 600 – 1960 mT, followed by immediate stepwise magnetization in the opposite direction, again to 600 – 1960 mT. Fifty points were measured along each sIRM and BIRM curve at a field ramp rate of 1000mT/s. The field of saturation was defined as the field at which no further remanence was gained, while B_{cr} was measured as the applied field at which the BIRM curve reached a remanence of zero.

Magnetic hysteresis loops were measured to determine the saturation magnetization (M_{Sat}), saturation remanent magnetization (M_{RSat}) and coercivity (B_c) of ferromagnetic and antiferromagnetic phases(Dunlop and Özdemir, 1997; Paterson et al., 2018). Each capsule was degaussed in a 1960mT field, before being magnetized bidirectionally in an induced field to a maximum field of 300 – 1000 mT. The generated loop of each subsample was processed using the HystLab program to correct for drift during measurement and remove the influence of paramagnetic mineralogies using the 'linear high-field' function (Paterson et al., 2018).

First-order reversal curve (FORC) diagrams are produced from partial hysteresis loops, which are amalgamated to determine the coercivity (B_C) and interaction field between particles (B_U) (Roberts et al., 2014). FORC diagrams are a sensitive tool in identifying multiple ferromagnetic mineral phases within a lithology, which complement the magnetic properties measured from sIRM/BIRM and magnetic hysteresis loops (Roberts et al., 2014; Harrison et al., 2018). FORCs were measured on the VSM using the same prepared capsules, being degaussed in a 1960mT field prior to measurement. 150 FORCs were generated for each subsample at a 1-second averaging time, with the maximum field varying from 750 – 1960mT. The FORC data was processed in FORCinel software using VARIFORC Smoothing (Harrison and Feinberg, 2008; Egli, 2013).

6.3.5 Rock Fabric Analysis

6.3.5.1 Anisotropy of Magnetic Susceptibility

Anisotropy of magnetic susceptibility (AMS) was measured to quantify bulk mineral alignment and as a semi-quantitative measure of the variation in strain distribution across the fault zone (Tarling and Hrouda, 1993; McCarthy et al., 2015a; Hrouda and Chadima, 2020). AMS was measured on all 435 subsamples, with magnetic susceptibility measurements taken in 320 orientations using a KLY-5A kappabridge and 3-D rotator subsample holder from AGICO (field of 400 Am^{-1} and frequency of 1220 Hz). These measurements are used to calculate a second-rank tensor whose maximum, intermediate and minimum principal axes represent the direction of maximum, intermediate, and minimum magnetic susceptibility (k_1 – k_3, respectively) (Khan, 1962). These axes can be used to form a so-called AMS ellipsoid, of which k_1 is the magnetic lineation and the plane of k_1 and k_2 axes, which k_3 is a pole of, is the magnetic foliation (Tarling and Hrouda, 1993). The AMS ellipsoid can be further characterized through a calculation of several parameters, most notably mean susceptibility (*Kmean*), corrected degree of anisotropy (*Pj*) and ellipsoid shape (*T*) (Jelinek, 1981; Tarling and Hrouda, 1993). *Kmean* reflects the arithmetic mean of the principal axes:

$$Kmean = \frac{k_1+k_2+k_3}{3}\,. \text{ (1)}$$

Pj describes the separation between the value of each principal axis and gives the strength of the magnetic fabric:

$$P_j = \exp\sqrt{2((\eta_1-\eta_{mean})^2+(\eta_2-\eta_{mean})^2+(\eta_3-\eta_{mean})^2)}. \text{ (2)}$$

Where:

$$\eta_x = \ln(k_x)\,, x = 1,2,3. \text{ (3)}$$

T describes the oblate to prolate nature of the AMS ellipsoid based on the length of each principal axis:

$$T = \frac{2\eta_2-\eta_1-\eta_3}{\eta_1-\eta_3}. \text{ (4)}$$

with *T*=1 defining an oblate ellipsoid, *T*=0 defining a triaxial ellipsoid and *T*=-1 defining a prolate fabric (Jelinek, 1981). The variation in *T* is comparable to the variation in Flinn diagram parameters *Z/Y* and *Y/X* for strain ellipsoids (Flinn, 1965; Jelinek, 1981; Hrouda and Chadima, 2020). This allows for the variation in *T* and *Pj* between sample sites to semi-quantify changes in strain distribution across the fault zone (Hrouda and Chadima, 2020). AMS data was collected using the Safyr7 software, with data reorientation and processing on Anisoft6 (Chadima, 2022; Chadima and Hrouda, 2023).

6.3.5.2 Anisotropy of Magnetic Remanence

Anisotropy of magnetic remanence (AMR) was measured to assess if the bulk mineral alignment within each subsample detected via AMS is representative of a single, normal magnetic fabric, an inverse magnetic fabric or an intermediate magnetic fabric (Potter and Stephenson, 1988; Ferré, 2002; Mattsson et al., 2021). Similar to the magnetic characterization experiments, AMR uses magnetic remanence rather than magnetic susceptibility; thus, the measured ellipsoid represents the alignment of ferromagnetic/antiferromagnetic phases only (McCabe and Jackson, 1985). AMR was measured via anisotropy of anhysteretic remanent magnetization (AARM), to measure the alignment of higher coercivity phases, and low-field anisotropy of isothermal remanent magnetization (AIRM) was used to measure the alignment of low coercivity phases (Jackson, 1991). This approach tested for the presence of sub-fabrics defined by ferromagnetic minerals of different grain sizes (e.g., Jackson, 1991; Latimer et al., 2024).

AARM and AIRM were measured on 43 subsamples across the fault zone, with subsamples magnetized in 15 orientations (P-Mode) to calculate the AARM and AIRM ellipsoid, respectively (Hext, 1963; Jelinek, 1978). Prior to each orientation of measurement, subsamples were demagnetized within a 200mT alternating current (AC) field using the LDA-5 demagnetizer. For AARM, subsamples were then magnetized in the first orientation using the PAM-1 pulse magnetizer from AGICO using a 140 mT AC field biased by a 100 μT direct current (DC) field. The imparted remanence was then measured using a JR-6A spinning magnetometer, before demagnetizing each subsample in the LDA-5 using a 160 mT AC field and repeating this process for the remaining fourteen orientations. For AIRM, the same procedure was followed, but with a 20 mT DC field used to magnetize the subsamples and a 120 mT AC field used to demagnetize them in each measurement. The remanent magnetization data were collected, and the AARM/AIRM tensor calculated using Rema6 software from AGICO (Chadima et al., 2018b). As with AMS, the maximum, intermediate and minimum principal axes from the AARM/AIRM tensor give the fabric from alignment of ferromagnetic phases with a subsample, which can also have *Pj*, *T* and mean remanence (*Rmean*) values calculated (Hext, 1963; Jelinek, 1981; McCabe & Jackson, 1985). We use a_1 – a_3 to describe the remanence axes of AARM measurements, while i_1 – i_3 are used for AIRM.

6.4 Results

6.4.1 Field Observations and Petrography

Field observations reveal three distinctive zones across the fault zone based on textural variations, rock fabrics and hydrothermal alteration patterns (Fig. 6.1b – c). Below, we describe each zone from the undeformed peripheral granite moving inwards towards the fault zone centre.

6.4.1.1 Zone A: Unaltered Granodiorite

The eastern and western periphery of the fault zone traverse is dominated by unaltered granodiorite, referred to as Zone A (Fig. 6.1b – c). In hand specimen, the granodiorite consists of coarse-grained (2 mm) white and pink feldspar, hornblende, biotite and quartz (Fig. 6.2a). Crystals are subhedral in nature with no clear mineral alignment present. Magmatic features such as enclaves are seen across the area, varying in size from a few centimetres to 3 m in length. There is evidence of fracturing across Zone A, particularly in the eastern exposure, which predominantly aligns with the NE – SW alignment of the fault zone, but with no hydrothermal alteration present.

In thin section, Zone A is a medium to coarse-grained (1 – 3 mm) granodiorite consisting of plagioclase feldspar (50%), quartz (20%), amphibole (10%), biotite (10%), alkali feldspar (10%) and accessory titanite, apatite, epidote and iron oxides. Crystals are subhedral to anhedral, with quartz infilling around the feldspars and mafic phases. Plagioclase exhibits evidence of partial sericitisation, with alkali feldspars being weakly zoned to unzoned and also partially altered. Individual amphibole and biotite are observed, but more commonly form 1 – 3 mm clusters, with partial chloritisation of biotite (Fig. 6.3a – b). Iron oxides are observed as inclusions within mafic crystals, primarily within mafic clusters, appearing as subhedral 100 – 200 μm crystals, or groups of ≤10 μm acicular crystals aligned to the faces of the mafic crystal they are included within (Fig. 6.3a – b). Minor, late-stage deformation textures are observed in all mineral phases, with deformation twinning within feldspars, kinking amphibole and biotite, and weak undulose extinction developed within quartz.

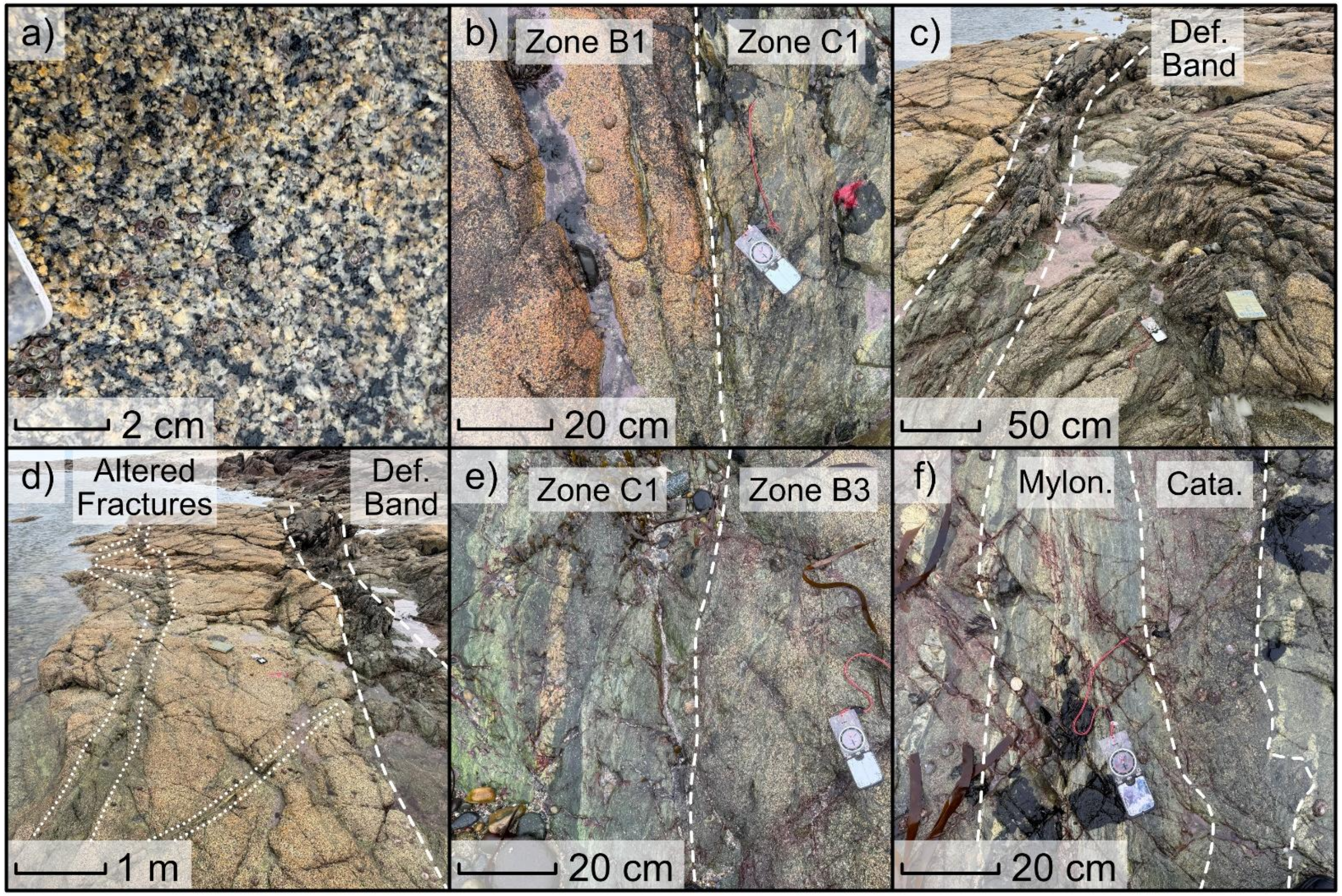

Figure 6.2 – (a) Close up of the unaltered granodiorite. (b) Contact between Zone B1, red-stained granodiorite and Zone C1, the outer fault core. (c) The deformation band (Def. Band) crosscutting the granodiorite in Zone B2. (d) The altered fractures in Zone B3, with the deformation band (Def. Band) of Zone B2 shown adjacent. (e) Contact between Zone B3 and Zone C1. (f) Mylonitic (Mylon.) and cataclastic (Cata.) bands within Zone C2, the centre of the fault core.

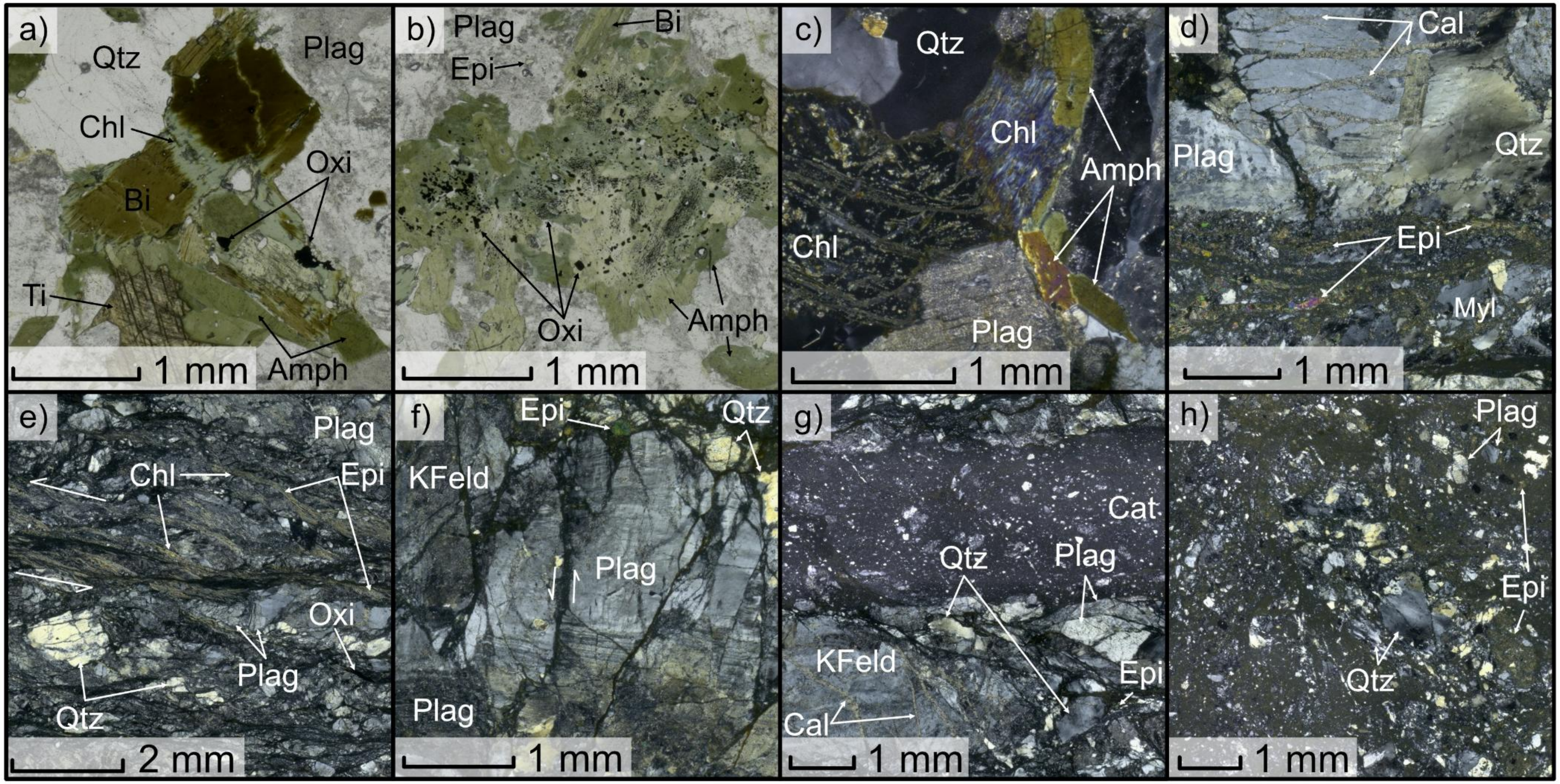
a)
Qtz
Plag
Chl
Oxi
Bi
Ti
Amph
1 mm
b)
Plag
Bi
Epi
Oxi
Amph
1 mm
c)
Qtz
Chl
Amph
Chl
Plag
1 mm
d)
Cal
Plag
Qtz
Epi
Myl
1 mm
e)
Plag
Chl
Epi
Oxi
Plag
Qtz
2 mm
f)
Epi
Qtz
KFeld
Plag
Plag
1 mm
g)
Cat
Qtz
Plag
KFeld
Epi
Cal
1 mm
h)
Plag
Epi
Qtz
1 mm

Figure 6.3 – (a) Plane Polarized Light (PPL) image of Zone A showing partial chloritization of biotite. (b) PPL image of Zone A showing the distribution of iron oxide inclusions within a mafic cluster. (c) Cross-polarized light (XPL) image of the Zone B1, showing alteration of plagioclase feldspar and the full replacement of biotite by chlorite. (d) XPL image of the granodiorite adjacent to the deformation band in Zone B2 showing crosscutting mylonitic bands and fractures, infilled with calcite. (e) XPL image of Zone B2 deformation band showing mylonitic fabric development. (f) XPL image of brittle fracturing and displacement of plagioclase feldspar in the granodiorite crosscut by altered fractures in Zone B3. (g) XPL image of Zone C1, showing ductile deformation textures crosscut by millimetre-scale cataclastic bands. (h) XPL image of cataclastite formation within Zone C2. Amph = amphibole; Bi = biotite; Cat = cataclastite; Cal = calcite; Chl = chlorite; Epi = epidote; KFeld = alkali feldspar; Myl = Mylonite; Oxi = Oxides; Plag = Plagioclase; Qtz = Quartz; Ti = titanite.

6.4.1.2 Zone B: Fault Damage Zone

Zone B represents a 15 m wide zone peripheral to the core of the fault zone with varying degrees of alteration intensity and strain partitioning along deformation bands and fractures crosscutting the granodiorite (Fig. 6.1b – c). Based on these features and their proximity to the fault centre, we refer to Zone B as the damage zone of the fault (Caine et al., 1996; Bense et al., 2013). Three subzones are defined based on these variations: Zone B1, a 4 m-wide a region of granodiorite with distinct red alteration at the western side of the fault zone; Zone B2, focused on a peripheral deformation band crosscutting the granodiorite at the edge of the damage zone; and Zone B3, a 5 – 10 m wide of the granodiorite crosscut by a bifurcating network of hydrothermally altered fractures which have branched off Zone B2 (Fig. 6.1b – c).

Zone B1 is seen only along the western side of the fault zone and features a gradational boundary with Zone A, and a sharp contact with the fault core (Fig. 6.2b). Red staining is a characteristic feature of Zone B1, interpreted to represent hydrothermal alteration of feldspars, with centimetre-scale bleaching halos around hairline fractures (Fig. 6.2b). In thin section, all feldspar crystals show a moderate to complete alteration to white mica, the modal abundance in iron oxides decreases relative to Zone A, and biotite is extensively replaced by chlorite (Fig. 6.3c).

In Zone B2, a sub-vertical 0.5 - 1 m wide deformation band trending NE – SW crosscuts the granodiorite, with intense hydrothermal alteration terminating against the margin of this deformation band (Fig. 6.2c). In thin section, the granodiorite adjacent to the deformation band shows a clear increase in deformation intensity relative to Zone A. Deformation twinning and kinking are pervasive within feldspars, amphibole and chlorite crystals, with quartz beginning to demonstrate subgrain development (Fig. 6.3d). As with Zone B1, biotite is fully replaced by chlorite, but with reduced alteration of alkali and plagioclase feldspar. The abundance of iron oxides in the granodiorite is also approximately equal to Zone B1. 30 – 80 μm mylonitic bands, consisting of subhedral to anhedral plagioclase, quartz and epidote are observed crosscutting sections of the granodiorite (Fig. 6.3d). Crystals within these bands are reduced in grain size to predominately 20 – 100 μm, with rare quartz and feldspar porphyroclasts in the 0.5 – 1 mm range (Fig. 6.3d). These porphyroclasts demonstrate brittle fracturing textures, with epidote surrounding porphyroclasts and infilling fractures (Fig. 6.3d). Immediately adjacent to these mylonite bands, parallel-trending fractures are infilled with calcite, orientated oblique to the fracture walls (Fig. 6.3d).

The deformation band itself consists of 3 – 10 mm wide heterogeneous bands of dark-green and pale-green hydrothermally altered material and rare quartz and feldspar porphyroclasts. In thin section, the deformation band shows development of a mylonitic fabric that completely destroys the previous granodioritic texture (Fig. 6.3e). Porphyroclasts of quartz and feldspar are anhedral and fragmented, with chlorite, epidote and calcite forming mineral fish and as mantles around these porphyroclasts, indicating a sinistral shear sense (Fig. 6.3e). Iron oxides are present in the deformation band as 0.5 – 1 mm elongate crystals associated with chlorite infilling around quartz and feldspar crystals (Fig. 6.3e).

In Zone B3, hydrothermally altered fractures are 50 – 100 mm in width and observed as isolated fracture planes or as clusters of hairline fractures with a 10 – 75 cm alteration halo (Fig. 6.2d). The average fracture plane orientation is sub-vertical (020 84 E), with the centre of fractures infilled with fine-grained hydrothermally altered material often a paler green than the material dominant in the alteration halo. The granodiorite around the fractures shows evidence of partial alteration with a distinct yellowing of feldspars and hairline fractures showing infill with a pale-green, fine-grained material. In thin section, the deformation textures observed in Zone B2 are further developed, with pervasive brittle fracturing of the granodiorite adjacent to the hydrothermally altered fractures (Fig. 6.3f). Deformation twinning in feldspars and kinking of amphibole and chlorite crystals, alongside subgrain formation in quartz, are observed, with fractures crosscutting these textures. Fracturing of crystals shows sinistral and dextral displacement, with multiple orientations of fractures observed. Epidote is observed as ≤150 μm crystals within the hydrothermally altered fractures and in the granodiorite immediately adjacent (Fig. 6.3f). Oxide modal abundance also decreases with proximity to the hydrothermally altered fracture, with the granodiorite distal from these fractures showing an oxide content equal to the rest of the fault damage zone.

6.4.1.3 Zone C: Fault Core

Zone C represents the 15m wide fault core, this area shows the most intense hydrothermal alteration and deformation (Caine et al., 1996; Bense et al., 2013). Based on field observations, the fault core is divided into a 2 – 3 m-wide outer zone (Zone C1) either side of a 10 m-wide central zone (Zone C2) (Fig. 6.1c).

The outer zone, Zone C1, is separated from the central zone of the fault core by the development of an inward-dipping, subvertical foliation (062 82 E and 030 80 W, respectively), defined by heterogeneous banding of fine-grained pale-green and dark green alteration materials (Figs. 6.1b & 6.2b & e). A sharp contact between Zone C1 and B1 is observed to the west of the fault core (Fig. 6.2b), while the eastern contact with Zone B3 is gradational in nature (Fig. 6.2e). At the eastern contact, the damage zone shows an increase in fracture density and alteration approaching the contact, with the primary texture of the granodiorite increasingly destroyed until being completely replaced by hydrothermally altered material (Fig. 6.2e). Thin sections show pervasive deformation textures, including deformation twinning, crystal fracturing and tiling, with these textures overprinted by 2 mm-wide cataclastic bands and adjacent fractures which show parallel and oblique trends (Fig. 6.3g). Where the granodiorite is not destroyed by cataclastic bands or fractures, ductile deformation textures such as deformation twinning and kinking and subgrain development in quartz are observed. Adjacent to the fracture planes, crystals show brittle fragmentation similar to Zone B3, with calcite often infilling these fractures (Fig. 6.3g). Within the cataclastic bands, material is predominantly fine-grained (<5 μm) with 60 – 100 μm porphyroclasts of quartz and feldspar. Thin-section petrographic analysis did not detect iron oxides in this zone.

Zone C2 represents the centre of the fault core, it is defined by NE-trending bands of moderately to highly altered mylonitised granodiorite and cataclastite (Fig. 6.1b – c). Mylonitised bands are defined by 0.4 – 2 m wide areas of foliated, fine-grained quartzofeldspathic material similar to the deformation band of Zone B, with the cataclastic bands 0.2 – 3m wide and featuring 1 – 2 mm grains of feldspar and quartz in a fine-grained matrix of dark green, hydrothermally altered materials (Fig. 6.2e – f). In thin section, the cataclastic textures observed as distinct bands in Zone C1 are the dominant texture (Fig. 6.3h). The original granodiorite is observed only as isolated porphyroclasts of quartz and feldspar, with some of these porphyroclasts retaining evidence of ductile deformation seen in the fault damage zone (Fig. 6.3h). Epidote is a modally significant component within the fault core (15%) infilling around the porphyroclasts and as larger 1 – 3 mm clusters of crystals. Iron oxides occur in very low abundance in this zone (< 0.5%).

6.4.2 Hyperspectral Characterisation

Full datasets for hyperspectral characterization are provided in the Supplementary Material, scalars D2200 and D2250 are shown here to summarize the most significant mineralogical changes detected by reflectance data i.e. flux in hydrous mineral assemblages across the fault zone (Fig. 6.4). Below, we describe the six scalars from west to east across the traverse of the fault zone, with 'D' denoting the depth of absorption troughs at a given wavelength range, 'W' denoting the wavelength trough minimum and the hydrous mineral targeted by each scalar provided in Table 6.1.

6.4.2.1 2200 nm Absorption Troughs

Across the western exposure of Zone A, D2200 shows a gradual rise from 0.05 – 0.4, with a subset of subsamples showing trough depths of 0.5 – 0.9, suggesting an increase in white mica modal abundance (Fig. 6.4). D2200 then declines sharply across Zone B1 and into Zone C1, with absorption troughs around 2200 nm becoming absent, suggesting white mica is not present, with troughs reappearing at the Zone C1/C2 contact with a trough depth of 0.05 – 0.2 (Fig. 6.4). Absorption troughs around 2200nm are then absent across the centre of the fault core, with a weak trough appearing at the transition to the eastern fault core contact, reaching depths of 0.06, before sharply rising to 0.2 – 0.4 at the eastern contact with the fault damage zone (Fig. 6.4). Across Zone B3, D2200 undulates from being absent in spot measurement of the altered fractures, to a maximum depth of 0.35 within the granodiorite they crosscut. D2200 then declines within the deformation band crosscutting Zone B2 to 1.5 –0.05, before stabilizing at 0.2 within the eastern extent of Zone A (Fig. 6.4).

W2200 shows very little variation across the traverse of the fault zone, with all absorption troughs occurring in the wavelength range of muscovite (Clark et al., 1990; Cloutier et al., 2021). Most absorption troughs occur around 2199 – 2200 nm, with a deviation in range to 2202 – 2206 nm within in the western outer fault core (Zone C1), where the reappearance of white mica is recorded by D2200. Similarly, a change in W2200 occurs within absorption troughs at the eastern contact of Zone C2 and Zone C1, where troughs occur at 2202 – 2216 and in the deformation band crosscutting Zone B2, ranging from 2201 – 2213 nm.

6.4.2.2. 2250 nm Absorption Troughs

For D2250, initial trough depth ranges from 0.01 – 0.02 within Zone A, indicating a low abundance of epidote and chlorite, increasing to 0.04 within Zone B1 (Fig. 6.4) (Clark et al., 1990; Cloutier et al., 2021). D2250 rapidly rises at the western contact of the fault core from 0.04 to 0.08, reaching a maximum absorption trough depth of 0.21 at the eastern edge of Zone C2 (Fig. 6.4). D2250 then declines across Zone C1 and into Zone B3 of the fault damage zone, with a similar undulating pattern to trough depths as D2200 (Fig. 6.4). However, these undulations show an inverse relationship to D2200 with local maxima ranging from 0.08 – 0.18 seen within subsamples of the hydrothermally altered fractures and shallower troughs of 0.07 – 0.03 observed in the adjacent granodiorite (Fig. 6.4). Similarly, D2250 shows an increase in trough depth within the deformation band of Zone B2, inverse to D2200, rising from 0.04 to 0.1. This is then followed by a gradual decline to a trough depth of 0.02 across the eastern exposure of Zone A (Fig. 6.4).

W2250 ranges suggest an intermediate Mg-Fe composition to chlorite across the fault zone (Cloutier et al., 2021). The trough ranges from 2250 – 2253.3 nm across Zone A, correlating with the rise of D2200, before declining across Zone B1 back to 2250 nm. Within the western outer fault core, W2250 shows another rise to a range of 2251.5 –2252.3 nm within the subsamples, which show the sudden decline in D2250 before returning to the wavelength range of 2250.5 – 2251nm across the rest of the fault core. Within Zone B3, absorption troughs occur in two wavelength ranges, with subsamples of the altered fractures featuring a W2250 range of 2250.7 – 2251.5 nm, while troughs in the granodiorite they crosscut range from 2251.5 – 2253.5 nm. Within Zone B2, W2250 is observed from 2251 – 2252 nm, with Zone A showing a slightly wider range of trough wavelengths from 2251 – 2252.5 nm.

6.4.2.3 2340 nm Absorption Toughs

D2340, reflecting the abundance of white mica and chlorite, correlates with D2250 across the fault zone (Clark et al., 1990; Cloutier et al., 2021). Across the western extent of Zone A and Zone B1, D2340 values range from 0.02 – 0.06, rising across the fault core contact to a range of 0.06 – 0.28. Similar to D2250, a decrease of D2340 to a range of 0.06 – 0.14 is seen in subsamples of the outer fault core, which feature an increase in D2200. Across Zone B3, subsamples of the hydrothermally altered fractures show a D2340 range of 0.06 – 0.24, with the range in the adjacent granodiorite 0.06 – 0.1. The variation in D2340 within the deformation band crosscutting the granodiorite in Zone B2 relative to Zone A is more subtle, elevating to 0.06 – 0.1 and then declining to 0.02. W2340 values across the fault zone support W2200 values, indicating that muscovite is the dominant white mica and W2250 values that chlorite is an intermediate Mg-Fe composition (Cloutier et al., 2021). W2340 values are constant at 2340 nm across the fault zone, except in Zone A, where they decline to a range of 2332 – 2340 nm.

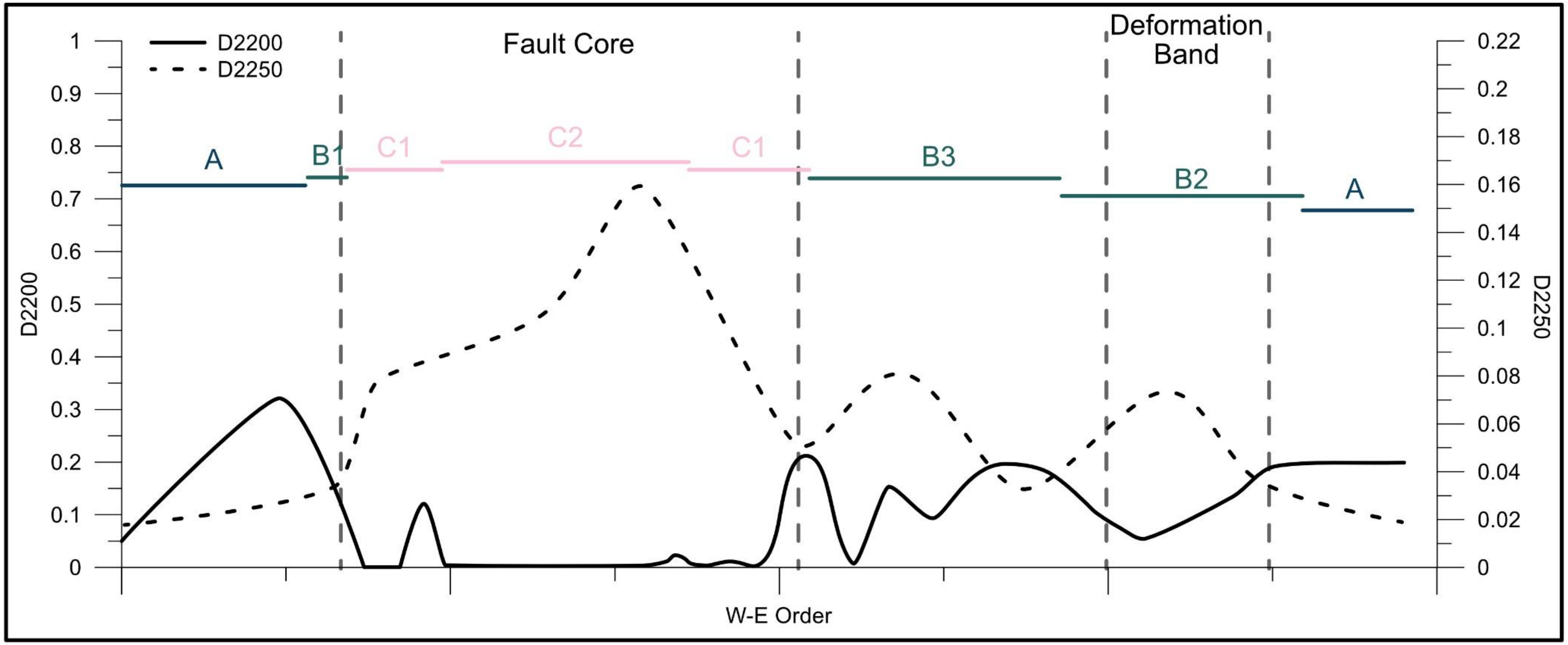

Figure 6.4 – W – E trends in D2200 (depth of absorption troughs at 2200nm) and D2250 (depth of absorption troughs at 2250nm) across the Currin Point Fault Zone and the observed alteration zones.

6.4.3 Magnetic Characterisation

We describe the results of the magnetic characterization from the periphery of the Currin Point Fault Zone towards the fault core. A representative subset of the characterized subsamples is shown graphically (Fig. 6.5), with tabulated data from coercivity spectra analysis provided in Table 6.2, and the full datasets available in the Supplementary Material.

Alteration Zone	Subsample	M_{Sat}	M_{RSat}	B_c	B_{cr}	M_{RSat}/M_{Sat}	B_{cr}/B_c
A	FS003_C2	6.26E-06	1.58E-07	2.9	22.4	0.03	8
	FA028_A5	1.95E-05	3.15E-07	1.8	17.8	0.02	10
	FA027_C3	1.10E-05	2.13E-07	2.3	17.8	0.02	8
	FA002_C3	1.11E-05	5.22E-07	5.8	21.1	0.05	4
	FA016_A3	3.89E-05	2.02E-06	6.0	21.1	0.05	4
B1	FA025_A3	9.42E-06	3.19E-07	4.4	25	0.03	6
	FA025_C3	5.27E-06	1.84E-07	4.6	21.1	0.03	5
	FA024_C4	4.86E-06	1.87E-07	4.7	22.4	0.04	5
B2	FA006_A3	1.18E-05	7.63E-07	8.4	29.7	0.06	4
	FA005_K2	8.25E-06	5.55E-07	7.8	29.7	0.07	4
	FA005_G3	6.73E-06	7.41E-07	16.1	76.3	0.11	5
	FA004_C4	8.94E-06	5.26E-07	5.9	25	0.06	4
B3	FA020_A2	9.06E-06	3.61E-07	4.5	17.8	0.04	4
	FA020_E4	1.05E-07	2.16E-08	11.2	41.7	0.21	4
	FA018_F3	7.54E-08	1.87E-08	14.3	35.1	0.25	2
	FA018_D3	7.62E-07	4.67E-08	7.7	35.2	0.06	5
	FA007_C1	5.95E-06	2.31E-07	4.5	25	0.04	6
	FA007_D1	5.43E-06	2.71E-07	3.8	21.1	0.05	6
C1	FA023_G2	6.88E-06	3.92E-07	6.9	25	0.06	4
	FA023_C4	2.11E-07	2.22E-08	10.5	35.2	0.11	3
	FA022_A1	2.66E-06	1.86E-07	7.1	21.1	0.07	3
	FA014_E3	2.52E-07	4.19E-08	10.0	29.7	0.17	3
	FA015_B2	2.11E-06	1.55E-07	7.5	25	0.07	3
C2	FA008_C4	1.56E-06	1.78E-08	2.2	695.7	0.01	316
	FA012_F3	3.36E-08	7.06E-09	14.2	69	0.21	5
	FA013_A1	9.42E-07	4.71E-08	4.3	20.3	0.05	5

Table 6.2 – Summary Data of Coercivity Spectra Analysis

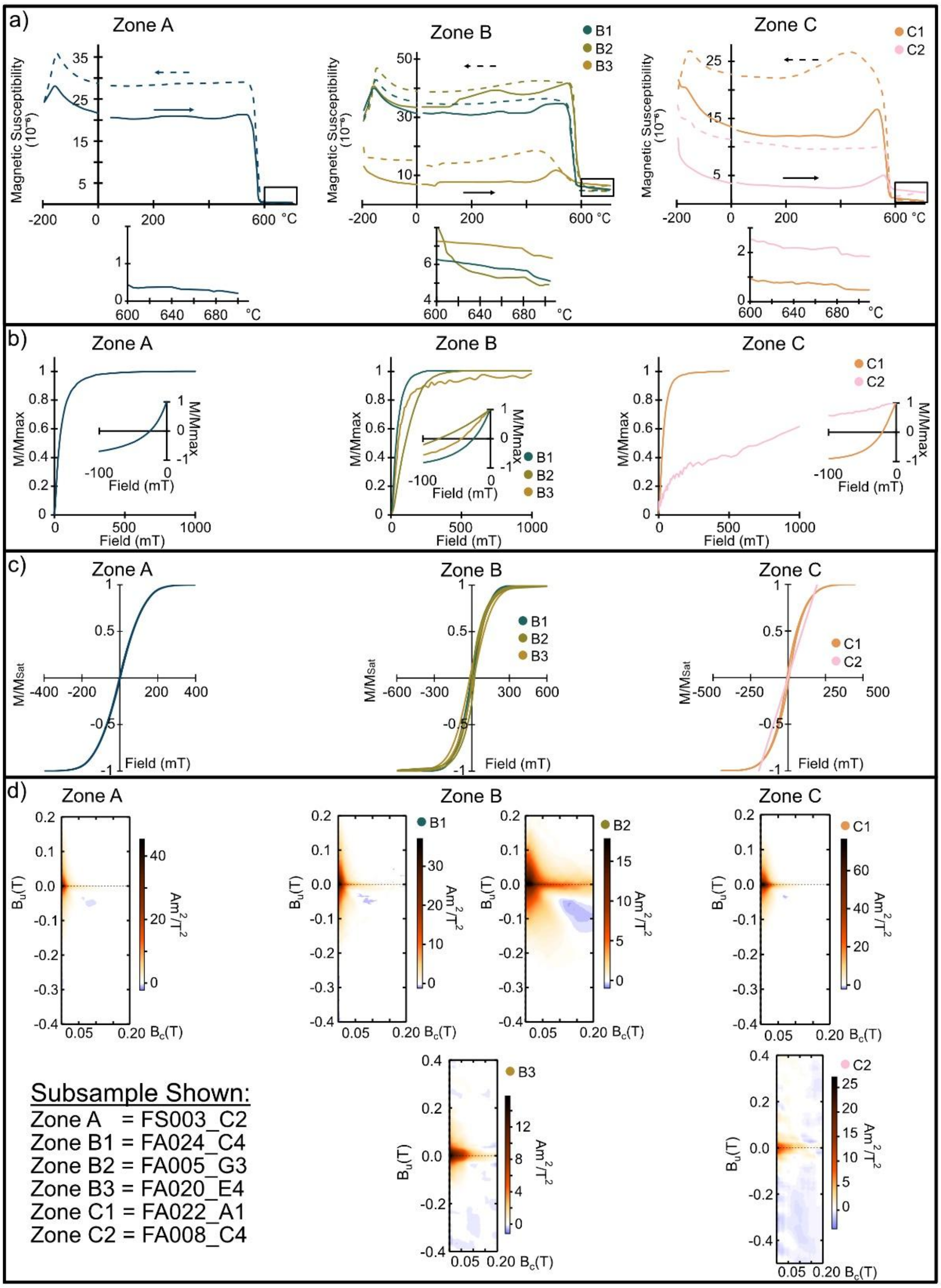

Figure 6.5 – Representative results of magnetic characterization experiments. (a) Results of temperature-dependent magnetic susceptibility experiments, inset below each heating-cooling trend, show results in the final one hundred degrees of heating. (b) Results of saturation and backfield isothermal remanence magnetization. (c) Result of hysteresis loop measurement. (d) First Order Reversal Curve Diagrams from each alteration zone.

6.4.3.1 Zone A: Unaltered Granodiorite

All T–χ data from Zone A show an immediate rise followed by a sudden decline in bulk magnetic susceptibility, inflecting at -154°C to define a Verwey transition (V_T) during the initial heating run (Fig. 6.5a) (Tarling and Hrouda, 1993; Dunlop and Özdemir, 1997). With the exception of one sample, bulk magnetic susceptibility is constant in all samples from 0 – 250°C where an inflection 'bump' is observed from 250 – 350°C, followed by a gradual rise from 450 – 550°C where the Curie Temperature (T_C) occurs. The V_T and T_C indicate that magnetite dominates bulk magnetic susceptibility, with the T_C temperature range and the lack of a Hopkinson peak being indicative of multidomain (MD) low-Ti titanomagnetite (Tarling and Hrouda, 1993; Dunlop and Özdemir, 1997). The bump in bulk magnetic susceptibility from 250 – 350°C is indicative of a minor contribution from maghemite, while the rise in bulk susceptibility from 450°C is likely due to the growth of new magnetite from the oxidation of the primary titanomagnetite and any minor non-magnetic sulphides and Fe-rich silicates present in the subsamples during heating (Dunlop and Özdemir, 1997; Petronis et al., 2011). This is also supported by the irreversible nature of the cooling curve, which shows an elevated bulk magnetic susceptibility and the absence of bumps along the trend, indicating the presence of new magnetite post-heating (Fig. 6.5a). Coercivity spectra analysis indicates the dominance of a single, low coercivity phase across Zone A (Fig. 6.5b – d). sIRM curves sharply rise to 95% saturation from 150 – 220 mT, with B_{cr} from BIRM ranging from 21 – 26 mT, indicating dominance of a single low coercivity phase (Fig. 6.5b). Similarly, hysteresis loops reach M_{Sat} by 350 – 540 mT with low B_c values of 1.8 – 5.8 mT (Fig. 6.5c). FORC diagrams show a ridge parallel to the B_u axis, with a peak in at the B_u/B_c axes origin, supportive of a low coercivity MD phase dominating the magnetic mineralogy (Fig. 6.5d). Based on the combined magnetic characterization, this phase is low-Ti titanomagnetite (Fig. 6.5).

6.4.3.2 Zone B: Fault Damage Zone

Within Zone B1, T-χ experiments display a V_T inflection at -154°C with a bump in bulk magnetic susceptibility at 210 – 310°C followed by a gradual rise from 420°C until the T_C at 540 – 550°C (Fig. 6.5a). These features along with the lack of a Hopkinson peak are indicative of MD low-Ti titanomagnetite dominating the magnetic mineralogy, with the bump from 210 – 310°C suggesting the presence of maghemite. After reaching T_C, bulk magnetic susceptibility continues declining, with a subtle inflection at 680°C, indicating the contribution of hematite to the magnetic mineralogy (Fig. 6.5a) (Orlický, 1990; Tarling and Hrouda, 1993). Cooling curves are irreversible, with bulk magnetic susceptibility elevated and the signature of hematite and titanomaghemite absent (Fig. 6.5a). Coercivity spectra analysis indicates a single low coercivity phase is dominant in the magnetic mineralogy (Fig. 6.5b – d). sIRM curves reach 95% saturation by 130 – 140 mT, with B_{cr} of 16 – 24 mT, similar to Zone A (Fig. 6.5b). Hysteresis loops reach M_{Sat} within 350 – 380 mT, elevated from Zone A, with B_c values of 4.4 – 4.7 mT (Fig. 6.5c). FORC diagrams show a ridge parallel to the B_u and B_c axes, with peak spread over a larger interaction field and coercivity range than in Zone A (Fig. 6.5d). The combined magnetic characterization experiments indicate that while dominated by a single MD ferromagnetic phase, low-Ti titanomagnetite, a higher coercivity phase is contributing to the magnetic mineralogy of Zone B1, most likely the hematite (Fig. 6.5b – d).

Zone B2 T-χ experiments display a V_T inflecting at -155°C, with a distinct bump in bulk magnetic susceptibility trend from 166 –310°C followed by a gradual rise until reaching T_C at 545 – 555°C (Fig. 6.5a). The T_C range indicates the dominance of low-Ti titanomagnetite, with a much larger contribution from maghemite based on the bump in the trend relative to Zone A or Zone B1 (Dunlop and Özdemir, 1997) (Fig. 6.5a). As with Zone B1, the decline in bulk magnetic susceptibility after the T_C inflecting at 680°C suggests a contribution of hematite to the magnetic mineralogy (Fig. 6.5a). Coercivity spectra analysis indicates increased contribution by a higher coercivity phase, sIRM curves reaching 95% saturation by 197 – 347 mT and B_{cr} values of 26 – 76 mT (Fig. 6.5b). Hysteresis loops reach M_{Sat} within 400 – 550 mT and have B_c values of 5.9 – 16.1 mT, elevated in comparison to Zone B1 or Zone A (Fig. 6.5c). FORC diagrams show a strong ridge along the B_c axis, with a large triangular peak dispersed along the B_u and B_c

axes (Fig. 6.5d). This suggests the magnetic mineralogy features the equal contribution and interaction a high coercivity phase, indicated to be hematite by T-χ experiments, with an MD phase, identified as low-Ti titanomagnetite (Fig. 6.5d).

In Zone B3, T-χ experiments from subsamples of altered fractures crosscutting the granodiorite lack a V_T, with a gradual decline in bulk magnetic susceptibility from -194°C to 0°C (Fig. 6.5a). A step is observed in the trend at 68°C, remaining constant until 400°C where a gradual rise occurs to 520°C (Fig. 6.5a). This is followed by a decline in bulk magnetic susceptibility to an inflection point at 574 – 584°C, followed by a second inflection at 680°C indicative of hematite (Fig. 6.5a). Cooling curves are irreversible, rising to a maximum at 435 – 470°C and featuring a weak V_T at -154°C (Fig. 6.5a). The lack of V_T or T_C during heating suggests a magnetite phase is not the dominant ferromagnetic phase of the magnetic mineralogy, with the increase in bulk magnetic susceptibility from 400 – 520°C and appearance of a V_T within cooling curves suggesting magnetite growth from subsample oxidation during heating (Fig. 6.5a). Coercivity spectra analysis correlates the change in magnetic mineralogy, with sIRM curves sharply rising from 0 – 180 mT, but only reached 95% saturation by 500mT, with B_{cr} of 36 – 44 mT (Fig. 6.5b). Hysteresis loops feature M_{Sat} fields of 160 mT, with B_c ranging from 11.2 – 14.3 mT showing higher coercivities relative to the unaltered granodiorite (Fig. 6.5c). FORC diagrams show a weak ridge along the B_c axis, with a distinct peak at the origin of the B_u/B_c axes which has a coercivity equal to the peak in FORCs within Zone B2 (Fig. 6.5d). Therefore, the combined characterization experiments suggest the magnetic mineralogy of the altered fractures is dominated by a single high coercivity phase, identified as hematite (Fig. 6.5).

6.4.3.3 Zone C: Fault Core

In Zone C1, T-χ experiments show a weak V_T inflection at -160°C, with a gradual rise observed from 432°C to a T_C of 540°C, consistent with the presence of primary MD low-Ti titanomagnetite, with growth of new magnetite during heating

(Fig. 6.5a). After T_C, bulk magnetic susceptibility continues declining with an inflection at 680°C indicative of hematite (Fig. 6.5a). Cooling curves are irreversible with bulk magnetic susceptibility rising to 450°C and a stronger V_T inflection at -140°C from the new magnetite growth during heating (Fig. 6.5a). Coercivity spectra analysis indicates the presence of a low and high coercivity phase contributing to the magnetic mineralogy (Fig. 6.5b – d). sIRM curves reach 95% saturation by 125 – 130 mT with B_{cr} of 22 – 26 mT, corresponding with hysteresis loops reaching M_{Sat} by 400mT and B_c of 7.1 mT (Fig. 6.5b – c). FORC diagrams show a strong ridge along the B_u axis, with a minor B_c axis ridge and a peak in values at the B_u/B_c axes origin (Fig. 6.5d). Unlike the unaltered granodiorite, the peak in FORC diagrams of Zone C1 extends along the B_c axis, indicating a mixed magnetic mineralogy of a low coercivity MD phase and higher coercivity phase (Fig. 6.5d). Combining all magnetic characterization experiments, the low coercivity phase of the magnetic mineralogy is low-Ti titanomagnetite and the high coercivity phase is hematite (Fig. 6.5).

Zone C2 T-χ experiments do not display a V_T during heating, with bulk magnetic susceptibility showing a gradual rise from 465°C – 560°C, suggesting the growth of new magnetite during heating, before declining to an inflection point at 680°C indicating the presence of hematite (Fig. 6.5a). Cooling curves are irreversible, showing a trend similar to the unaltered granodiorite, supporting magnetite growth during heating of subsamples controlling the trend of bulk magnetic susceptibility (Fig. 6.5a). Coercivity spectra analysis supports the dominance of a high coercivity phase within Zone C2, with sIRM curves initially showing a sharp rise, but failing to reach saturation by 1960 mT and B_{cr} values of 57 – 96 mT (Fig. 6.5b). Similarly, hysteresis loops do not reach a M_{Sat} with B_c values of 12.5 mT (Fig. 6.5c). FORC diagrams show a single weak peak at the B_u/B_c axes origin which extends along the B_c axis, similar to Zone B3 (Fig. 6.5d). This suggests the magnetic mineralogy is controlled by a single high coercivity phase, indicated as hematite from the T-χ experiments (Figs. 6.5a & d).

6.4.4 Anisotropy of Magnetic Susceptibility

Results of anisotropy of magnetic susceptibility (AMS) are described at a sample-site scale from the undeformed granodiorite at the periphery of the fault zone towards the fault core (Fig. 6.6). The full datasets for AMS measurements are provided in the Supplementary Material.

6.4.4.1 Zone A: Unaltered Granodiorite

Mean susceptibility (*Kmean*) varies from 1.51 x 10^{-3} to 3.19 x 10^{-3} (mean = 2.26 x 10^{-3}), with corrected degree of anisotropy (*Pj*) of 1.057 to 1.090 (mean = 1.073) and shape (*T*) values of -0.587 to 0.709 (mean = 0.310) (Fig. 6.6). *Pj* and *T* show no relationship to *Kmean*, with core samples across Zone A measuring similar values of all three statistical parameters (Fig. 6.6b – d). *T* values suggest the dominance of triaxial to oblate fabrics, with only six core samples measuring a prolate fabric, and k_1 and k_2 axes observed forming a girdle plane (Fig. 6.6a). k_3 axes define a consistent sub-horizontal NW – SE aligned magnetic foliation within Zone A (average orientation = 134 16 NE) (Fig. 6.6a).

6.4.4.2 Zone B: Fault Damage Zone

Within Zone B1, *Kmean* ranges from 1.04 x 10^{-3} to 2.40 x 10^{-3} (mean = 1.87 x 10^{-3}) with *Pj* of 1.037 to 1.068 (mean = 1.056) and *T* of -0.058 to 0.468 (mean = 0.205) (Fig. 6.6). No relationship between *Pj* or *T* with changes in *Kmean* is observed, but a positive linear relationship between *Pj* and *T* is present (Fig. 6.6b – d). Oblate fabrics are measured in four of the six core samples within Zone B1, yet no girdling of the k_1 and k_2 axes observed (Fig. 6.6a). The magnetic fabric orientations across the subzone are more dispersed on a stereographic projection less consistent relative to the unaltered granodiorite subsamples, with k_3 and k_1 axes broadly defining a shallow to sub-horizontal NE – SW aligned magnetic foliation (average orientation = 079 19 E) and lineation (average orientation = 06→057), respectively (Fig. 6.6).

Zone B2 *Kmean* values vary from 0.67 x 10^{-3} to 4.11 x10^{-3} (mean = 2.41 x 10^{-3}), with *Pj* of 1.103 to 1.386 (mean = 1.211) and *T* of -0.563 to 0.905 (mean = 0.497) (Fig.

6.6). While no correlation is observed between changes in *Kmean* and *Pj*, a negative linear relationship is present between *T* and *Kmean* and a positive linear relationship to *Pj* (Fig. 6.6b – d). AMS measures a dominantly oblate fabric across the deformation band, with only three core samples producing a prolate fabric. k_1 and k_2 axes form a girdle plane, with k_3 defining a steeply dipping NE – SW magnetic foliation (average orientation = 042 62 W) (Fig. 6.6a). This magnetic foliation correlates with field measurements of the deformation band (Fig. 6.1b).

Across Zone B3, *Kmean* values range from 0.30 x 10^{-3} to 3.39 x 10^{-3} (mean = 1.85 x 10^{-3}), with *Pj* ranging from 1.028 to 1.184 (mean = 1.092) and *T* of -0.545 to 0.766 (mean = 0.121) (Fig. 6.6). No systematic pattern is observed between *Kmean* and *Pj* or *Pj* and *T*, but a negative linear relationship is observed between *T* and *Kmean* (Fig. 6.6b – d). A greater number of prolate core samples were measured in Zone B3 relative to the rest of the fault damage zone, with twenty of thirty-two cores showing triaxial to prolate *T* values. *Kmean* shows a bimodal distribution, with core samples of the altered fractures producing anomalously low values (0.30 x 10^{-3} to 0.975 x 10^{-3}) relative to the granodiorite they crosscut (1.49 x 10^{-3} to 3.339 x 10^{-3}). AMS measures a separate fabric within the granodiorite and the crosscutting altered (Fig. 6.6). Within both fabrics, k_1 axes show a strong clustering to define a NE – SW shallow plunging magnetic lineation (average orientation = 08→045) (Fig. 6.6a). k_3 axes in the altered fractures define a moderately to steeply dipping NE – SW trending magnetic foliation (average orientation = 046 70 W), correlating with field measurements of the fractures (Fig. 6.6a). In contrast, k_3 axes of the adjacent granodiorite define a W – E trending shallowly dipping magnetic foliation (average orientation = 090 22 N), similar to the Zone A magnetic fabric (Fig. 6.6a).

6.4.4.3 Zone C: Fault Core

Zone C1 *Kmean* varies from 0.21 x 10^{-3} to 1.10 x 10^{-3} (mean = 0.40 x 10^{-3}), with *Pj* of 1.009 to 1.141 (mean = 1.058) and *T* values of -0.175 to 0.761 (mean = 0.285) (Fig. 6.6). *Pj* and *T* show a positive linear relationship with *Kmean*, with a similar relationship also seen between *Pj* and *T* (Fig. 6.6b – d). *T* values are predominantly oblate, with only two core samples showing prolate *T* value; however, k_1 axes form a tight cluster, defining a NE – SW shallowing plunging lineation (average orientation = 03 →056). k_3 axes define a steeply dipping NE – SW foliation (average orientation = 067 66 E/W), dipping inwards from both sides towards the centre of the fault core, correlating with field measurements (Figs. 6.1b & 6.6a).

Within Zone C2, *Kmean* ranges from 0.17 x 10^{-3} to 0.49 x 10^{-3} (mean = 0.26 x 10^{-3}), *Pj* varies from 1.007 to 1.029 (mean = 1.015) and *T* values of -0.441 to 0.371 (Fig. 6.6). All core samples measure similar statistical parameter values, with no obvious relationship between them (Fig. 6.6b – d). Magnetic fabrics from AMS vary in orientation and inclination across the centre of the fault core, with the k_1 – k_3 defining girdles in their orientation (Fig. 6.6a). Generally, fabrics are steeper at the contacts with Zone C1, becoming shallower towards the centre of Zone C2. Within the girdles of the k1 and k_3 axes, broad clustering is observed, which defines a roughly NE – SW trending magnetic lineation and foliation across the centre of the fault core (Fig. 6.6a). This correlates with the field measurements of the fault core contacts.

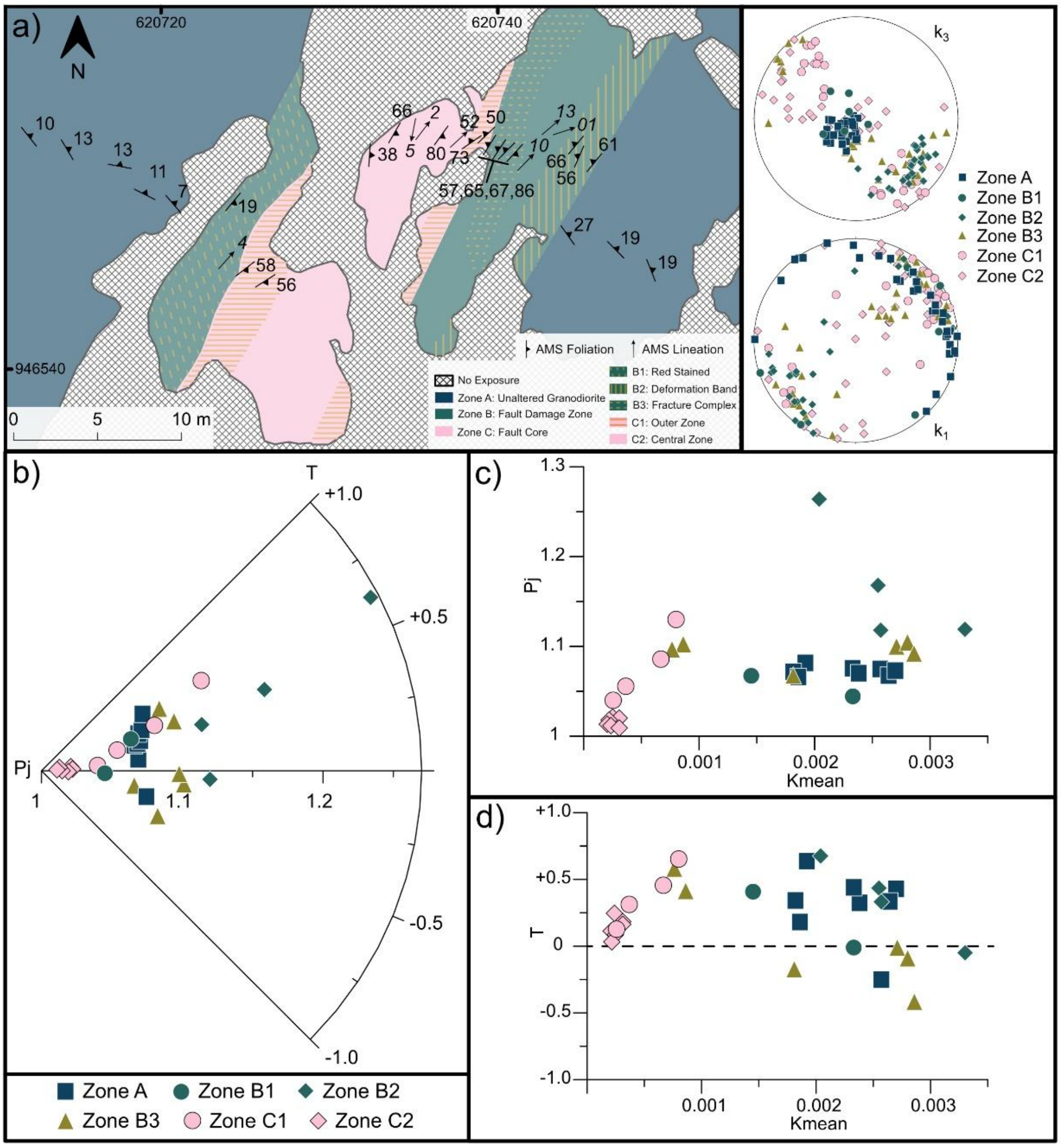

Figure 6.6 – (a) Map of the Currin Point Fault Zone showing results of anisotropy of magnetic susceptibility (AMS), with stereonets of the maximum (k_1) and minimum (k_3) susceptibility axes. (b) Polar plot of corrected degree of anisotropy (P_j) vs shape (T) from AMS sample sites across the Currin Point Fault Zone. (c) Plot of mean susceptibility (*Kmean*) vs P_j from AMS sample sites across the Currin Point Fault Zone. (d) Plot of *Kmean* vs T from AMS sample sites across the Currin Point Fault Zone.

6.4.5 Anisotropy of Magnetic Remanence

As with AMS, results of anisotropy of isothermal remanent magnetization (AIRM) and anisotropy of anhysteretic remanent magnetization (AARM) are described from the granodiorite at the periphery of the fault zone towards the fault core (Fig. 6.7). Full datasets for AIRM and AARM measurements are provided in the Supplementary Material.

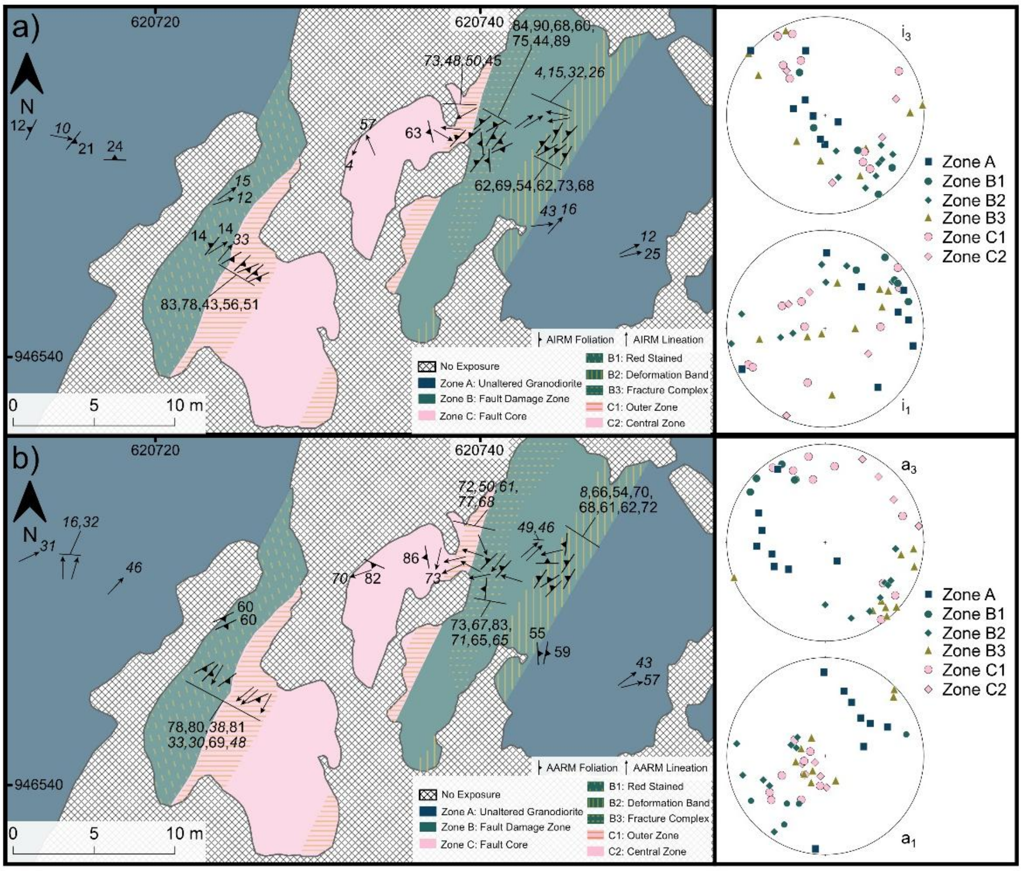

Figure 6.7 – (a) Map of the Currin Point Fault Zone showing results of anisotropy of isothermal remanent magnetization (AIRM), with stereonets of the maximum (i_1) and minimum (i_3) remanence axes. (b) Map of the Currin Point Fault Zone showing results of anisotropy of anhysteretic remanent magnetization (AARM), with stereonets of the maximum (a_1) and minimum (a_3) remanence axes.

6.4.5.1 Zone A: Unaltered Granodiorite

AIRM mean remanence (*Rmean*) values range from 0.35 x 10^{-4} to 1.67 x 10^{-4} (mean = 1.08 x 10^{-4}), with *Pj* values of 1.151 to 1.440 (mean = 1.293) and *T* values of -0.246 to 0.799 (mean = 0.071). Unlike AMS, the majority show triaxial to prolate *T* values and only three of the eight subsamples are oblate. i_1 shows a broad cluster, defining a shallow plunging magnetic lineation (average orientation =

18→069), with a similar cluster of i_3, defining a shallow dipping ENE – WSW trending foliation (average orientation = 164 18 E). The magnetic lineation and foliation defined by AIRM correlates with the orientation of the AMS fabric across Zone A, with the AIRM foliation strike within 20° and the foliation dip, lineation plunge and trend within ≤5° (Figs. 6.6a & 6.7a). AARM features a *Rmean* of 1.50 x 10^{-3} to 2.81 x 10^{-3} (mean = 2.12 x 10^{-3}), *Pj* of 1.057 to 1.186 (mean = 1.121) and *T* values of -0.768 to 0.712 (mean = -0.138). As with AIRM, *T* is predominantly prolate in the measured subsamples, with a_1 defining moderately plunging NE-trending magnetic lineations (average orientation = 38→036) (Fig. 6.7b). a_3 axes form a similar cluster to define a N – S trending moderately dipping foliation (average orientation 179 52 E) (Fig. 6.7b). AARM is consistent with the AMS fabric in orientation, but with a steeper inclination (Fig. 6.7b).

6.4.5.2 Zone B: Fault Damage Zone

In Zone B1, AIRM *Rmean* values of 0.37 x 10^{-4} to 1.12 x 10^{-4} (mean = 0.82 x 10^{-4}), *Pj* of 1.115 to 1.273 (mean = 1.166) and *T* values of -0.646 to 0.008 (mean = -0.356) are recorded. Only one measured subsample features an oblate *T* value, with the rest recording a prolate fabric and a strong girdling of i_2 and i_3 axes (Fig. 6.7a). i_1 axes define a NE – SW lineation (average orientation 12→055), trending within 5° of the magnetic lineation from AMS (Figs. 6.6a & 6.7a). AARM measures a *Rmean* range of 1.17 x 10^{-3} to 2.57 x 10^{-3} (mean = 1.95 x 10^{-3}), *Pj* of 1.091 to 1.220 (mean = 1.133) and *T* values of -0.573 to 0.529 (mean = 0.171). In contrast to AIRM, AARM fabrics are oblate except for one subsample, with a clustering of a_1 – a_3 axes (Fig. 6.7b). A moderately dipping magnetic lineation (average orientation = 25→222) and a steeply dipping NE – SW trending magnetic foliation (average orientation = 053 73 E) is observed (Fig. 6.7b). The foliation defined by AARM has a parallel strike to the AMS foliation, but with a much steeper dip, with the lineation plunging in the opposite direction to the AIRM.

AIRM measurements of Zone B2 have *Rmean* values of 1.40 x 10^{-4} to 7.20 x 10^{-4} (mean = 2.20 x 10^{-4}), *Pj* of 1.370 to 3.994 (mean = 2.332) and *T* values -0.224 to 0.881 (mean = 0.438). AIRM ellipsoids are predominantly oblate within Zone B2 with a girdling of i_1 and i_2 axes (Fig. 6.7a). AIRM defines a steeply dipping NE – SW trending magnetic foliation, correlating with the fabric from AMS (Figs. 6.6a & 6.7a). AARM measures *Rmean* values of 2.02×10^{-3} to 4.67×10^{-3} (mean = 3.22×10^{-3}), *Pj* values of 1.141 to 1.595 (mean = 1.334) and *T* values -0.051 to 0.917 (mean = 0.657). As with AIRM and AMS, oblate ellipsoids are dominant from AARM, with a_1 and a_2 forming a girdle plane (Fig. 6.7b). AARM measures a NE – SW trending steeply dipping magnetic foliation (average orientation 046 65 W), correlating with the foliation from AIRM and AMS (Fig. 6.7a – b).

In Zone B3, AIRM *Rmean* values range from 0.06×10^{-4} to 1.81×10^{-4} (mean = 0.92×10^{-4}), *Pj* of 1.240 to 1.691 (mean = 1.390) and *T* range of -0.421 to 0.711 (mean = 0.224). *T* values are oblate in seven of nine subsamples, with the two prolate fabrics from the granodiorite furthest away from the hydrothermally altered fractures (Fig. 6.7a). These subsamples produce a shallow-dipping NE-trending lineation (average orientation = 29→056), subparallel to the lineation measured with AMS (Figs. 6.6a & 6.7a). The remaining subsamples, taken within and adjacent to the hydrothermally altered fractures, record a girdle plane of i_1 and i_2 axes to define a NE–SW trending steeply dipping foliation (average orientation = 032 84 W). This magnetic foliation correlates with the foliation from AMS and field measurements (Figs 6.6a & 6.7a). AARM measures *Rmean* values of 0.66×10^{-3} to 2.91×10^{-3} (mean = 1.70×10^{-3}), *Pj* of 1.124 to 1.295 (mean = 1.199), and *T* of -0.675 to 0.552 (mean = -0.174).

In contrast to AIRM data, in Zone B3 AARM measures an oblate fabric in only three subsamples, with subsamples of the hydrothermally altered fractures measuring a different fabric to the adjacent granodiorite (Fig. 6.7b). Within this adjacent granodiorite, a sub-horizontal lineation is observed (average orientation = 06→047) which correlates with the magnetic lineation measured from AMS (Figs. 6.6a & 6.7b). The remaining subsamples show a tight clustering to the $a_1 – a_3$ axes, defining a steeply dipping NE – SW foliation (average orientation = 026 80 W) and steep plunging SW trending lineation (average orientation = 75→246) (Fig. 6.7b). The foliation of AARM correlates with AIRM and AMS, with the magnetic lineation trending subparallel to the lineation from AARM measurements in Zone B1 (Fig. 6.7a – b).

6.4.5.3 Zone C: Fault Core

In Zone C1, AIRM *Rmean* ranges from 0.02×10^{-4} to 0.82×10^{-4} (mean = 0.03×10^{-4}), *Pj* of 1.235 to 1.874 (mean = 1.381) and *T* values of -0.070 to 0.515 (mean = 0.160). i_1 and i_2 axes are observed girdling along a plane to define a NE – SW trending foliation, dipping steeply towards the centre of the fault core (average orientation = 059 59 E & 044 56 W) (Fig. 6.7a). This magnetic foliation correlates to the AMS and field-measured foliation within the outer fault core (Figs. 6.6a & 6.7a). AARM measures *Rmean* values 0.23×10^{-3} to 4.22×10^{-3} (mean = 1.29×10^{-3}), *Pj* of 1.063 to 1.217 (mean = 1.144) and *T* of -0.596 to 0.739 (mean = -0.147).

Unlike AIRM data, Zone C1 AARM measurements are predominantly prolate, with a girdling of a_2 and a_3 axes (Fig. 6.7b). a_1 axes define a steeply plunging SW trending lineation (average orientation = 63→237), sub-parallel to the AARM lineation in Zone B1 and Zone B3 (Fig. 6.7b).

In Zone C2, AIRM *Rmean* ranges from 0.01×10^{-4} to 0.09×10^{-4} (mean = 0.04×10^{-4}), *Pj* of 1.097 to 1.329 (mean = 1.189) and *T* of -0.542 to 0.666 (mean = -0.118). Similar to AMS, fabrics from AIRM measurements show no obvious trend, with an apparent random orientation to lineations and foliations across the centre of the fault core (Fig. 6.7a). for AARM, *Rmean* ranges from 0.07×10^{-3} to 0.69×10^{-3} (mean = 0.44×10^{-3}), *Pj* of 1.083 to 1.148 (mean = 1.105) and *T* values -0.736 to 0.727 (mean = 0.147). While half of the measured subsamples record oblate *T* values, a_2 and a_3 axes form a tight girdle plane, with a_1 defining a steeply dipping SW-trending lineation (average orientation = 77→207) (Fig. 6.7b). This lineation is subparallel to the other lineations measured from AARM within the fault damage zone adjacent to, and within the fault core (Fig. 6.7b).

6.5 Discussion

Our data reveal a systematic relationship between the type and intensity of hydrothermal alteration and variations in the shape, orientation, and strength of magnetic fabrics across the Currin Point Fault Zone. Field observations define three distinct alteration zones: the peripheral unaltered granodiorite (Zone A), a 4–7 m wide damage zone (Zone B), and a 15 m wide fault core (Zone C). These zones are characterized by a consistent distribution of hydrothermal alteration, supported by integrated field, hyperspectral, and magnetic data. Variations in magnetic fabric parameters correspond with the style of hydrothermal alteration, suggesting that contrasting magnetic fabrics may record the interplay of magmatic, tectonic, and hydrothermal processes. Here, we evaluate our data to constrain the nature of alteration across the fault zone and its relationship to the strain record, to assess the threshold at which hydrothermal alteration intensity overprints petrofabrics and the significance of magnetic fabrics in hydrothermally altered rocks.

6.5.1 A Quantitative Approach to Characterising Hydrothermal Alteration

6.5.1.1 Zone A: Unaltered Granodiorite

Field mapping and thin section petrography define Zone A as minimally deformed, with only minor alteration textures observed (Figs. 6.2a & 6.3b – c). Hyperspectral data corroborate with this qualitative evaluation, indicating that white mica is the dominant hydrous phase with a minor contribution from epidote and chlorite (Fig. 6.4). These data correlate well with observed alteration of feldspars into micaceous material in thin sections and the presence chlorite and epidote as accessory minerals, with variation in white mica content across Zone A indicating variable feldspar alteration (Figs. 6.3a & 6.4). Magnetic characterization experiments highlight multidomain, low-Ti titanomagnetite as the primary iron oxide phase, with T-χ experiments detecting a minor contribution from maghemite (Fig. 6.5). While the presence of maghemite indicates minor hydrothermal alteration is present, we attribute this to subtle oxidation during late-stage cooling interactions with deuteric fluids, which is common in plutonic rocks, rather than pervasive hydrothermal overprinting (Petronis et al., 2012; Tomek et al., 2015; Sant'Ovaia et al., 2024). This makes the granodiorite in Zone A altered *sensu stricto*, but with the mineral assemblage unmodified from fault zone fluid processes. Therefore, the unaltered granodiorite samples are taken as a background signature to compare hydrothermal alteration distribution across the other zones. Similarly, these data suggest that the magnetic fabrics of Zone A archive magmatic processes unrelated to the fault zone activity (Latimer et al., 2025).

6.5.1.2 Zone B: Alteration in the Fault Damage Zone

Zone B is characterized as the fault damage zone, with field mapping demonstrating a systematic distribution of hydrothermal alteration associated with fault zone structures (Fig. 6.2b – d).

In Zone B1, the western damage zone, red-stained granodiorite occurs immediately adjacent to Zone C, indicating permeation of hydrothermal fluids from the fault core into the unaltered granodiorite of Zone A. This is supported by the rise in D2250, reflecting an increased chlorite and epidote signature relative to Zone A, with a decline in D2200 indicating a decrease in relative white mica abundance (Fig. 6.4). Hematite was detected in Zone B1 and is expected to contribute to the magnetic fabrics alongside low-Ti magnetite that is also detected in this zone (Fig. 6.5). Importantly, hematite is not detected in the unaltered granodiorite, with this mineral known to be a product of hydrothermal alteration in granitic intrusions (Nédélec et al., 2015). We therefore attribute the occurrence of hematite, and its associated fabric, to fault zone hydrothermal alteration processes.

On the eastern side of the damage zone, the intensity of hydrothermal alteration fluctuates between intense alteration within the deformation band and altered fractures of Zone B2 and Zone B3, and the relatively unaltered granodiorite they crosscut. Hyperspectral and magnetic data from the relatively fresh granodiorite replicate data from Zone A, with white mica and low-Ti titanomagnetite as dominant hydrous and iron oxide phases with minor contributions from chlorite, epidote and maghemite, suggesting minimal alteration (Figs. 6.4 & 6.5).

In Zone B2, hyperspectral data from the deformation band shows a marked increase in D2250 reflecting an increase chlorite and epidote alongside a decline in D2200 indicative of a weaker white mica signature relative to Zone A (Fig. 6.4). Magnetic coercivity data and a dip in mean magnetic susceptibility (*Kmean*) show a relative decrease in Low-Ti titanomagnetite and increase in hematite, relative to Zone A and B1(Fig. 6.5a & d). The greater contribution of high coercivity phases suggests further removal of low coercivity iron oxides and more substantial growth of hydrothermal hematite, supporting the increase in alteration intensity seen from hyperspectral data.

Alteration haloes around fractures in Zone B3 carry an extremely weak D2200 reflectance profile, indicating a relatively low abundance or absence of white mica (Fig. 6.4). This occurs in step with an abrupt decrease in magnetic susceptibility and an abrupt increase in magnetic coercivity. These data reflect the removal of magnetite from the system and the growth of new hydrothermal hematite as the dominant iron oxide phase (Fig. 6.5).

6.5.1.3 Zone C: Alteration in the Fault Core

Zone C represents the fault core, a 15m wide area of pervasive hydrothermal alteration and deformation (Fig. 6.2e – f). Zone C1, the outer zone of the fault core, is defined by the development of a sub-vertical foliation, with cataclastic bands formed parallel to the rock fabric (Fig. 6.3g), while Zone C2, the centre of the core, is fully cataclastised (Fig. 6.3h).

Zone C1 is characterized by low-Ti titanomagnetite as the primary iron oxide phase, with hematite as a secondary phase (Fig. 6.5), and a strong D2250 absorption feature indicating elevated chlorite and epidote abundance compared to Zone A and Zone B (Fig. 6.4). A weak to zero D2200 response suggests that white mica is present as a minor to trace hydrous phase only (Fig. 6.4). These data demonstrate that the intensity of alteration in Zone C1 is distinct and more intense than in Zone B1 and Zone B2, and we expect the magnetic fabrics from this zone to be dominated by the new hydrothermal iron oxide phases.

In Zone C2, the D2250 absorption feature indicates epidote and chlorite reach their highest relative abundances within the Currin Point Fault Zone (Fig. 6.4). Further reduction of magnetic susceptibility relative to Zone C1, with the dominance of hematite as the high magnetic coercivity phase suggests the removal of low-Ti titanomagnetite during alteration, with hematite becoming the primary iron oxide phase that is expected to significantly contribute to magnetic fabric analysis (Fig. 6.5). The mineral assemblage is similar to the altered fractures of Zone B3 however, the elevated chlorite and epidote absorption feature, and lower iron oxide content, suggests a greater alteration intensity within Zone C2 (Figs. 6.4 & 6.5).

6.5.2 Formation and Destruction of Magnetic Fabrics in Hydrothermally Altered Rocks

Magnetic fabric data are routinely used within igneous intrusions to test competing models of magma emplacement (e.g., Siegesmund & Becker, 2000; Stevenson et al., 2007), tectonic processes (e.g., Petronis et al., 2012; McCarthy et al., 2015b; Burton-Johnson et al., 2019) and fluid migration pathways (Köpping et al., 2023; Jones et al., 2025a; Williams et al., 2025). Whilst the AMS tensor measures the combined alignment of ferromagnetic and paramagnetic minerals, AIRM is only sensitive to the alignment of low coercivity ferromagnetic minerals, with high coercivity mineral alignment measured through AARM (Borradaile & Jackson, 2010). The AMS tensor can thus be deconvoluted to identify the presence of sub fabrics through its comparison with AIRM and AARM. However, magnetic fabric data are represented by an ellipsoid that has only a size, shape and orientation; these data do not carry information on the process that caused the fabric to form. Petrographic, microstructural and mineralogical information is required to contextualize magnetic data in order to arrive at a robust, meaningful interpretation (e.g., Mattsson et al., 2021; Koopmans et al., 2022; Latimer et al., 2024).

It is well established that granitoid intrusions contain a strain archive that may reflect processes such as ascent, emplacement and tectonic deformation (Bouchez, 1997). It follows that hydrothermal alteration will act to rearrange the magnetic mineralogy to produce overprinted, intermediate AMS tensors with increasing alteration intensity (Ferré et al., 1999; Nédélec et al., 2015). Just et al. (2004) demonstrate the progressive destruction of magmatic state magma flow fabrics may occur in step with hydrothermal alteration, resulting in the obliteration of the original AMS fabrics. However, Petronis et al. (2011) demonstrate that hydrothermal alteration can coarsen protolith iron oxide phases, changing the properties of magnetic fabrics within altered regions of an intrusion to the extent that they could be interpreted as a separate intrusive unit without sufficient field context to complement the magnetic data. Alternatively, when contextualized with stratigraphic logs, CPO and EPMA data, AMS and AMR are reported to detect postcumulus hydrothermal fluid migration pathways through magma modal layers in some of the world's largest REE deposits (O'Driscoll et al., 2024; Jones et al., 2025a, 2025b). However, recent work by Quintela et al. (2025) highlights the challenge of extracting primary magma emplacement fabrics from extensively altered sub-volcanic granitoid intrusions, highlighting the need for a robust alteration characterization to underpin AMS data interpretations.

Across the Currin Point Fault Zone, our combined petrographic, hyperspectral and magnetic data delineate zones where the magnetic mineralogy, and by extension the magnetic fabric record, is disrupted by alteration. Below, we compare these mineralogical data with AMS, AARM and AIRM data to assess how primary and secondary fabrics are preserved, destroyed and created across the study area with a view to confidently ascribe different magnetic fabrics to successive magmatic, tectonic and hydrothermal processes. In doing so, we establish a threshold of alteration intensity, from which the significance of magnetic fabrics from hydrothermally altered rocks can be determined.

6.5.2.1 Zone A: Magmatic Petrofabric Formation

In Zone A, the unaltered granodiorite, magnetic fabrics from AMS, AIRM and AARM consistently define a sub-horizontal NW – SE fabric (Fig. 6.8). The characterized alteration mineral assemblage and textural properties suggest no alteration from the fault zone, with petrofabric development relating to magmatic processes, rather than tectonic strain (Figs. 6.4 & 6.5). The measured petrofabric correlates with AMS fabrics recorded across Currin Point and is interpreted as lateral magma transport fabrics associated with the construction of the Fanad Pluton (Latimer et al., 2025).

6.5.2.2 Zone C: Tectonic Petrofabric Formation and Destruction

Zone C, the fault core, is marked by extensive hydrothermal alteration and deformation, with alteration intensity and cataclasis increasing from the outer zone (Zone C1) towards the centre of the core (Zone C2) (Figs. 6.3 – 6.5). AMS and AIRM fabrics in Zone C1 are coaxial, defining a steep NE – SW fabric parallel to the field measured foliation (Fig. 6.8). Ductile deformation textures such as deformation twinning and subgrain development in quartz suggest rotation of bulk mineral alignment to the trend of the fault zone is indicative of tectonic strain overprinting the previous magmatic fabric measured in Zone A (Figs. 6.3g & 6.8). The coaxial nature of AIRM to AMS indicates alignment of low coercivity iron oxides and the bulk mineral fabric, identified from magnetic characterization as low-Ti titanomagnetite (Figs. 6.5 & 6.8). In Zone C2, neither AMS nor AIRM measure a consistent fabric, varying in trend and inclination (Fig. 6.8). The dispersion of magnetic fabrics is consistent with the pervasive cataclasis of the fault core, not forming the tectonic petrofabric observed at Zone C1 (Fig. 6.3h).

6.5.2.3 Zone B: Successive Petrofabric Formation and Destruction

Zone B provides interesting results in that AMS and AIRM fabrics differ across zones B1, B2 and B3.

Within Zone B1, the red strained granodiorite, AMS and AIRM measure a sub-horizontal fabric, that is parallel to fabrics observed in Zone A, although we note a broader distribution of principal axes (Fig. 6.8). The alteration mineral assemblage is indicative of very low intensity alteration, defined by a decrease in *Kmean* relative to the unaltered granodiorite with the removal of low coercivity titanomagnetite and the growth of hematite (Figs. 6.4 & 6.5). AMS and AIRM fabrics defined by bulk mineral alignment and alignment of low-Ti titanomagnetite are parallel to Zone A fabrics, measuring the same magmatic process, but with a subtle scattering of principal axes (Fig. 6.8). This scattering reflects the residual nature to both AMS and AIRM fabrics in Zone B1, with the precursor magmatic fabric being partially overprinted by new hydrothermal mineral growth at low alteration intensities.

Zone B3 and the deformation band in Zone B2 return coaxial AMS and AIRM magnetic fabrics with a NE – SW foliation, parallel to the trend of the observed fault structures (Fig. 6.8). The characterized mineral assemblages of both structures indicate high alteration intensity, with varying degrees of destruction to low coercivity iron oxides and their partial or complete replacement by newly formed hematite (Fig. 6.5). Therefore, similar to Zone C1, the AMS and AIRM fabrics detect tectonic strain overprinting the precursor magmatic state fabric. We note that AIRM axes are more dispersed in samples collected along fractures in Zone B3, where the relative abundance of residual titanomagnetite is at its lowest, shown by an abrupt decrease in *Kmean* (Fig. 6.8).

6.5.2.4 AARM Fabrics in the Damage Zone and Fault Core: A Fabric of Hydrothermal Fluid Transport?

AARM data from Zone B and C consistently return a sub-vertical lineation that plunges to the SW (Fig. 6.8). AARM detects the alignment of higher coercivity, ferromagnetic minerals only, with hematite shown to occur in samples with these steeply inclined fabrics (Fig. 6.5). Furthermore, these AARM fabrics are highly oblique to AMS and AIRM results, suggesting that it is not caused by tectonic or magmatic processes (Fig. 6.8). We consider three main processes that may explain the AARM lineation: 1) martitisation of iron oxides already present within the fault zone (Just and Kontny, 2012; Nédélec et al., 2015); 2) exsolution within altered silicate phases (Petronis et al., 2011; Ageeva et al., 2022); or 3) precipitation along fluid transport pathways (Jones et al., 2025a; Williams et al., 2025).

While it is difficult to unequivocally correlate the measured fabric to one process, we note that the subvertical AARM lineation is highly oblique to AMS and AIRM fabrics (Fig. 6.8). If the AARM fabric was related to hematite formed as a product of martitisation or exsolved within silicates, we would expect a systematic correlation to the other magnetic fabrics, with hematite alignment controlled by the crystallographic orientation of the phases they exsolve from or replace (Just et al., 2004; Ageeva et al., 2022). We would also expect the AARM fabric anisotropy to decrease and disappear within the centre of the fault core, as seen in AMS and AIRM fabric, where cataclasis obliterates any previous rock texture (Fig. 6.8).

The strength and consistent trend of the AARM fabric lineation suggest it must relate to a process active in both the damage zone and core of the fault zone. Based on our alteration characterization, and the absence of this distinctive AARM lineation within Zone A, the unaltered granodiorite, we tentatively interpret the sub-vertical AARM fabric to reflect the migration of fluids associated with hydrothermal alteration. This suggests the measured alignment of hematite reflects a petrofabric of hydrothermal fluid transport, with the subtle variation in plunge and trend interpreted to reflect the exploitation of different fluid pathways by migrating fluids as they permeated around clasts in the fault zone.

Fluid transport pathways within fault zones vary as processes of fluid-rock interaction and deformation alter the permeability of the surrounding host rock and the fault structure itself (Caine et al., 1996). In the Currin Point Fault Zone, we demonstrate that cataclasis of the fault core correlates to the highest relative abundance of chlorite and epidote, indicative of a lock-up in fault core displacement as hydrous silicates and iron oxides derived from hydrothermal fluids infilled the cataclastite (Bense et al., 2013). This lock-up causes the core to become a barrier to fluid migration and strain accommodation, partitioning strain along planes of weakness in the adjacent granodiorite, causing formation and expansion of the damage zone (Caine et al., 1996; Faulkner et al., 2010). This suggests that the deformation band and fractures of Zone B reflect structures formed and activated as fluid corridors after lock-up of the fault core, supported by the elevated alteration intensity along these structures relative to the rest of the fault damage zone (Figs. 6.4 – 6.5).

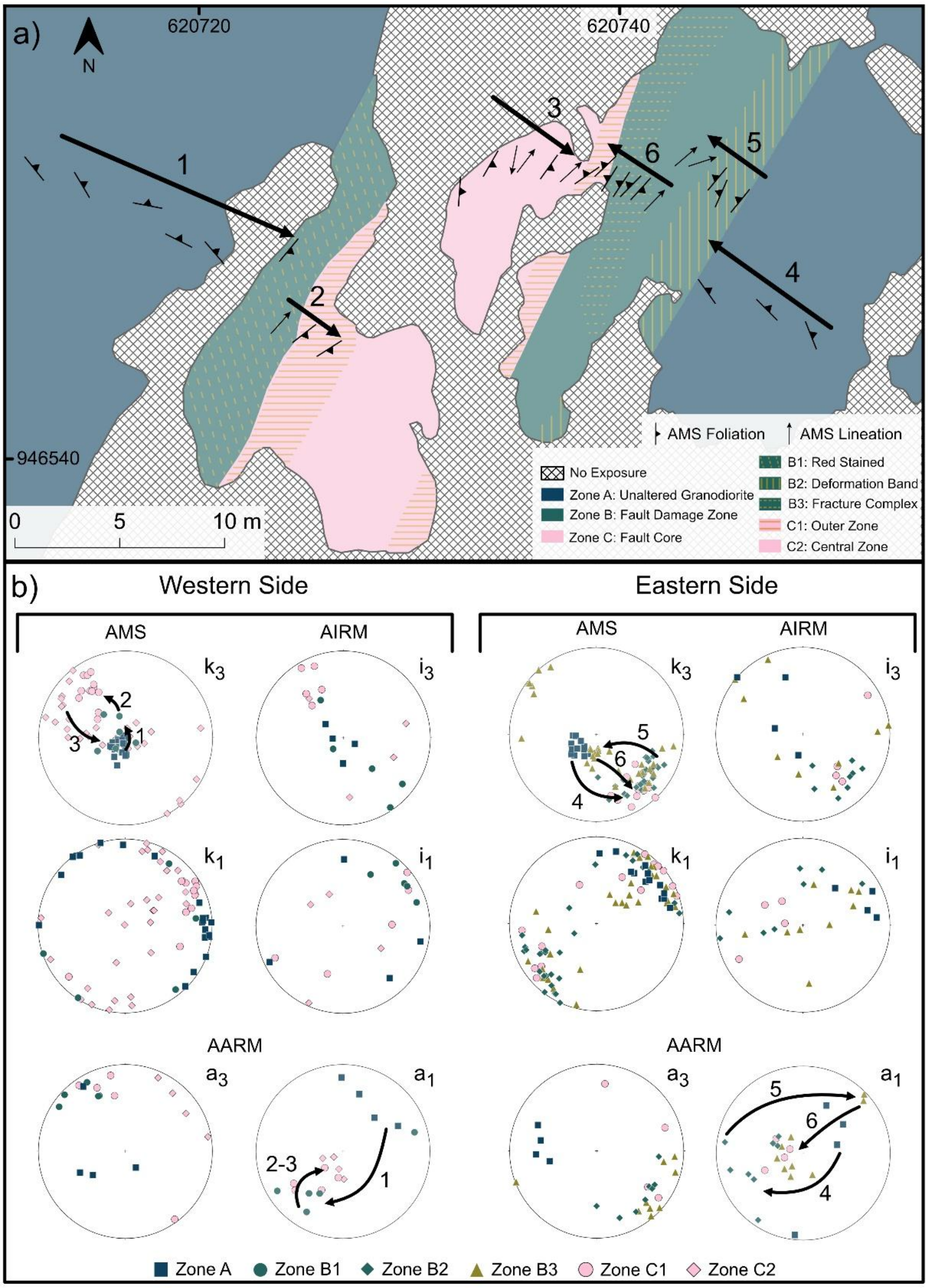

Figure 6.8 – (a) Map of the Currin Point Fault Zone showing results of anisotropy of magnetic susceptibility (AMS) with numbered transitions in fabric moving inwards towards the fault core. (b) Stereonets of AMS k_1 and k_3 axes, anisotropy of isothermal remanent magnetization (AIRM) i_1 and i_3 axes and anisotropy of anhysteretic remanent magnetization (AARM) a_1 and a_3 axes for the western and eastern sides of the fault zone with the numbered transitions in AMS fabric labelled.

6.6 Conclusions

This study establishes a systematic approach to determining the significance of magnetic fabrics within hydrothermally altered rocks, to identify a threshold at which alteration intensity overprints precursor magmatic and tectonic petrofabrics.

Our combined hyperspectral and magnetic approach facilitates the delineation of alteration zones based on the appearance and removal of oxide and hydrous silicate mineral phases from the system. We note that changes to AMS, AIRM and AARM fabrics occur in step with changes in oxide and hydrous silicate mineralogy and conclude that magnetic fabric data can be reliably attributed to magmatic, tectonic and hydrothermal alteration processes when the mineral alteration assemblage is well constrained. In the case of this study, the onset of hydrothermal alteration is identified from a subtle removal of white mica and low coercivity iron oxides (titanomagnetite) and the growth of new, high coercivity iron oxides (hematite) alongside chlorite and epidote. AMS and AIRM fabrics demonstrate a partial breakdown of magmatic petrofabrics at the onset of this hydrothermal alteration, causing a subtle scattering to fabrics (Fig. 6.9). As alteration intensity increases, we observe the complete destruction of tectonic and magmatic fabrics as magnetic susceptibility abruptly drops, coinciding with the removal of titanomagnetite, white mica and the predominance of hematite, epidote and chlorite in the system. We therefore conclude that key indicators such as changes in D2200, D2250, increasing coercivity, and abrupt decreases in magnetic susceptibility, indicate a reduced confidence that magnetic fabrics reliably reflect magmatic and tectonic processes, and instead are more likely influenced by hydrothermal alteration.

Importantly, we find that more subtle petrofabrics (i.e. those with a low total degree of anisotropy) are more readily overprinted by hydrothermal alteration than those with a higher degree of anisotropy. This indicates that the alteration intensity threshold above which pre-existing fabrics are obliterated depends on fabric strength. In this study, we found that magmatic fabrics consistently exhibited a low degree of anisotropy ($P_j < 1.100$), within the same range reported in many studies of magma flow fabrics (e.g., Stevenson et al., 2007a; Stevenson and Grove, 2018; Burchardt et al., 2019). We emphasize that robust characterisation of hydrothermal alteration mineral assemblages is essential when using AMS to measure subtle fabrics in altered rocks, before attributing them to magma transport, tectonic, or hydrothermal processes. The data and analysis provided here above may provide a useful benchmark in addressing this challenge.

We demonstrate the presence of a consistent AARM rock fabric that occurs only in hydrothermally altered samples and is defined by minerals that formed during hydrothermal alteration. Here, we interpret this petrofabric to be a product of hydrothermal fluid transport. Further work is required to better understand the origin of fabric in hydrothermally altered rocks, and their significance to the broader hydrothermal system. We highlight that this methodology could be utilized in the tracing of fluids associated with ore-forming and hydrothermal processes.

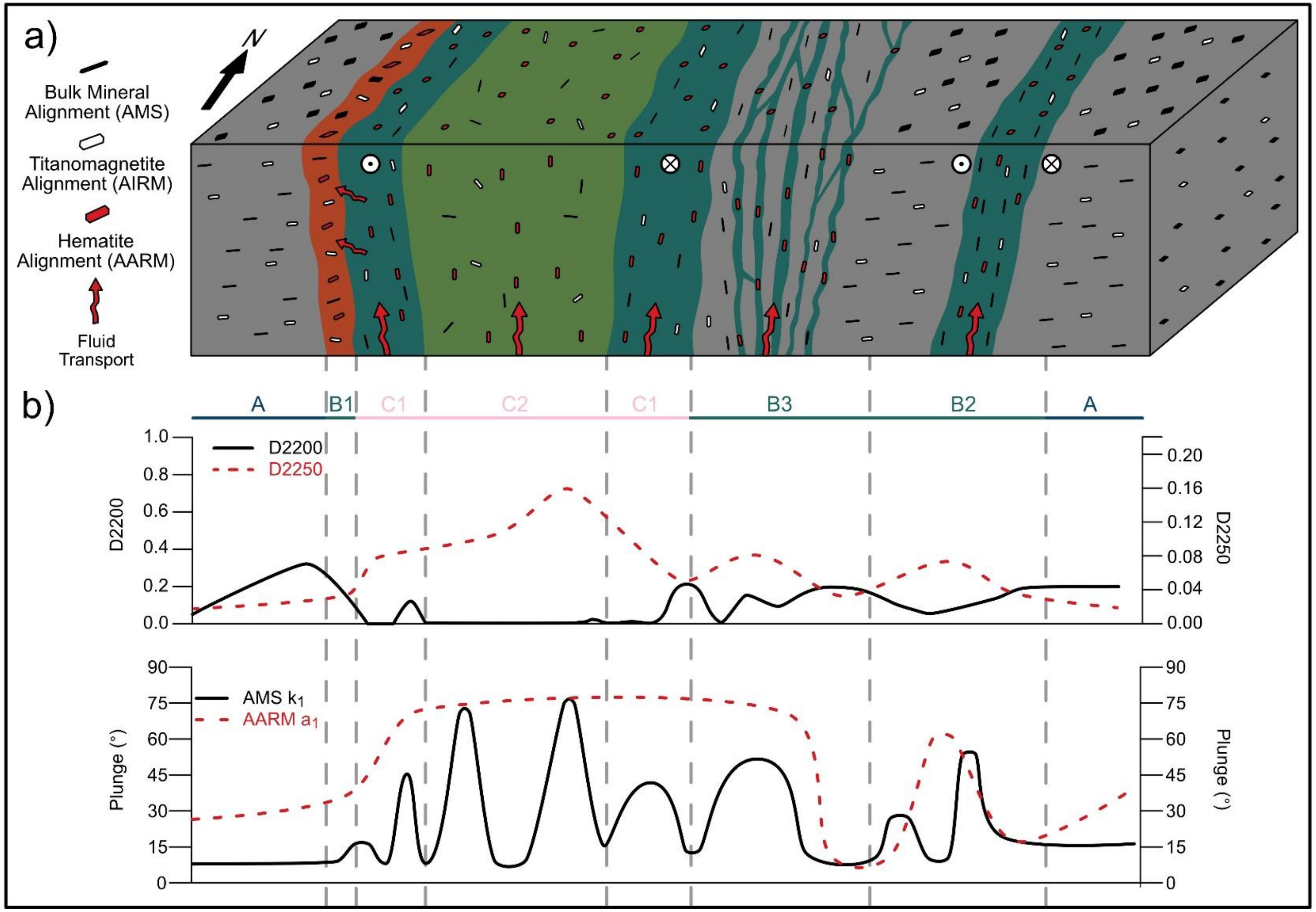

Figure 6.9 – (a) Schematic of mineral alignment across the Currin Point Fault Zone and the interpreted petrofabric of hydrothermal fluid transport from anisotropy of anhysteretic remanent magnetization (AARM). (b) Corresponding changes from D2200, D2250 and the plunge of lineations defined by the k_1 axes of AMS and a_1 axes of AARM.

Chapter 7: Synthesis

7.1 Introduction

The results from the data chapters are now synthesised, highlighting three significant advancements to our understanding of archives of internal and external stress regimes within igneous intrusions. The potential directions of future work are then explored which can supplement the current research and develop them further.

7.2 Implications of Current Work

7.2.1 Determining the Origin of Magmatic Fabrics

The first data chapter of this thesis (Chapter 4) investigates the significance of internal enclave petrofabrics relative to their morphological properties and to establish if these internal fabrics can provide insight into the palaeostress responsible for magmatic fabrics within the wider igneous intrusion.

The results of the chapter demonstrate the potential for enclaves to archive multiple internal fabrics, providing a unique insight into wider petrofabric development within the Fanad Pluton. Enclaves within the magma mingling zone at Ballyhoorisky Point are shown to develop a precursor magmatic fabric related to strain from their transport through the intrusion, with this fabric subsequently overprinted whilst in a mush-state by tectonic stress derived from the adjacent Melmore Shear Zone. This precursor fabric was only observed after comparison of multiple magnetic fabrics (AMS, AIRM and AARM) and CPO data from enclaves whose long-axis alignment was both parallel and oblique to the magmatic fabric within the host intrusion. The data definitively demonstrate that the magmatic petrofabric within the host intrusion is a tectonic overprint, recording external palaeostress rather than stress from an internal magmatic process. Resolving the origin of the magmatic fabric would ultimately not be possible from analysis of the host intrusion alone, with the rheological contrast between the enclaves and the surrounding host intrusion allowing enclaves to preserve and lock in fabrics due to their fast-cooling rate.

The results of this chapter ultimately call into question the interpretation of magmatic fabrics as an archive of internal stress, without a proper assessment of their origin by comparing fabrics of coevally formed but compositionally contrasting magmas. It also highlights the unique archive of strain which can be identified within a single intrapluton feature, provided multiple techniques of petrofabric measurement are compared. In this case, magnetic fabrics and CPO data were compared; however, integration of alternative data types such as shape preferred orientation (SPO) and X-ray computed tomography (XCT) may also give valuable insight.

7.2.2 The Sensitivity of Intrusions to Successive Strain Events

Chapter 5 aims to investigate the sensitivity of a single pluton to multiple, successive palaeostress regimes throughout its crystallisation, providing a record of multiple magmatic and/or tectonic processes.

The results of the chapter demonstrate that by comparing strain archived within magmatic, submagmatic and subsolidus features, a highly sensitive and temporal record of strain can be identified. The Currin Point area of the Fanad Pluton is shown to feature structures which record strain from internal magma chamber processes and from external tectonic stress. Through a combination of UAV imagery, field mapping and measurement of rock magnetic fabrics, crosscutting relationships between structures are established and used to provide a relative temporal archive of strain within the intrusion. Three phases of strain are identified, recording an initial phase from internal magmatic strain, the onset of regional tectonic deformation and its subsequent rotation in shortening direction from NNE – SSW to NE – SW. The archive of strain at Currin Point was then contextualised with available geochronology data and the results from Chapter 4, defining a temporal record of strain across the Fanad Pluton, with the onset of tectonic strain at *ca.* 416 Ma and its rotation at *ca.* 411 Ma.

When compared to the Donegal Batholith, an archive of tectonic stress is recorded throughout crystallisation of the Fanad Pluton, preserved in magmatic and submagmatic features, with similar records reportedly absent in other intrusions of the DIC. However, when data from the Fanad Pluton is integrated with data from the rest of the DIC and other late Caledonian igneous complexes in Ireland and the UK, a collective archive of strain is observed which supports kinematic models favouring transcurrent stress at the end of the Caledonian Orogeny. The detailed analysis of the Fanad Pluton provides the first study to detect the transition from sinistral transpression to sinistral transtension within the strain archive of a single intrusion.

The results of Chapter 5 highlight that the strain archive of igneous intrusions may be more sensitive than previously appreciated. A key aspect of this sensitivity is the integration of records of strain from features formed at different rheological settings. In particular, the ability to link strain preserved in submagmatic features to the record from subsolidus features unlocks a record of strain which is often excluded.

7.2.3 Does Hydrothermal Alteration Destroy Strain Archives

Chapter 6 aims to provide a framework of analysis to detect the threshold of alteration intensity at which magnetic fabrics from hydrothermally altered rocks are no longer meaningful in understanding petrofabric development in response to precursor magmatic and/or tectonic processes.

Across the Currin Point Fault Zone, the multi-disciplinary approach of combining hyperspectral and rock magnetic characterisation systematically delineates the distribution of hydrothermal alteration based on changes in hydrous silicate and iron oxide phases. Changes in alteration intensity are characterised quantitatively based on the removal of low coercivity iron oxides (in this case titanomagnetite) and white mica, being replaced by high coercivity iron oxides (hematite), epidote and chlorite.

Multiple magnetic fabrics were then measured (AMS, AIRM and AARM), with changes in magnetic fabric identified in response to magmatic, tectonic and hydrothermal processes. From AMS and AIRM fabrics, a general trend is observed of pre-existing petrofabrics becoming progressively destroyed as alteration intensity increases. It is noted that while partial destruction of low degree of anisotropy (i.e. low strength) fabrics occurs from the onset of hydrothermal alteration, fabrics with higher degrees of anisotropy (i.e. high strength) are preserved at much higher alteration intensities. In contrast to AMS and AIRM, AARM detects a separate subfabric within hydrothermally altered samples, appearing to reflect a petrofabric of hydrothermal fluid transport.

The results of this chapter extract two key points on the significance of magnetic fabrics measured from hydrothermally altered rocks. Firstly, high coercivity iron oxides, chlorite and epidote are identified as diagnostic of hydrothermal alteration within igneous intrusions, with changes in their relative abundance to low coercivity iron oxides and white mica used to indicate changes in alteration intensity. The presence of these phases in first pass observations can therefore be used as a first pass indicator that any magnetic fabrics should be interpreted cautiously until a full characterisation can be carried out. Secondly, magnetic fabrics within hydrothermally altered rocks are shown to have the potential to retain significant records of strain from processes active prior to alteration when below a threshold of alteration intensity. However, it is noted that this threshold varies with overall fabric strength, likely being much lower when precursor fabrics have low degrees of anisotropy. It is therefore important that when investigating petrofabric development in response to a process which routinely forms low strength fabrics, such as magmatic flow, that a robust characterisation is carried out on altered samples before asserting an origin to their formation.

7.3 Future Directions

7.3.1 Refining the Role of Magma Composition on Enclave Strain Archives

A key aspect of Chapter 4 is the presence of a rheology contrast between the enclaves and their surrounding host intrusion, allowing for multiple fabrics to be preserved within the enclaves. This develops as a function of the compositional difference between the magma of the enclaves and the host intrusion, with the more mafic enclaves crystallising at a faster rate than the more felsic host intrusion. In the Fanad Pluton, the enclaves are dioritic in composition, while the host intrusion ranges from a quartz monzodiorite to a granodiorite. While making the enclaves more mafic, both magmas are fundamentally intermediate in composition, meaning their rheological state was likely similar for long periods of time.

A potential direction of future work from Chapter 4 is to constrain the role of magma composition, and therefore rheology contrast, on strain archives within enclaves. For example, if enclaves are more mafic in composition or injected to a highly silicic host magma, is the ability of enclaves to archive multiple internal fabrics restricted relative to intrusions where both magmas are of relatively similar compositions. Refining the impact of magma composition on enclave strain archives would further constrain their significance as a marker of strain within intrusions, as questioned in previous work (Paterson et al., 2004; Caricchi et al., 2012). Future studies could utilise a field-based approach, implementing a similar methodology to Chapter 4, but within intrusions with larger compositional contrasts between magmas, determining if the overall sensitivity of enclaves to strain is similar or reduced. An alternative and complementary approach may be the thermodynamic modelling of magma compositions where enclaves have been shown to archive multiple fabrics, constraining the temperature range at which enclaves can act as mush-state strain archives.

7.3.2 Integrating Mesoscale and Macroscale Strain Archives within an Intrusion

This thesis has shown the sensitivity of strain archives within igneous plutons when intrapluton features are examined in detail. While this highlights that a comprehensive archive of strain can be determined even when exposure of the entire intrusion is unavailable, a potential direction of future work may be to compare detailed records of strain from a subarea of an intrusion to the strain record from a pluton-scale analysis. As mentioned in Chapter 5, a number of late Caledonian intrusions in Ireland and the UK already feature datasets of petrofabric development across the entire pluton, making these ideal test sites to understand if integrating more detailed studies across a subarea of an intrusion can provide new insight into trends measured at the pluton-scale.

7.3.3 Detecting Successive Internal Stress Regimes

In Chapter 5, the Fanad Pluton is shown to archive successive magmatic and tectonic stress regimes. Based on these results, it would be interesting to investigate the ability to record successive internal stress regimes within intrusions with minimal tectonic deformation. For example, within the Palaeogene igneous centres of the UK and Ireland (e.g., Geoffroy et al., 1997; Petronis et al., 2009; Troll et al., 2021), and the Miocene-aged intrusions in SE Iceland (e.g., Blake 1966; Burchardt et al., 2012; Rhodes et al., 2021), previous work reports the influence of multiple magma chamber processes during their formation with minimal influence from external tectonic stress. Both complexes feature intrusions with zones of magma mingling, providing test sites to compare strain archives and investigate if strain records for successive magma chamber processes can be identified, or a greater influence from external stress than previously reported.

7.3.4 The Impact of Hydrothermal Alteration and Fluid Transport Across a Wider Range of Geological Settings

In Chapter 6, the recognition of a threshold to alteration intensity and its impact on magnetic fabrics across the Currin Point Fault Zone opens a number of directions of future research.

The most obvious of these is in understanding how hydrothermal alteration impacts magnetic fabrics within other rock types, using the methodology within Chapter 6 as a framework for analysis. For instance, it would be interesting to compare the distribution and intensity of alteration around similar fault zones within porous, sedimentary lithologies and the resistance of their precursor petrofabrics to destruction in comparison to impermeable, crystalline lithologies.

Similarly, future work could apply the same approach to understand alteration associated with other hydrothermal systems. Previous work implementing a hyperspectral-magnetic characterisation of alteration haloes around massive ore bodies reports a similar ability to identify systematic changes in hydrothermal alteration distribution (e.g., McCarthy and Cloutier, 2016; Dixon et al., 2021; Dixon, 2023) suggesting this approach may also be applicable to other deposit types (e.g., vein-hosted or skarn-type). While systematic alteration changes are already established for several mineral deposit types (e.g., Sillitoe 2010) the characterisation method outlined in Chapter 6 may provide new insight on systematic alteration changes, which also correlates directly to the controls of magnetic fabrics. This may allow magnetic fabrics alongside traditional geochemical signatures to be used as part of mineral exploration.

Finally, further work is required to constrain the origin of the measured AARM subfabric across the Currin Point Fault Zone, interpreted as a petrofabric of hydrothermal fluid transport. While a similar hydrothermally-derived fabric is observed within layered igneous intrusions and magmatic sills (Jones et al., 2025a, 2025b; Williams et al., 2025), studies of other hydrothermal systems using the same robust alteration characterisation and measurement of multiple magnetic fabrics are required to determine if AARM subfabrics consistently form in response to alteration. If proven correct, this may provide a highly sensitive tool to trace fluid migration, particularly applicable in the tracking of ore-bearing fluids associated with hydrothermal ore deposits.

Bibliography

Ageeva, O., Habler, G., Gilder, S.A., Schuster, R., Pertsev, A., Pilipenko, O., Bian, G., and Abart, R., 2022, Oriented Magnetite Inclusions in Plagioclase: Implications for the Anisotropy of Magnetic Remanence: Geochemistry, Geophysics, Geosystems, v. 23, doi:10.1029/2021GC010272.

Akaad, M.K., 1956, The Ardara granitic diapir of county Donegal, Ireland: Quarterly Journal of the Geological Society of London, v. 112, p. 263–290, doi:https://doi.org/10.1144/GSL.JGS.1956.112.01-04.13.

Akimoto, S., 1962, Magnetic properties of FeO-Fe2O3-TiO2 system as a basis of rock magnetism: Proceedings on the International Conference on Magnetism and Crystallography, v. 17, p. 706–710.

Alasino, P.H., Ardill, K.E., and Paterson, S.R., 2025, Magmatic faults: Challenges, progress, and possibilities: Earth-Science Reviews, v. 260, doi:10.1016/j.earscirev.2024.104992.

Alasino, P.H., Ardill, K., Stanback, J., Paterson, S.R., Galindo, C., and Leopold, M., 2019, Magmatically folded and faulted schlieren zones formed by magma avalanching in the Sonora pass intrusive suite, Sierra Nevada, California: Geosphere, v. 15, p. 1677–1702, doi:10.1130/GES02070.1.

Allmendinger, R.W., Cardozo, N., and Fisher, D.M., 2012, Structural Geology Algorithms: Vectors and Tensors: Cambridge, Cambridge University Press.

Almqvist, B.S.G., Hirt, A.M., Herwegh, M., and Leiss, B., 2011, Magnetic anisotropy reveals Neogene tectonic overprint in highly strained carbonate mylonites from the Morcles nappe, Switzerland: Journal of Structural Geology, v. 33, p. 1010–1022, doi:10.1016/j.jsg.2011.02.002.

Alsop, G.I., 1992, Late Caledonian sinistral strike-slip displacement across the Leannan Fault system, northwest Ireland: Geological Journal, v. 27, p. 119–125, doi:10.1002/gj.3350270203.

Anderson, P.E., Stevenson, C.T., Cooper, M.R., Meighan, I.G., Reavy, R.J., Hurley, C.T., Inman, J., and Ellam, R.M., 2018, Refined model of incremental emplacement based on structural evidence from the granodioritic Newry igneous complex, Northern Ireland: Geological Society of America Bulletin, v. 130, p. 740–756, doi:10.1130/B31756.1.

Annen, C., Blundy, J.D., Leuthold, J., and Sparks, R.S.J., 2015, Construction and evolution of igneous bodies: Towards an integrated perspective of crustal magmatism: Lithos, v. 230, p. 206–221, doi:10.1016/j.lithos.2015.05.008.

Archibald, D.B., Macquarrie, L.M.G., Murphy, J.B., Strachan, R.A., McFarlane, C.R.M., Button, M., Larson, K.P., and Dunlop, J., 2021, The construction of the Donegal composite batholith, Irish Caledonides: Temporal constraints from U-Pb dating of zircon and titanite: Bulletin of the Geological Society of America, v. 133, p. 2335–2354, doi:10.1130/B35856.1.

Archibald, D.B., and Murphy, J.B., 2021, A slab failure origin for the Donegal composite batholith, Ireland as indicated by trace-element geochemistry, *in* Murphy, J.B., Strachan, R.A., and Quesada, C. eds., Geological Society, London, Special Publication: Pannotia to Pangaea: Neoproterozoic and Paleozoic Orogenic Cycles in the Circum-Atlantic Region, Geological Society of London, v. 503, p. 347–370, doi:10.1144/SP503-2020-6.

Ardill, K.E., Paterson, S.R., Stanback, J., Alasino, P.H., King, J.J., and Crosbie, S.E., 2020, Schlieren-Bound Magmatic Structures Record Crystal Flow-Sorting in Dynamic Upper-Crustal Magma-Mush Chambers: Frontiers in Earth Science, v. 8, doi:10.3389/feart.2020.00190.

Atherton, M.P., and Ghani, A.A., 2002, Slab breakoff: a model for Caledonian, Late Granite syn-collisional magmatism in the orthotectonic (metamorphic) zone of Scotland and Donegal, Ireland: Lithos, v. 62, p. 65–85, www.elsevier.com/locate/lithos.

Audétat, A., 2019, The Metal Content of Magmatic-Hydrothermal Fluids and Its Relationship to Mineralization Potential: Economic Geology, v. 114, p. 1033–1056, doi:10.5382/econgeo.4673.

Bachmann, O., and Huber, C., 2016, Silicic magma reservoirs in the Earth's crust: American Mineralogist, v. 101, p. 2377–2404, doi:10.2138/am-2016-5675.

Bella Nké, B.E., Njanko, T., Mamtani, M.A., Njonfang, E., and Rochette, P., 2018, Kinematic evolution of the Mbakop Pan–African granitoids (western Cameroon domain): An integrated AMS and EBSD approach: Journal of Structural Geology, v. 111, p. 42–63, doi:10.1016/j.jsg.2018.03.006.

Bella Nke, B.E., Njanko, T., Mamtani, M.A., Rochette, P., and Njonfang, E., 2022, Time relationship between emplacement, fabric development and regional deformation of the Manchi granitic pluton (western - Cameroon domain)-an integrated AMS, CPO and microstructural investigation: Journal of Structural Geology, v. 160, doi:10.1016/j.jsg.2022.104619.

Benn, K., 2009, Anisotropy of magnetic susceptibility fabrics in syntectonic plutons as tectonic strain markers: The example of the Canso pluton, Meguma Terrane, Nova Scotia, *in* Earth and Environmental Science Transactions of the Royal Society of Edinburgh, v. 100, p. 147–158, doi:10.1017/S1755691009016028.

Bense, V.F., Gleeson, T., Loveless, S.E., Bour, O., and Scibek, J., 2013, Fault zone hydrogeology: Earth-Science Reviews, v. 127, p. 171–192, doi:10.1016/j.earscirev.2013.09.008.

Bergantz, G.W., Schleicher, J.M., and Burgisser, A., 2017, On the kinematics and dynamics of crystal-rich systems: Journal of Geophysical Research: Solid Earth, v. 122, p. 6131–6159, doi:10.1002/2017JB014218.

Biedermann, A.R., 2018, Magnetic anisotropy in single crystals: A review: Geosciences (Switzerland), v. 8, doi:10.3390/geosciences8080302.

Biedermann, A.R., Bender Koch, C., Lorenz, W.E.A., and Hirt, A.M., 2014a, Low-temperature magnetic anisotropy in micas and chlorite: Tectonophysics, v. 629, p. 63–74, doi:10.1016/j.tecto.2014.01.015.

Biedermann, A.R., and Bilardello, D., 2021a, Practical Magnetism VII: Avoiding common misconceptions in magnetic fabric interpretation: IRM Q, v. 31, https://www.researchgate.net/publication/356617560.

Biedermann, A., and Bilardello, D., 2021b, Quarterly The IRM: The IRM Quaterly, v. 31, p. 1–18.

Biedermann, A.R., Koch, C.B., Pettke, T., and Hirt, A.M., 2015, Magnetic anisotropy in natural amphibole crystals: American Mineralogist, v. 100, p. 1940–1951, doi:10.2138/am-2015-5173.

Biedermann, A.R., Kunze, K., and Hirt, A.M., 2018, Interpreting magnetic fabrics in amphibole-bearing rocks: Tectonophysics, v. 722, p. 566–576, doi:10.1016/j.tecto.2017.11.033.

Biedermann, A.R., Pettke, T., Reusser, E., and Hirt, A.M., 2014b, Anisotropy of magnetic susceptibility in natural olivine single crystals: Geochemistry, Geophysics, Geosystems, v. 15, p. 3051–3065, doi:10.1002/2014GC005386.

Bilardello, D., 2021, Late Paleozoic Depositional Environments and Sediment Transport Directions of the Itararé Group Rocks From the State of São Paulo, Brazil, Determined From Rock Magnetism and Magnetic Anisotropy: Earth and Space Science, v. 8, doi:10.1029/2021EA001703.

Blake, D.H., 1966, The Net-Veined Complex of the Austurhorn Intrusion, Southeastern Iceland: The Journal of Geology, v. 74, p. 891–907, doi:jstor.org/stable/30062470.

Borradaile, G.J., 2001, Magnetic fabrics and petrofabrics: their orientation distributions and anisotropies: Journal of Structural Geology, v. 23, p. 1581–1596, www.elsevier.com/locate/jstrugeo.

Borradaile, G.J., and Jackson, M., 2004, Anisotropy of magnetic susceptibility (AMS): magnetic petrofabrics of deformed rocks: Geological Society, London, Special Publications, v. 238, p. 299–360, doi:10.1144/GSL.SP.2004.238.01.18.

Borradaile, G.J., and Jackson, M., 2010, Structural geology, petrofabrics and magnetic fabrics (AMS, AARM, AIRM): Journal of Structural Geology, v. 32, p. 1519–1551, doi:10.1016/j.jsg.2009.09.006.

Bouchez, J.L., 1997, Granite is Never Isotropic: An Introduction to AMS Studies of Granitic Rocks, *in* Bouchez, J.L., Hutton, D.H.W., and Stephens, W.E. eds., p. 95–112, doi:10.1007/978-94-017-1717-5_6.

Brown, P.E., Ryan, P.D., Soper, N.J., and Woodcock, N.H., 2008, The Newer Granite problem revisited: a transtensional origin for the early Devonian trans-suture suite: Geological Magazine, v. 145, p. 235–256, doi:10.1017/S0016756807004219.

Burchardt, S., Mattsson, T., Palma, J.O., Galland, O., Almqvist, B., Mair, K., Jerram, D.A., Hammer, Ø., and Sun, Y., 2019, Progressive Growth of the Cerro Bayo Cryptodome, Chachahuén Volcano, Argentina—Implications for Viscous Magma Emplacement: Journal of Geophysical Research: Solid Earth, v. 124, p. 7934–7961, doi:10.1029/2019JB017543.

Burchardt, S., Tanner, D., and Krumbholz, M., 2012, The Slaufrudalur pluton, southeast Iceland--An example of shallow magma emplacement by coupled cauldron subsidence and magmatic stoping: Geological Society of America Bulletin, v. 124, p. 213–227, doi:10.1130/B30430.1.

Burgisser, A., Carrara, A., and Annen, C., 2020, Numerical simulations of magmatic enclave deformation: Journal of Volcanology and Geothermal Research, v. 392, doi:10.1016/j.jvolgeores.2020.106790.

Burton-Johnson, A., Macpherson, C.G., Muraszko, J.R., Harrison, R.J., and Jordan, T.A., 2019, Tectonic strain recorded by magnetic fabrics (AMS) in plutons, including Mt Kinabalu, Borneo: A tool to explore past tectonic regimes and syn-magmatic deformation: Journal of Structural Geology, v. 119, p. 50–60, doi:10.1016/j.jsg.2018.11.014.

Burton-Johnson, A., Riley, T.R., Harrison, R.J., Mac Niocaill, C., Muraszko, J.R., and Rowley, P.D., 2022a, Does tectonic deformation control episodic continental arc magmatism? Evidence from granitic magnetic fabrics (AMS): Gondwana Research, v. 112, p. 1–23, doi:10.1016/j.gr.2022.09.006.

Burton-Johnson, A., Riley, T.R., Harrison, R.J., Mac Niocaill, C., Muraszko, J.R., and Rowley, P.D., 2022b, Does tectonic deformation control episodic continental arc magmatism? Evidence from granitic magnetic fabrics (AMS):

Caine, J.S., Evans, J.P., and Forster, C.B., 1996, Fault zone architecture and permeability structure: Geology, v. 24, p. 1025–1028, doi:10.1130/0091-7613(1996)024%3C1025:FZAAPS%3E2.3.CO;2.

Caricchi, L., Annen, C., Rust, A., and Blundy, J., 2012, Insights into the mechanisms and timescales of pluton assembly from deformation patterns of mafic enclaves: Journal of Geophysical Research B: Solid Earth, v. 117, doi:10.1029/2012JB009325.

Carrara, A., Burgisser, A., and Bergantz, G.W., 2024, Numerical simulations of the mingling caused by a magma intruding a resident mush: Volcanica, v. 7, p. 89–104, doi:10.30909/vol.07.01.89104.

Carreras, J., Druguet, E., Griera, A., and Soldevila, J., 2004, Strain and deformation history in a syntectonic pluton. The case of the Roses granodiorite (Cap de Creus, Eastern Pyrenees): Geological Society, London, Special Publications, v. 224, p. 307–319, http://sp.lyellcollection.org/.

Cashman, K. V., Sparks, R.S.J., and Blundy, J.D., 2017, Vertically extensive and unstable magmatic systems: A unified view of igneous processes: Science, v. 355, doi:10.1126/science.aag3055.

Chadima, M., 2012, Cureval8:

Chadima, M., 2022, Safyr7:

Chadima, M., and Hrouda, F., 2023, Anisoft6:

Chadima, M., Hrouda, F., and Jelinek, V., 2018a, Anisoft 5.1.01.:

Chadima, M., Pokorny, J., and Dusek, M., 2018b, Rema6:

Chatterjee, S., Singh, S., Shalivahan, and Mondal, S., 2023, Magneto-tectonic framework of the East Indian Shield: The present state of knowledge: Journal of Asian Earth Sciences, v. 251, doi:10.1016/j.jseaes.2023.105667.

Chew, D.M., and Stillman, C.J., 2009, Late Caledonian Orogeny and magmatism, *in* Holland, C.H. and Sanders, I.S. eds., The Geology of Ireland, Edinburgh, Dunedin Academic Press, p. 143–173, https://www.researchgate.net/publication/236344121.

Di Chiara, A., Morris, A., Anderson, M.W., Menegon, L., and Tremblay, A., 2020, Magnetic anisotropy reveals Acadian transpressional fabrics in an Appalachian ophiolite (Thetford Mines, Canada): Geophysical Journal International, v. 222, p. 1034–1045, doi:10.1093/gji/ggaa173.

Clark, R.N., King, T.V.V., Klejwa, M., Swayze, G.A., and Vergo, N., 1990, High spectral resolution reflectance spectroscopy of minerals: Journal of Geophysical Research, v. 95, doi:10.1029/jb095ib08p12653.

Cloutier, J., and Piercey, S.J., 2020, Tracing mineralogy and alteration intensity using the spectral alteration index and depth ratios at the northwest zone of the lemarchant volcanogenic massive sulfide deposit, Newfoundland, Canada: Economic Geology, v. 115, p. 1055–1078, doi:10.5382/econgeo.4723.

Cloutier, J., Piercey, S.J., and Huntington, J., 2021, Mineralogy, mineral chemistry and swir spectral reflectance of chlorite and white mica: Minerals, v. 11, doi:10.3390/min11050471.

Condon, D.J., Hodges, K.V., Alsop, G.I., and White, A., 2006, Laser ablation 40Ar/39Ar dating of metamorphic fabrics in the Caledonides of north Ireland: Journal of the Geological Society, v. 163, p. 337–345, doi:10.1144/0016-764904-066.

Cooper, M., Anderson, P., Condon, D., Stevenson, C., Ellam, R., Meighan, I., and Crowley, Q., 2016, Shape and intrusion history of the Late Caledonian Newry Igneous Complex, Northern Ireland, *in* Young, M.E. ed., Unearthed: impacts of the Tellus surveys of the north of Ireland, Dublin, Royal Irish Academy, p. 145–156, doi:10.3318/978-1-908996-88-6.ch11.

Cooper, M.R., Crowley, Q.G., Hollis, S.P., Noble, S.R., and Henney, P.J., 2013, A U-Pb age for the late Caledonian Sperrin Mountains minor intrusions suite in the north of Ireland: Timing of slab break-off in the Grampian terrane and the significance of deep-seated, crustal lineaments: Journal of the Geological Society, v. 170, p. 603–614, doi:10.1144/jgs2012-098.

Cruden, A.R., and Weinberg, R.F., 2018, Mechanisms of Magma Transport and Storage in the Lower and Middle Crust—Magma Segregation, Ascent and Emplacement, *in* Burchardt, S. ed., Volcanic and Igneous Plumbing Systems, Elsevier, p. 13–53, doi:10.1016/B978-0-12-809749-6.00002-9.

Cruz, C., Sant'Ovaia, H., McCarthy, W., and Noronha, F., 2022, Anisotropy of Out-of-Phase Magnetic Susceptibility: A Non-Standard Approach for Magnetic Subfabrics Determination in Variscan Granites of Iberian Massif: Minerals, v. 12, doi:10.3390/min12111376.

CSIRO, 2022, The Spectral Geologist :

El Desouky, M., Feely, M., and Mohr, P., 1996, Diorite-granite magma mingling and mixing along the axis of the Galway Granite batholith, Ireland: Journal of the Geological Society, v. 153, p. 361–374, doi:10.1144/gsjgs.153.3.0361.

Dewey, J.F., and Strachan, R.A., 2003, Changing Silurian-Devonian relative plate motion in the Caledonides: sinistral transpression to sinistral transtension: Journal of the Geological Society, v. 160, p. 219–229, http://jgs.lyellcollection.org/.

Dixon, O.J., 2023, A quantitative classification tool for porphyry Cu alteration systems [PhD Thesis]: University of St Andrews , doi:10.17630/sta/641.

Dixon, O., McCarthy, W., Madani, N., Petronis, M., McRobbie, S., and Cloutier, J., 2021, Classifying Copper-Molybdenum-Gold Porphyry Deposit Alteration using Magnetic and Spectral data: EGU General Assembly , doi:10.5194/egusphere-egu21-15817.

D’lemos, R.S., 1996, Mixing between granitic and dioritic crystal mushes, Guernsey, Channel Islands, UK: Lithos, v. 38, p. 233–257.

Domeier, M., and Torsvik, T.H., 2014, Plate tectonics in the late Paleozoic: Geoscience Frontiers, v. 5, p. 303–350, doi:10.1016/j.gsf.2014.01.002.

Dunlop, D., and Özdemir, O., 1997, Rock Magnetism: Fundamentals and frontiers: Cambridge, Cambridge University Press.

Egli, R., 2013, VARIFORC: An optimized protocol for calculating non-regular first-order reversal curve (FORC) diagrams: Global and Planetary Change, v. 110, p. 302–320, doi:10.1016/j.gloplacha.2013.08.003.

Ellis, J.F., and Blenkinsop, T., 2019, Analogue modelling of fracturing in cooling plutonic bodies: Tectonophysics, v. 766, p. 14–19, doi:10.1016/j.tecto.2019.05.019.

ESRI, 2020, ArcMap:

Evans, D., and Whittington, R.J., 1976, The Submarine Extensions of the Thorr and Fanad Plutons, County Donegal: Proceedings of the Royal Irish Academy. Section B: Biological, Geological, and Chemical Science, v. 76, p. 111–120, https://www.jstor.org/stable/20519007 (accessed November 2019).

Faulkner, D.R., Jackson, C.A.L., Lunn, R.J., Schlische, R.W., Shipton, Z.K., Wibberley, C.A.J., and Withjack, M.O., 2010, A review of recent developments concerning the structure, mechanics and fluid flow properties of fault zones: Journal of Structural Geology, v. 32, p. 1557–1575, doi:10.1016/j.jsg.2010.06.009.

Ferré, E.C., 2002, Theoretical models of intermediate and inverse AMS fabrics: Geophysical Research Letters, v. 29, p. 31-1-31–4, doi:10.1029/2001GL014367.

Ferré, E.C., Wilson, J., and Gleizes, G., 1999, Magnetic susceptibility and AMS of the Bushveld alkaline granites, South Africa: Tectonophysics, v. 307, p. 113–133, doi:10.1016/S0040-1951(99)00122-5.

Fiannacca, P., Russo, D., Fazio, E., Cirrincione, R., and Mamtani, M.A., 2021, Fabric analysis in upper crustal post-collisional granitoids from the serre batholith (Southern italy): Results from microstructural and ams investigations: Geosciences (Switzerland), v. 11, doi:10.3390/geosciences11100414.

Flinn, D., 1965, On the Symmetry Principle and the Deformation Ellipsoid: Geological Magazine, v. 102, p. 36–45, doi:10.1017/S0016756800053851.

Friedrich, A.M., Hodges, K. V, Bowring, S.A., and Martin, M.W., 1999, Geochronological constraints on the magmatic, metamorphic and thermal evolution of the Connemara Caledonides, western Ireland.:

Friend, C.R.L., Jones, K.A., and Burns, I.M., 2000, New high-pressure granulite event in the Moine Supergroup, northern Scotland: Implications for Taconic (early Caledonian) crustal evolution: Geology, v. 28, p. 543–546, doi:10.1130/0091-7613(2000)28%3C543:NHGEIT%3E2.0.CO;2.

Geoffroy, L., Olivier, P., and Rochette, P., 1997, Structure of a hypovolcanic acid complex inferred from magnetic susceptibility anisotropy measurements: the Western Red Hills granites (Skye, Scotland, Thulean Igneous Province): Bulletin of Volcanology, v. 59, p. 147–159, doi:10.1007/s004450050182.

Ghani, A.A., and Atherton, M.P., 2006, The chemical character of the Late Caledonian Donegal Granites, Ireland, with comments on their genesis: Transactions of the Royal Society of Edinburgh, Earth Sciences, v. 97, p. 437–454, doi:10.1017/S0263593300001553.

Gonçalves, A., Sant'Ovaia, H., and Noronha, F., 2025, Anisotropy of magnetic susceptibility as the key to understand the ascending and emplacement mechanisms of granitic plutons: a review: Journal of Iberian Geology, v. 51, p. 153–178, doi:10.1007/s41513-024-00272-8.

Görz, I., and Hielscher, P., 2010, An explicit plate kinematic model for the orogeny in the southern Uralides: Tectonophysics, v. 493, p. 1–26, doi:10.1016/j.tecto.2010.07.005.

Goswami, S., Mamtani, M.A., and Rana, V., 2018, Quartz CPO and kinematic analysis in deformed rocks devoid of visible stretching lineations: An integrated AMS and EBSD investigation: Journal of Structural Geology, v. 115, p. 270–283, doi:10.1016/j.jsg.2018.04.008.

Grégoire, V., Darrozes, J., Gaillot, P., Nédélec, A., and Launeau, P., 1998, Magnetite grain shape fabric and distribution anisotropy vs rock magnetic fabric: a three-dimensional case study: Journal of Structural Geology , v. 20, p. 937–944.

Harland, W.B., 1971, Tectonic transpression in Caledonian Spitsbergen: Geological Magazine, v. 108, p. 27–41, doi:10.1017/S0016756800050937.

Harrison, R.J., and Feinberg, J.M., 2008, FORCinel: An improved algorithm for calculating first-order reversal curve distributions using locally weighted regression smoothing: Geochemistry, Geophysics, Geosystems, v. 9, p. n/a-n/a, doi:10.1029/2008GC001987.

Harrison, R.J., Muraszko, J., Heslop, D., Lascu, I., Muxworthy, A.R., and Roberts, A.P., 2018, An Improved Algorithm for Unmixing First-Order Reversal Curve

Diagrams Using Principal Component Analysis: Geochemistry, Geophysics, Geosystems, v. 19, p. 1595–1610, doi:10.1029/2018GC007511.

Heap, M.J. et al., 2022, The tensile strength of hydrothermally altered volcanic rocks: Journal of Volcanology and Geothermal Research, v. 428, doi:10.1016/j.jvolgeores.2022.107576.

Heap, M.J., Gravley, D.M., Kennedy, B.M., Gilg, H.A., Bertolett, E., and Barker, S.L.L., 2020, Quantifying the role of hydrothermal alteration in creating geothermal and epithermal mineral resources: The Ohakuri ignimbrite (Taupō Volcanic Zone, New Zealand): Journal of Volcanology and Geothermal Research, v. 390, doi:10.1016/j.jvolgeores.2019.106703.

Hext, G.R., 1963, The estimation of second-order tensors, with related tests and designs: Biometrika, v. 50, p. 353–373, https://academic.oup.com/biomet/article-abstract/50/3-4/353/255956.

Hibbard, M.J., and Watters, R.J., 1985, Fracturing and diking in incompletely crystallized granitic plutons: Lithos, v. 18, p. 1–12.

Horsman, E., Tikoff, B., and Morgan, S., 2005, Emplacement-related fabric and multiple sheets in the Maiden Creek sill, Henry Mountains, Utah, USA: Journal of Structural Geology, v. 27, p. 1426–1444, doi:10.1016/j.jsg.2005.03.003.

Hrouda, F., 2010, Modelling relationship between bulk susceptibility and AMS in rocks consisting of two magnetic fractions represented by ferromagnetic and paramagnetic minerals - Implications for understanding magnetic fabrics in deformed rocks: Journal of the Geological Society of India, v. 75, p. 254–266, doi:10.1007/s12594-010-0013-0.

Hrouda, F., and Chadima, M., 2020, Examples of tectonic overprints of magnetic fabrics in rocks of the Bohemian Massif and Western Carpathians: International Journal of Earth Sciences, v. 109, p. 1321–1336, doi:10.1007/s00531-019-01786-8.

Hrouda, F., Táborská, S., Schulmann, K., Jezek, J., and Dolejs, D., 1999, Magnetic fabric and rheology of co-mingled magmas in the Nasavrky Plutonic Complex (E Bohemia): implications for intrusive strain regime and emplacement mechanism: Tectonophysics, v. 307, p. 93–111, www.elsevier.com/locate/tecto.

Hunt, G.R., 1977, Spectral signatures of particulate minerals in the visible and near infrared: Geophysics, v. 42, p. 501–511.

Hunt, G.R., and Ashley, R.M., 1979, Spectra of Altered Rocks in the Visible and Near Infrared: Economic Geology, v. 74, p. 1613–1629, http://pubs.geoscienceworld.org/segweb/economicgeology/article-pdf/74/7/1613/3486457/1613.pdf.

Hutton, D.H.W., 1982, A tectonic model for the emplacement of the Main Donegal Granite, NW Ireland: Journal of the Geological Society. London, v. 139, p. 615–631, https://pubs.geoscienceworld.org/jgs/article-pdf/139/5/615/4795430/gsjgs.139.5.0615.pdf.

Hutton, D.H.W., 1988, Granite emplacement mechanisms and tectonic controls: Inferences from deformation studies: Transactions of the Royal Society of Edinburgh: Earth Sciences, v. 79, p. 245–255, doi:10.1017/S0263593300014255.

Hutton, D.H.W., and Alsop, G.I., 1996, The Caledonian strike-swing and associated lineaments in NW Ireland and adjacent areas: sedimentation, deformation and igneous intrusion patterns: Journal of the Geological Society. London, v. 153, p. 345–360, https://pubs.geoscienceworld.org/jgs/article-pdf/153/3/345/2783472/gsjgs.153.3.0345.pdf.

Jackson, M., 1991, Anisotropy of Magnetic Remanence: A Brief Review of Mineralogical Sources, Physical Origins, and Geological Applications, and Comparison with Susceptibility Anisotropy: Pure and Applied Geophysics, v. 136, p. 1–28.

Jacques, J.M., and Reavy, R.J., 1994, Caledonian plutonism and major lineaments in the SW Scottish Highlands: Journal of the Geological Society, London, v. 151, p. 955–964, https://pubs.geoscienceworld.org/jgs/article-pdf/151/6/955/4890038/gsjgs.151.6.0955.pdf.

Jelinek, V., 1981, Characterization of the magnetic fabric of rocks: Tectonophysics, v. 79, p. T63–T67.

Jelinek, V., 1984, On a mixed quadratic invariant of the magnetic susceptibility tensor: Journal of Geophysics, v. 56, p. 58–60.

Jelinek, V., 1978, Statistical processing of anisotropy of magnetic susceptibility measured on groups of specimens: Studia Geophysica et Geodaetica volume, v. 22, p. 50–62.

Jelinek, V., 1977, The statistical theory of measuring anisotropy of magnetic susceptibility of rocks and its application: Brno, Geofyzika, v. 1, 0–87 p.

Johnson, T.E., Kirkland, C.L., Viete, D.R., Fischer, S., Reddy, S.M., Evans, N.J., and McDonald, B.J., 2017, Zircon geochronology reveals polyphase magmatism and crustal anatexis in the Buchan Block, NE Scotland: Implications for the Grampian Orogeny: Geoscience Frontiers, v. 8, p. 1469–1478, doi:10.1016/j.gsf.2017.02.002.

Jones, E., McCarthy, W., Magee, C., Mattsson, T., Piazolo, S., Hutchison, W., and Humphreys, M.C.S., 2025a, Igneous layering and magma dynamics in alkaline intrusions: textural evidence for gravitational settling and compaction within cumulates: Journal of the Geological Society, v. 182, doi:10.1144/jgs2024-181.

Jones, E., McCarthy, W., Piazolo, S., Magee, C., Humphreys, M.C.S., and Hutchison, W., 2025b, Microstructures Reveal Mechanical Compaction and Volatile-Rich Liquid Migration in the Layered Alkaline Ilímaussaq Complex, South Greenland: Journal of Petrology, v. 66, doi:10.1093/petrology/egaf067.

Just, J., and Kontny, A., 2012, Thermally induced alterations of minerals during measurements of the temperature dependence of magnetic susceptibility: A case study from the hydrothermally altered Soultz-sous-Forêts granite, France: International Journal of Earth Sciences, v. 101, p. 819–839, doi:10.1007/s00531-011-0668-9.

Just, J., Kontny, A., Wall, H. DE, Hirt, A.M., and Martin-Hernandez, F., 2004, Development of magnetic fabrics during hydrothermal alteration in the Soultz-sous-Forêts granite from the EPS-1 borehole, Upper Rhine Graben: Geological Society, London, Special Publications, v. 238, p. 509–526, doi:10.1144/GSL.SP.2004.238.01.26.

Khan, M.A., 1962, The Anisotropy of Magnetic Susceptibility of Some Igneous and Metamorphic Rocks: Journal of Geophysical Research, v. 67, p. 2873–2885.

Kirkland, C.L., Alsop, G.I., and Prave, A.R., 2008, The brittle evolution of a major strike-slip fault associated with granite emplacement: a case study of the Leannan Fault, NW Ireland: Journal of the Geological Society, v. 165, p. 341–352, doi:10.1144/0016-76492007-064.

Knight, H., Stevenson, C., Maffione, M., McCarthy, W., Burton-Johnson, A., and Lawrence, A., 2024, Testing the sensitivity of anisotropy of magnetic susceptibility (AMS) to the regional tectonic strain field in granite plutons: insights from two orogen-scale studies: Tektonika, v. 2.2, p. 181–208, doi:10.55575/tektonika2024.2.2.58.

Kocks, H., Strachan, R.A., Evans, J.A., and Fowler, M., 2014, Contrasting magma emplacement mechanisms within the Rogart igneous complex, NW Scotland, record the switch from regional contraction to strike-slip during the Caledonian orogeny: Geological Magazine, v. 151, p. 899–915, doi:10.1017/S0016756813000940.

Koopmans, L., McCarthy, W., and Magee, C., 2022, Dyke Architecture, Mineral Layering, and Magmatic Convection; New Perspectives From the Younger Giant Dyke Complex, S Greenland: Geochemistry, Geophysics, Geosystems, v. 23, doi:10.1029/2021GC010260.

Köpping, J., Cruden, A.R., Magee, C., McCarthy, W., Geissman, J., and Holm, D., 2023, Magnetic fabrics reveal three-dimensional flow processes within elongate magma fingers at the margin of the Shonkin Sag laccolith (MT, USA): Journal of Structural Geology, v. 169, doi:10.1016/j.jsg.2023.104829.

Krása, D., and Herrero-Bervera, E., 2005, Alteration induced changes of magnetic fabric as exemplified by dykes of the Koolau volcanic range: Earth and Planetary Science Letters, v. 240, p. 445–453, doi:10.1016/j.epsl.2005.09.028.

Laakso, K., Peter, J.M., Rivard, B., and White, H.P., 2016, Short-Wave Infrared Spectral and Geochemical Characteristics of Hydrothermal Alteration at the Archean Izok Lake Zn-Cu-Pb-Ag Volcanogenic Massive Sulfide Deposit, Nunavut, Canada: Application in Exploration Target Vectoring: Economic Geology, p. 1223–1239, doi:https://doi-org.ucc.idm.oclc.org/10.2113/econgeo.111.5.1223.

Lamont, T.N. et al., 2024, Porphyry copper formation driven by water-fluxed crustal melting during flat-slab subduction: Nature Geoscience, v. 17, p. 1306–1315, doi:10.1038/s41561-024-01575-2.

Lamont, T.N., McCarthy, W., Strachan, R., Roberts, N.M.W., Mackay-Champion, T., Bird, A., and Searle, M., 2025, Late Ordovician regional high-pressure metamorphism in Scotland, UK: Caledonian metamorphic climax predated the closure of the Iapetus Ocean: Geological Society of America Bulletin, doi:10.1130/B38370.1.

Latimer, B., McCarthy, W., Mattsson, T., and Reavy, J., 2024, Enclaves as mushy magma strain archives: New perspectives on composite magmatic fabrics in plutons: Geosphere, v. 20, p. 1390–1410, doi:10.1130/GES02786.1.

Latimer, B., McCarthy, W., Mattsson, T., and Reavy, J., 2025, Intrusions are Sensitive, Temporally Constrained Strain Archives: Journal of the Geological Society, doi:10.1144/jgs2025-066.

Lattard, D., Engelmann, R., Kontny, A., and Sauerzapf, U., 2006, Curie temperatures of synthetic titanomagnetites in the Fe-Ti-O system: Effects of composition, crystal chemistry, and thermomagnetic methods: Journal of Geophysical Research: Solid Earth, v. 111, doi:10.1029/2006JB004591.

Law, R.D., Strachan, R., Thirlwall, M., and Thigpen, J.R., 2024, 8: The Caledonian Orogeny: Late Ordovician–Early Devonian tectonic and magmatic events associated with closure of the Iapetus Ocean, *in* Smith, M. and Strachan, R.A. eds., The Geology of Scotland, The Geological Society of London, p. 205–257, doi:10.1144/GOS5-2022-71.

Lawrence, A., Maffione, M., and Stevenson, C.T.E., 2022, Mush ado about the Ratagain Complex, NW Scotland: insights into Caledonian granitic magmatism and emplacement from magnetic fabric analyses: Scottish Journal of Geology, v. 58, p. 1–25, doi:10.6084/m9.figshare.c.5941375.

Lescoutre, R., and Manatschal, G., 2020, Role of rift-inheritance and segmentation for orogenic evolution: Example from the Pyrenean-Cantabrian system: BSGF - Earth Sciences Bulletin, v. 191, doi:10.1051/bsgf/2020021.

Lypaczewski, P., Rivard, B., Lesage, G., Byrne, K., D’angelo, M., and Lee, R.G., 2020, Characterization of mineralogy in the highland valley porphyry cu district using hyperspectral imaging, and potential applications: Minerals, v. 10, doi:10.3390/min10050473.

Maffione, M., Hernandez-Moreno, C., Ghiglione, M.C., Speranza, F., van Hinsbergen, D.J.J., and Lodolo, E., 2015, Constraints on deformation of the Southern Andes since the Cretaceous from anisotropy of magnetic susceptibility: Tectonophysics, v. 665, p. 236–250, doi:10.1016/j.tecto.2015.10.008.

Magee, C., Muirhead, J., Schofield, N., Walker, R.J., Galland, O., Holford, S., Spacapan, J., Jackson, C.A.L., and McCarthy, W., 2019, Structural signatures of igneous sheet intrusion propagation: Journal of Structural Geology, v. 125, p. 148–154, doi:10.1016/j.jsg.2018.07.010.

Magee, C., Stevenson, C.T.E., O’Driscoll, B., and Petronis, M.S., 2012, Local and regional controls on the lateral emplacement of the Ben Hiant Dolerite intrusion, Ardnamurchan (NW Scotland): Journal of Structural Geology, v. 39, p. 66–82, doi:10.1016/j.jsg.2012.03.005.

Marsh, B.D., 1989, Magma Chambers: Annual Review of Earth and Planetary Sciences, v. 17, p. 439–472, doi:10.1146/annurev.ea.17.050189.002255.

Marsh, B.D., 1996, Solidification fronts and magmatic evolution: Mineralogical Magazine, v. 60, p. 5–40, doi:10.1180/minmag.1996.060.398.03.

Matenco, L., Balázs, A., Nader, F.H., Haq, B.U., and Fodor, L., 2022, Advances in the understanding of multi-scale and coupled evolution of orogens, sedimentary basins and the underlying lithosphere: Global and Planetary Change, v. 208, p. 103689, doi:10.1016/j.gloplacha.2021.103689.

Mattsson, T., Burchardt, S., Almqvist, B.S.G., and Ronchin, E., 2018, Syn-emplacement Fracturing in the Sandfell Laccolith, Eastern Iceland—Implications for Rhyolite Intrusion Growth and Volcanic Hazards: Frontiers in Earth Science, v. 6, doi:10.3389/feart.2018.00005.

Mattsson, T., McCarthy, W., and Schmiedel, T., 2024, Transport of Magma in Granitic Mush Systems; an Example From the Götemar Pluton, Sweden: Geochemistry, Geophysics, Geosystems, v. 25, doi:10.1029/2023GC011061.

Mattsson, T., Petri, B., Almqvist, B., McCarthy, W., Burchardt, S., Palma, J.O., Hammer, Ø., and Galland, O., 2021, Decrypting Magnetic Fabrics (AMS, AARM, AIRM) Through the Analysis of Mineral Shape Fabrics and Distribution Anisotropy: Journal of Geophysical Research: Solid Earth, v. 126, doi:10.1029/2021JB021895.

McAteer, C., 2009, Provenance of Metasedimentary Sequences in the Scottish and Irish Caledonides [PhD Thesis]: University College Dublin, 0–79 p.

McCabe, C., and Jackson, M., 1985, Magnetic anisotropy in the Trenton Limestone: results if a new technique, anisotropy of anhysteretic susceptibility: Geophysical Research Letters, v. 12, p. 333–336.

McCaffrey, K.J.W., 1994, Magmatic and solid state deformation partitioning in the Ox Mountains granodiorite: Geological Magazine, v. 131, p. 639–652, doi:10.1017/S0016756800012437.

McCarthy, W.J., 2013, An evaluation of orogenic kinematic evolution utilizing crystalline and magnetic anisotropy in granitoids: UCC, http://hdl.handle.net/10468/1669.

McCarthy, W., and Cloutier, J., 2016, Hyperspectral reflectance and magnetic alteration of the Mace Mo-Cu deposit, Co Galway. (Professional Report for SLR ltd., Agreement No. 501.00343.00005.).:

McCarthy, D.J., Meere, P.A., and Petronis, M.S., 2015a, A comparison of the effectiveness of clast based finite strain analysis techniques to AMS in sandstones from the Sevier Thrust Belt, Wyoming: Tectonophysics, v. 639, p. 68–81, doi:10.1016/j.tecto.2014.11.014.

McCarthy, W., Petronis, M.S., Reavy, R.J., and Stevenson, C.T., 2015b, Distinguishing diapirs from inflated plutons: an integrated rock magnetic fabric and structural study on the Roundstone Pluton, western Ireland: Journal of the Geological Society, v. 172, p. 550–565, doi:10.1144/jgs2014-067.

McCarthy, W., Reavy, R.J., Stevenson, C.T., and Petronis, M.S., 2015c, Late Caledonian transpression and the structural controls on pluton construction; new insights from the Omey Pluton, western Ireland: Earth and Environmental Science Transactions of the Royal Society of Edinburgh, v. 106, p. 11–28, doi:10.1017/S1755691015000201.

McKerrow, W.S., Mac Niocaill, C., and Dewey, J.F., 2000, The Caledonian Orogeny redefined: Journal of the Geological Society, v. 157, p. 1149–1154, doi:10.1144/jgs.157.6.1149.

Miles, A.J., Woodcock, N.H., and Hawkesworth, C.J., 2016, Tectonic controls on post-subduction granite genesis and emplacement: The late Caledonian suite of Britain and Ireland: Gondwana Research, v. 39, p. 250–260, doi:10.1016/j.gr.2016.02.006.

Miller, R.B., and Paterson, S.R., 1994, The transition from magmatic to high-temperature solid-state deformation: implications from the Mount Stuart batholith, Washington: Journal of Structural Geology, v. 16, p. 853.

Milne, E.J.M., Neill, I., Bird, A.F., Millar, I.L., McDonald, I., Dempsey, E.D., Olive, V., Odling, N., and Waters, E.C., 2022, Caledonian hot zone magmatism in the "Newer Granites": insight from the Cluanie and Clunes plutons, Northern Scottish Highlands: Journal of the Geological Society, doi:10.1144/jgs2022-076.

Molyneux, S.J., and Hutton, D.H.W., 2000, Evidence for significant granite space creation by the ballooning mechanism: The example of the Ardara pluton, Ireland: GSA Bulletin, p. 1543–1558, http://pubs.geoscienceworld.org/gsa/gsabulletin/article-pdf/112/10/1543/3384045/i0016-7606-112-10-1543.pdf.

Moore, D.E., and Byerlee, J., 1992, Relationships between sliding behavior and internal geometry of laboratory fault zones and some creeping and locked strike-slip faults of California: Tectonophysics, v. 211, p. 305–316, doi:10.1016/0040-1951(92)90067-G.

Moskowitz, B.M., 1981, Methods for estimating curie temperatures of titanomaghemites from experimental Js-T data: Earth and Planetary Science Letter, v. 53, p. 84–88.

Muir, R.J., and Vaughan, A.P.M., 2017, Digital mapping and three-dimensional model building of the ben nevis igneous complex, Southwest Highlands, Scotland: New insights into the emplacement and preservation of postorogenic magmatism: Journal of Geology, v. 125, p. 607–636, doi:10.1086/693858.

Nédélec, A., Trindade, R., Peschler, A., Archanjo, C., Macouin, M., Poitrasson, F., and Bouchez, J.L., 2015, Hydrothermally-induced changes in mineralogy and magnetic properties of oxidized A-type granites: Lithos, v. 212–215, p. 145–157, doi:10.1016/j.lithos.2014.11.007.

Neilson, J.C., Kokelaar, B.P., and Crowley, Q.G., 2009a, Timing, relations and cause of plutonic and volcanic activity of the Siluro-Devonian post-collision magmatic episode in the Grampian Terrane, Scotland: Journal of the Geological Society, v. 166, p. 545–561, doi:10.1144/0016-76492008-069.

Neilson, J.C., Kokelaar, B.P., and Crowley, Q.G., 2009b, Timing, relations and cause of plutonic and volcanic activity of the Siluro-Devonian post-collision magmatic episode in the Grampian Terrane, Scotland: Journal of the Geological Society, v. 166, p. 545–561, doi:10.1144/0016-76492008-069.

Neves, S.P., Góis Dantas, C.X., Carrino, T.A., Mariano, G., and Correia, P. de B., 2023, Multiple fabrics in the Tavares pluton (NE Brazil): Insights on the interplay between emplacement mechanism, internal magmatic processes, and tectonic deformation: Journal of Structural Geology, v. 167, doi:10.1016/j.jsg.2023.104793.

O'Driscoll, B., Petronis, M.S., Marks, M.A.W., McCarthy, W.S., Mariani, E., Stevenson, C.T.E., Clay, P.L., and Geissman, J.W., 2024, Magnetic Fabrics in Laminated Rocks of the Ilímaussaq Igneous Complex, Southern Greenland: The Canadian Journal of Mineralogy and Petrology, v. 62, p. 821–846, doi:10.3749/2400008.

O'Driscoll, B., Troll, V.R., Reavy, R.J., and Turner, P., 2006, The Great Eucrite intrusion of Ardnamurchan, Scotland: Reevaluating the ring-dike concept: Geology, v. 34, p. 189, doi:10.1130/G22294.1.

Oliver, G.J.H., Wilde, S.A., and Wan, Y., 2008, Geochronology and geodynamics of Scottish granitoids from the late neoproterozoic break-up of Rodinia to Palaeozoic collision: Journal of the Geological Society, v. 165, p. 661–674, doi:10.1144/0016-76492007-105.

Olšanská, I., Tomek, F., Robustelli Test, C., Zanella, E., Svojtka, M., Trubač, J., Cifelli, F., and Finger, F., 2025, From Magma Formation to Eruption: Temperature Path of Two Late Carboniferous Post-Collisional Calderas (Bohemian Massif): Geochemistry, Geophysics, Geosystems, v. 26, doi:10.1029/2025GC012217.

Oriolo, S., Gómez, A.L.R., Maffini, M.N., Oyhantçabal, P., Demarco, M.M., Vargas Perucca, M.S., Bastías Torres, M.V., and Rubinstein, N.A., 2024, Transtension, brittle-ductile shear zones and hydrothermal ore deposits: Towards quantitative structural and kinematic models: Journal of Structural Geology, v. 185, p. 1–17, doi:10.1016/j.jsg.2024.105173.

Orlický, O., 1990, Detection of magnetic carriers in rocks: results of susceptibility changes in powdered rock samples induced by temperature: Physics of the Earth and Planetary Interiors, v. 63, p. 66–70, doi:10.1016/0031-9201(90)90060-B.

Parés, J.M., 2004, How deformed are weakly deformed mudrocks? Insights from magnetic anisotropy: Geological Society, London, Special Publications, v. 238, p. 191–203, doi:10.1144/GSL.SP.2004.238.01.13.

Passchier, C.W., and Trouw, R.A.J., 2005, Microtectonics: New York, Springer.

Pastor-Galán, D., Ursem, B., Meere, P.A., and Langereis, C., 2015, Extending the Cantabrian Orocline to two continents (from Gondwana to Laurussia). Paleomagnetism from South Ireland: Earth and Planetary Science Letters, v. 432, p. 223–231, doi:10.1016/j.epsl.2015.10.019.

Paterson, S.R., Ardill, K., Vernon, R., and Žák, J., 2019, A review of mesoscopic magmatic structures and their potential for evaluating the hypersolidus evolution of intrusive complexes: Journal of Structural Geology, v. 125, p. 134–147, doi:10.1016/j.jsg.2018.04.022.

Paterson, S.R., Pignotta, G.S., and Vernon, R.H., 2004, The significance of microgranitoid enclave shapes and orientations: Journal of Structural Geology, v. 26, p. 1465–1481, doi:10.1016/j.jsg.2003.08.013.

Paterson, S.R., and Vernon, R.H., 1995, Bursting the bubble of ballooning plutons: A return to nested diapirs emplaced by multiple processes: Geological Society of America Bulletin, v. 107, p. 1356–1380, http://pubs.geoscienceworld.org/gsa/gsabulletin/article-pdf/107/11/1356/3382193/i0016-7606-107-11-1356.pdf.

Paterson, S.R., Vernon, R.H., and Tobisch, O.T., 1989, A review of criteria for the identification of magmatic and tectonic foliations in granitoids: Journal of Structural Geology, v. 1, p. 349–363.

Paterson, S.R., Žák, J., and Janoušek, V., 2008, Growth of complex sheeted zones during recycling of older magmatic units into younger: Sawmill Canyon area, Tuolumne batholith, Sierra Nevada, California: Journal of Volcanology and Geothermal Research, v. 177, p. 457–484, doi:10.1016/j.jvolgeores.2008.06.024.

Paterson, G.A., Zhao, X., Jackson, M., and Heslop, D., 2018, Measuring, Processing, and Analyzing Hysteresis Data: Geochemistry, Geophysics, Geosystems, v. 19, p. 1925–1945, doi:10.1029/2018GC007620.

Pawley, M.J., and Collins, W.J., 2002, The development of contrasting structures during the cooling and crystallisation of a syn-kinematic pluton: Journal of Structural Geology, v. 24, p. 469–483, www.elsevier.com/locate/jstrugeo.

Pereira, M.L., Zanon, V., Fernandes, I., Pappalardo, L., and Viveiros, F., 2024, Hydrothermal alteration and physical and mechanical properties of rocks in a volcanic environment: A review: Earth-Science Reviews, v. 252, p. 1–27, doi:10.1016/j.earscirev.2024.104754.

Petford, N., 2009, Which effective viscosity? Mineralogical Magazine, v. 73, p. 167–191, doi:10.1180/minmag.2009.073.2.167.

Petronis, M.S., O'Driscoll, B., and Lindline, J., 2011, Late stage oxide growth associated with hydrothermal alteration of the Western Granite, Isle of Rum, NW Scotland: Geochemistry, Geophysics, Geosystems, v. 12, doi:10.1029/2010GC003246.

Petronis, M.S., O'Driscoll, B., Stevenson, C.T.E., and Reavy, R.J., 2012, Controls on emplacement of the Caledonian Ross of Mull Granite, NW Scotland: Anisotropy of magnetic susceptibility and magmatic and regional structures: Bulletin of the Geological Society of America, v. 124, p. 906–927, doi:10.1130/B30362.1.

Petronis, M.S., O'Driscoll, B., Troll, V.R., Emeleus, C.H., and Geissman, J.W., 2009, Palaeomagnetic and anisotropy of magnetic susceptibility data bearing on the emplacement of the Western Granite, Isle of Rum, NW Scotland: Geological Magazine, v. 146, p. 419–436, doi:10.1017/S0016756808005827.

Pickering, K.T., Bassett, M.G., and Siveter, D.J., 1988, Late Ordovician—early Silurian destruction of the Iapetus Ocean: Newfoundland, British Isles and Scandinavia—a discussion: Transactions of the Royal Society of Edinburgh: Earth Sciences, v. 79, p. 361–382, doi:10.1017/S0263593300014358.

Pitcher, W.S., and Berger, A.R., 1972, The Geology of Donegal, a study of granite emplacement and unroofing: London, Wiley Interscience.

PIX4D S.A., 2024, PIX4Dmapper:

Potter, D.K., 2004, A comparison of anisotropy of magnetic remanence methods- a user's guide for application to palaeomagnetism and magnetic fabric studies, *in* Martín-Hernández, F., Lüneberg, C.M., Aubourg, C., and Jackson, M. eds., Magnetic Fabric: Methods and Applications, London, Geological Society of London, v. 238, p. 21–35, http://sp.lyellcollection.org/.

Potter, D.K., and Stephenson, A., 1988, Single-domain particles in rocks and magnetic fabric analysis: Geophysical Research Letters, v. 15, p. 1097–1100, doi:10.1029/GL015i010p01097.

Prave, A.R., Stephens, W.E., Fallick, A.E., Williams, I.S., and Kirsimäe, K., 2024, How great is the Great Glen Fault? Journal of the Geological Society, v. jgs2024-085, p. 1–12, doi:10.6084/m9.figshare.c.7389974.

Prior, D.J. et al., 1999, The application of electron backscatter diffraction and orientation contrast imaging in the SEM to textural problems in rocks: American Mineralogist, v. 84, p. 1741–1759.

Prior, D.J., Mariani, E., and Wheeler, J., 2009, EBSD in the earth sciences: Applications, common practice, and challenges, *in* Electron Backscatter Diffraction in Materials Science, Springer US, p. 345–360, doi:10.1007/978-0-387-88136-2_26.

Pueyo Anchuela, Ó., María Casas-Sainz, A., Pocoví Juan, A., and Gil Imaz, A., 2011, Lithology-dependent reliability of AMS analysis: A case study of the Eocene turbidities in the southern Pyrenees (Aragón, Spain): Comptes Rendus - Geoscience, v. 343, p. 11–19, doi:10.1016/j.crte.2010.11.003.

Quintela, O. et al., 2025, The Magnetic Fingerprint of Pulsed Granite Magma Emplacement and Alteration: Slaufrudalur Pluton, Iceland: Geochemistry, Geophysics, Geosystems, v. 26, doi:10.1029/2025GC012199.

Raposo, M.I.B., Chaves, A.O., Lojkasek-Lima, P., D'Agrella-Filho, M.S., and Teixeira, W., 2004, Magnetic fabrics and rock magnetism of Proterozoic dike swarm from the southern São Francisco Craton, Minas Gerais State, Brazil: Tectonophysics, v. 378, p. 43–63, doi:10.1016/j.tecto.2003.10.017.

Ren, J., Zhang, Z., Gai, H., and Kang, W., 2021, Typical Riedel shear structures of the coseismic surface rupture zone produced by the 2021 Mw 7.3 Maduo earthquake, Qinghai, China, and the implications for seismic hazards in the block interior: Natural Hazards Research, v. 1, p. 145–152, doi:10.1016/j.nhres.2021.10.001.

Renjith, A.R., Mamtani, M.A., and Urai, J.L., 2016, Fabric analysis of quartzites with negative magnetic susceptibility - Does AMS provide information of SPO or CPO of quartz? Journal of Structural Geology, v. 82, p. 48–59, doi:10.1016/j.jsg.2015.11.005.

Rhodes, E.L., Barker, A.K., Burchardt, S., Hieronymus, C.F., Rousku, S.N., McGarvie, D.W., Mattsson, T., Schmiedel, T., Ronchin, E., and Witcher, T., 2021, Rapid Assembly and Eruption of a Shallow Silicic Magma Reservoir, Reyðarártindur Pluton, Southeast Iceland: Geochemistry, Geophysics, Geosystems, v. 22, doi:10.1029/2021GC009999.

Rhodes, E., Burchardt, S., Greiner, S.H.M., Mattsson, T., Sigmundsson, F., Schmiedel, T., Barker, A.K., and Witcher, T., 2024, Volcanic unrest as seen from the magmatic source: Reyðarártindur pluton, Iceland: Scientific Reports, v. 14, doi:10.1038/s41598-023-50880-0.

Riedel, W., 1929, Zur Mechanik Geologischer Brucherscheinungen: Centralblatt für Mineralogie, Geologie und Paläontologie, v. 8, p. 354–368, https://oceanrep.geomar.de/id/eprint/52902 (accessed November 2024).

Roberts, A.P., Heslop, D., Zhao, X., and Pike, C.R., 2014, Understanding fine magnetic particle systems through use of first-order reversal curve diagrams: Reviews of Geophysics, v. 52, p. 557–602, doi:10.1002/2014RG000462.

Roberts, A.P., Hu, P., Harrison, R.J., Heslop, D., Muxworthy, A.R., Oda, H., Sato, T., Tauxe, L., and Zhao, X., 2019, Domain State Diagnosis in Rock Magnetism: Evaluation of Potential Alternatives to the Day Diagram: Journal of Geophysical Research: Solid Earth, v. 124, p. 5286–5314, doi:10.1029/2018JB017049.

Roberts, A.P., Pike, C.R., and Verosub, K.L., 2000, First-order reversal curve diagrams: A new tool for characterizing the magnetic properties of natural samples: Journal of Geophysical Research: Solid Earth, v. 105, p. 28461–28475, doi:10.1029/2000jb900326.

Rochette, P., Jackson, M., and Aubourg, C., 1992, Rock magnetism and the interpretation of anisotropy of magnetic susceptibility: Reviews of Geophysics, v. 30, p. 209–226, doi:10.1029/92RG00733.

Rosenbaum, G., 2014, Geodynamics of oroclinal bending: Insights from the Mediterranean: Journal of Geodynamics, v. 82, p. 5–15, doi:10.1016/j.jog.2014.05.002.

van Ruitenbeek, F.J.A., Cudahy, T., Hale, M., and van der Meer, F.D., 2005, Tracing fluid pathways in fossil hydrothermal systems with near-infrared spectroscopy: Geology, v. 33, p. 597–600, doi:10.1130/G21375.1.

De Saint Blanquat, M., Horsman, E., Habert, G., Morgan, S., Vanderhaeghe, O., Law, R., and Tikoff, B., 2011, Multiscale magmatic cyclicity, duration of pluton construction, and the paradoxical relationship between tectonism and plutonism in continental arcs: Tectonophysics, v. 500, p. 20–33, doi:10.1016/j.tecto.2009.12.009.

Sanderson, D.J., Andrews, J.R., Phillips, W.E.A., and Hutton, D.H.W., 1980, Deformation studies in the Irish Caledonides: J. geol. Soc. London, v. 137, p. 289–302, http://pubs.geoscienceworld.org/jgs/article-pdf/137/3/289/4886228/gsjgs.137.3.0289.pdf.

Sanderson, D.J., and Marchini, W.R.D., 1984, Transpression: Journal of Structural Geology, v. 6, p. 449–458, doi:10.1016/0191-8141(84)90058-0.

Sanderson, D.J., and Peacock, D.C.P., 2020, Making rose diagrams fit-for-purpose: Earth-Science Reviews, v. 201, doi:10.1016/j.earscirev.2019.103055.

Sant'Ovaia, H., Cruz, C., Gonçalves, A., Nogueira, P., and Noronha, F., 2024, Deciphering Iberian Variscan Orogen Magmatism Using the Anisotropy of Magnetic Susceptibility from Granites: Minerals, v. 14, doi:10.3390/min14030309.

Sawyer, E.W., 2000, Grain-scale and outcrop-scale distribution and movement of melt in a crystallising granite: Transactions of the Royal Society of Edinburgh: Earth Sciences, v. 91, p. 73–85.

Scaillet, B., Whittington, A., Martel, C., Pichavant, M., and Holtz, F., 2000, Phase equilibrium constraints on the viscosity of silicic magmas II: Implications for mafic—silicic mixing processes: Transactions of the Royal Society of Edinburgh, Earth Sciences, v. 91, p. 61–72, doi:10.1017/S026359330000729X.

Searle, M.P., 2021, Tectonic evolution of the Caledonian orogeny in Scotland: a review based on the timing of magmatism, metamorphism and deformation: Geological Magazine, p. 1–29, doi:10.1017/S0016756821000947.

Searle, M.P., Shail, R.K., Pownall, J.M., Jurkowski, C., Watts, A.B., and Robb, L.J., 2024, The Permian Cornubian granite batholith, SW England; Part 1: Field, structural, and petrological constraints: Geological Society of America Bulletin, doi:10.1130/b37457.1.

Shaw, J., Johnston, S.T., Gutiérrez-Alonso, G., and Weil, A.B., 2012, Oroclines of the Variscan orogen of Iberia: Paleocurrent analysis and paleogeographic implications: Earth and Planetary Science Letters, v. 329–330, p. 60–70, doi:10.1016/j.epsl.2012.02.014.

Siachoque, A., Morales, A., Cardona, A., Marulanda, U.M., and Zapata, S., 2024, Mineral fabrics unravel syn-magmatic deformation and constrain Permian and Jurassic tectonic regimes in arc plutons from the southern Colombian Andes: International Geology Review, p. 1–22, doi:10.1080/00206814.2024.2415098.

Siegesmund, S., and Becker, J.K., 2000, Emplacement of the Ardara pluton (Ireland): new constraints from magnetic fabrics, rock fabrics and age dating: Int J Earth Sci, v. 89, p. 307–327.

Sillitoe, R.H., 2010, Porphyry Copper Systems: Economic Geology, p. 3–41.

Smith, J. V, 1997, Shear thickening dilatancy in crystal-rich flows: Journal of Volcanology and Geothermal Research , v. 79, p. 1–8.

Smith, J. V, 2000, Structures on interfaces of mingled magmas, Stewart Island, New Zealand: Journal of Structural Geology, v. 22, p. 123–133, www.elsevier.nl/locate/jstrugeo.

Soper, N.J., Strachan, R.A., Holdsworth, R.E., Gayer, R.A., and Greiling, R.O., 1992, Sinistral transpression and the Silurian closure of Iapetus: Journal of the Geological Society of London, v. 149, p. 871–880, http://pubs.geoscienceworld.org/jgs/article-pdf/149/6/871/4892074/gsjgs.149.6.0871.pdf.

Soper, N.J., and Woodcock, N.H., 2003, The lost Lower Old Red Sandstone of England and Wales: A record of post-Iapetan flexure or Early Devonian transtension? Geological Magazine, v. 140, p. 627–647, doi:10.1017/S0016756803008380.

Sparks, R.S.J., Annen, C., Blundy, J.D., Cashman, K. V., Rust, A.C., and Jackson, M.D., 2019, Formation and dynamics of magma reservoirs: Philosophical Transactions of the Royal Society A: Mathematical, Physical and Engineering Sciences, v. 377, doi:10.1098/rsta.2018.0019.

Spencer, C.J., Murphy, J.B., Kirkland, C.L., Liu, Y., and Mitchell, R.N., 2018, A Palaeoproterozoic tectono-magmatic lull as a potential trigger for the supercontinent cycle: Nature Geoscience, v. 11, p. 97–101, doi:10.1038/s41561-017-0051-y.

Stephenson, A., Sadikun, S., and Potter, D.K., 1986, A theoretical and experimental comparison of the anisotropies of magnetic susceptibility and remanence in rocks and minerals: Geophysical Journal International, v. 84, p. 185–200, https://academic.oup.com/gji/article/84/1/185/593598.

Stern, R.J., and Gerya, T. V., 2024, The importance of continents, oceans and plate tectonics for the evolution of complex life: implications for finding extraterrestrial civilizations: Scientific Reports, v. 14, p. 8552, doi:10.1038/s41598-024-54700-x.

Stevenson, C., 2009, The relationship between forceful and passive emplacement: The interplay between tectonic strain and magma supply in the Rosses Granitic Complex, NW Ireland: Journal of Structural Geology, v. 31, p. 270–287, doi:10.1016/j.jsg.2008.11.009.

Stevenson, C.T.E., and Grove, C., 2018, Laccolithic Emplacement of the Northern Arran Granite, Scotland, Based on Magnetic Fabric Data, *in* Advances in Volcanology, Springer Science and Business Media Deutschland GmbH, p. 377–401, doi:10.1007/11157_2014_3.

Stevenson, C.T.E., Hutton, D.H.W., and Price, A.R., 2008a, The Trawenagh Bay Granite and a new model for the emplacement of the Donegal batholith: Transactions of the Royal Society of Edinburgh, Earth Sciences, v. 97, p. 455–477, doi:10.1017/s0263593300001565.

Stevenson, C.T.E., O'Driscoll, B., Holohan, E.P., Couchman, R., Reavy, R.J., and Andrews, G.D.M., 2008b, The structure, fabrics and AMS of the Slieve Gullion ring-complex, Northern Ireland: Testing the ring-dyke emplacement model: Geological Society Special Publication, v. 302, p. 159–184, doi:10.1144/SP302.12.

Stevenson, C.T.E., Owens, W.H., and Hutton, D.H.W., 2007a, Flow lobes in granite: The determination of magma flow direction in the Trawenagh Bay Granite, northwestern Ireland, using anisotropy of magnetic susceptibility: Bulletin of the Geological Society of America, v. 119, p. 1368–1386, doi:10.1130/B25970.1.

Stevenson, C.T.E., Owens, W.H., Hutton, D.H.W., Hood, D.N., and Meighan, I.G., 2007b, Laccolithic, as opposed to cauldron subsidence, emplacement of the Eastern Mourne pluton, N. Ireland: evidence from anisotropy of magnetic susceptibility: Journal of the Geological Society, v. 164, p. 99–110, doi:10.1144/0016076492006-008.

Stimac, J., Goff, F., and Goff, C.J., 2015, Intrusion-Related Geothermal Systems, *in* The Encyclopedia of Volcanoes, Elsevier, p. 799–822, doi:10.1016/B978-0-12-385938-9.00046-8.

Strachan, R.A., Alsop, G.I., Ramezani, J., Frazer, R.E., Burns, I.M., and Holdsworth, R.E., 2020, Patterns of Silurian deformation and magmatism during sinistral oblique convergence, northern Scottish Caledonides:, doi:10.6084/m9.figshare.c.4962251.

Tarling, D.H., and Hrouda, F., 1993, The magnetic anisotropy of rocks: Chapman & Hall, 217 p.

Tauxe, L., 1998, Paleomagnetic Principles and Practice: Dordrecht: Kluwer Academic Publishers.

Tauxe, L., Mullender, T.A.T., and Pick, T., 1996, Potbellies, wasp-waists, and superparamagnetism in magnetic hysteresis: Journal of Geophysical Research: Solid Earth, v. 101, p. 571–583, doi:10.1029/95jb03041.

Tomek, F., Žák, J., and Chadima, M., 2015, Granitic magma emplacement and deformation during early-orogenic syn-convergent transtension: The Staré Sedlo complex, Bohemian Massif: Journal of Geodynamics, v. 87, p. 50–66, doi:10.1016/j.jog.2015.02.007.

Tomek, F., Žák, í, Verner, K., Holub, F. V, Sláma, í, Paterson, S.R., and Memeti, V., 2017, Mineral fabrics in high-level intrusions recording crustal strain and volcano-tectonic interactions: the Shellenbarger pluton, Sierra Nevada, California: Journal of the Geological Society, v. 174, p. 193–208, doi:10.6084/m9.figshare.c.3582749.

Tomek, F., Žák, J., Verner, K., Ježek, J., and Paterson, S.R., 2024, A Complex Interplay Between Pluton Emplacement, Tectonic Deformation, and Plate Kinematics in the Cretaceous Sierra Nevada Magmatic Arc, California: Tectonics, v. 43, doi:10.1029/2023TC007822.

Troll, V.R., Nicoll, G.R., Ellam, R.M., Emeleus, C.H., and Mattsson, T., 2021, Petrogenesis of the Loch Bà ring-dyke and Centre 3 granites, Isle of Mull, Scotland: Contributions to Mineralogy and Petrology, v. 176, doi:10.1007/s00410-020-01763-4.

Vernon, R.H., 2018, A Practical Guide to Rock Microstructure: Cambridge, Cambridge University Press, doi:https://doi.org/10.1017/9781108654609.

Vernon, R.H., 1990, Crystallization and hybridism in microgranitoid enclave magmas: microstructural evidence: Journal of Geophysical Research, v. 95, doi:10.1029/jb095ib11p17849.

Vernon, R.H., 1984, Microgranitoid enclaves in granite - globules of hybrid magma quenched in a plutonic environment.: Nature, v. 309, p. 438–439.

Vernon, R.H., 2014, Microstructures of microgranitoid enclaves and the origin of S-type granitoids: Australian Journal of Earth Sciences, v. 61, p. 227–239, doi:10.1080/08120099.2014.886623.

Vernon, R.H., and Paterson, S.R., 1993, The Ardara pluton, Ireland: deflating an expanded intrusion: Lithos, v. 31, p. 17–32.

Verwey, E.J.W., and Haayman, P.W., 1941, Electronic conductivity and transition point of magnetite (“Fe3O4”): Physica, v. 8, p. 979–987, doi:10.1016/S0031-8914(41)80005-6.

Vigneresse, J.L., Barbey, P., and Cuney, M., 1996, Rheological Transitions During Partial Melting and Crystallization with Application to Felsic Magma Segregation and Transfer: Journal of Petrography, v. 37, p. 1579–1600, https://academic.oup.com/petrology/article/37/6/1579/1406720.

Weinberg, R.F., Vernon, R.H., and Schmeling, H., 2021, Processes in mushes and their role in the differentiation of granitic rocks: Earth-Science Reviews, v. 220, doi:10.1016/j.earscirev.2021.103665.

White, N.J., and Hutton, D.H.W., 1985, The Structure of the Dalradian Rocks in West Fanad, County Donegal: Irish Journal of Earth Sciences, v. 7, p. 79–92, https://www.jstor.org/stable/30002385 (accessed September 2021).

Williams, K.M., Urbani, S., Mariani, E., Biggin, A., Wheeler, J., and Kavanagh, J.L., 2025, Unravelling the complex record of magma flow and solidification in sills: Journal of the Geological Society, v. 182, doi:10.1144/jgs2024-120.

Witcher, T., Burchardt, S., Mattsson, T., Heap, M.J., and McCarthy, W., 2024, Development of permeable networks by viscous-brittle deformation in a shallow rhyolite intrusion. Part 1: Field evidence: Journal of Volcanology and Geothermal Research, v. 454, doi:10.1016/j.jvolgeores.2024.108166.

Woodcock, N.H., 1990, Sequence stratigraphy of the Palaeozoic Welsh Basin: Journal of the Geological Society, v. 147, p. 537–547, doi:10.1144/gsjgs.147.3.0537.

Worm, H. -U, Clark, D., and Dekkers, M.J., 1993, Magnetic Susceptibility of Pyrrhotite: Grain Size, Field and Frequency Dependence: Geophysical Journal International, v. 114, p. 127–137, doi:10.1111/j.1365-246X.1993.tb01472.x.

Žák, J., Hrouda, F., and Holub, F. V., 2010, Plane-confined magnetic lineations in mingled mafic and felsic magmas, the Sázava pluton, Bohemian Massif: Journal of Volcanology and Geothermal Research, v. 190, p. 312–324, doi:10.1016/j.jvolgeores.2009.12.002.

Žák, J., and Klomínský, J., 2007, Magmatic structures in the Krkonoše-Jizera Plutonic Complex, Bohemian Massif: evidence for localized multiphase flow and small-scale thermal-mechanical instabilities in a granitic magma chamber: Journal of Volcanology and Geothermal Research, v. 164, p. 254–267, doi:10.1016/j.jvolgeores.2007.05.006.

Žák, J., Paterson, S.R., and Memeti, V., 2007, Four magmatic fabrics in the Tuolumne batholith, central Sierra Nevada, California (USA): Implications for interpreting fabric patterns in plutons and evolution of magma chambers in the upper crust: Bulletin of the Geological Society of America, v. 119, p. 184–201, doi:10.1130/B25773.1.

Žák, J., Verner, K., Holub, F. V., Kabele, P., Chlupáčová, M., and Halodová, P., 2012, Magmatic to solid state fabrics in syntectonic granitoids recording early Carboniferous orogenic collapse in the Bohemian Massif: Journal of Structural Geology, v. 36, p. 27–42, doi:10.1016/j.jsg.2011.12.011.

Žák, J., Verner, K., Klomínský, J., and Chlupáčová, M., 2009, “Granite tectonics” revisited: Insights from comparison of K-feldspar shape-fabric, anisotropy of magnetic susceptibility (AMS), and brittle fractures in the Jizera granite, Bohemian Massif: International Journal of Earth Sciences, v. 98, p. 949–967, doi:10.1007/s00531-007-0292-x.

Žák, J., Verner, K., and Týcová, P., 2008a, Grain-scale processes in actively deforming magma mushes: New insights from electron backscatter diffraction (EBSD) analysis of biotite schlieren in the Jizera granite, Bohemian Massif: Lithos, v. 106, p. 309–322, doi:10.1016/j.lithos.2008.08.006.

Žák, J., Verner, K., and Týcová, P., 2008b, Multiple magmatic fabrics in plutons: An overlooked tool for exploring interactions between magmatic processes and regional deformation? Geological Magazine, v. 145, p. 537–551, doi:10.1017/S0016756808004573.

Zaniewski, A., Reavy, R.J., and Harris, A.L., 2006, Field relationships and emplacement of the Caledonian Ross of Mull Granite, Argyllshire: Scottish Journal of Geology, v. 42, p. 179–189, doi:10.1144/sjg42020179.

Zibra, I., Kruhl, J.H., Montanini, A., and Tribuzio, R., 2012, Shearing of magma along a high-grade shear zone: Evolution of microstructures during the transition from magmatic to solid-state flow: Journal of Structural Geology, v. 37, p. 150–160, doi:10.1016/j.jsg.2012.01.011.